COPPER AND IRON COMPLEXES WITH UNUSUAL COORDINATION GEOMETRIES ENFORCED BY PHOSPHINE CHELATES

Thesis by

Neal P. Mankad

In Partial Fulfillment of the Requirements

for the Degree of

Doctor of Philosophy

California Institute of Technology

Pasadena, CA

2010

(Defended December 4, 2009)

Acknowledgments

First I would like to thank my thesis advisor, Professor Jonas Peters. It seems to me that I gain important lessons not only about chemistry but also about logic, the scientific method, group management, and interpersonal relationships every single time I sit in a meeting run by Jonas. When integrated over the course of several years, this means that many of my mental algorithms and thought processes have been molded directly by Jonas (whether or not he realizes it), and for this I am proud and grateful. Graduate school occurs at a tumultuous and formative span of one's life, and as a result it can be a roller coaster ride of emotions and life events outside the lab. Throughout my time in graduate school I have experienced not only the highest of highs, but also many very deep lows. Regarding the latter, Jonas went above and beyond what should be expected of a research advisor in order to provide support for me. There have been many periods of time over the last several years during which I did not think I would make it to the point of writing this document. These instances of help from Jonas are in large part responsible for my arrival here.

Professor John Bercaw, as the chairperson of my candidacy and thesis committees, has been a wealth of knowledge and helpful suggestions. (He even got into the lab and showed me how to perform a Toepler pump analysis at one time!) When observing my peers, I realize that few committee chairs are as conscientious and thorough as John is, and for this I am thankful. The other professors on my committees (Professors Brian Stoltz, Robert Grubbs, and Sarah Reisman), have been sources of terrific advice during oral exams and meetings.

I have had the pleasure of collaborating with two professors from other institutions during the course of my research. I particularly enjoyed traveling to Stanford's synchrotron to collect XAS data with Professor Robert Szilagyi. Those days at the beamline were sleepless, intense, and extremely educational. The work that came out of our collaboration really transformed the way I think about molecules, and the lessons learned provide an underlying basis for much of the work in this thesis, either directly or indirectly. Though I have never actually met Professor William Antholine, our collaboration regarding multifrequency EPR spectroscopy has been extremely stimulating and educational. The emails we continuously bounced back and forth were exchanges to which I always looked forward, and I hope to meet Bill someday soon. Both Professors Szilagyi and Antholine were striking in their promptness in collecting and analyzing data, and this was the cherry on top of all the other positive aspects of our collaborations.

I have had tremendous coworkers, in fact too many to name individually. I would like to list the folks with whom I coauthored papers, as these people necessarily had a large impact on my research: Dr. Seth Harkins, Dr. Matthew Whited, Dr. Yunho Lee, Paul Oblad, Alex Miller, Professor Christine Thomas, and Professor Eric Rivard. Ayumi Takaoka (the *real* Grand Master) contributed insightful discussions about my research even though he does not appear on the list above. In addition, I am thankful for the friendship, support, distracting lunch trips, and/or beer outings from the following group members: Dr. Bruce MacKay, Kathleen Hand, Professor Mark Mehn, Professor Xile Hu, Dr. Nate Szymczak, and Professor Louise Berben. During the time at MIT, there have been more glove box malfunctions and other issues than I care to remember, and getting through them has been an adventure through which Charlene Tsay was my invaluable

partner; to her I wish all possible luck in research and life. Caroline Saouma was my partner in founding and operating the Metals in Synthesis seminar series at MIT, and I am very proud of what we accomplished. It is impossible for one's science to be unaffected by any research groupmate, and so I am also thankful for all the co-workers who have been omitted here for the sake of brevity, and I hope for them continued success. People outside of the Peters group whom I wish to acknowledge for their friendship include Dr. Michelle Farkas, Dr. and Mrs. Kevin and Melissa Kuhn, Nathaniel Sherden, Dr. Jeff Byers, Miranda Priebe, Philip Guo, and Adam Kumpf. Dr. Charles Hamilton alerted me to the quotation from *Hitchhiker's Guide to the Galaxy* that begins this dissertation.

One of the methods key to my research has been X-ray crystallography. Larry Henling taught me most of what I know about selecting and mounting crystalline samples as well as solving and refining X-ray structures. It is amazing to me how available Larry was at all hours of day or night, and how much time he devoted to teaching me and others. Not only did he provide scientific assistance, but also he was a friend to me and to the group as a whole. Unfortunately, I did not have as many interactions with Dr. Peter Müller while doing crystallography at MIT as I would like, but it is striking how much I could learn from him in just a short time. The following individuals provided other types of technical assistance: Dr. Angelo DiBilio (EPR), John Keith (DFT), and Tim Kowalczyk (DFT). Professor Seth Brown provided useful suggestions regarding the work presented in Chapter 5.

I also would like to thank Dr. Joseph Sadighi, who was my undergraduate research advisor. He was kind enough to hire me when I had absolutely no experience and shockingly minimal knowledge about chemistry, and I feel lucky that he molded

much of the research interests and laboratory skills that I hold to this day. I hope that Joseph is happy, successful, and above all safe in his new role in the U.S. Army.

I want to acknowledge the mental-health facilities at both Caltech and MIT for the services they provide to their respective institutions. It is no secret to many of my coworkers that professionals at both facilities have assisted me, and I suspect many of them also have sought help. Especially at pressure-rich environments such as Caltech and MIT, it is essential to have trained professionals available to help us through these turbulent times. I hope that as time moves forward, the social stigma associated with seeking mental-health counseling will continue to become marginalized.

Obtaining a Caltech degree while spending the final years doing research at MIT has been (not surprisingly) an administrative nightmare of sorts. Several people have made the whole process easier, most notably Karen Fosher, Rich Wilk, and Agnes Tong. Janet MacLaughlin has been extremely helpful with laboratory financial matters while I was managing the group's purchasing at MIT.

My first three years of graduate school were funded by a NSF Graduate Research Fellowship. Additionally, my research been supported financially at various times by BP MC^2, NSF, and NIH. XAS data was collected at the Stanford Synchrotron Radiation Lightsource, which is supported by DOE and NIH. Multifrequency EPR studies were conducted at the National Biomedical EPR Center at the Medical College of Wisconsin, which is supported by NIH. Computational studies in Chapter 2 were conducted at the Materials and Process Simulation Center at Caltech. X-ray crystallography studies in Chapters 2, 4, and 6 were conducted at the Beckman Institute Crystallography Facility at Caltech; those in Chapters 3 and 5 were conducted at the MIT X-ray Diffraction Facility.

Of course, none of this would be possible without my parents, Pankaj and Minaxi Mankad. They made me who I am today, allowed me to attend such wonderful schools that educated me as a scientist, and provided never-ending love and support. My wife, Lindsey McQuade, helped me through times thick and thin during the last couple of years, and I anxiously look forward to our journey together during our next stage of life and beyond.

Abstract

Chelating phosphine ligands were used to enforce targeted coordination geometries onto complexes of iron and copper, thereby imparting molecular properties distinct relative to species studied previously in other geometries. The bulky bis(phosphino)borate ligand $[Ph_2B(CH_2P^tBu_2)_2]^-$ was used to provide trigonal planar complexes of Cu. This structural motif provided a rare opportunity for a single framework to stabilize Cu complexes in three discrete oxidation levels and allowed for the study of unique ligands including diazoalkanes, a diphenylcarbene, diarylamides, and a diarylaminyl radical. In the latter case, physical measurements (multiedge XAS and multifrequency EPR spectroscopy) and theoretical methods (DFT) were used to quantitate the delocalization of spin density between the Cu center and the NAr_2 unit, providing a comprehensive electronic structure picture for L_2CuER_2 (E = C or N) complexes in this system. In separate studies, trigonal bipyramidal Fe complexes were generated using the bulky, anionic tris(phosphino)silyl ligands $[(2\text{-}R_2PC_6H_4)_3Si]^-$ (R = Ph or *i*Pr). Low-valent Fe species in this system were found to activate dinitrogen, providing labile N_2 ligands *trans* to the silyl donor, including the first instance of a terminally bound N_2 ligated to a paramagnetic Fe center. Subsequent reactions involving these Fe^I-N_2 species and organoazides provided entry to unusual catalytic N-N coupling reactions. These reactions were found to involve reactive FeNAr intermediates, destabilized by virtue of the trigonal bipyramidal coordination geometry, which subsequently coupled bimolecularly in the N-N bond-forming step. The effects of perturbing previously studied C_3-symmetric pseudotetrahedral iron complexes to their trigonal bipyramidal analogues proved key to uncovering the chemistry of interest.

Table of Contents

List of Figures

Chapter 1

Chapter 2

Chapter 3

Chapter 4

Chapter 5

Appendix 2

List of Tables

Chapter 4

Chapter 5

Chapter 6

Appendix 1

Appendix 5

List of Abbreviations

A^x	Hyperfine coupling due to nucleus x
A_t	Absorption at time t
Ac	Acetyl
Ad	1-Adamantyl
Anal	Analysis
Ar	Generic aryl group
$Ar_2BP^R_2$	$Ar_2B(CH_2PR_2)_2$
Ar^F	$3,5\text{-}(F_3C)_2C_6H_3$
atm	Atmosphere
ATP	Adenosine triphosphate
AZ	Arizona
B	Applied magnetic field
B(38)HFP86	A specific hybrid gradient-corrected density functional
B3LYP	Beck 3-parameter function with Lee-Yang-Parr correlation
BP_3	Generic tris(phosphino)borate ligand
br	Broad
Bu	*n*-Butyl
C	Concentration
C_3, D_{2d}	Schoenflies symmetry designations
ca	Circa
calcd	Calculated
CCD	Charge-coupled device

cm	Centimeter
cm^{-1}	Wavenumber
COD	Cyclooctadiene
Cp	Cyclopentadienyl
Cp*	Pentamethylcyclopentadienyl
CV	Cyclic voltammetry
Cy	Cyclohexyl
Cys	Cysteine
D	Deuterium
d	Doublet
dB	Decibel
ddm	Doublet of doublet of multiplets
deg	Degree
depe	1,2-Bis(diethylphosphino)ethane
DFT	Density functional theory
DHA	9,10-Dihydroanthracene
diff	Difference
dm	Doublet of multiplets
DMSO	Dimethylsulfoxide
dppe	1,2-Bis(diphenylphosphino)ethane
dt	Doublet of triplets
DTBN	Di-*tert*-butylnitroxyl radical
dtbpe	1,2-Bis-(di-*tert*-butylphosphino)ethane

E	Generic main-group element
e	Electron
$E^{0'}$	Potential at standard conditions
EPR	Electron paramagnetic resonance
eq	Equation
equiv	Equivalents
esd	Estimated standard deviation
ESI	Electrospray ionization
est	Estimated
ET	Electron transfer
Et	Ethyl
eV	Electron volt
F	Structure factor
Fc	Ferrocene
FeMo cofactor	Iron-molybdenum cofactor of nitrogenase
fig	Figure
FT	Fourier transform
G	Gauss
g	Gram
g	Electron *g*-factor
GC	Gas chromatography
GHz	Gigahertz
Gln	Glutamine

GT	Gaussian-type
h	Hour
HAT	Hydrogen atom transfer
His	Histidine
HOMO	Highest occupied molecular orbital
Hz	Hertz
I	Nuclear spin *or* intensity
Inc	Incorporated
*i*Pr	*iso*-Propyl
IR	Infrared
J	NMR coupling constant
${}^{x}J_{yz}$	x-bond NMR coupling constant between nuclei y and z
K	Kelvin
kcal	Kilocalorie
k_H/k_D	Deuterium isotope effect
KS	Kansas
k_S	Self-exchange rate constant
L	Generic neutral ligand
L^R	Generic β-diketiminate ligand with substituents R
LACVP	Los Alamos core valence potential
LLC	Limited liability company
l.s.	Least squares
LUMO	Lowest unoccupied molecular orbital

Lut	2,6-Lutidine
M	Generic transition metal *or* molar
m	Multiplet
m	*meta*
MA	Massachusetts
max	Maximum
Me	Methyl
Mes	Mesityl
Met	Methionine
MeTHF	Methyltetrahydrofuran
mg	Milligram
MHz	Megahertz
MIDI!	A specific basis set for DFT
min	Minute *or* minimum
mL	Milliliter
MLCT	Metal-to-ligand charge transfer
mM	Millimolar
mm	Millimeter
mmol	Millimole
MO	Molecular orbital
mol	Mole
MS	Mass spectrometry
ms	Millisecond

mV	Millivolt
*n*Bu	*n*-Butyl
nm	Nanometer
NMR	Nuclear magnetic resonance
NP_3	e.g., $N(CH_2CH_2PR_2)_3$
o	*ortho*
OR	Oregon
p	*para*
PA	Pennsylvania
Ph	Phenyl
$Ph_2BP^{tBu}_2$	$Ph_2B(CH_2P^tBu_2)_2$
$PhBP^R_3$	$PhB(CH_2PR_2)_3$
ppm	Parts per million
p-Tol	*p*-tolyl
pyr	Pyridine
q	Quartet
R	Generic organic group *or* residual *or* R-factor
RAMO	Redox-active molecular orbital
ref	Reference
rt	Room temperature
S	Goodness-of-fit *or* spin
s	Singlet *or* second
SCF	Self-consistent field

SiP_3	Generic tris(phosphino)silyl ligand
SiP^R_3	$(2\text{-}R_2PC_6H_4)_3Si$
st	Stretch
T	Tesla
t	Triplet *or* time
$t_{1/2}$	Half-life
TBP	Trigonal bipyramidal
*t*Bu	*tert*-Butyl
td	Triplet of doublets
temp	Temperature
Tf	SO_2CF_3
THF	Tetrahydrofuran
Tol	*p*-tolyl
TP	Trigonal pyramidal
tq	Triplet of quartets
tt	Triplet of triplets
UV	Ultraviolet
V	Volt
v	Version
Vis	Visible
vs	Versus
W	Linewidth
wR	Weighted R-factor

wt	Weight
X	Generic anionic ligand
XAS	X-ray absorption spectroscopy
δ	Chemical shift *or* bend
ε	Extinction coefficient in units of $M^{-1}cm^{-1}$
η^x	Hapticity of order x
λ	Reorganization energy *or* wavelength
λ_{max}	Wavelength of local maximum intensity
μ	Absorption coefficient
μ-X	Bridging X ligand
μ_B	Bohr magneton
μ_{eff}	Effective magnetic moment
μL	Microliter
ν	Frequency *or* stretch
$\nu_{1/2}$	Full width at half maximum
Σ	Summation
σ	(In X-ray diffraction) standard deviation
τ	Index of trigonality for 5-coordinate complexes
θ	Angle in X-ray diffraction
χ	Mole fraction
$\parallel$	Parallel
$\perp$	Perpendicular
$^\circ$	Degree

°C	Degrees Celsius
Å	Angstrom
∠	Angle
12-C-4	12-crown-4
*n*E	*n* number of element E
^{1}H	Hydrogen-1
^{13}C	Carbon-13
^{19}F	Fluorine-19
^{29}Si	Silicon-29
^{31}P	Phosphorus-31
^{195}Pt	Platinum-195
{^{1}H}	Proton-decoupled
6-311G, etc.	Basis sets for DFT

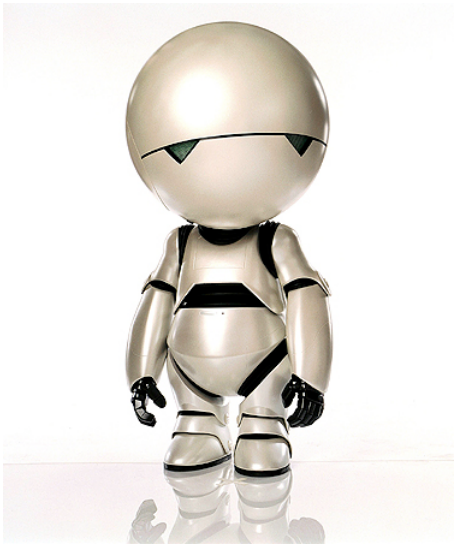

“The first ten million years were the worst, and the second ten million years, they were the worst too. The third ten million I didn't enjoy at all. After that I went into a bit of a decline.”

– Marvin, *Hitchhiker’s Guide to the Galaxy* by Douglas Adams

Chapter 1: Introduction

1.1 Opening Remarks

One theme unifying the various research projects presented in this dissertation is the use of coordination geometry to control the properties of transition metal complexes, in particular focusing on structure, spectroscopy, and chemical reactivity.

Chapters 2 and 3 concern copper complexes with trigonal planar coordination geometries. Though copper(I) is known to be quite promiscuous with regard to its coordination number and geometry, classical complexes of copper(II) and copper(III) tend to require coordination numbers of 4 or higher and place themselves in tetragonal geometries. The results presented here involve the use of a bulky, chelating, anionic bis(phosphino)borate ligand to enforce trigonal planar geometries onto such oxidized copper complexes, allowing for studies of species with ligands such as carbenes ($:CR_2$, Chapter 2) and aminyl radicals ($\cdot NR_2$, Chapter 3).

Chapters 4 and 5 feature iron complexes with trigonal bipyramidal (TBP) coordination geometries. Previous studies in the Peters group have focused on iron complexes in pseudotetrahedral environments enforced by bulky, chelating, anionic tris(phosphino)borate (BP_3) ligands. The design strategy utilized here involves replacing the non-coordinating borate anchor of the BP_3 frameworks with a tightly coordinating silyl anchor while retaining threefold symmetry, thereby shifting the paradigm from 4-coordinate, tetrahedral systems to 5-coordinate, TBP systems. This goal was achieved with tris(phosphino)silyl (SiP_3) ligands. Chapter 4 presents the synthesis of these ligands and several corresponding Fe-containing complexes that served as precursors for N_2 activation and reduction. In Chapter 5, one of these low-valent iron-dinitrogen species is used as a precursor to study interactions of iron centers with organoazides, leading

eventually to studies of unusual catalytic N-N coupling reactions and the unique reactivity of high-energy iron-imido complexes (FeNR) that are destabilized by virtue of the trigonal bipyramidal geometry. In both chapters, subtle but important differences arising from the shift from tetrahedral to TBP iron centers contributed to the findings and are highlighted in this dissertation.

The remainder of this introductory chapter will provide discussions of the importance of coordination geometry as it relates to these various topics, contextualizing them within larger problems of interest in inorganic chemistry.

1.2 Electron Transfer at Copper-Containing Active Sites

Transition metal active sites are found regularly in proteins for which rapid and efficient electron transfer (ET) processes are crucial. One such motif is the well-known set of iron-sulfur cluster structures.[1] Other electron transfer sites contain either mono- or dicopper cores (Figure 1.1).[1b] For example, the dinuclear Cu_A site is a structural motif found in the enzymes cytochrome *c* oxidase and nitrous oxide reductase.[2] The Cu_A sites contain highly covalent dicopper bis(μ-cystein) cores, often referred to as "diamond cores," supported by additional Met and Gln residues. On the other hand, the type-1 copper active sites are monometallic cores found in the "blue copper" family of proteins.[3] The common link between all of the type-1 active sites is a highly covalent His_2Cys donor set conferring trigonal symmetry to the copper centers; the various proteins further stabilize the low-coordinate copper center with zero, one, or two additional residues at long (>2.6 Å) distances. Both the dinuclear Cu_A sites and the mononuclear type-1 sites are able to mediate electron transfer processes with extremely rapid rates.

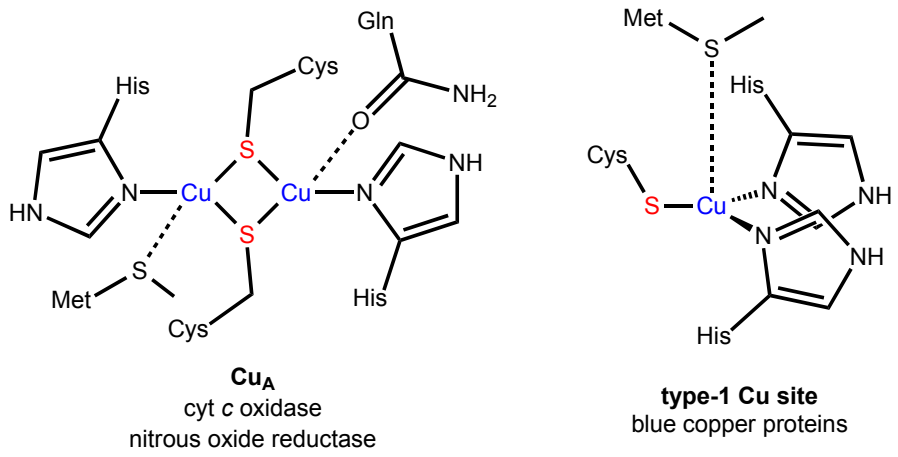

Figure 1.1. Schematics of the (*left*) Cu_A and (*right*) type-1 active sites found in biological electron transfer proteins.

A fascinating question is how Nature has been able to utilize these copper-containing active sites for efficient electron transfer, considering that ET in non-biological copper-containing systems is typically inefficient because it is accompanied by significant structural rearrangements and/or ligand redistributions. For example, cupric ions tend to reside in tetragonal geometries that distort severely to tetrahedral or trigonal geometries upon reduction to the cuprous state (Figure 1.2).[4] Clearly, biological systems are able to minimize redox-induced structural change (and thus the reorganizational term λ)[5] in order to maximize ET efficiency. Research from several research groups over several decades has established two main hypotheses concerning this phenomenon.

One hypothesis involves the "entatic state," wherein it is proposed that a protein matrix confers a strained ("entatic") geometry that is intermediary between the two limiting structures (Figure 1.2).[6] The ground state geometry therefore resembles the transition state geometry during ET, and thus λ is extremely small and ET rates are

extremely large. Several groups, most notably that of Rorabacher,[4] have sought Cu model compounds that demonstrate this principle.

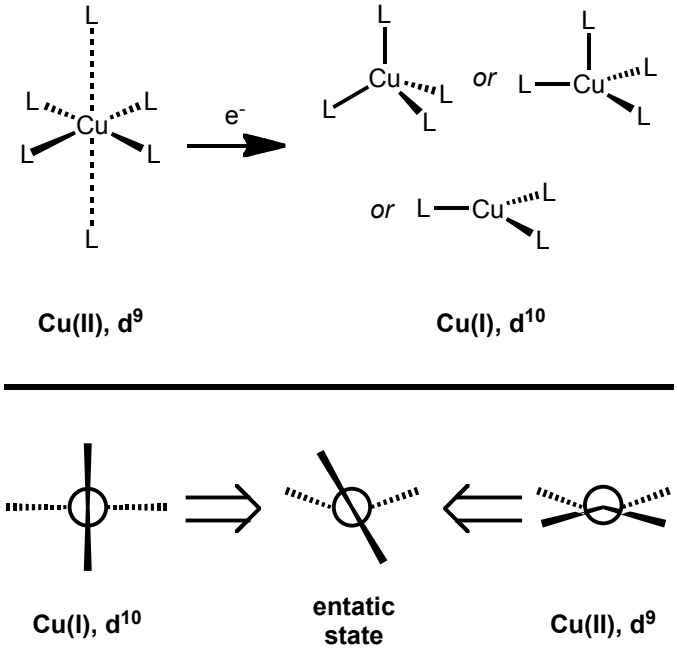

Figure 1.2. Schematics representing (*top*) redox-induced structural reorganization in nonbiological Cu systems, and (*bottom*) the entatic state geometry of Cu centers.

The second hypothesis concerns intimate electron structure, wherein metal-ligand covalency, as opposed to strained geometry, stabilizes electronic states. Solomon, in particular, has advanced this idea with detailed studies of the electronic structures of the type-1 and Cu_A sites,[7] both of which contain short and highly covalent Cu-thiolate bonds (Figure 1.1). For example, a combination of spectroscopic and theoretical analyses have shown that the redox-active molecular orbital (RAMO) of Cu_A is highly delocalized, and that in fact the unpaired spin of the oxidized, formally $Cu^{1.5}Cu^{1.5}$ state resides to a larger extent on the two bridging S atoms (46%) than on the two Cu centers (44%).[7b] Dicopper

model complexes from the Peters group featuring $Cu_2(\mu\text{-}XR_2)$ diamond cores (X = N or P)[8] exhibit similar covalency[8c,9] (Figure 1.3) and match the efficiency of Cu_A during self-exchange ET reactions.[8a] Highly covalent $Cu_2(\mu\text{-}SR)_2$ cores also have been detailed by Tolman,[10] though they do not mediate reversible redox chemistry.

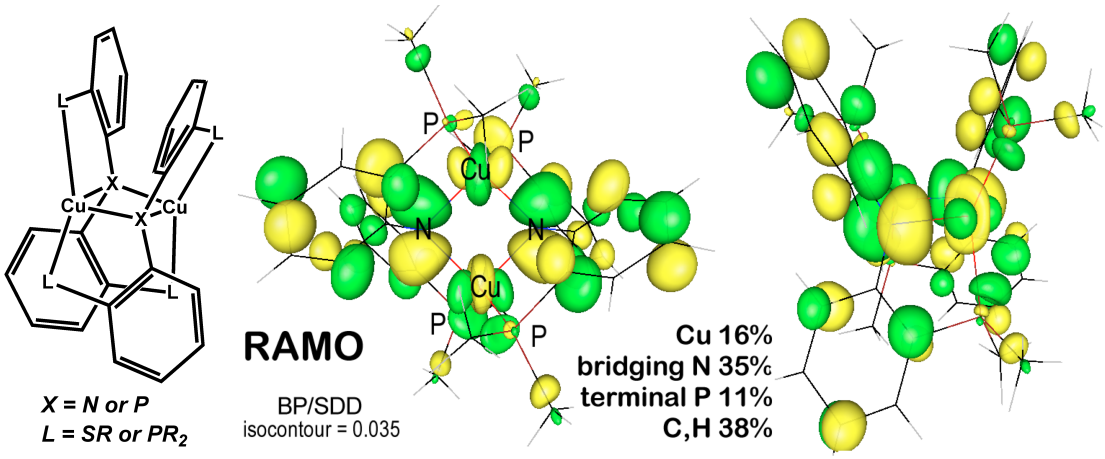

Figure 1.3. (*left*) Generalized drawing of the dicopper model complexes of the Peters group. (*right*) Spin density plots (top and side views) for a complex with X = N and L = di(*iso*-butyl)phosphino taken from ref 8c.

The collection of model compounds relevant to the trigonally symmetric type-1 active sites is less well developed. Though large ET rate constants in the range observed for blue copper proteins have been achieved in certain synthetic monocopper systems using geometries distinct from trigonal environments,[11] ET studies had yet to be conducted in synthetic systems featuring isolated, trigonally disposed copper centers prior to our work. The simplest such systems would contain trigonal planar geometries, and the dearth of model compounds results in part from the marked absence of three-coordinate cupric ions in the literature. Tolman's set of (β-diketiminate)copper(II)

complexes[12] were the only three-coordinate, formally copper(II) complexes known prior to our work.

During our work with trigonal planar, copper(I) amide anions (see Chapter 2), we became interested in the possibility of 1-electron oxidation to provide access to neutral, formally copper(II) amides. Chapter 3 describes the properties of this reversible redox process. This synthetic L_2CuX framework is related conceptually to the $(His)_2Cu(Cys)$ framework found in type-1 active sites, and so the electron structure of the Cu-N linkage in these complexes became the focus of our attention.

At this point it is useful to consider the possible electronic structures of the L_2CuER_2 fragment (E = C (Chapter 2) or N (Chapter 3)). Figure 1.4 depicts the two limiting conformations for the ER_2 moiety relative to the L_2Cu plane. Placing the R substituents in the L_2CuE plane results in a destabilizing filled-filled dπ-pπ interaction that is perpendicular to the plane, resulting in a completely filled π* level and no net π-bonding. On the other hand, placing the ER_2 plane perpendicular to the L_2Cu plane causes a E pπ orbital to mix with a dπ-orbital that is also destabilized by σ* interaction with the L donors. Thus, in this scenario the π* orbital is unoccupied (E = C) or partially occupied (E = N), resulting in some degree of net π-bonding. This more stable conformation is observed experimentally for known $Cu{=}CR_2$ complexes[13] and for the $Cu\text{-}NR_2$ complex presented in Chapter 3.

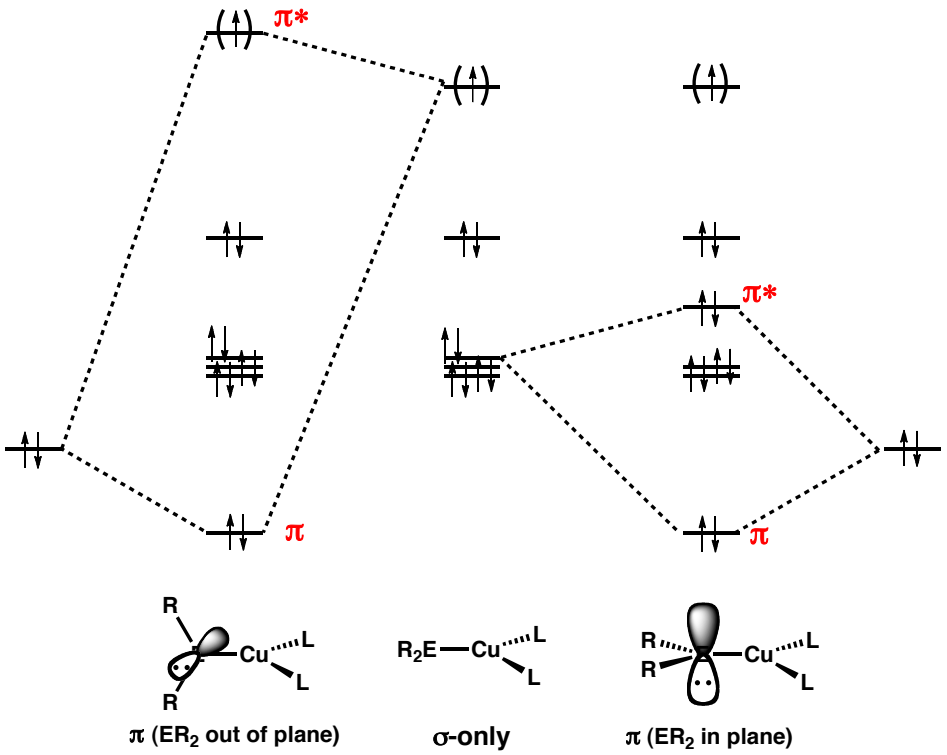

Figure 1.4. (*middle*) Qualitative d-orbital splitting diagram for a trigonal planar Cu center considering only σ-symmetric interactions (E = C or N). Perturbations resulting from two different ER_2 conformations: ER_2 substituents oriented (*left*) perpendicular to the L_2Cu plane and (*right*) in the L_2Cu plane.

The stabilized electronic structure depicted in the left portion of Figure 1.4 is a direct result of the coordination geometry enforced by the chelating ligand architecture and places the Cu-E π* level at high energy. This destabilized orbital is, as a result, highly redox active. Accordingly, it ranges from completely filled in the cuprous precursor species, to partially filled in the neutral copper aminyl of Chapter 3, and to completely empty in the copper carbene of Chapter 2. It is highly unusual for a single geometry to support three distinct oxidation levels for a mononuclear copper species, but

here the trigonal planar geometry enables it by delocalizing the RAMO across highly covalent Cu-E linkages (Figure 1.4). Chapter 3 describes in detail the physical measurements we have used to measure quantitatively the degree Cu-N bond covalency and the physical nature of the RAMO.

1.3 Nitrogen fixation using iron

The Haber-Bosch process is arguably the most important reaction in synthetic chemistry. In this atom-economical, though energy-intensive process, gaseous N_2 and H_2 are passed over a catalyst, usually consisting of iron, at high temperatures (400-500 °C) and high pressures (100-300 atm) to produce NH_3 on scales of approximately 130 metric tons per year worldwide. The majority of this synthetic ammonia is devoted to making fertilizers. It has been estimated that, as a result, approximately 75% of all nitrogen in human dietary protein comes from synthetic ammonia, and furthermore that approximately half of the nitrogen atoms in the human body currently come ultimately from the Haber-Bosch process.[14] In short, contemporary human population levels could not be sustained without the existence of the large-scale Haber-Bosch facilities we have today. The amount of energy devoted to this process worldwide is staggering. Because of the high temperatures and pressures required, the resulting elaborate reactor facilities, and the processes associated with obtaining the hydrogen feedstock, the Haber-Bosch process accounts for about 2% of the world's total energy consumption.[14]

Conversely, the bacterial nitrogenase enzymes are able to catalyze the reduction of dinitrogen to ammonia at ambient conditions (albeit at a large cost of 16 equivalents of the biological energy currency ATP). In the most common form of nitrogenase, substrate

binding and catalytic turnover occurs at a multinuclear cluster called the FeMo cofactor,[15] which consists of 7 Fe centers, 10 S atoms, a single Mo site, a homocitrate ligand, and a central unidentified ("X") atom that is either C, N, or O (Figure 1.5).[16]

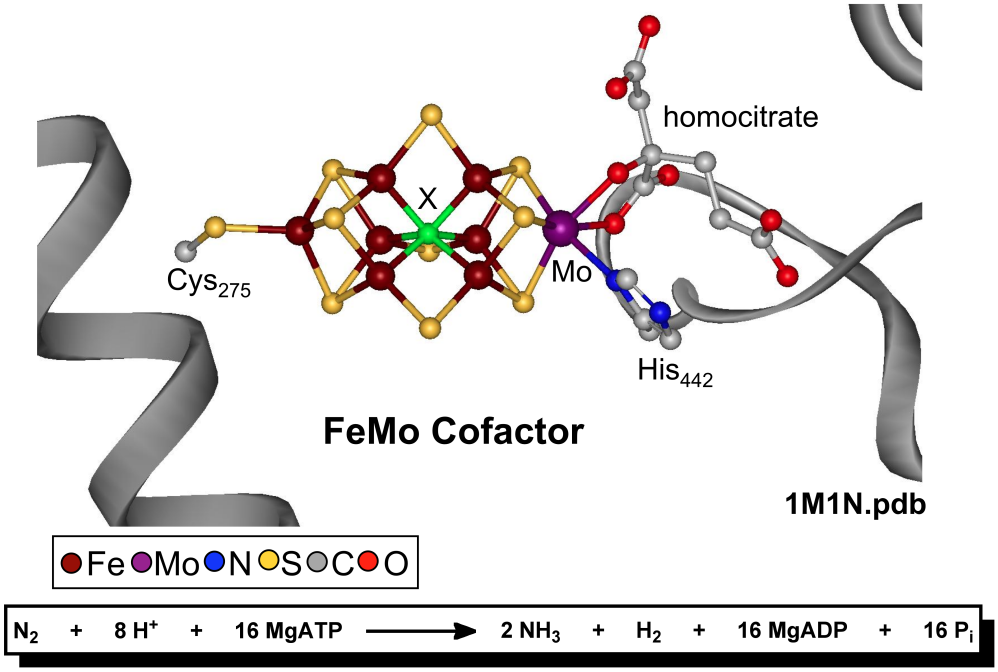

Figure 1.5. The FeMo cofactor cluster at the core of nitrogenase that catalyzes the reduction of N_2 to NH_3 at ambient conditions.

Very little is known about the mechanism of N_2 reduction at the FeMo cofactor, and so it is the source of copious discussion and has inspired model compounds for several decades.[17] Yandulov and Schrock recently showed that catalytic N_2 reduction can be achieved at a single Mo center at ambient temperature and pressure,[18] and moreover that system likely follows the classical N_2 reduction mechanism outlined by Chatt.[19]

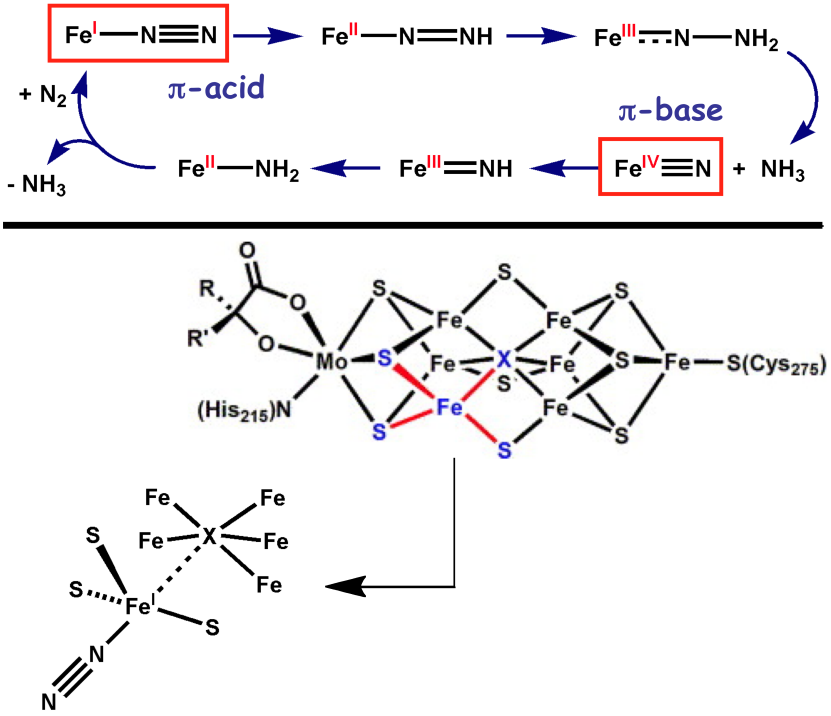

Figure 1.6. (*top*) A putative Chatt cycle for N_2 reduction at a single Fe center. (*bottom*) Possible coordination of N_2 to a single trigonal pyramidal Fe center in the FeMo cofactor to produce a terminal, trigonal bipyramidal Fe-N_2 moiety. This figure has been reproduced in part from reference 20.

Considering the structure of the FeMo cofactor, another possibility is that N_2 binding and reduction occurs at one or more Fe centers. Studies of the enzyme itself under turnover conditions have implied that this is likely the case.[16] If a single Fe center were involved in a Chatt-type mechanism, it would have to access several oxidation states and stabilize a wide variety of ligands ranging from strong π-acids to strong π-bases (Figure 1.6). Though such rich redox chemistry traditionally has been considered unlikely for Fe, the recent literature of small-molecule Fe model compounds with multielecton redox properties and stable metal-ligand multiple bonding is growing.[17b,21]

Were the N_2 substrate to bind and/or get reduced at a single Fe center in nitrogenase, the initial species formed would contain a terminal Fe-N_2 linkage. Considering both a Fe^{I}/Fe^{IV} Chatt cycle for N_2 reduction (Figure 1.6) and also the fact that detectable substrate-bound intermediates in the enzyme are known to possess *paramagnetic* Fe-N_xH_y moieties,[16] an intriguing target molecule is a terminally bound iron(I)-dinitrogen species. Though terminal N_2 complexes of iron(0) and iron(II) are well known,[17] prior to this work no terminal N_2 complexes of iron(I) (or any paramagnetic iron center) were known. The Peters group has worked previously with pseudotetrahedral iron complexes supported by tris(phosphino)borate ligands, and the Holland group has studied trigonal planar iron complexes supported by β-diketiminate ligands.[17] In both cases, bridging diiron(I) (μ-N_2) species of were synthesized (Figure 1.7), but terminal Fe^{I}-N_2 complexes were not accessible.[22]

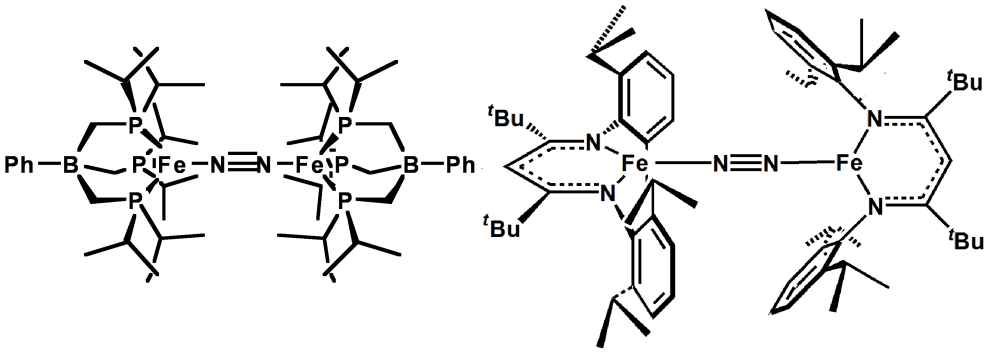

Figure 1.7. Previous examples of dinitrogen complexes of iron(I) reported by the groups of Peters (*left*) and Holland (*right*). This figure ahs been reproduced in part from reference 17b.

The most accurate crystal structure of the FeMo cofactor features six "belt irons" that all possess trigonal pyramidal coordination geometries (Figure 1.6). Therefore, were an N_2 ligand to coordinate one of these Fe centers, a trigonal bipyramidal Fe-N_2 moiety would result (Figure 1.6). For this reason, we targeted a trigonal bipyramidal Fe^{I}-N_2 species, and Chapter 4 describes the successful synthesis and characterization of a set of such complexes. There is a timely need for the synthesis of such species, as their spectroscopic features are of tremendous utility for comparison to data being obtained for intermediates within the cofactor itself under turnover conditions.[16] As is detailed in Chapter 4, subtle differences between pseudotetrahedral and trigonal bipyramidal coordination geometries cause the TBP complexes presented here to avoid dinuclear structures even though they are roughly isosteric with the tetrahedrally coordinated complex shown in Figure 1.7.

1.4 Iron complexes with multiply bonded ligands

Complexes of iron with multiply bonded ligands are important in many biological contexts[21,23] as well as for atom transfer and group transfer processes in synthetic catalysis.[24] The Peters group has focused in particular on multiple bonds between iron and nitrogenous ligands. For reasons outlined in Section 1.3, such species are interesting in the context of biological process such as N_2 fixation at the FeMo cofactor of nitrogenase.[21] In addition, species such as iron-imido (FeNR) complexes are thought to be the key reactive intermediates in many catalytic reactions involving nitrene transfer to organic substrates.[24a] Therefore, understanding the underlying principles dictating their stability, reactivity, and physical properties is fundamentally important.

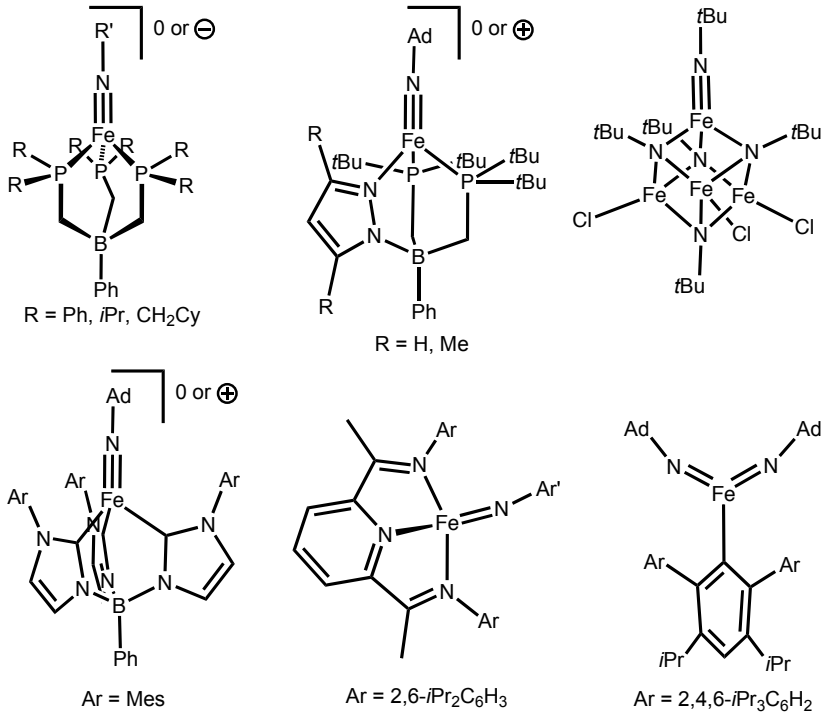

Figure 1.8. Structurally characterized iron-imido species.

During attempts to study iron-imido species, several groups have reported unobserved FeNR intermediates that are hypothesized to be unstable toward hydrogen atom abstraction and/or intramolecuar ligand oxidation. These systems span a wide variety of coordination numbers and geometries and include trigonal planar,[25] tetrahedral,[25,26] octahedral,[27] and trigonal bipyramidal[28] systems. Stable, structurally characterized examples of terminal iron-imido linkages are represented in Figure 1.8. The first example of a terminal iron-imido species came from Lee,[29] who reported the tetrairon cluster shown in Figure 1.8 that contains four bridging and one terminal imido group. The first mononuclear iron-imido species came from the Peters group and feature tetrahedral iron centers supported by bulky tris(phosphino)borate ligands.[30] The collection of tetrahedral FeNR complexes has since grown to include complexes of

bis(phosphine)pyrazolylborate ligands from the Peters group[31] and tris(carbene)borate ligands from Smith.[32] Terminal arylimidoiron complexes with highly distorted square planar geometries subsequently were reported by Chirik,[33] and recently a bis(imido)iron complex with trigonal planar geometry was synthesized by Power.[34]

The stability of the tetrahedral (BP_3)FeNR complexes has allowed for detailed chemical, spectroscopic, and theoretical studies.[30,31] Collectively, these analyses have led to a cohesive electronic structure picture. Key to the stability of these species is the fact that all frontier d-electrons (d^4, d^5, or d^6) reside in non-bonding orbitals, while a degenerate set of orbitals with both σ^*_{FeP} and π^*_{FeN} character remain unoccupied (Figure 1.9). As a result, these complexes contain formal Fe-N triple bonds.

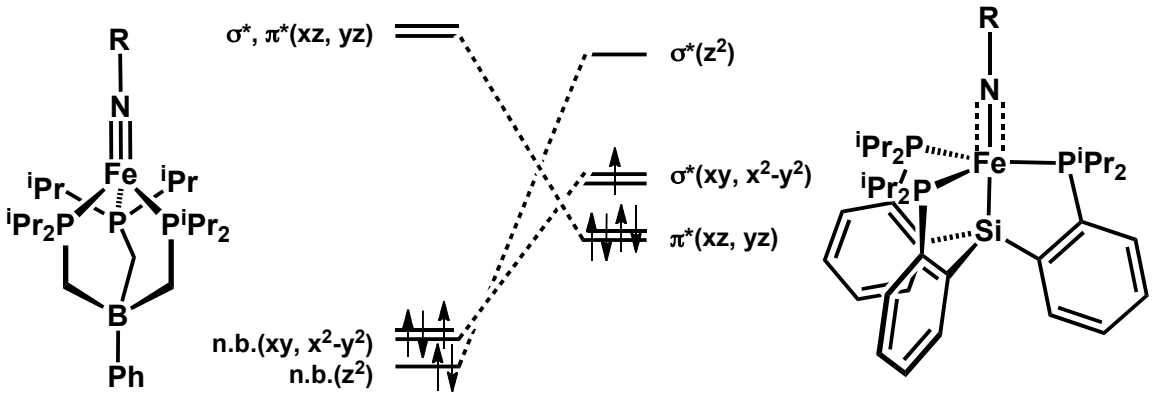

Figure 1.9. Qualitative d-orbital splitting diagrams for (*left*) a $(BP_3)Fe^{III}NR$ complex and (*right*) a hypothetical (SiP_3)FeNR complex.

Quite a different picture emerges when shifting from a tetrahedral to a TBP coordination environment. Due to the introduction of an axial ligand and the related shift of the Fe center into the P_3 plane, the frontier orbitals of Fe d-orbital parentage are all antibonding in character (Figure 1.9). In addition, unlike stable, low-spin $(BP_3)Fe^{III}NR$ complexes, a formal d^5 configuration is expected to populate the degenerate π^*_{FeN} set,

thus obliterating a significant amount of Fe-N π-bonding and vastly destabilizing the FeNR moiety. A thorough discussion of this effect has been presented by Nocera in the context of TBP metal-oxo species.[35] Therein, it is proposed that such an electronic structure, particularly for metal-oxo species that place unpaired spins in the $\pi^*_{M\text{-}O}$ levels, could induce radical O-O coupling, which is an important elementary step of water oxidation but has not been understood on a fundamental level.

In this context, it is intriguing not only that the putative (SiP_3)FeNR species described in Chapter 5 undergo N-N coupling, but also that they can do so catalytically when converting aryl azides into azoarenes. This unusual chemical reactivity has not been demonstrated with the previous iron-imido systems described above and presumably results directly from the TBP coordination geometry being enforced by the (SiP_3) ligands.

References Cited

1 (a) Munck, E.; Bomiaar, E. L. *Science* **2008**, *321*, 1452-1453. (b) Solomon, E. I.; Xie, X.; Dey, A. *Chem. Soc. Rev.* **2008**, *37*, 623-638.

2 (a) Ferguson-Miller, S.; Babcock, G. T. *Chem. Rev.* **1996**, *96*, 2239. (b) Ramirez, B. E.; Malmstrom, B. G.; Winkler, J. R.; Gray, H. B. *Proc. Natl. Acad. Sci. U.S.A.* **1995**, *92*, 11949.

3 (a) Ducros, V.; Brozowski, A. M.; Wilson, K. S.; Brown, S. H.; Ostergaard, P.; Scheider, P.; Yaver, D. S.; Pederson, A. H.; Davies, G. J. *Nat. Struct. Biol.* **1998**, *5*, 310. (b) Zaitseva, I; Zaitsev, V.; Card, G.; Moshkov, K.; Bax, B.; Ralph, A.; Lindley, P. *J. Biol. Inorg. Chem.* **1996**, *1*, 15. (c) Karlsson, B. G.; Nordling, M.; Pascher, T.; Tsai, L.-C.; Sjölin, L.; Lundberg, L. G. *Protein Eng.* **1991**, *4*, 343.

4 Rorabacher, D. B. *Chem. Rev.* **2004**, *104*, 651.

5 Marcus, R. A.; Sutin, N. *Biochim. Biophys. Acta* **1985**, *811*, 265.

6 Vallee, B. L.; Williams, R. J. P. *Proc. Natl. Acad. Sci. U.S.A.* **1968**, *59*, 498.

7 (a) Gamelin, D. R.; Randall, D. W.; Hay, M. T., Houser, R. P.; Mulder, T. C.; Canters, G. W.; de Vries, S.; Tolman, W. B.; Lu, Y.; Solomon, E. I. *J. Am. Chem. Soc.* **1998**, *120*, 5246. (b) DeBeer-George, S.; Metz, M.; Szilagyi, R. K.; Wang, J.; Cramer, S. P.; Lu, Y.; Tolman, W. B.; Hedman, B.; Hodgson, K. O.; Solomon, E. I. *J. Am. Chem. Soc.* **2001**, *123*, 5757.

8 (a) Harkins, S. B.; Peters, J. C. *J. Am. Chem. Soc.* **2004**, *126*, 2885. (b) Mankad, N. P.; Rivard, E.; Harkins, S. B.; Peters, J. C. *J. Am. Chem. Soc.* **2005**, *127*, 16032.

(c) Harkins, S. B.; Mankad, N. P.; Miller, A. J. M.; Szilagyi, R. K.; Peters, J. C. *J. Am. Chem. Soc.* **2008**, *130*, 3478.

9 Mankad, N. P.; Harkins, S. B.; Antholine, W. E.; Peters, J. C. *Inorg. Chem.* **2009**, *48*, 7026-7032.

10 Houser, R. P.; Young, V. G., Jr.; Tolman, W. B. *J. Am. Chem. Soc.* **1996**, *118*, 2101.

11 Selected examples: (a) Chaka, G.; Sonneberg, J. L.; Schlegel, H. B.; Heeg, M. J.; Jaeger, G.; Nelson, T. J.; Ochrymowycz, L. A.; Rorabacher, D. B. *J. Am. Chem. Soc.* **2007**, *129*, 5217. (b) Fujisawa, K.; Fujita, K.; Takahashi, T.; Kitajima, N.; Moro-oka, Y.; Mutsunaga, Y.; Miyashita, Y.; Okamoto, K. *Inorg. Chem. Commun.* **2004**, *7*, 1188.

12 (a) Jazdzewski, B. A.; Holland, P. L.; Pink, M.; Young, V. G., Jr.; Spencer, D. J. E.; Tolman, W. B. *Inorg. Chem.* **2001**, *40*, 6097. (b) Holland, P. L.; Tolman, W. B. *J. Am. Chem. Soc.* **1999**, *121*, 7270.

13 Dai, X.; Warren, T. H. *J. Am. Chem. Soc.* **2004**, *126*, 10085.

14 (a) Morrison, P.; Morrison, P. *American Scientist* **2001**, *89*, 1. (b) Haller, C. (ed.) *Science-Week* **1999**, *3*, 2-4.

15 (a) Seefeldt, L. C.; Dance, I. G.; Dean, D. R. *Biochemistry* **2004**, *43*, 1401. (b) Einsle, O.; Tezcan, F. A.; Andrade, S. L. A.; Schmid, B.; Yoshida, M.; Howard, J. B.; Rees, D. C. *Science* **2002**, *297*, 1696.

16 Barney, B. M.; Lee, H.-I.; Dos Santos, P. C.; Hoffman, B. M.; Dean, D. R.; Seefeldt, L. C. *Dalton Trans*. **2006**, 2277.

17 (a) MacKay, B. A.; Fryzuk, M. D. *Chem. Rev*. **2004**, *104*, 385. (b) Peters, J. C.; Mehn, M. P. In *Activation of Small Molecules*, W. B. Tolman (ed.), New York: Wiley, **2006**, p. 81.

18 Yandulov, D. V.; Schrock, R. R. *Science* **2003**, *301*, 76.

19 Chatt, J.; Dilworth, J. R.; Richards, R. L. *Chem. Rev*. **1978**, *78*, 589.

20 MacBeth, C. E.; Harkins, S. B.; Peters, J. C.; *Can. J. Chem*.; **2005**; *83*; 332-340.

21 Mehn, M. P.; Peters, J. C. *J. Inorg. Biochem*. **2006**, *100*, 634.

22 (a) Smith, J. M.; Sadique, A. R.; Cundari, T. R.; Rodgers, K. R.; Lukat-Rodgers, G.; Lachicotte, R. J.; Flaschenriem, C. J.; Vela, J.; Holland, P. L. *J. Am. Chem. Soc*. **2006**, *128*, 756. (b) Betley, T. A.; Peters, J. C. *J. Am. Chem. Soc*. **2003**, *125*, 10782.

23 (a) Krebs, C.; Fujimori, D. G.; Walsh, C. T.; Bollinger, J. M., Jr. *Acc. Chem. Res*. **2007**, *40*, 484-492. (b) Decker, A.; Clay, M. D.; Solomon, E. I. *J. Inorg. Biochem*. **2006**, *100*, 697-706.

24 (a) Halfen, J. A. *Curr. Org. Chem*. **2005**, *9*, 657-669. (b) Eikey, R. A.; Abu-Omar, M. M. *Coord. Chem. Re*v. **2003**, *243*, 83. (c) Chen, M. S.; White, M. C. *Science* **2007**, *318*, 783-787. (d) Que, L., Jr.; Tolman, W. B. *Nature* **2008**, *455*, 333-340.

25 Eckert, N. A.; Vaddadi, S.; Stoian, S.; Flaschenriem, C. J.; Cundari, T. R.; Holland, P. L. *Angew. Chem., Int. Ed. Engl*. **2006**, *45*, 6868.

26 King, E. R.; Betley, T. A. *Inorg. Chem.* **2009**, *48*, 2361.

27 Jensen, M. P.; Mehn, M. P.; Que, L., Jr. *Angew. Chem., Int. Ed.* **2003**, *42*, 4357.

28 Lucas, R. L.; Powell, D. R.; Borovik, A. S. *J. Am. Chem. Soc.* **2005**, *127*, 11596.

29 Verma, A. K.; Nazif, T. N.; Achim, C.; Lee, S. C. *J. Am. Chem. Soc .***2000**, *122*, 11013.

30 (a) Brown, S. D.; Betley, T. A.; Peters, J. C. *J. Am. Chem. Soc.* **2003**, *125*, 322. (b) Brown, S. D.; Peters, J. C. *J. Am. Chem. Soc.* **2005**, *127*, 1913. (c) Betley, T. A.; Peters, J. C. *J. Am. Chem. Soc.* **2003**, *125*, 10782. (d) Lu, C. C.; Saouma, C. T.; Day, M. W.; Peters, J. C. *J. Am. Chem. Soc.* **2007**, *129*, 4.

31 Thomas, C. M.; Mankad, N. P.; Peters, J. C. *J. Am. Chem. Soc.* **2006**, *128*, 4956.

32 Nieto, I.; Ding, F.; Bontchev, R. P.; Wang, H.; Smith, J. M. *J. Am. Chem. Soc.*, **2008**, *130*, 2716.

33 Bart, S. C.; Lobkovsky, E.; Bill, E.; Chirik, P. J. *J. Am. Chem. Soc.* **2006**, *128*, 5302.

34 Ni, C.; Fettinger, J. C.; Long, G. J.; Brynda, M.; Power, P. P. *Chem. Commun.* **2008**, *45*, 6045.

35 (a) Betley, T. A.; Wu, Q.; Van Voorhis, T.; Nocera, D. G. *Inorg. Chem.* **2008**, *47*, 1849. (b) Betley, T. A.; Surendranath, Y.; Childress, M. V.; Alliger, G. E.; Fu, R.; Cummins, C. C.; Nocera, D. G. *Phil. Trans. Royal Soc. B* **2007**, *363*, 1293.

Chapter 2: Diazoalkane Chemistry of Bis(phosphino)borate Copper(I) Complexes

Reproduced in part with permission from

Mankad, N. P. and Peters, J. C. *Chemical Communications* **2008**, 1061-1063.

2.1 Introduction

Metal-catalyzed carbene transfer from diazoalkanes to organic substrates has become a versatile technique in synthesis, and copper catalysts have been particularly well studied in this regard.[1,2] Careful study of copper carbene complexes ($Cu{=}CR_2$), the presumed reactive intermediates in these reactions, serves to deepen understanding of these copper-catalyzed transformations. Identifying factors that affect copper carbene stability, characterizing specific decomposition pathways, and understanding the nature of copper-diazoalkane interactions prior to copper-carbene bond formation are therefore issues of fundamental interest.

Whereas α-heteroatom stabilized copper carbenes are well known,[3] only two examples of non-heteroatom stabilized copper carbenes have been reported. Both of these derivatives are stabilized by bidentate, monoanionic N-chelates. The first such example was reported by Hofmann in 2001 and assigned using spectroscopic data.[4] Warren and co-workers later reported X-ray structural data for a β-diketiminato $Cu{=}CPh_2$ complex.[5] Both of these systems mediate catalytic cyclopropanation reactions and employ diazoalkane precursors to generate the carbenes of interest. In this context we note that the presumed diazoalkane adduct intermediates *en route* to carbene formation were not observed, and to our knowledge no such species have been previously characterized for copper systems.

Our group has had an interest in exploiting (phosphino)borate ligands to stabilize mid-to-late first-row metals featuring metal ligand multiple bonds.[6] In this chapter, we describe the utility of the bulky bis(phosphino)borate ligand[7] $[Ph_2BP^{tBu}{}_2]$ = $Ph_2B(CH_2P^tBu_2)_2$ to generate unusual diazoalkane adducts of Cu^I. In addition, we

establish that N_2CPh_2 reacts to generate the copper carbene complex $[Ph_2BP^{tBu}_2]Cu{=}CPh_2$ as verified by NMR spectroscopy and group transfer of the carbene unit. This latter species is unstable in the presence of additional N_2CPh_2 in solution and as such generates the structurally novel azine adduct $[Ph_2BP^{tBu}_2]Cu\text{-}N(CPh_2)(NCPh_2)$ as a side product.

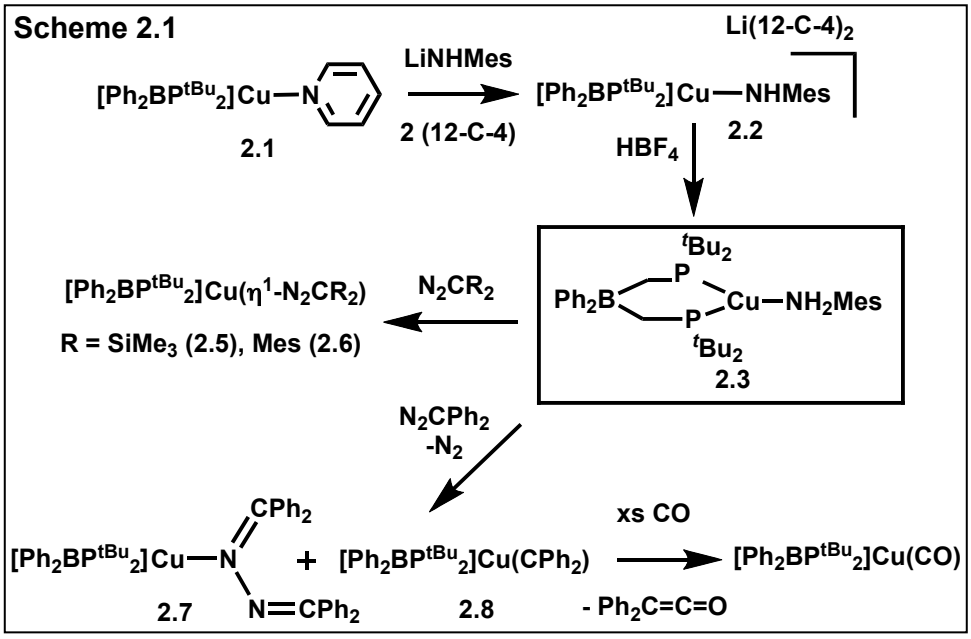

2.2 Results and Discussion

The synthesis of copper(I) species of the type $[Ar_2BP^R_2]Cu\text{-}L$ (L = e.g., CH_3CN, PR_3, CO) was reported recently.[8] Preliminary group transfer studies with diazoalkanes suggested the necessity of a $[Ar_2BP^R_2]Cu\text{-}L$ precursor with a sufficiently labile L ligand to expose reactions of interest. The aniline adduct $[Ph_2BP^{tBu}_2]Cu(NH_2Mes)$ (Mes = 2,4,6-trimethylphenyl) proved key in this regard. Its synthesis (Scheme 2.1) proceeded from the neutral pyridine adduct $[Ph_2BP^{tBu}_2]Cu(pyridine)$ (**2.1**). Reaction of LiNHMes and excess 12-crown-4 with yellow **2.1** provided the anionic colorless amido complex $\{[Ph_2BP^{tBu}_2]CuNHMes\}\{Li(12\text{-crown-}4)_2\}$ (**2.2**). Protonation of **2.2** with HBF_4 (toluene,

-90 °C) produced the colorless aniline adduct $[Ph_2BP^{tBu}{}_2]Cu(NH_2Mes)$ (**2.3**). Recrystallization of **2.3** from a THF/petroleum ether mixture provided the THF adduct $[Ph_2BP^{tBu}{}_2]Cu(THF)$ (**2.4**). The solid-state structures of **2.1** and **2.4** have been placed in Appendix 1.

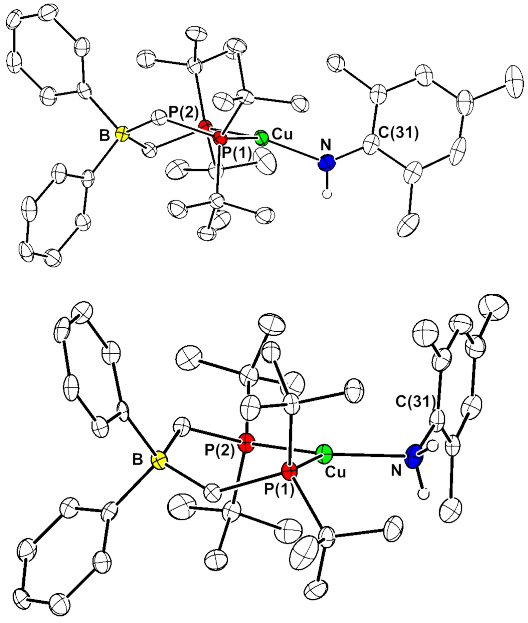

Figure 2.1. Solid-state structures of $\{[PhBP^{tBu}{}_2]Cu(NH_2Mes)\}\{Li(12\text{-crown-4})_2\}$ (**2.2**) (*top*) and $[PhBP^{tBu}{}_2]Cu(NH_2Mes)$ (**2.3**) (*bottom*) as 50% ellipsoids. Only the anion of **2.2** is shown. N-H hydrogens are shown in calculated positions, and C-H hydrogens have been omitted for clarity. Selected bond distances (Å) and angles (°) for **2.2**: Cu-N, 1.967(3); Cu-P(1), 2.2806(14); Cu-P(2), 2.2806(14); P(1)-Cu-P(2), 105.04(5); P(1)-Cu-N, 120.15(10); P(2)-Cu-N, 131.96(10); Cu-N-C(31), 136.3(3). For **2.3**: Cu-N, 2.076(2); Cu-P(1), 2.2667(11); Cu-P(2), 2.2464(14); P(1)-Cu-P(2), 107.89(5); P(1)-Cu-N, 120.17(8); P(2)-Cu-N, 131.81(8); Cu-N-C(31), 118.46(19).

The X-ray crystal structures of complexes **2.2** and **2.3**, which are related by a proton transfer, are shown in Figure 2.1. The crystal structure of **2.3** features a longer Cu-N distance (2.0758(3) Å) and more compressed Cu-N-C angle (118.46(2)°) when compared to its conjugate base **2.2** (1.962(1) Å and 136.43(1)°, respectively). Gunnoe has recently reported that the structurally related but neutral complex (dtbpe)Cu(NHPh) (dtbpe = $^{t}Bu_2PCH_2CH_2P^{t}Bu_2$) has an appreciably shorter Cu-N distance of 1.890(6) Å.[9]

When either **2.3** or **2.4** were mixed with $N_2C(SiMe_3)_2$ or N_2CMes_2, the stable diazoalkane adducts yellow $[Ph_2BP^{tBu}_2]Cu(\eta^1\text{-}N_2C(SiMe_3)_2)$ (**2.5**) and red $[Ph_2BP^{tBu}_2]Cu(\eta^1\text{-}N_2CMes_2)$ (**2.6**) formed rapidly and could be readily isolated (Scheme 2.1). We were surprised to find that these adducts are the only characterized examples of Cu^{I}-diazoalkane complexes to be reported, though Hofmann has described a formally Cu^{III}-diazoalkane complex resulting from reduction of a chelating diazoalkane unit by a Cu^{I} precursor.[10] The observed $N_2\mathit{C}R_2$ $^{13}C\{^{1}H\}$ chemical shifts (δ 29.5 for **2.5** and δ 99.3 for **2.6**) and CN_2 vibrational frequencies (2108 cm^{-1} for **2.5** and 2041 cm^{-1} for **2.6**) are very similar to the corresponding values for the free diazoalkanes,[11] indicating that the diazoalkane moieties have not been significantly perturbed upon coordination to copper. The molecular structures of **2.5** (Appendix 1) and **2.6** (Figure 2.2) feature N-N distances (1.200(8) Å for **2.5** and 1.1630(6) Å for **2.6**), N-C distances (1.237(9) Å for **2.5** and 1.3188(7) Å for **2.6**), and N-N-C angles (180.000(7)° for **2.5** and 176.50(6)° for **2.6**) that are notably similar to the corresponding parameters for the free diazoalkanes.[11] The Cu-N-N angle of **2.5** is linear (180.000(2)°) whereas for **2.6** the angle drops to 156.95(5)°. For comparison, Hofmann's Cu^{III}-diazoalkane complex has severely bent Cu-N-N and N-

N-C angles (123.8(2)° and 134.3(3)°, respectively) owing to the reduced diazoalkane ligand.[10]

Complex **2.5** is stable to 110 °C in toluene solutions even in the presence of Lewis acid catalysts. Complex **2.6** decomposes to a complicated mixture of products when heated in hydrocarbon solutions, and though the product profile simplifies when $Sm(OTf)_3$ is added as a catalyst, no stable products were isolated from these thermolysis experiments, and no evidence for $Cu{=}CR_2$ bond formation was detected. The diazoalkane complex (dtbpe)Ni(η^2-N_2CPh_2) has been isolated by Hillhouse and co-workers and was shown to extrude N_2 and form (dtbpe)Ni=CPh_2 upon thermolysis in the presence of catalytic $Sm(OTf)_3$.[12] Perhaps an important distinction to note between this Ni system and the Cu-diazoalkane adducts **2.5** and **2.6** is that N_2CPh_2 binds in an η^2-NN mode to the L_2Ni^0 fragment, whereas $N_2C(SiMe_3)_2$ and N_2CMes_2 bind in an η^1-N fashion to the L_2Cu^I fragment described here.

When the less-bulky diazoalkane reagent N_2CPh_2 was added to **2.3** or **2.4** at ambient temperature, N_2 release occurred spontaneously with concomitant formation of an inky blue solution and free NH_2Mes (in the case of **2.3**). A mixture of two Cu-containing species, ultimately assigned as $[Ph_2BP^{tBu}_2]$Cu-N(=CPh_2)NCPh_2 (**2.7**, δ 39.9) and $[Ph_2BP^{tBu}_2]$Cu=CPh_2 (**2.8**, δ 64.8), could be detected by $^{31}P\{^1H\}$ NMR (Scheme 2.1). Quantitative conversion to **2.7** exclusively was achieved by the use of 2 equiv or more of N_2CPh_2, and its assignment as a benzophenone azine adduct was verified by single-crystal X-ray diffraction (Figure 2.2). The N-N bond distance of 1.3962(3) Å in **2.7** is consistent with the azine N-N single-bond formulation. The Cu center in **2.7** is best described as trigonal planar, as the Cu-N_{distal} distance (2.7649(3) Å) is much longer than

the Cu-$N_{proximal}$ bond length of 2.0166(2) Å. Complex **2.7** presumably forms from the reaction between the intermediate carbene species **2.8** and unreacted N_2CPh_2; such C-N bond forming reactions between isolated terminal metal carbenes and diazoalkanes have been observed for metals other than copper.[13]

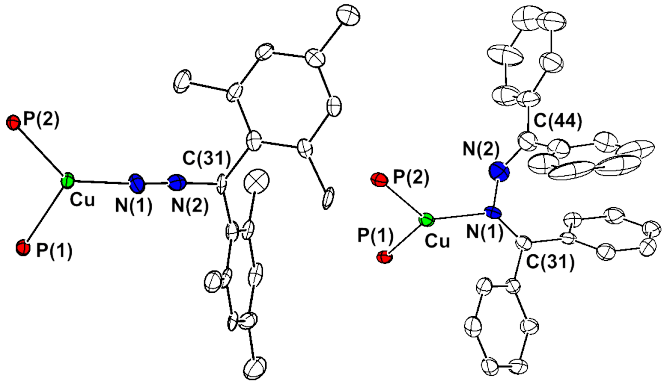

Figure 2.2. Solid-state structures of $[Ph_2BP^{tBu}_2]Cu(N_2CMes_2)$ (**2.6**) (*left*) and $[Ph_2BP^{tBu}_2]Cu\text{-}N(=CPh_2)NCPh_2$ (**2.7**) (*right*) as 50% ellipsoids. Non-phosphorus atoms of the $[Ph_2BP^{tBu}_2]$ ligands have been omitted for clarity. Selected bond distances (Å) and angles (°) for **2.6**: Cu-N(1), 1.858(5); Cu-P(1), 2.2521(17); Cu-P(2), 2.2473(17); N(1)-N(2), 1.163(6); N(2)-C(31), 1.321(7); P(1)-Cu-P(2), 107.06(6); P(1)-Cu-N(1), 119.67(15); P(2)-Cu-N(1), 133.01(15); Cu-N(1)-N(2), 156.9(5); N(1)-N(2)-C(31), 176.4(6). For **2.7**: Cu-N(1), 2.017(2); Cu-P(1), 2.2595(8); Cu-P(2), 2.2595(8); N(1)-N(2), 1.396(3); N(1)-C(31), 1.296(3); N(2)-C(44), 1.322(4); P(1)-Cu-P(2), 107.62(3); P(1)-Cu-N(1), 129.57(7); P(2)-Cu-N(1), 120.11(7); Cu-N(1)-N(2), 106.81(18).

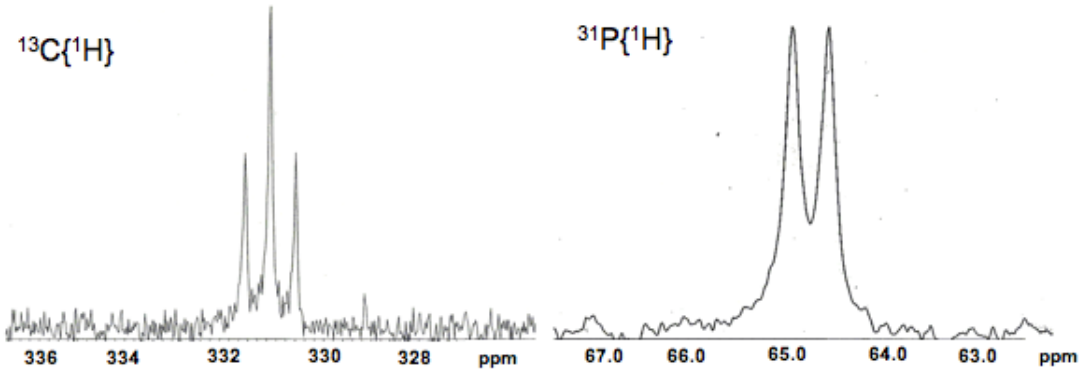

Figure 2.3. $^{13}C\{^1H\}$ signal (*left*) and $^{31}P\{^1H\}$ signal (*right*) for $[Ph_2BP^{tBu}_2]Cu=^{13}CPh_2$ (**2.8-^{13}C**).

Under dilute conditions, as high as 70% conversion to carbene complex **2.8** has been achieved. This species features an intense band at λ_{max} = 583 nm (ε = (est.) 12000 M^{-1} cm^{-1}) that likely arises from MLCT charge transfer into the Cu=*CPh*$_2$ unit. Warren has observed an optical transition of similar energy and intensity in the related β-diketiminato $Cu=CPh_2$ species.[5] To cement the assignment of **2.8**, solutions of $[Ph_2BP^{tBu}_2]Cu=^{13}CPh_2$ (**2.8-^{13}C**) were generated using $N_2{}^{13}CPh_2$ in place of unlabelled diphenyldiazomethane. A diagnostic triplet at δ 331.5 was clearly visible in the $^{13}C\{^1H\}$ NMR spectrum ($^2J_{PC}$ = 41 Hz) (Figure 2.3), and the $^{31}P\{^1H\}$ NMR spectrum of **2.8-^{13}C** featured a corresponding sharp doublet (δ 64.8, $^2J_{PC}$ = 41 Hz). A slightly larger value for $^2J_{PC}$ was observed for Hillhouse's (dtbpe)Ni=CPh_2 species (δ 222, $^2J_{PC}$ = 51 Hz).[12] Interestingly, the Cu=*C*Ph_2 $^{13}C\{^1H\}$ NMR chemical shift in **2.8-^{13}C** is considerably further downfield than for other reported copper carbene species,[3-5] though it is certainly within the range typically observed for terminal metal carbene complexes.[14,15] As further evidence for the presence of the "CPh_2" carbene functionality in **2.8**, we observed

quantitative carbene transfer to CO to generate ketene $Ph_2C{=}C{=}O$ and $[Ph_2BP^{tBu}{}_2]Cu(CO)$ upon exposure of solutions of **2.8** to excess carbon monoxide (Scheme 2.1). Carbene transfer to CO is also characteristic of the Ni and Cu carbenes of Hillhouse and Warren, respectively.[5,12] Complex **2.8** did not readily transfer its carbene unit to olefins such as 1-hexene or styrene.

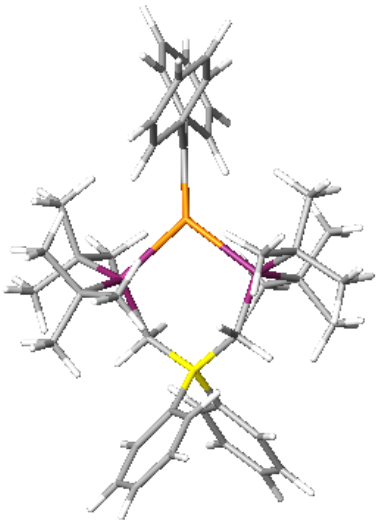

Figure 2.4. Optimized structure of **2.8**, as determined by DFT. Selected bond distance: Cu-C, 1.933 Å.

Whereas Warren's β-diketiminato copper carbene complex is stable at room temperature, complex **2.8** loses $Ph_2C{=}CPh_2$ even at -30 °C. This fact has thus far precluded its crystallization from solution. The β-diketiminato $Cu{=}CPh_2$ species degrades similarly upon thermolysis.[5]

A computational study of **2.8** was undertaken to probe the Cu-C distance by DFT methods.[16] A diphenylcarbene unit was attached to the $[Ph_2BP^{tBu}{}_2]Cu$ fragment taken

from the atomic coordinates in the solid-state structure of **2.1**. Geometry optimization calculations using various initial Cu-C distances all gave the same optimized geometry (Figure 2.4), featuring trigonal planar geometries at both the copper center and the carbene carbon atom, with a Cu-C distance of 1.933 Å. Significantly shorter distances have been determined experimentally for the previously reported $M{=}CR_2$ (M = Cu, Ni) complexes (1.834-1.859 Å).[5,12] It is possible that the long-predicted Cu-C distance in **2.8** is experimentally manifested by the relatively small value for $^2J_{PC}$ and the significantly deshielded carbene carbon atom. It must, however, be noted that optimizing the geometry of **2.8** while fixing the Cu-C distance to be either 1.830 or 2.030 Å gave structures whose energies spanned a range of only 1.0 kcal/mol, indicating that the molecule's potential energy surface is quite flat with regard to the Cu-C distance.

2.3 Experimental Section

2.3.1 General Considerations

All manipulations were carried out using standard Schlenk or glovebox techniques under a dinitrogen atmosphere. Unless otherwise noted, solvents were deoxygenated and dried by thoroughly sparging with N_2 gas followed by passage through an activated alumina column. Non-halogenated solvents were tested with a standard purple solution of sodium benzophenone ketyl in tetrahydrofuran in order to confirm effective oxygen and moisture removal. All reagents were purchased from commercial vendors and used without further purification unless otherwise stated. Lithium 2,4,6-trimethylanilide was prepared by deprotonation of 2,4,6-trimethylaniline with *n*-

butyllithium. $[Ph_2BP^{tBu}_2]Li(OEt_2)$,[17] diphenyldiazomethane,[18] bis(2,4,6-trimethylphenyl)diazomethane,[19] and bis(trimethylsilyl)diazomethane[20] were prepared according to literature procedures. $N_2{}^{13}CPh_2$ was prepared from benzophenone-(carbonyl-^{13}C) (Cambridge Isotopes, Cambridge, MA) according to literature procedures.[18] Elemental analyses were performed by Desert Analytics, Tucson, AZ. Deuterated solvents were purchased from Cambridge Isotope Laboratories, degassed, and dried over activated 3 Å molecular sieves prior to use.

2.3.2 Spectroscopic Measurements

A Varian Mercury-300 spectrometer was used to record ^{1}H, ^{13}C, ^{19}F, and ^{31}P NMR spectra at ambient temperature. ^{1}H and ^{13}C chemical shifts were referenced to the residual solvent peaks. ^{19}F and ^{31}P chemical shifts were referenced to external hexafluorobenzene (δ = -165 ppm) and phosphoric acid (δ = 0 ppm) respectively. Optical spectroscopy measurements were taken on a Cary 50 UV/Vis Spectrophotometer using a 1 cm quartz cell.

2.3.3 Computational Methods

All calculations were performed using the Jaguar 5.0 program package (Jaguar 5.0, Schrodinger, LLC, Portland, OR). The calculations employed the hybrid DFT functional B3LYP. The LACVP** basis set[21] was used for the Cu atom. The 6-31G** basis set was used for the P atoms, as well as the carbene C atom. The MIDI! basis set[22] was used for all other C atoms, as well as B and H atoms. Input coordinates for the geometry optimizations were derived as described in the text. The calculations were spin

restricted, and no symmetry constraints were used. The default values for geometry and SCF iteration cutoffs were used, and all structures converged under these criteria.

2.3.4 X-ray Crystallography Procedures

X-ray diffraction studies were carried out at the Beckman Institute Crystallography Facility on a Brüker Smart 1000 CCD diffractometer and solved using SHELX v. 6.14.[23] X-ray quality crystals were grown as indicated in the experimental procedures per individual complex. The crystals were mounted on a glass fiber with Paratone N oil. Structures were determined using direct methods with standard Fourier techniques using the Bruker AXS software package. Spatial refinement details: Refinement of F^2 against ALL reflections. The weighted R-factor (*w*R) and goodness of fit (S) are based on F^2, conventional R-factors (R) are based on F, with F set to zero for negative F^2. The threshold expression of $F^2 > 2\sigma(F^2)$ is used only for calculating R-factors(gt) etc. and is not relevant to the choice of reflections for refinement. R-factors based on F^2 are statistically about twice as large as those based on F, and R-factors based on ALL data will be even larger. All esds (except the esd in the dihedral angle between two l.s. planes) are estimated using the full covariance matrix. The cell esds are taken into account individually in the estimation of esds in distances, angles, and torsion angles; correlations between esds in cell parameters are only used when they are defined by crystal symmetry. An approximate (isotropic) treatment of cell esds is used for estimating esds involving l.s. planes. Crystallographic details have been placed in Appendix 1.

2.3.5 Synthesis

Synthesis of [$Ph_2BP^{tBu}_2$]Cu(pyr) (2.1). [$Ph_2BP^{tBu}_2$]Li(OEt_2) (1.83 g, 3.25 mmol) and [$Cu(CH_3CN)_4$][BF_4] (1.02 g, 3.25 mmol) were combined in a 250 mL flask equipped with a stir bar and dissolved in diethyl ether (100 mL). The initially cloudy purple mixture was stirred for 3.5 h, yielding a cloudy white suspension. The solvent was removed *in vacuo*, and the residues were suspended in minimal acetonitrile. A white powder was collected on a sintered glass frit, dissolved in minimal THF, and filtered through Celite. Pyridine (2 mL) was added to the colorless filtrate, giving a clear, bright yellow solution that gradually became cloudy. After stirring for 1 h, the solvent was removed *in vacuo* to yield analytically pure **2.1** (1.48 g, 73%). X-ray quality crystals were obtained by slow diffusion of petroleum ether vapors into a concentrated THF solution of **2.1**. ^{1}H (THF-d_8, δ): 8.74 (dt, J = 2.2 and 4.4 Hz, 2H, pyridine *ortho*-C<u>H</u>), 7.80 (tt, J = 1.4 and 7.7 Hz, 1H, pyridine *para*-C<u>H</u>), 7.55 (tq, J = 1.4 and 6.9 Hz, 2H, pyridine *meta*-C<u>H</u>), 7.37 (br, 4H, phenyl *ortho*-C<u>H</u>), 6.88 (t, J = 7.3 Hz, 4H, phenyl *meta*-C<u>H</u>), 6.67 (t, J = 7.2 Hz, 2H, phenyl *para*-C<u>H</u>), 1.58 (br, 4H, BC<u>H_2</u>P), 1.09 (d, $^3J_{PH}$ = 6.3 Hz, 18H, P[C(C<u>H_3</u>)$_3$]$_2$), 1.07 (d, $^3J_{PH}$ = 6.1 Hz, 18H, P[C(C<u>H_3</u>)$_3$]$_2$). ^{13}C{^{1}H} (THF-d_8, δ): 152.5 (m, *ipso*-<u>C</u>), 150.6 (s, pyridine <u>C</u>2), 136.7 (s, pyridine <u>C</u>4), 134.8, 133.7, 126.8, 122.5 (s, pyridine <u>C</u>3), 35.8 (br, P[<u>C</u>(CH_3)$_3$]$_2$), 34.5 (br, P[<u>C</u>(CH_3)$_3$]$_2$), 31.0 (d, $^2J_{PC}$ = 4.2 Hz, P[C(<u>C</u>H_3)$_3$]$_2$), 30.9 (d, $^2J_{PC}$ = 4.1 Hz, P[C(<u>C</u>H_3)$_3$]$_2$), 28.0 (m, B<u>C</u>H_2P). ^{31}P{^{1}H} (THF-d_8, δ): 35.7 (s). IR (KBr, cm^{-1}): 3055, 3030, 2976, 2941, 1595, 1470, 1444, 1383, 1362, 1155, 1103, 1067, 1016, 934, 861, 810. Anal. Calcd for $C_{35}H_{55}BCuNP_2$: C, 67.14; H, 8.85; N, 2.24. Found: C, 66.75; H, 8.62; N, 2.34.

Synthesis of {[$Ph_2BP^{tBu}_2$]Cu(NHMes)}{Li(12-C-$4)_2$} (2.2). **2.1** (1.07 g, 1.71 mmol) and LiNHMes (0.242 g, 1.71 mmol) were combined in THF (50 mL), giving a cloudy brown solution. After stirring for 5 min, 12-crown-4 (0.690 mL, 4.26 mmol) was added. The resulting clear yellow-brown solution was stirred for 0.5 h, and then the solvent was removed *in vacuo*. The residues were triturated with petroleum ether (50 mL), and a tan powder was collected on a sintered glass frit. Subsequent washes with petroleum ether (5 x 10 mL) gave spectroscopically pure **2.2** (1.71 g, 96%). X-ray quality crystals were obtained by slow diffusion of petroleum ether vapors into a concentrated THF solution of **2.2**. ^{1}H (THF-d_8, δ): 7.37 (br, 4H, *ortho*-C<u>H</u>), 6.82 (t, J = 7.3 Hz, 4H, phenyl *meta*-C<u>H</u>), 6.61 (t, J = 7.0 Hz, 2H, *para*-C<u>H</u>), 6.38 (s, 2H, mesityl *meta*-C<u>H</u>), 3.60 (s, 32H, O(C<u>H</u>$_2$)$_2$O), 2.80 (br, 1H, CuN<u>H</u>Mes), 2.19 (s, 6H, *ortho*-C<u>H</u>$_3$), 2.01 (s, 3H, *para*-C<u>H</u>$_3$), 1.41 (br, 4H, BC<u>H</u>$_2$P), 1.06 (d, $^3J_{PH}$ = 5.5 Hz, 18H, P[C(C<u>H</u>$_3$)$_3$]$_2$), 1.05 (d, $^3J_{PH}$ = 5.5 Hz, 18H, P[C(C<u>H</u>$_3$)$_3$]$_2$). ^{13}C{^{1}H} (THF-d_8, δ): 160.0 (s, mesityl *ipso*-<u>C</u>), 155.4 (br, phenyl *ipso*-<u>C</u>), 134.1, 129.1, 126.4, 121.9, 120.7, 114.0, 69.4 (s, O(<u>C</u>H$_2$)$_2$O), 34.0 (br, P[<u>C</u>(CH$_3$)$_3$]$_2$), 31.1 (d, $^2J_{PC}$ = 7.2 Hz, P[C(<u>C</u>H$_3$)$_3$]$_2$), 31.0 (d, $^2J_{PC}$ = 7.2 Hz, P[C(<u>C</u>H$_3$)$_3$]$_2$), 21.4 (s, *ortho*-<u>C</u>H$_3$), 21.2 (s, *para*-<u>C</u>H$_3$), 14.6 (br, B<u>C</u>H$_2$P). ^{31}P{^{1}H} (THF-d_8, δ): 29.0 (s). IR (KBr, cm^{-1}): 3374 (N-H st), 2909, 2864, 1629 (N-H δ), 1603, 1475, 1445, 1362, 1289, 1248, 1136, 1098, 1024, 916, 853, 812. Anal. Calcd for $C_{55}H_{94}BCuLiNO_8P_2$: C, 63.48; H, 9.11; N, 1.35. Found: C, 62.12; H, 8.73; N, 1.24. Note: Satisfactory combustion analysis results could not be obtained, even when doubly recrystallized material was submitted for analysis. ^{1}H and ^{31}P{^{1}H} NMR spectra indicated that the material was spectroscopically pure.

Synthesis of [$Ph_2BP^{tBu}_2$]Cu(NH_2Mes) (2.3). **2.2** (1.66 g, 1.60 mmol) was dissolved in toluene (50 mL) and cooled to -90 ºC. Separately, tetrafluoroboric acid (0.219 mL of a 48 wt% solution in diethyl ether, 1.60 mmol) was diluted with toluene (10 mL) and cooled to -30 ºC. The acid solution was then added slowly at -90 ºC, giving a cloudy brown mixture that was allowed to warm gradually to room temperature. After stirring for 2 h at room temperature, the mixture was filtered through Celite. Concentration of the gold-yellow filtrate gave a tacky yellow residue, which was triturated with petroleum ether (20 mL) and collected by filtration. Subsequent washes with petroleum ether (3 x 10 mL) gave analytically pure **2.3** (0.813 g, 74%). X-ray quality crystals were obtained by slow diffusion of petroleum ether vapors into a concentrated dichloromethane solution of **2.3**. ^{1}H (C_6D_6, δ): 7.92 (br d, J = 5.4 Hz, 4H, *ortho*-C<u>H</u>), 7.39 (t, J = 7.5 Hz, 4H, phenyl *meta*-C<u>H</u>), 7.13 (t, J = 7.2 Hz, 2H, *para*-C<u>H</u>), 6.56 (s, mesityl *meta*-C<u>H</u>), 3.43 (br, 2H, CuN<u>H</u>$_2$Mes), 2.05 (s, 3H, *para*-C<u>H</u>$_3$), 1.9 (br, 4H, BC<u>H</u>$_2$P), 1.87 (s, 6H, *ortho*-C<u>H</u>$_3$), 1.01 (d, $^3J_{PH}$ = 6.0 Hz, 18H, P[C(C<u>H</u>$_3$)$_3$]$_2$), 0.99 (d, $^3J_{PH}$ = 6.0 Hz, 18H, P[C(C<u>H</u>$_3$)$_3$]$_2$). ^{13}C{^{1}H} (C_6D_6, δ): 150.9, 144.2, 136.7, 134.4, 133.7, 127.3, 124.5, 123.3, 36.1 (br, P[<u>C</u>(CH$_3$)$_3$]$_2$), 33.9 (br, P[<u>C</u>(CH$_3$)$_3$]$_2$), 31.1 (d, $^2J_{PC}$ = 7.2 Hz, P[C(<u>C</u>H$_3$)$_3$]$_2$), 31.0 (d, $^2J_{PC}$ = 7.2 Hz, P[C(<u>C</u>H$_3$)$_3$]$_2$), 28.1 (s, *ortho*-<u>C</u>H$_3$), 27.7 (s, *para*-<u>C</u>H$_3$), 17.9 (br, B<u>C</u>H$_2$P). ^{31}P{^{1}H} (C_6D_6, δ): 37.1 (s). IR (KBr, cm^{-1}): 3353 (N-H st), 3292 (N-H st), 3053, 2938, 1580, 1480, 1428, 1381, 1364, 1305, 1260, 1219, 1156, 1105, 1015, 940, 860, 808. Anal. Calcd for $C_{39}H_{63}BCuNP_2$: C, 68.66; H, 9.31; N, 2.05. Found: C, 68.51; H, 9.28; N, 1.79.

Preparation of [$Ph_2BP^{tBu}_2$]Cu(THF) (2.4). Petroleum ether vapors were diffused slowly into a saturated THF solution of **2.3** to provide a quantitative yield of **2.4**. ^{1}H

(C_6D_6, δ): 7.90 (d, *J* = 5.8 Hz, 4H, phenyl *ortho*-C<u>H</u>), 7.39 (t, *J* = 7.7 Hz, 4H, phenyl *meta*-C<u>H</u>), 7.13 (t, *J* = 8.3 Hz, 2H, phenyl *para*-C<u>H</u>), 3.55 (m, 4H, O-(C<u>H</u>$_2$-CH$_2$)$_2$), 1.84 (br, 4H, BC<u>H</u>$_2$P), 1.38 (m, 4H, O-(CH$_2$-C<u>H</u>$_2$)$_2$), 1.02 (d, $^3J_{PH}$ = 6.0 Hz, 18H, P[C(C<u>H</u>$_3$)$_3$]$_2$), 1.00 (d, $^3J_{PH}$ = 6.3 Hz, 18H, P[C(C<u>H</u>$_3$)$_3$]$_2$). $^{13}C\{^1H\}$ (C_6D_6, δ): 136.4, 135.9, 133.6, 123.3, 68.7 (br, O-(<u>C</u>H$_2$-CH$_2$)$_2$), 34.8 (br, P[<u>C</u>(CH$_3$)$_3$]$_2$), 34.1 (br, P[<u>C</u>(CH$_3$)$_3$]$_2$), 31.4 (P[C(<u>C</u>H$_3$)$_3$]$_2$), 30.7 (P[C(<u>C</u>H$_3$)$_3$]$_2$), 27.7 (m, B<u>C</u>H$_2$P), 26.1 (O-(CH$_2$-<u>C</u>H$_2$)$_2$). $^{31}P\{^1H\}$ (C_6D_6, δ): 37.5 (s). IR (KBr, cm^{-1}): 3054, 2941, 1474, 1364, 1103, 860, 815. Anal. Calcd for $C_{34}H_{58}BCuOP_2$: C, 65.96; H, 9.44. Found: C, 66.21; H, 9.22.

Synthesis of [Ph$_2$BP$^{tBu}_2$]Cu(N$_2$C(SiMe$_3$)$_2$) (2.5). Bis(trimethylsilyl)diazomethane (0.0598 mL of a 1.87 M stock solution in hexanes, 0.112 mmol) was added to a stirring solution of **2.3** (63.6 mg, 0.0932 mmol) in benzene (5 mL). The resulting yellow solution was heated to 60 °C for 24 h, and then concentrated *in vacuo* to a solid yellow-orange residue. Recrystallization from petroleum ether (1.5 mL, -30 °C) gave **2.5** as faint yellow crystals (7.3 mg, 11%). X-ray quality crystals were obtained by slow evaporation of a petroleum ether solution of **2.5**. ^1H (C_6D_6, δ): 8.01 (br d, *J* = 5.4 Hz, 4H, *ortho*-C<u>H</u>), 7.42 (t, *J* = 7.3 Hz, 4H, *meta*-C<u>H</u>), 7.16 (t, *J* = 7.2 Hz, 2H, *para*-C<u>H</u>), 1.91 (br, 4H, BC<u>H</u>$_2$P), 1.22 (d, $^3J_{PH}$ = 6.3 Hz, 18H, P[C(C<u>H</u>$_3$)]$_2$), 1.20 (d, $^3J_{PH}$ = 5.8 Hz, 18H, P[C(C<u>H</u>$_3$)$_2$]), -0.03 (s, 12H, Si(C<u>H</u>$_3$)$_2$). $^{13}C\{^1H\}$ (C_6D_6, δ): 166.1 (m, *ipso*-<u>C</u>), 133.6, 127.4, 132.2, 34.1 (d, $^1J_{PC}$ = 5.8 Hz, P[<u>C</u>(CH$_3$)$_3$]$_2$), 34.0 (d, $^1J_{PC}$ = 5.8 Hz, P[<u>C</u>(CH$_3$)$_3$]$_2$), 30.8 (d, $^2J_{PC}$ = 4.1 Hz, P[C(<u>C</u>H$_3$)$_3$]$_2$), 30.7 (d, $^2J_{PC}$ = 4.1 Hz, P[C(<u>C</u>H$_3$)$_3$]$_2$), 29.5 (br m, N$_2$<u>C</u>(SiMe$_3$)$_2$), 12.5 (br q, $^1J_{BC}$ = 42.0 Hz, B<u>C</u>H$_2$P), -0.4 (s, Si(<u>C</u>H$_3$)$_2$). $^{31}P\{^1H\}$ (C_6D_6, δ): 39.2 (s). IR (C_6H_6, cm^{-1}): 2932, 2865, 2108 (CN$_2$ st), 1477, 1425, 1364, 1260, 1102, 1071, 899, 867, 817. Anal.

Calcd for $C_{37}H_{68}BCuN_2P_2Si_2$: C, 60.59; H, 9.35; N, 3.82. Found: C, 60.47; H, 9.43; N, 3.59.

Synthesis of $[Ph_2BP^{tBu}_2]Cu(N_2CMes_2)$ (2.6). **2.3** (0.200 g, 0.293 mmol) and bis(2,4,6-trimethylphenyl)diazomethane (0.0816 g, 0.293 mmol) were combined in benzene (10 mL), giving a clear red-orange solution that was stirred for 40 min and then concentrated *in vacuo*. Petroleum ether (20 mL) was added, and the solution was cooled to -78 °C. A pre-cooled solution of tetrafluoroboric acid (0.0402 mL of a 48 wt% solution in diethyl ether, 0.293 mmol) was added in one portion, and the solution was allowed to warm gradually to room temperature with stirring. After 25 min at room temperature, a white precipitate was filtered off, and the filtrate was concentrated to a red-orange powder (0.130 g, 54%). X-ray quality crystals were obtained by slow evaporation of a petroleum ether solution of **2.6**. ^{1}H (C_6D_6, δ): 7.95 (br d, J = 6.9 Hz, 4H, *ortho*-C<u>H</u>), 7.40 (t, J = 7.4 Hz, 4H, phenyl *meta*-C<u>H</u>), 7.14 (t, 2H, *para*-C<u>H</u>), 6.70 (s, 4H, mesityl *meta*-C<u>H</u>), 2.09 (s, 6H, *para*-C<u>H</u>$_3$), 2.06 (s, 12H, *ortho*-C<u>H</u>$_3$), 1.91 (br, 4H, BC<u>H</u>$_2$P), 1.07 (d, $^3J_{PH}$ = 6.3 Hz, 18H, P[C(C<u>H</u>$_3$)$_3$]$_2$), 1.05 (d, $^3J_{PH}$ = 6.0 Hz, 18H, P[C(C<u>H</u>$_3$)$_3$]$_2$). ^{13}C{^{1}H} (C_6D_6, δ): 137.8 (br, phenyl *ipso*-<u>C</u>), 137.6, 133.6, 130.6, 129.7, 127.4, 126.6, 123.4, 99.3 (N_2<u>C</u>Mes$_2$), 34.0 (d, $^1J_{PC}$ = 6.7 Hz, P[<u>C</u>(CH$_3$)$_3$]$_2$), 33.9 (d, $^1J_{PC}$ = 6.7 Hz, P[<u>C</u>(CH$_3$)$_3$]$_2$), 30.7 (d, $^2J_{PC}$ = 3.7 Hz, P[C(<u>C</u>H$_3$)$_3$]$_2$), 30.6 (d, $^2J_{PC}$ = 3.7 Hz, P[C(<u>C</u>H$_3$)$_3$]$_2$), 21.3 (s, *para*-<u>C</u>H$_3$), 21.1 (s, *ortho*-<u>C</u>H$_3$), 14.3 (br, B<u>C</u>H$_2$P). ^{31}P{^{1}H} (C_6D_6, δ): 45.9 (s). IR (C_6H_6, cm^{-1}): 2921, 2868, 2041 (CN_2 st), 1444, 1366, 1099, 812. Anal. Calcd for $C_{49}H_{72}BCuN_2P_2$: C, 71.30; H, 8.79; N, 3.39. Found: C, 71.41; H, 8.43; N, 5.42. Note: High levels of N were found consistently by elemental analysis. ^{1}H and ^{31}P{^{1}H}

NMR spectra indicated that the material was spectroscopically pure. In addition, the IR spectrum of the material precluded the presence of residual free N_2CMes_2.

Synthesis of $[Ph_2BP^{tBu}_2]Cu(N(=CPh_2)(NCPh_2))$ (2.7). Diphenyldiazomethane (32.0 mg, 0.165 mmol) was dissolved in benzene (5 mL) and added to solid **2.3** (56.3 mg, 0.0825 mmol), giving a deep inky-blue solution. Over several hours, the solution turned orange-brown. After 24 h, a crude reaction aliquot showed >90% conversion to the desired product (by ^{31}P NMR). The solution was concentrated *in vacuo* to a solid brown residue, which was recrystallized from diethyl ether (1.5 mL, -30 °C) to give **2.7** as dark orange crystals (23.8 mg, 32%). X-ray quality crystals were obtained by slow diffusion of hexamethyldisiloxane vapors into a diethyl ether solution of **2.7** at -30 °C. ^1H (C_6D_6, δ): 9.10 (br, 2H), 8.05 (br d, J = 6.3 Hz, 4H, *ortho*-B<u>Ph</u>$_2$), 7.67 (m, 8H), 7.42 (t, J = 7.3 Hz, 4H, *meta*-B<u>Ph</u>$_2$), 7.33 (m, 8H), 7.13-6.89 (m, 34H), 1.91 (br, 4H, BC<u>H</u>$_2$P), 1.09 (d, $^3J_{PH}$ = 5.8 Hz, 18H, P[C(C<u>H</u>$_3$)]$_2$), 1.07 (d, $^3J_{PH}$ = 5.5 Hz, 18H, P[C(C<u>H</u>$_3$)]$_2$). $^{13}C\{^1H\}$ (C_6D_6, δ): 176.5 (m, Cu-N=<u>C</u>Ph$_2$), 166.3 (br m, *ortho*-B<u>Ph</u>$_2$), 160.4 (s, Cu-N-N=<u>C</u>Ph$_2$), 139.1, 136.7, 132.5, 131.5, 130.2, 130.1, 129.6, 129.1, 128.7, 128.4, 127.3, 123.3, 33.9 (d, $^1J_{PC}$ = 5.8 Hz, P[<u>C</u>(CH$_3$)$_3$]$_2$), 33.8 (d, $^1J_{PC}$ = 5.8 Hz, P[<u>C</u>(CH$_3$)$_3$]$_2$), 30.8 (d, $^2J_{PC}$ = 3.8 Hz, P[C(<u>C</u>H$_3$)$_3$]$_2$), 30.7 (d, $^2J_{PC}$ = 3.8 Hz, P[C(<u>C</u>H$_3$)$_3$]$_2$), 14.0 (br q, $^1J_{BC}$ = 41.7 Hz, B<u>C</u>H$_2$P). $^{31}P\{^1H\}$ (C_6D_6, δ): 39.9 (s). IR (KBr, cm^{-1}): 3055, 2940, 2866, 1584 (C=N st), 1561 (C=N st), 1487, 1445, 1393, 1362, 1319, 1178, 1157, 1103, 1074, 955, 865. Anal. Calcd for $C_{56}H_{70}BCuN_2P_2$: C, 74.12; H, 7.77; N, 3.09. Found: C, 74.10; H, 7.48; N, 3.21.

Observation of the optical spectrum for $[Ph_2BP^{tBu}_2]Cu{=}CPh_2$ (2.8). Diphenyldiazomethane (0.5 mg, 0.0026 mmol) was dissolved in benzene (3 mL) and added to solid **2.3** (1.8 mg, 0.0026 mmol) in a volumetric flask, resulting in an immediate

color change to an intense inky blue. The volume was brought up to 20.0 mL, and an aliquot was removed for observation by UV-Vis. A intense feature at 583 nm was observed. In a separate experiment under identical conditions, **2.8** was present in ca. 70 mol% by $^{31}P\{^{1}H\}$ spectroscopy. On this basis, an ε value of ca. 12000 was estimated.

Observation of ^{13}C-labelled 2.8. $N_2{}^{13}CPh_2$ (13.1 mg, 0.0671 mmol) was dissolved in benzene-d_6 (1 mL) and added to solid 2.**3** (49.8 mg, 0.730 mmol), resulting in an immediate color change to an intense inky blue. The reaction was monitored by ^{1}H, $^{13}C\{^{1}H\}$, and $^{31}P\{^{1}H\}$ NMR. In the initial reaction mixture, the salient features attributed to 2.**8-^{13}C** were as follows. $^{13}C\{^{1}H\}$ (δ): 331.5 (t, $^{2}J_{PC}$ = 40.4 Hz, Cu=$\underline{C}Ph_2$). $^{31}P\{^{1}H\}$ (δ): 64.8 (d, $^{2}J_{PC}$ = 41.2 Hz).

Carbene transfer to CO. Using the reaction conditions described above, **2.8** was generated *in situ* and transferred to a J. Young NMR tube. The solution was frozen, and then the dinitrogen atmosphere was evacuated and replaced with carbon monoxide (1 atm). The reaction mixture was examined by ^{1}H and $^{31}P\{^{1}H\}$ NMR, showing quantitative conversion of **2.8** to the previously characterized $[Ph_2BP^{tBu}{}_2]Cu(CO)$.[8] The solution was then transferred to a solution IR cell and examined by IR spectroscopy, revealing diagnostic CO stretching vibrations for both $[Ph_2BP^{tBu}{}_2]Cu(CO)$ and $Ph_2C{=}C{=}O$, 2082 cm^{-1}.[24] In a separate experiment, the copper-containing components of the product mixture were precipitated with petroleum ether, and analysis of the supernatant by ESI-MS revealed the presence of $Ph_2C{=}C{=}O$.

References Cited

1 Selected reviews: W. Kirmse, *Angew. Chem., Int. Ed.* **2003**, *42*, 1088; H. M. L. Davies, S. A. Panaro, *Tetrahedron* **2000**, *56*, 4871; M. P. Doyle, D. C. Forbes, *Chem. Rev.* **1998**, *98*, 911.

2 For recent advances see, for example, M. R. Fructos, T. R. Belderrain, M. C. Nicasio, S. P. Nolan, H. Kaur, M. M. Díaz-Requejo, P. J. Pérez, *J. Am. Chem. Soc.* **2004**, *126*, 10846 and references therein.

3 Selected examples: J. Barluenga, L. A. López, O. Löber, M. Tomás, S. García-Granda, C. Alvarez-Rúa, J. Borge, *Angew. Chem., Int. Ed.* **2001**, *126*, 10085; D. S. Laitar, P. Müller, J. P. Sadighi, *J. Am. Chem. Soc.* **2005**, *127*, 17196; H. Kaur, F. Kauer, E. D. Stevens, S. P. Nolan, *Organometallics* **2004**, *23*, 1157.

4 B. Straub, P. Hofmann, *Angew. Chem., Int. Ed.* **2001**, *40*, 1288.

5 Y. M. Badiei, T. H. Warren, *J. Organomet. Chem.* **2005**, *690*, 5989; X. Dai, T. H. Warren, *J. Am. Chem. Soc.* **2004**, *126*, 10085.

6 Selected examples: D. M. Jenkins, T. A. Betley, J. C. Peters, *J. Am. Chem. Soc.* **2002**, *124*, 11238; S. D. Brown, T. A. Betley, J. C. Peters, *J. Am. Chem. Soc.* **2003**, *125*, 322; T. A. Betley, J. C. Peters, *J. Am. Chem. Soc.* **2004**, *126*, 6252; C. E. MacBeth, J. C. Thomas, T. A. Betley, J. C. Peters, *Inorg. Chem.* **2004**, *43*, 4645.

7 J. C. Thomas, J. C. Peters, *J. Am. Chem. Soc.* **2003**, *125*, 8870; J. C. Thomas, J. C. Peters, *Inorg. Chem.* **2003**, *42*, 5055.

8 J. C. Thomas, J. C. Peters, *Polyhedron* **2004**, *23*, 2901.

9 Blue, E. D.; Davis, A.; Conner, D.; Gunnoe, T. B.; Boyle, P. D.; White, P. S. *J. Am. Chem. Soc.* **2003**, *125*, 9435.

10 B. F. Straub, F. Rominger, P. Hofmann, *Organometallics* **2000**, *19*, 4305.

11 E. Glozbach, J. Lorberth, *J. Organomet. Chem.* **1980**, *191*, 371; H. E. Zimmerman, D. H. Paskovich, *J. Am. Chem. Soc.* **1964**, *86*, 2149.

12 R. Waterman, G. L. Hillhouse, *J. Am. Chem. Soc.* **2003**, *125*, 13350; D. J. Mindiola, G. L. Hillhouse, *J. Am. Chem. Soc.* **2002**, *124*, 9976.

13 Selected examples: H. Zhu, J. Chai, A. Stasch, H. W. Roesky, T. Blunk, D. Vidovic, J. Magull, H.-G. Schmidt, M. Noltemeyer, *Eur. J. Inorg. Chem.* **2004**, 4046; K. Okuma, K. Kojima, K. Oyama, K. Kubo, K. Shioji, *Eur. J. Org. Chem.* **2004**, 820; H. Werner, P. Schwab, E. Bluel, N. Mahr, B. Windmüller, J. Wolf, *Chem. Eur. J.* **2000**, *6*, 4461.

14 R. H. Crabtree, *The Organometallic Chemistry of the Transition Metals*; Wiley-Interscience: New York, 2001.

15 Warren has shown that the μ-CPh_2 binding mode in the β-diketiminato system shifts the copper carbene peak to higher field (δ 189.4) relative to the terminal CPh_2 complex (δ 253.1). See ref 5.

16 B3LYP functional; LACVP** basis set for Cu atoms, 6-31G** basis set for carbene C and P atoms; MIDI! basis set for all other atoms.

17 J. C. Thomas, J. C. Peters, *Inorg. Chem.* **2003**, *42*, 5055.

18 J. B. Miller, *J. Org. Chem.* **1959**, *24*, 560.

19 H. E. Zimmerman, D. H. Paskovich, *J. Am. Chem. Soc.*, **1964**, *86*, 2149.

20 E. Glozbach, J. Lorberth, *J. Organomet. Chem.* **1980**, *191*, 371.

21 P. J. Hay, W. R. Wadt, *J. Chem. Phys.* **1985**, 299.

22 R. E. Easton, D. J. Giesen, A. Welch, C. J. Cramer, D. G. Truhlar, *Theo. Chim. Acta* **1996**, 281.

23 G. M. Sheldrick, *Acta Cryst*. **2008**, *A64*, 112.

24 A. E. Taggi, A. M. Ahmed, H. Wack, B. Young, D. Ferraris, T. Leckta, *J. Am. Chem. Soc*. **2002**, *23*, 6626.

Chapter 3: Three-Coordinate Copper(I) Amido and Aminyl Radical Complexes

Reproduced in part with permission from

Mankad, N. P., Antholine, W. E., Szilagyi, R. K., and Peters, J. C. *Journal of the American Chemical Society* **2009**, *131*, 3878-3880.

3.1 Introduction

Electron transfer (ET) through proteins often utilizes copper-containing active sites as efficient one-electron relays. The type-1 active sites of the blue copper proteins are prominent examples.[1,2,3] It is generally thought that rapid ET rates through type-1 redox sites derive from the protein environments enforcing unusual trigonally distorted coordination spheres to allow for minimal structural reorganization during ET.[1,4] Though large Cu^{II}/Cu^{I} self-exchange ET rate constants (k_S) in the range observed for type-1 sites have been achieved in certain synthetic monocopper systems using geometries distinct from trigonal environments,[5] ET studies have yet to be conducted in a synthetic system featuring isolated, trigonally disposed copper centers. The simplest such systems would contain a trigonal planar geometry.

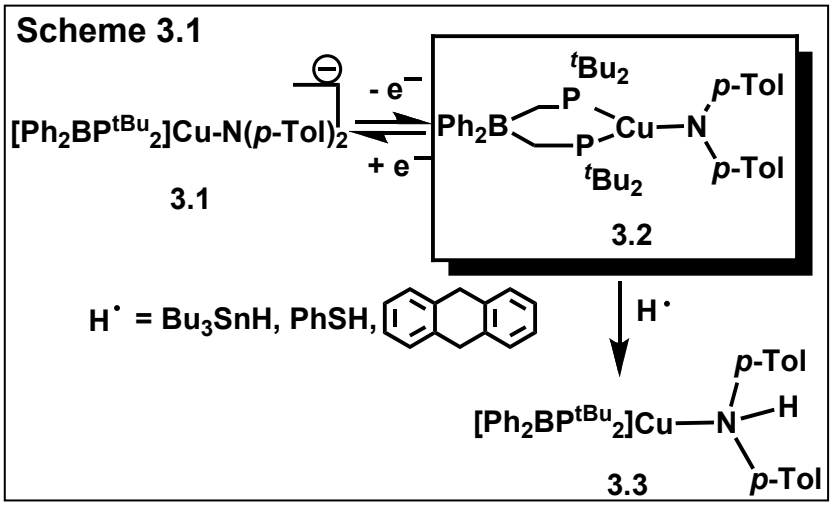

Here we report structural characterization of a trigonal planar system featuring formally Cu^{II} and Cu^{I} amido complexes related by a reversible one-electron redox event. We find in this system that ET is extremely rapid and is accompanied by a small degree of structural reorganization during redox. We propose that this structural rigidity in the absence of secondary coordination sphere effects results from significant covalency of

the copper-amide linkages. In fact, a Cu^{I}-aminyl radical description of the formally Cu^{II} amide complex may be most appropriate.

3.2 Results and Discussion

3.2.1 Synthesis, Characterization, and Electron Transfer Kinetics

The anionic Cu^{I} amido complex {[$Ph_2BP^{tBu}_2$]Cu($NTol_2$)} {Li(12-crown-4)$_2$} (**3.1**) ([$Ph_2BP^{tBu}_2$] = $Ph_2B(CH_2P^tBu_2)_2$, Tol = *p*-tolyl) was synthesized by the reaction between [$Ph_2BP^{tBu}_2$]Cu(pyridine) and $LiNTol_2$ in the presence of excess 12-crown-4,[6] and isolated as a yellow, diamagnetic solid. The cyclic voltammogram of **3.1** features a fully reversible redox event at -0.882 V vs $FeCp_2^+/FeCp_2$ (see Section 3.5.3). Chemical oxidation of **3.1** with [$FeCp_2$][$B(3,5\text{-}(CF_3)_2C_6H_3)_4$] produced paramagnetic [$Ph_2BP^{tBu}_2$]Cu($NTol_2$) (**3.2**) as red needles with optical bands at 365 nm (ε = 870 M^{-1} cm^{-1}) and 480 nm (ε = 600 M^{-1} cm^{-1}) (Scheme 3.1).

Both **3.1** and **3.2** were studied by single-crystal X-ray crystallography (Figure 3.1; also see Appendix 2). Immediately evident upon comparison of the two oxidation states is the minimal degree of structural rearrangement at the Cu centers upon ET (see Figure 3.1B for overlay). In both structures, the Cu centers have rigorously planar coordination geometries ($\Sigma\angle$ = 359.97(14)° (**3.1**) and 359.97(17)° (**3.2**)). The Cu-P distances, P-Cu-P angles, and P-Cu-N angles are all essentially identical in both **3.1** and **3.2**. The most notable structural difference is the Cu-N contraction seen upon oxidation from **3.1** (2.0019(18) Å) to **3.2** (1.906(2) Å). The UV-Vis spectra of **3.2** in benzene and acetonitrile are identical (see Section 3.5.5), consistent with **3.2** being three coordinate in

solution as well as in the solid state. A series of trigonal planar β-diketiminato Cu^{II} complexes synthesized by Tolman and coworkers remain the only other reported examples of three-coordinate, formally Cu^{II} complexes.[7]

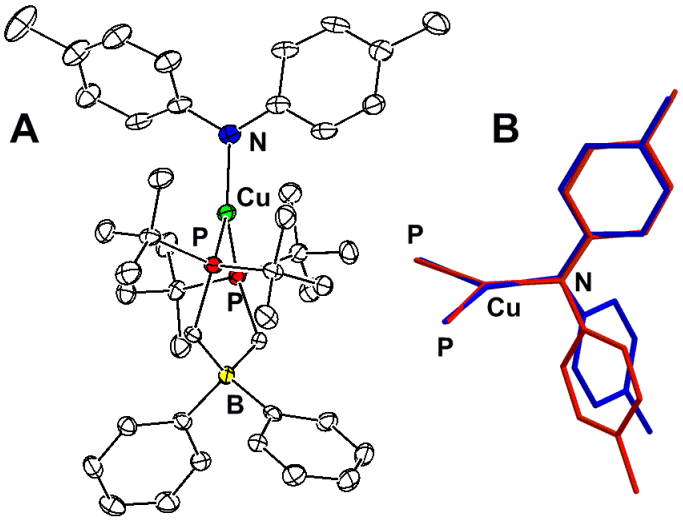

Figure 3.1. (A) Solid-state structure of **3.2**. (B) Structural overlay of anion **3.1** (red) and **3.2** (blue) with only phosphorus atoms of $[Ph_2BP^{tBu}_2]$ shown. Selected bond lengths (Å) and angles (°) for **3.1**: Cu-N, 2.0019(18); Cu-P(1), 2.2921(6); Cu-P(2), 2.2684(6); P(1)-Cu-P(2), 105.67(2); P(1)-Cu-N, 124.07(6); P(2)-Cu-N, 130.23(6). For **3.2**: Cu-N, 1.906(2); Cu-P(1), 2.2816(7); Cu-P(2), 2.2806(8); P(1)-Cu-P(2), 104.04(3); P(1)-Cu-N, 123.99(7); P(2)-Cu-N, 131.94(7).

Taken together, complexes **3.1** and **3.2** represent the only three-coordinate copper system to be isolated and structurally characterized in two distinct redox states.[8] Therefore, it was of interest to study the **3.2**/**3.1** self-exchange ET rate constant (k_S). As discussed in Section 3.5.6, we determined that k_S in this system is too large to measure

accurately by NMR linewidth analysis, implying a lower limit of $k_S \geq 10^7$ M^{-1} s^{-1}.[9] For comparison, type-1 active sites typically exhibit values of k_S on the order of 10^6 M^{-1} s^{-1}.[1]

3.2.2 Multiedge X-ray Absorption Spectroscopy

Spectroscopic studies of the dinuclear Cu_A ET sites in cytochrome *c* oxidase and nitrous oxide reductase have revealed significant covalency in the $Cu_2(\mu\text{-}SR)_2$ cores, resulting in significant sulfur-centered redox during ET.[10] This covalency likely contributes to the extremely efficient ET rates mediated by Cu_A,[11] and this concept has been discussed in the context of synthetic $Cu_2(\mu\text{-}X)_2$ model complexes.[9,12] It is also likely that such Cu-ligand covalency likewise plays a role in the functional properties of the type-1 active sites in blue copper proteins.[11] We therefore sought to probe the intimate electronic structures of **3.1** and **3.2**, in particular questioning whether oxidation of the amido ligand occurs during the interchange of **3.1** and **3.2**. In other words, we wondered if the Cu^I-aminyl radical form of **3.2** is an important resonance contributor. A Rh complex from Grützmacher and coworkers in 2005 was the first reported example of an isolable 1:1 aminyl radical complex of a transition metal,[13] and, unlike their aryloxy radical analogues, such complexes remain quite rare.[14] To our knowledge, examples of non-chelated aminyl radical ligands have not yet been reported.

Cu K-edge X-ray absorption spectroscopy (XAS) was used to probe the effective Cu oxidation states in **3.1** and **3.2**. The Cu K-edge spectra for **3.1** and **3.2** in Figure 3.2A show a high degree of similarity in their respective pre-edge features and rising-edge energy positions, indicating practically identical Cu effective nuclear charges and ligand fields. The first electric dipole allowed Cu 1s→4s transitions at 8982.2 and 8982.5 eV in

3.1 and **3.2**, respectively, are well resolved from the rising-edge features, which is indicative of trigonal planar coordination geometry.[15] The small shift of 0.3 eV upon oxidation of **3.1** indicates that **3.1** and **3.2** have similar effective oxidation states that are closer to cuprous than cupric when compared to the reference spectra for CuCl and $CuCl_2$ (Figure 3.2A).

Cu L-edge XAS was used to directly probe the Cu 3d character of the frontier orbitals in **3.1** and **3.2**. Figure 3.2B compares a set of features observed at the L_3-edge for complexes **3.1**, **3.2**, CuCl, and $CuCl_2$. The intense pre-edge feature at 930.4 eV for $CuCl_2$ is due to the transition of a Cu 2p electron to the unoccupied, Cu 3d-based LUMO. The Cu 3d character of the LUMO is determined to be about 65% based upon the area under this pre-edge feature. This intense feature disappears in the spectrum of CuCl.[16] The group of features between 936 and 937 eV in the spectrum of **3.1** arise due to Cu→L back donation. Similar but more intense features have been observed for dinuclear Cu-amidophosphine complexes.[12] Upon oxidation to **3.2**, a new feature at 931.9 eV appears, consistent with an electron being removed from an orbital with Cu 3d character. The proportion between the area of this feature and of the pre-edge feature in $CuCl_2$ indicates that the redox active molecular orbital in **3.2** has about 14% 3d character, and that therefore the remainder of the electron density has to be ligand centered.

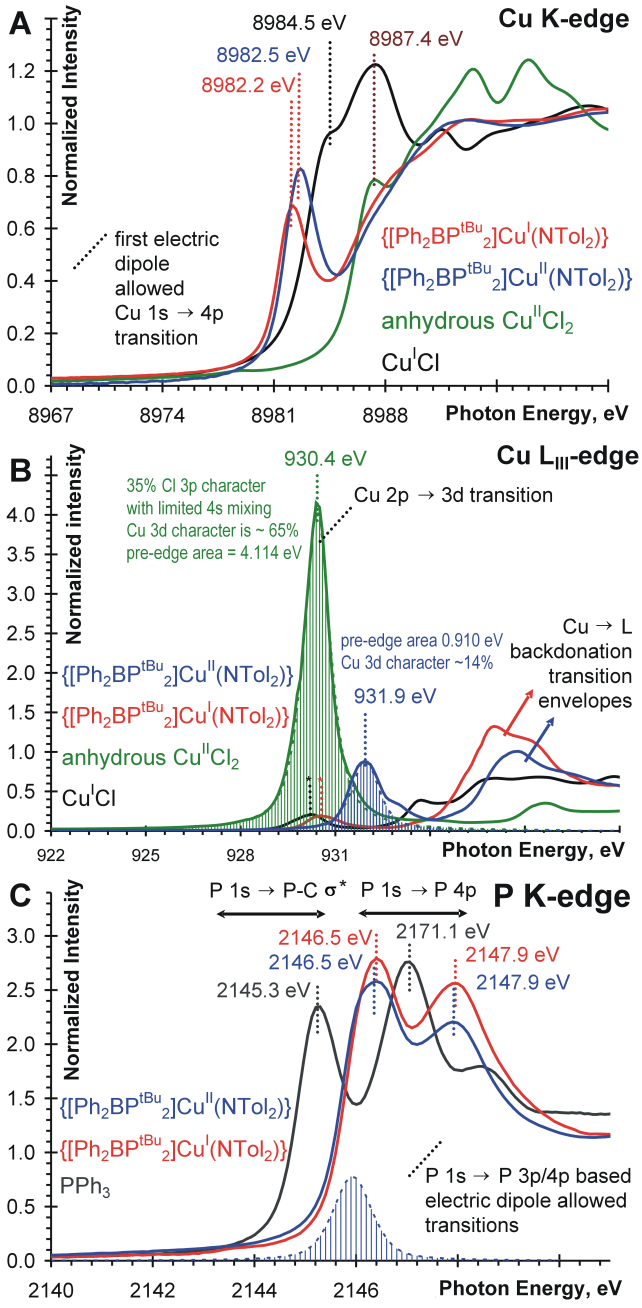

Figure 3.2. (A) Cu K-edge spectra, (B) Cu L_3-edge spectra, and (C) P K-edge spectra of CuCl (black), **3.1** (red), $CuCl_2$ (green), **3.2** (blue), and PPh_3 (gray); * = trace impurity.

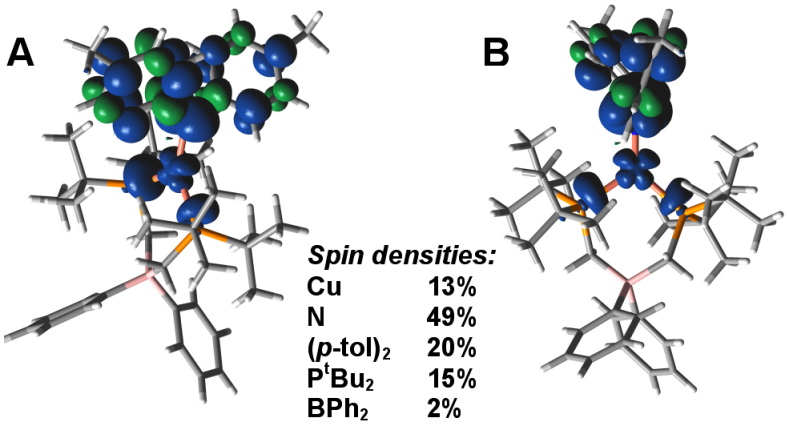

Figure 3.3. Atomic spin density plots[17] (0.002 isocontours) for $[Ph_2BP^{tBu}_2]Cu(NTol_2)$ viewed A) parallel and B) perpendicular to the P_2CuN plane.

To dissect the role of the phosphine ligands in redox, we collected P K-edge XAS data (Figure 3.2C). In comparison to the reference PPh_3, the spectra of **3.1** and **3.2** are shifted toward higher energy due to increase in P effective nuclear charge of the phosphines involved in P→Cu donation. Upon oxidation, an electron hole is created in an orbital that has phosphorous character of about 20% (see Appendix 2). This with the 14% Cu 3d character clearly indicates that close to 70% of the redox active frontier orbital of **3.1** and **3.2** must have N, C, and H character. This estimate is in good agreement with spin densities calculated using DFT,[17] which indicate 13% unpaired spin character on Cu, 49% on N, 15% on P, and 20% on C/H of the *p*-tolyl groups (see Figure 3.3 for spin density plots).

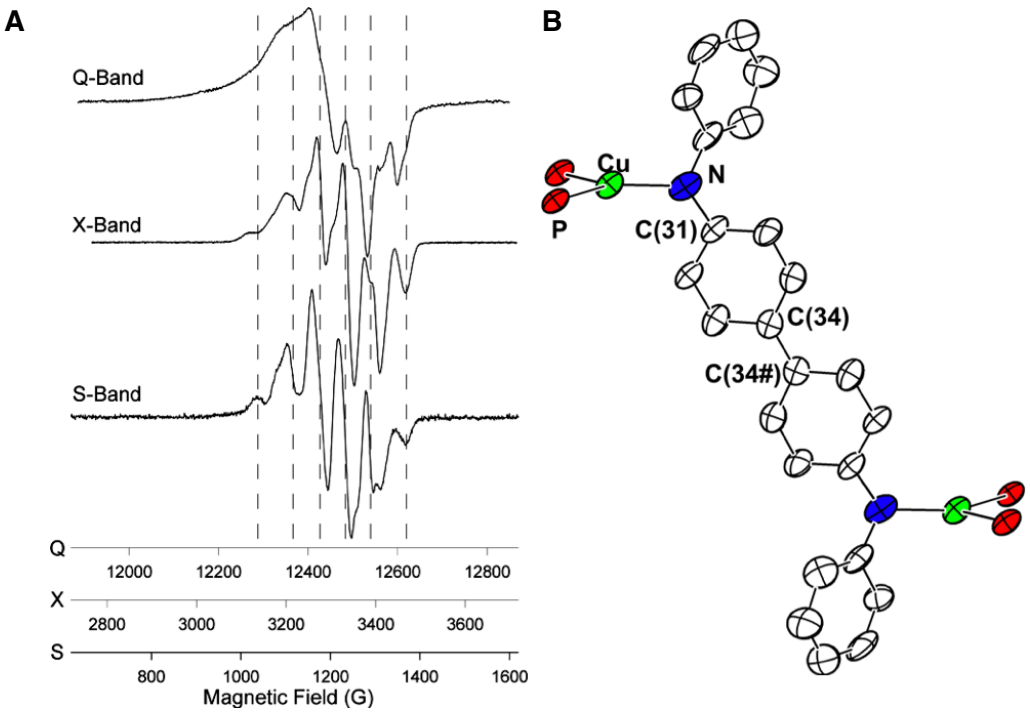

Figure 3.4. A) Multifrequency EPR spectroscopy of **3.2**. Spectra were recorded in a frozen dichloromethane/toluene glass. Microwave frequency (temperature): 35.100 GHz (123 K), 9.188 GHz (77 K), and 3.392 (123 K) for Q-, X-, and S-band, respectively. B) Core structure of **3.5**, with only phosphorus atoms of $[Ph_2BP^{tBu}_2]$ shown. Selected bond lengths (Å): Cu-N, 1.944(11); N-C(31), 1.344(14); C(34)-C(34#), 1.40(2).

3.2.3 Multifrequency EPR Spectroscopy

EPR spectra of **3.2** were collected at the S-, X-, and Q-bands and are quite unusual compared to typical cupric complexes (Figure 3.4A). The S- and X-band spectra are dominated by six lines, each with several shoulders, unlike the typical four-line

pattern expected for a single cupric center. In all three spectra, sharp high-field lines are evident. (The spectra depicted in Figure 3.4A are aligned with these high-field lines.) A line on the low-field side is well resolved in the S- and X-band spectra and is a shoulder at Q-band. By assigning these outer lines as purely Cu lines, a reasonable simulation of the X-band spectrum can be obtained. However, accurate simulation parameters should give satisfactory fits at all frequencies; this is not the case here, particularly at the Q-band (Figure 3.5).

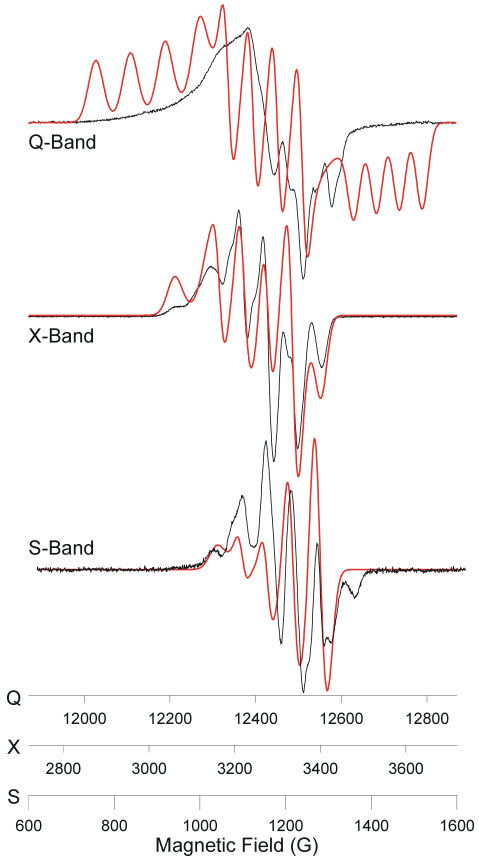

Figure 3.5. Experimental (black) and simulated (red) EPR spectra of **3.2** resulting from assigning outer lines as deriving purely from Cu.

On the other hand, one way to get a six-line pattern is to have A^{Cu} approximately equal to A^{P} for two equivalent phosphorus donor atoms, resulting in lines with intensities 1:3:4:4:3:1. Experimentally, if the outer lines are set to intensity 1, then the measured intensities of the adjacent lines are close to 3. Using this as a guideline, approximate simulations (Figure 3.6) were obtained using the following parameters: g_x, g_y, g_z = 2.008, 2.008, 2.030; $A^{Cu}{}_x$, $A^{Cu}{}_y$, $A^{Cu}{}_z$ = 34, 34, 170 MHz; $A^{P}{}_x$, $A^{P}{}_y$, $A^{P}{}_z$ = 148, 148, 173 MHz; $A^{N}{}_x$, $A^{N}{}_y$, $A^{N}{}_z$ = 24, 100, 24 MHz. (Figure 3.6B depicts simulated spectra obtained by holding all other parameters constant and varying $A^{N}{}_y$.) Though these simulation parameters are consistent with but not proof of physical EPR parameters, reasonable fits were obtained using the same parameters at all three bands (Figure 3.6A), lending weight to their assignments. For comparison, one of Tolman's (β-diketiminate)Cu^{II}Cl complexes, a more typical three-coordinate Cu^{II} complex, has the parameters $g_{\|}$ = 2.20, $g_{\perp}$ = 2.05, $A^{Cu}{}_{\|}$ = 398 MHz, $A^{Cu}{}_{\perp}$ = 52 MHz.[7] An example of a typical nitrogen radical is di-*t*-butylnitroxide (DTBN), which exhibits anisotropic hyperfine tensors of A^{N} = 89.6, 16.7, and 21.3 MHz.[18] The comparatively small A^{Cu} and large $A^{N}{}_y$ values in **3.2**, as well as the proximity of $g_{average}$ in **3.2** to the value for the free electron, indicate a significant degree of spin delocalization between the Cu and N centers.

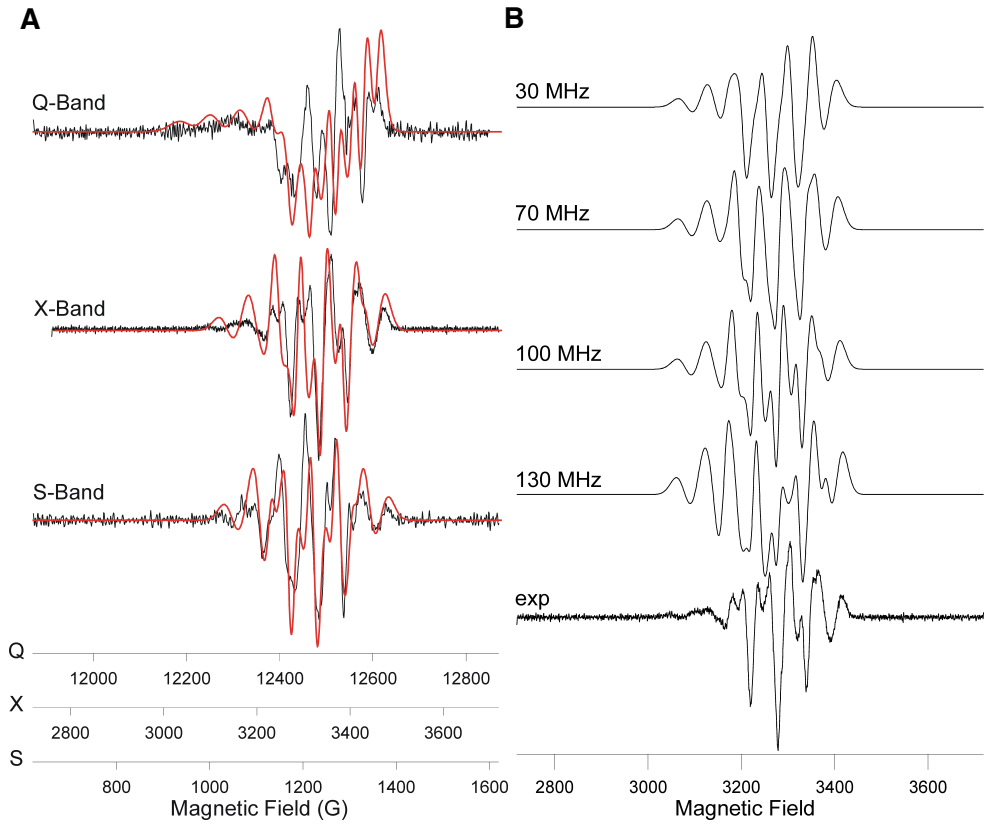

Figure 3.6. A) Experimental (black) and simulated (red) second derivative EPR spectra of **3.2** at Q-, X-, and S-bands. B) Simulated second derivative X-band spectra of **3.2** resulting from maintaining all other simulation parameters while varying A^{N}_{y} as indicated.

3.2.4 Reactivity

XAS, DFT, and EPR analyses collectively suggest that **3.2** is better considered as a Cu^{I}-aminyl radical than a Cu^{II}-amido complex. This unusual electronic structure is also manifested in the chemical reactivity of the system. For instance, the addition of H-atom donors such as Bu_3SnH, PhSH, or 9,10-dihydroanthracene to solutions of **3.2** cleanly produced $[Ph_2BP^{tBu}_2]Cu(NHTol_2)$ (**3.3**) (Scheme 3.1). The by-products $Bu_3Sn\text{-}SnBu_3$,

PhS-SPh, and anthracene were detected by ^{1}H NMR and GC-MS, and the presence of an N-H linkage in **3.3** was confirmed by ^{1}H NMR (δ(N-H) = 4.93) and IR spectroscopy (ν(N-H) = 3405 cm^{-1}). The hydrogen atom transfer (HAT) reactivity of **3.2** is, to our knowledge, unprecedented for the formal Cu^{II} oxidation state. Instead, HAT reactions have been observed at Cu^{III} centers,[19] or alternatively, Cu^{II}-aryloxy radicals.[20] The reaction between **3.2** and either Bu_3SnD or Bu_3SnH provided a kinetic deuterium isotope effect of k_H/k_D = 4.8(6) at room temperature. This value is more consistent with a concerted hydrogen atom abstraction mechanism rather than rate-limiting ET followed by proton transfer, and it is within the range observed for other Cu-containing systems.[20]

Scheme 3.2

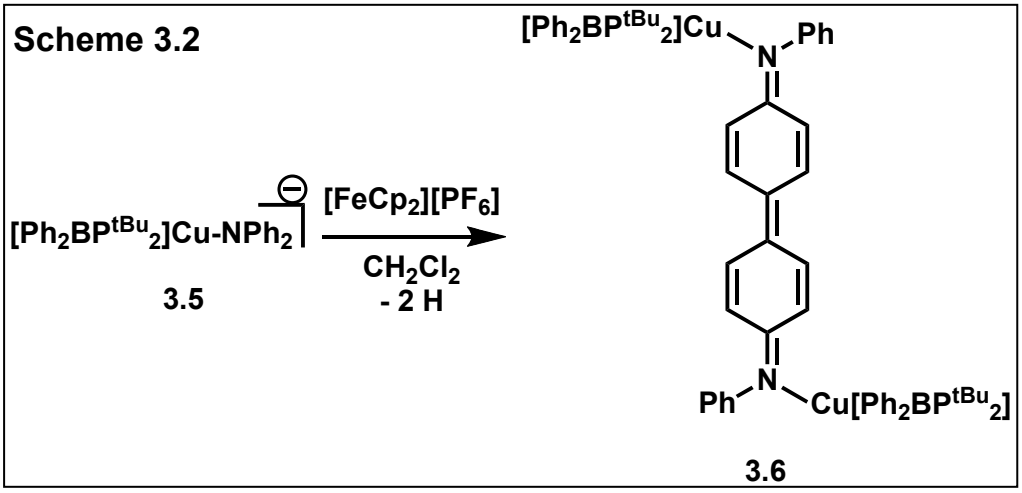

Further indication of radical character delocalized into the aromatic rings in **3.2** comes from the oxidation chemistry of {[$Ph_2BP^{tBu}_2$]Cu(NPh_2)}{Li(12-crown-4)$_2$} (**3.4**), which lacks methyl groups *para* to the amido nitrogen (Scheme 3.2). The reaction between **3.4** and [$FeCp_2$][PF_6] produces a bright red, diamagnetic dicopper product (**3.5**) in which two diphenyl amido groups have been fused together at the positions *para* to the N atoms (Figure 3.44B). The identity of **3.5** was established using a relatively low-quality X-ray crystal structure. Nonetheless, the short length of the new C-C bond (1.40(2) Å) in

3.5 and the planar geometries at these carbons indicate that two hydrogen atom equivalents have been lost subsequent to C-C coupling. Similar ligand-centered radical coupling has been observed in an oxidized $Cu_2(\mu\text{-}NR_2)_2$ complex[12] and from a putative three-coordinate Cu^{II}-aryloxide intermediate synthesized by Tolman.[7]

3.3 Conclusions

In conclusion, we have isolated and thoroughly characterized a highly covalent, three-coordinate Cu-NAr_2 system in two distinct oxidation states, with the unusual oxidized form being best regarded as an aminyl radical ligated to Cu^I. Chemical reactivity facilitated by this electronic structure includes HAT, C-C coupling, and efficient electron transfer, the latter being reminiscent of protein active sites bearing similar Cu coordination geometries.

3.4 Experimental Section

3.4.1 General Considerations

All manipulations were carried out using standard Schlenk or glovebox techniques under a dinitrogen atmosphere. Unless otherwise noted, solvents were deoxygenated and dried by thoroughly sparging with N_2 gas followed by passage through an activated alumina column. Non-halogenated solvents were tested with a standard purple solution of sodium benzophenone ketyl in tetrahydrofuran in order to confirm effective oxygen and moisture removal. All reagents were purchased from commercial vendors and used without further purification unless otherwise stated. Lithium amides

were prepared by deprotonation of the corresponding amines with *n*-butyllithium. $[Ph_2BP^{tBu}{}_2]Cu(pyridine)$[21] and $[FeCp_2][B(3,5\text{-}(F_3C)_2C_6H_3)_4]$ [22] were prepared by literature procedures. Elemental analyses were performed by Desert Analytics, Tucson, AZ. Deuterated solvents were purchased from Cambridge Isotope Laboratories (Cambridge, MA), degassed, and dried over activated 3 Å molecular sieves prior to use. A Varian Mercury-300 spectrometer was used to record ^1H, ^{13}C, and ^{31}P NMR spectra at ambient temperature. ^1H and ^{13}C chemical shifts were referenced to the residual solvent peaks. ^{31}P chemical shifts were referenced to external phosphoric acid ($\delta = 0$ ppm).

3.4.2 Synthesis

Synthesis of $\{[Ph_2BP^{tBu}{}_2]Cu(NTol_2)\}\{Li(12\text{-crown-}4)_2\}$ (3.1). $[Ph_2BP^{tBu}{}_2]Cu(pyridine)$ (0.203 g, 0.324 mmol) and $LiNTol_2$ (0.0659 g, 0.324 mmol) were combined in THF (10 mL), giving a clear yellow solution. After stirring for 5 min, 12-crown-4 (0.131 mL, 0.810 mmol) was added. The resulting bright yellow solution was stirred for 0.5 h, and then the solvent was removed *in vacuo*. The residues were triturated with petroleum ether (10 mL), and a yellow powder was collected on a sintered glass frit. Subsequent washes with petroleum ether (5 x 5 mL) gave analytically pure **3.1** (0.299 g, 84%). X-ray quality crystals were obtained by slow diffusion of petroleum ether vapors into a concentrated THF solution of **3.1**. ^1H (THF-d_8, δ): 7.36 (br, 4H, borate *ortho*-C<u>H</u>), 6.8-7.0 (m, 8H, Ar-<u>H</u>), 6.61 (m, 6H, Ar-<u>H</u>), 3.63 (s, 32H, O(C<u>H</u>$_2$)$_2$O), 2.08 (s, 6H, *para*-C<u>H</u>$_3$), 1.46 (br, 4H, BC<u>H</u>$_2$P), 1.01 (d, $^3J_{PH}$ = 5.8 Hz, 18H, P[C(C<u>H</u>$_3$)$_3$]$_2$), 1.00 (d, $^3J_{PH}$ = 5.5 Hz, 18H, P[C(C<u>H</u>$_3$)$_3$]$_2$). $^{13}C\{^1H\}$ (THF-d_8, δ): 162.3 (br, borate *ipso*-<u>C</u>), 156.0 (s, tolyl *ipso*-<u>C</u>), 133.7, 128.4, 125.4, 121.1, 120.4, 69.4 (s, O(<u>C</u>H$_2$)$_2$O), 33.0 (br, P[<u>C</u>(CH$_3$)$_3$]$_2$),

30.2 (P[C($\underline{C}H_3)_3]_2$), 30.1 (P[C($\underline{C}H_3)_3]_2$), 20.3 (s, *para*-$\underline{C}H_3$), 13.3 (br, B$\underline{C}H_2$P). $^{31}P\{^1H\}$ (THF-d_8, δ): 30.9 (s). IR (KBr, cm^{-1}): 2914, 2865, 1597, 1491, 1362, 1323, 1290, 1246, 1136, 1098, 1024, 920, 858, 809. Anal. Calcd for $C_{60}H_{96}BCuLiNO_8P_2$: C, 65.36; H, 8.78; N, 1.27. Found: C, 65.22; H, 8.55; N, 1.33.

Synthesis of [$Ph_2BP^{tBu}_2$]Cu($NTol_2$) (3.2). A solution of [$FeCp_2$][B(3,5-$(F_3C)_2C_6H_3)_4$] (0.230 g, 0.219 mmol) in dichloromethane (12 mL) was added in one portion to solid **3.1** (0.242 g, 0.219 mmol), resulting in a cherry-red solution. After stirring for 15 min, the solvent was removed *in vacuo*, leaving a dark-red oily residue that was dissolved in petroleum ether (10 mL), filtered through Celite, and allowed to stand at -30 °C for 16 h, resulting dark red needles that were crushed and washed thoroughly with petroleum ether to yield analytically pure **3.2** (41.4 mg, 25%). X-ray quality crystals were obtained by diffusion of hexamethyldisiloxane vapors in a concentrated solution of **3.2** in petroleum ether at -30 °C. IR (KBr, cm^{-1}): 2941, 2865, 1583, 1509, 1474, 1364, 1258, 1154, 1019, 936, 864, 813. Anal. Calcd for $C_{44}H_{64}BCuNP_2$: C, 71.10; H, 8.68; N, 1.88. Found: C, 71.17; H, 8.42; N, 1.85.

Synthesis of [$Ph_2BP^{tBu}_2$]Cu($NHTol_2$) (3.3). Tributyltin hydride (8.28 mL, 0.0308 mmol) was added to a stirring solution of **3.2** (21 mg, 0.028 mmol) in benzene (7 mL). After stirring for 4 h, the light-yellow solution was concentrated *in vacuo*. The residues were washed thoroughly with petroleum ether (3 x 2 mL), leaving behind **3.3** as a tan powder (7.8 mg, 37%). The petroleum ether fraction was filtered through alumina and analyzed by GC-MS to reveal the stoichiometric hexabutyldistannane by-product. Similar results were achieved using 1,2-dihydroanthracene (0.5 eq) or thiophenol in place of tributyltin hydride, yielding anthracene or PhS-SPh (0.5 eq), respectively. Though **3.3**

was isolated in low yield due in part to its petroleum ether solubility, ^{1}H NMR studies established that it was generated quantitatively in the initial reaction mixtures. Attempts to recrystallize **3.3** from THF/pentane produced the previously characterized [$Ph_2BP^{tBu}_2$]Cu(THF) just as was observed for [$Ph_2BP^{tBu}_2$]Cu(NH_2Mes),[21] and thus far other solvent systems have not yielded crystals suitable for either combustion analysis or X-ray crystallography. Characterization of **3.3**: ^{1}H (C_6D_6, δ): 7.95 (br, 4H, borate *ortho*-C<u>H</u>), 7.39 (t, *J* = 6.9 Hz, 4H, borate *meta*-C<u>H</u>), 6.95 (d, *J* = 8.4 Hz, 4H, tolyl *ortho*-C<u>H</u>), 6.84 (d, *J* = 8.4 Hz, 4H, tolyl *meta*-C<u>H</u>), 6.73 (t, *J* = 7.2 Hz, 2H, borate *para*-C<u>H</u>), 4.93 (br s, 1H, N-<u>H</u>), 2.15 (s, 6H, *para*-C<u>H_3</u>), 1.84 (br, 4H, BC<u>H_2</u>P), 1.03 (br, 36H, P[C(C<u>H_3</u>)$_3$]$_2$). ^{13}C{^{1}H} (CD_2Cl_2, d): 132.9, 130.3, 128.8, 126.9, 126.6, 122.2, 118.1, 34.5 (br, P[<u>C</u>(CH_3)$_3$]$_2$), 30.9 (P[C(<u>C</u>H_3)$_3$]$_2$), 30.3 (P[C(<u>C</u>H_3)$_3$]$_2$), 28.1 (s, *para*-<u>C</u>H_3). ^{31}P{^{1}H} (C_6D_6, δ): 37.7 (br s). IR (C_6H_6, cm^{-1}): 3405 (N-H st), 2922, 2866, 1365, 1293, 1081, 880, 811.

Synthesis of {[$Ph_2BP^{tBu}_2$]Cu(NPh_2)}{Li(12-crown-4)$_2$} (3.4). A THF solution (8 mL) of lithium diphenylamide (0.050 g, 0.29 mmol) was added to solid [$Ph_2BP^{tBu}_2$]Cu(pyridine) (0.180 g, 0.287 mmol). After stirring for 2 min, 12-crown-4 (0.100 mL, 0.618 mmol) was added by syringe. The resulting cloudy yellow solution was stirred for 12 h, and then volatiles were removed *in vacuo*. Faint yellow residues were washed with pentane (3 x 10 mL) and then recrystallized from THF/pentane (-30 ºC). Though combustion analysis of the crystals indicates the formula {[$Ph_2BP^{tBu}_2$]Cu(NPh_2)}{Li(12-crown-4)$_3$}, crushing these crystals and washing with pentane gives a product whose NMR spectroscopy is consistent with the indicated stoichiometry of **3.4**, i.e., two equivalents of 12-crown-4. Two-crop yield: 0.169 g, 55%. ^{1}H (THF-d_8, δ): 7.36 (br, 4H, borate *ortho*-C<u>H</u>), 6.98 (d, *J* = 7.5 Hz, 4H, borate *meta*-

C<u>H</u>), 6.86-6.75 (m, 8H, amido phenyl *meta*- and *ortho*-C<u>H</u>), 6.62 (t, J = 7.1 Hz, 2H, amido phenyl *para*-C<u>H</u>), 6.18 (t, J = 6.6 Hz, 2H), 3.63 (s, 32H, O(C<u>H</u>$_2$)$_2$O), 1.48 (br, 4H, BC<u>H</u>$_2$P), 1.01 (d, $^3J_{PH}$ = 5.4 Hz, 18H, P[C(C<u>H</u>$_3$)$_3$]$_2$), 0.99 (d, $^3J_{PH}$ = 5.7 Hz, 18H, P[C(C<u>H</u>$_3$)$_3$]$_2$). ^{13}C{^{1}H} (THF-d_8, δ): 133.7, 132.8, 129.5, 125.4, 121.7, 121.1, 117.3, 69.6 (s, O(<u>C</u>H$_2$)$_2$O), 33.0 (br, P[<u>C</u>(CH$_3$)$_3$]$_2$), 30.1 (P[C(<u>C</u>H$_3$)$_3$]$_2$), 13.5 (br, B<u>C</u>H$_2$P). ^{31}P{^{1}H} (THF-d_8, δ): 31.0 (s). IR (KBr, cm^{-1}): 3055, 2969, 2918, 2861, 1575, 1478, 1364, 1332, 1313, 1247, 1136, 1098, 1024, 920, 858, 809. Anal. Calcd for $C_{66}H_{108}BCuLiNO_{12}P_2$: C, 63.38; H, 8.70; N, 1.12. Found: C, 63.13; H, 8.62; N, 1.12.

Alternate synthesis of 3.4. THF (10 mL) was added to the solids **3.1** (0.345 g, 0.313 mmol) and diphenylamine (0.031 g, 0.33 mmol). The resulting clear, yellow solution was stirred for 12 h, and then volatiles were removed *in vacuo*. The tacky yellow residues were washed with diethyl ether (3 x 10 mL) and dried to yield **3.4** as an off-white powder (0.223 g, 66%).

Synthesis of {[Ph$_2$BP$^{tBu}_2$]Cu-N(Ph)C$_6$H$_4$}$_2$ (3.5). A dichloromethane solution (10 mL) of $FeCp_2PF_6$ (0.067 g, 0.20 mmol) was added to solid **3.4** (0.216 g, 0.201 mmol) in one portion, immediately resulting in a clear, dark-red solution. After stirring for 15 min, volatiles were removed *in vacuo*. Diethyl ether (10 mL) was added, the resulting mixture was filtered, and the red filtrate was concentrated *in vacuo* to a red residue. After washing with pentane (10 mL), the remaining tacky red solids were lyophilized from benzene to yield **3.5** as a dark red powder (0.034 g, 23%). Crystals suitable for X-ray diffraction were grown by diffusion of pentane vapors into a concentrated dichloromethane solution of **3.5**. Performing the initial stage of the procedure in deuterated dichloromethane and monitoring the reaction *in situ* by NMR spectroscopy reveals clean and quantitative

conversion to **3.5** and one equiv of $FeCp_2$. However, over a period of 2 days, **3.5** decomposes to a mixture of unknown colorless species, and hence satisfactory combustion analysis was not obtained. ^1H (CD_2Cl_2): 8.00 (d, J = 6.6 Hz, 2H), 7.51 (t, J = 7.5 Hz, 2H), 7.41 (br, 4H, borate *ortho*-C<u>H</u>), 7.35-7.00 (m, 5H), 6.99 (t, J = 7.5 Hz, 4H, borate *meta*-C<u>H</u>), 6.95-6.85 (m, 4H), 6.79 (t, J = 7.2 Hz, 2H, borate *para*-C<u>H</u>), 1.56 (br, 4H, BC<u>H</u>$_2$P), 1.12 (d, $^3J_{PH}$ = 6.0 Hz, 18H, P[C(C<u>H</u>$_3$)$_3$]$_2$), 1.10 (d, $^3J_{PH}$ = 5.4 Hz, 18H, P[C(C<u>H</u>$_3$)$_3$]$_2$). $^{31}P\{^1H\}$ (CD_2Cl_2, d): 37.4 (br). IR (KBr, cm^{-1}): 3056, 3040, 2945, 2865, 1590, 1584, 1471, 1427, 1364, 1310, 1180, 1156, 1101, 1018, 937, 862, 812.

3.4.3 Electrochemistry

Electrochemical measurements were carried out in a glovebox under a dinitrogen atmosphere in a one-compartment cell using a CH Instruments 600B electrochemical analyzer. A glassy carbon electrode was used as the working electrode and platinum wire was used as the auxillary electrode. The reference electrode was $Ag/AgNO_3$ in THF. The ferrocene couple Fc^+/Fc was used as an external reference. Solutions (THF) of electrolyte (0.3 M tetra-*n*-butylammonium hexafluorophosphate) and analyte were also prepared under an inert atmosphere.

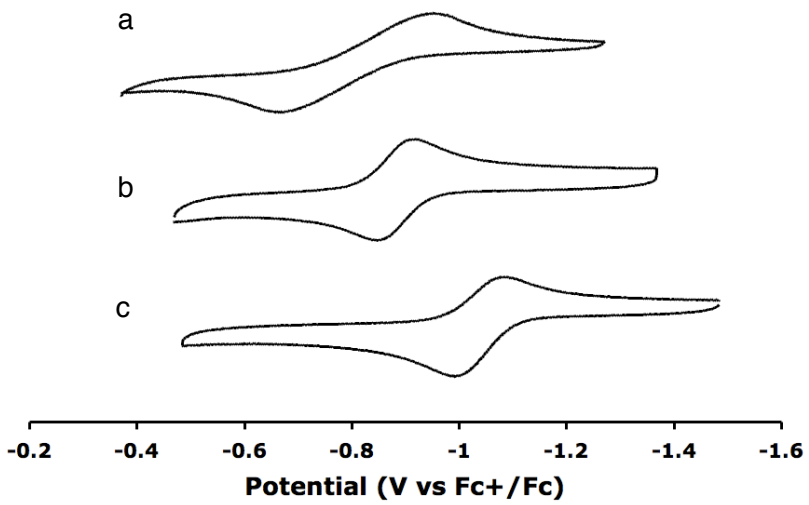

Figure 3.7. Cyclic voltammograms of (a) {[$Ph_2BP^{tBu}_2$]$CuNPh_2$}{Li(12-crown-4)$_2$} (**3.4**), (b) {[$Ph_2BP^{tBu}_2$]$CuNPh_2$}{Li(12-crown-4)$_2$} (**3.1**), and (c) {[$Ph_2BP^{tBu}_2$]$CuNHMes_2$}{Li(12-crown-4)$_2$}.[21] Conditions: THF, 0.3 M [$^nBuN_4$][PF_6] electrolyte, 200 mV/s scan rate.

3.4.4 X-ray Crystallography Procedures

X-ray diffraction studies were carried out at the MIT Department of Chemistry X-Ray Diffraction Facility on a Brüker three-circle Platform diffractometer, equipped with a CCD detector. Data was collected at 100K using Mo Kα (λ = 0.710 73 Å) radiation for all structures and solved using SHELX v. 6.14.[23] X-ray quality crystals were grown as described in the experimental procedures. The crystals were mounted on a glass fiber or nylon loop with Paratone N oil. Structures were determined using direct methods with standard Fourier techniques using the Bruker AXS software package. Disordered solvent and 12-crown-4 regions of **3.1** and **3.2** were modeled extensively and restrained using

DFIX, SIMU, DELU, and BUMP commands where appropriate. Crystallographic details have been placed in Appendix 2.

3.4.5 UV-Vis Measurements

Optical spectroscopy measurements were taken on a Cary 50 UV/Vis spectrophotometer using a 1 cm quartz cell sealed with a Teflon stopper.

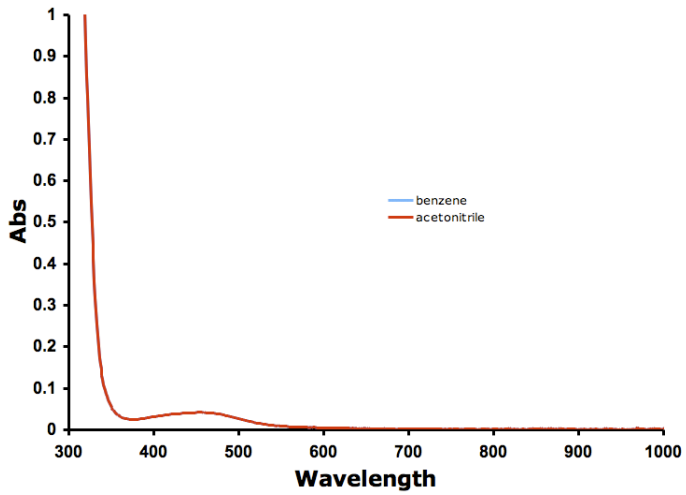

Figure 3.8. Optical spectra of **3.2** as equally concentrated benzene and acetonitrile solutions. Note: the blue line corresponding to the spectrum in benzene is invisible because of near-perfect overlap with the red line.

3.4.6 Self-Exchange Rate Constant Measurements

Self-exchange rate constant measurements were conducted using ^{1}H NMR line-broadening analysis.[24] Stock solutions of **3.1** in CD_3CN and **3.2** in C_6D_6 were prepared. The stock solution of **3.1** (400 mL) was placed in a J. Young NMR tube and the initial chemical shift (δ) and linewidth ($\nu_{1/2}$) of the tolyl methyl resonance were recorded. Increasing amounts of the stock solution of **3.2** were then added volumetrically, and the

mole fraction of **3.2** (χ_2), concentration of **3.2** ([**3.2**]), and δ and $\nu_{1/2}$ for the tolyl methyl peak were recorded, each time locking, shimming, and referencing the ^{1}H NMR spectrum to the residual solvent peaks. A linear relationship between δ and χ_2 as well as between $\nu_{1/2}$ and χ_2 verified that electronic exchange between **3.1** and **3.2** was occurring in the fast-exchange regime. The plots for one data run are reproduced below. NMR parameters are as follows: frequency = 300.080 MHz, acquisition time = 1.995 s, sweep width = 4506.5 Hz, pulse width = 7.0 ms, relaxation delay = 5 s, number of transients = 16, spectrometer temperature = 20.0 °C.

The relation between linewidth and the exchange rate (k) is given in eq (1), where W denotes linewidth, χ denotes mole fraction, C denotes concentration, and subscripts P, D, and PD denote paramagnet (i.e., **3.2**), diamagnet (i.e., **3.1**), and paramagnet/diamagnet mixtures, respectively.

$$W_{PD} = \chi_P W_P + \chi_D W_D + \frac{\chi_P \chi_D \left(4\pi(\delta\nu)^2\right)}{kC_{PD}} \qquad \text{eq (1)}$$

For all data points we measured (15 pts), the difference between W_{PD} and the sum $\chi_P W_P + \chi_D W_D$ was less than or equal to 1 Hz. In other words, the third term on the right-hand side of eq (1) was immeasurably small when considering the error associated with linewidth measurement. Because k is in the denominator of that term, it follows that k is too large to be measured accurately by this technique.

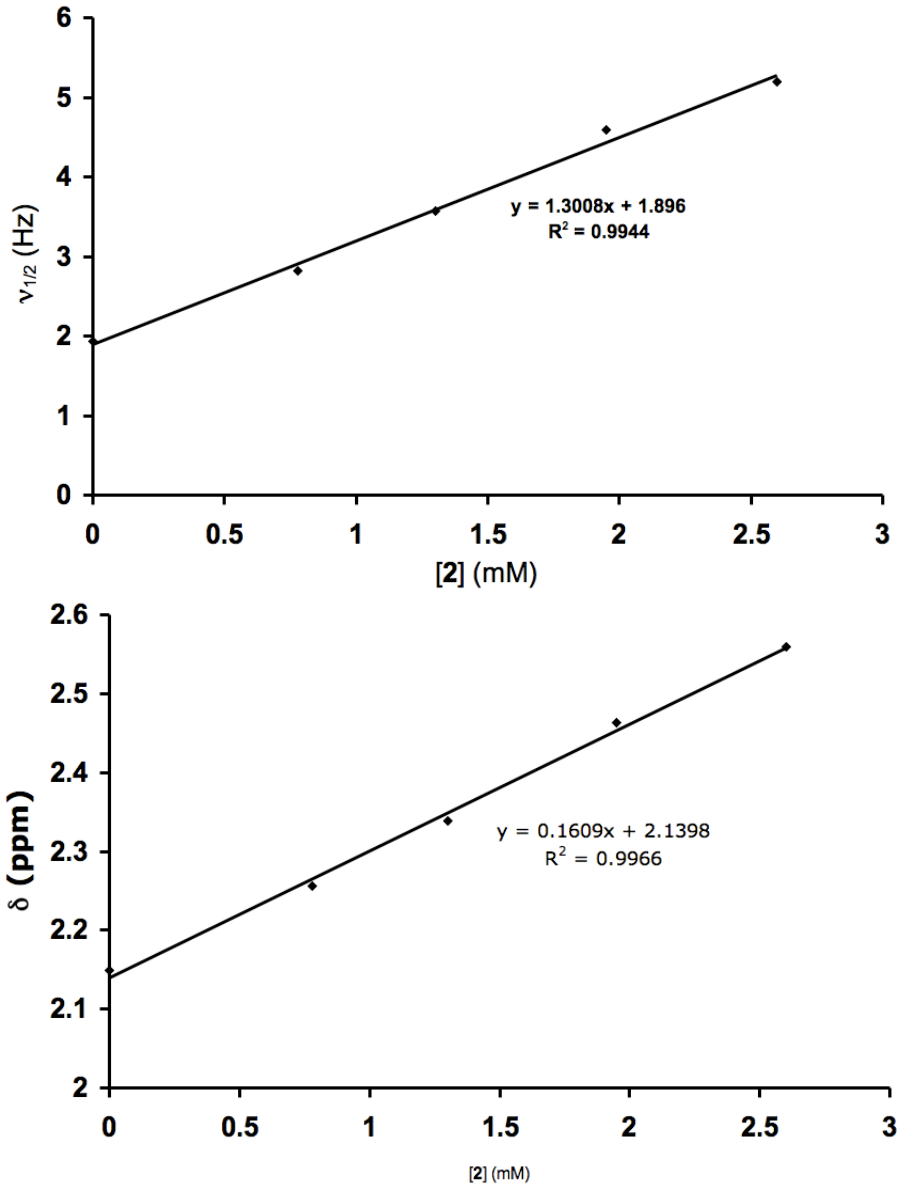

Figure 3.9. Plots of linewidth (*top*) and chemical shift (*bottom*) of the *p*-tolyl methyl ^{1}H NMR resonance in mixtures of **3.1** and **3.2** as a function of concentration of **3.2**.

3.4.7 Electronic Structure Calculations

Density functional calculations were carried out using the Gaussian03 suite.[25] The electronic structures of the computational models $\{(Ph_2BP^{tBu}{}_2]Cu^{I}(NTol)_2\}^{1-}$ and

{$(Ph_2BP^{tBu}_2]Cu^{II}(NTol)_2$} and their ionic fragments were calculated by employing a hybrid gradient-corrected density functional composed of 62% Becke nonlocal and Slater local density functional exchange[26a], 38% HF exact exchange, and 100% Perdew nonlocal and Vosko-Wilk-Nussair local density functional correlation[26b] functions. This hybrid functional (B(38)HFP86) has been shown to provide the most reasonable ground state electronic structures[27] for copper complexes among the most commonly used density functionals. Calculations were carried out using Gaussian-type all electron basis sets[26c-d] with polarization and diffuse functions 6-311+G(d).[26e-g] We have utilized an ionic-fragment based approach[28] to achieve rapid wave function convergence and to compare and contrast the possibility of metal versus ligand localized as well as delocalized electronic structures. The molecular orbital contour plots were generated using GaussView 4.1.[29]

3.4.8 Details of XAS Data Collection

The copper K-, phosphorus K-, and copper L-edge XAS measurements were carried out at beam lines 7-3, 6-2, and 10-1, respectively, of Stanford Synchrotron Radiation Laboratory under storage ring (SPEAR3) conditions of 3 GeV energy and 100-80 mA current. BL7-3 is a 20-pole, 2 T Wiggler beam line equipped with a Si(220) downward reflecting, double-crystal monochromator. Data was collected in the energy range of 8660-9690 eV using an unfocused beam. The samples were placed in a liquid He cryostat and about 11 K temperature was maintained throughout the measurements. The beam intensity was maximized at 9685 eV. The data was collected in transmission mode. BL6-2 is a 56-pole, 0.9 T Wiggler beam line with a liquid-nitrogen-cooled, Si(111)

double-crystal monochromator. P K-edge spectra were collected in the energy range of 2120- 2250 eV using an unfocused beam in a He-purged beam path at room temperature and a 3-element Lytle fluorescence detector. The beam line was optimized at 2320 eV. BL10-1 has a 30-pole 1.45 T Wiggler insertion device with 6 m spherical grating monochromator. The samples were placed in a vacuum chamber with operating pressures below 10^{-5} torr. The incident beam energy was scanned between 925 and 955 eV and beam line optics were optimized at 920 eV. Data collection was carried out in electron yield mode by a channeltron detector with 300 V accelerating potential.

The samples were ground and pasted onto a contaminant-free Kapton tape from Shercon or carbon tape from Specs CertiPrep in a glovebox with sub parts per million oxygen and moisture levels. Samples for transmission measurements were diluted in and ground together with boronitride to minimize incident beam absorption. Samples were protected by a thin polypropylene window (Specs CertiPrep) from exposure to air during sample mounting and change. Sample holders for Cu L-edge measurements were mounted in a He-purged glove bag tightly wrapped around the vacuum chamber. The sensitivity of the finely dispersed samples on the sample cells were tested by exposing them immediately after measurements for about 30 s to air followed by a repeated data collection. Even in the most sensitive samples such as CuCl, we only observed negligible change in the spectral feature intensities or energy positions.

The incident photon energy was scanned in 0.5 eV steps outside the rising edge regions for each edges where the step size was 0.1 eV. At least five scans were averaged to obtain a good signal-to-noise ratio. Radiation damage was observed at the Cu L-edge for the radical complex $\{(Ph_2BP^{tBu}_2)Cu^{II}(NTol_2)\}$, which was corrected for by estimating

the rate of change from two scans of three with 1 s and 0.5 s dwell times for two different sample positions. The incident photon energy was calibrated to the spectra of copper foil at the Cu K-edge (first inflection point at 8979 eV), difluorocopper(II) at the Cu L_3- and L_2-edges (white line positions at 930.5 and 950.5 eV, respectively), and triphenylphosphineoxide at the P K-edge (maximum of pre-edge feature at 2147.5 eV).

The averaged raw data was background subtracted using a second-order polynomial fit to the approximately 30 eV energy range before any spectral feature and normalized with a second order spline function above the edge jump at 9200, 980, 2890, and 2190 eV for the Cu K-, Cu L-, Cl K-, and P K-edges, respectively. Due to the different number of absorbers per molecule, the Cl K-edge spectra had to be renormalized in order to compare the pre-edge features of $CuCl_2$ and Cs_2CuCl_4 samples. The pre-edge features at the P K-, Cl K-, and Cu L-edges were fitted using the edg_fit program of EXAFSPAK.[30] Fits to the pre-edge features at the Cl K-edge were used to determine the Cl 3p covalency in anhydrous $CuCl_2$ using the reference spectra and pre-edge fits for D_{2d} Cs_2CuCl_4.[31] Due to the complementarity of orbital coefficients, 100% less the above Cl 3p covalency gave the amount of Cu 3d character in the probed unoccupied, frontier orbitals of the $CuCl_2$. This provided a Cu 2p→3d transition dipole moment, which was used to quantitate the Cu L-edge pre-edge features of the $\{(Ph_2BP^{tBu}{}_2)Cu^{II}(NTol_2)\}$ sample. Due to the lack of good standards the P character represented by the pre-edge feature at the P K-edge was estimated from results of electronic structure calculations.

Background corrected and normalized data, as well as representative fits, have been placed in Appendix 2.

3.4.9 EPR Measurements

EPR spectra were obtained at the National Biomedical EPR center in Milwaukee using Varian E-9 and E-109 spectrometers operating at 9.188 GHz (X-band), 3.392 GHz (S-band), and 35.100 GHz (Q-band). The low frequency 3.3 GHz (S-band) spectrometer is based on the loop-gap resonator designed by Froncisz and Hyde.[32] The Q-band bridge was modified with the addition of a GaAs field-effect transistor signal amplifier and low-noise Gunn diode oscillator.[33] Microwave frequencies were measured with an EIP model 331 counter. Spectra were recorded in a frozen glass of dichloromethane/toluene at 123 K (S- and Q-band) or 77 K (X-band). Spectra are reported from 4 scans with time constant 0.128 s, modulation amplitude 5 G, and microwave power 30 dB (Q-band) or 16 dB (X- and S-band). The second derivative of the spectra was obtained by using SUMSPC92, a data manipulation program available upon request from the National Biomedical EPR Center. The second derivative spectra emphasize sharp lines. A 1% argument was used to obtain the second derivative spectrum. EPR simulations were carried out using the program W95EPR.[34]

3.4.10 Determination of k_H/k_D

A dilute solution of **3.2** in C_6H_6 (~70 mM) was placed in a cuvette and stopped with a rubber septum. UV-Vis scans were obtained every 1 min, and after the first scan either neat Bu_3SnH or neat Bu_3SnD (> 25 equiv per Cu) was added to the cuvette through the septum by syringe. An example of the resulting decomposition of **3.2** as monitored by UV-Vis is reproduced below. A plot of $|\ln(A_{365})|$ vs t revealed linear relationships in both

cases, and the ratio of the slopes provided the kinetic isotope effect (see plot below). The average of three trials is reported.

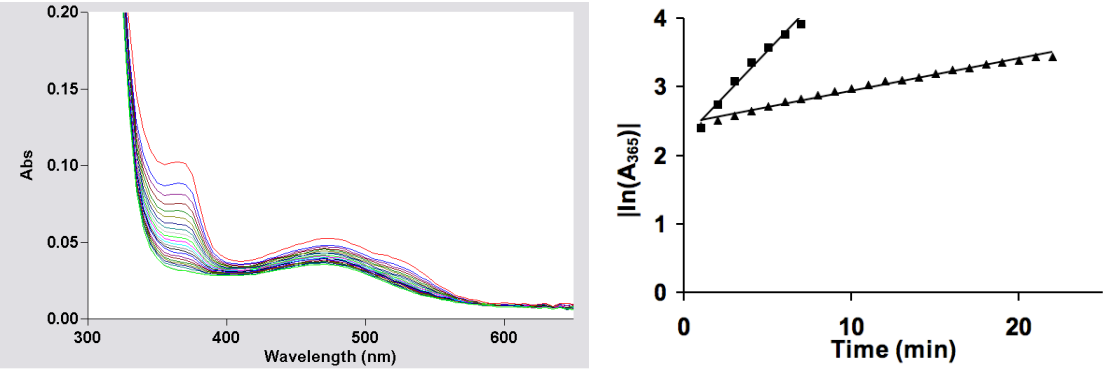

Figure 3.10. (*left*) Example of UV-Vis spectroscopy used to monitor the decomposition of **3.2**, in this case with the addition of ~25 equiv Bu_3SnD. (*right*) Plot of $|\ln(A_{365})|$ vs time for Bu_3SnH (squares) and Bu_3SnD (triangles).

References Cited

1 (a) Vallee, B. L.; Williams, R. J. P. *Proc. Nat. Acad. Sci. U.S.A.* **1968**, *59*, 498. (b) Gray, H. B.; Malmström, B. G. *Comments Inorg. Chem.* **1983**, *2*, 203.

2 (a) Ducros, V.; Brzozowski, A. M.; Wilson, K. S.; Brown, S. H.; Ostergaard, P.; Schneider, P.; Yaver, D. S.; Pederson, A. H.; Davies, G. J. *Nature Struct. Biol.* **1998**, *5*, 310. (b) Zaitseva, I.; Zaitsev, V.; Card, G.; Moshkov, K.; Bax, B.; Ralph, A.; Lindley, P. *J. Biol. Inorg. Chem.* **1996**, *1*, 15. (c) Karlsson, B. G.; Nordling, M.; Pascher, T.; Tsai, L.-C.; Sjölin, L.; Lundberg, L. G. *Protein Eng.* **1991**, *4*, 343.

3 Rorabacher, D. B. *Chem. Rev.* **2004**, *104*, 651.

4 (a) Marcus, R. A.; Sutin, N. *Biochim. Biophys. Acta* **1985**, *2*, 203. (b) Gray, H. B.; Malmström, B. G.; Williams, R. J. P. *J. Biol. Inorg. Chem.* **2000**, *5*, 551.

5 Selected examples: (a) Chaka, G.; Sonneberg, J. L.; Schlegel, H. B.; Heeg, M. J.; Jaeger, G.; Nelson, T. J.; Ochrymowycz, L. A.; Rorabacher, D. B. *J. Am. Chem. Soc.* **2007**, *129*, 5217. (b) Fujisawa, K.; Fujita, K.; Takahashi, T.; Kitajima, N.; Moro-oka, Y.; Matsunaga, Y.; Miyashita, Y.; Okamoto, K. *Inorg. Chem. Commun.* **2004**, *7*, 1188.

6 Mankad, N. P.; Peters, J. C. *Chem. Commun.* **2008**, 1061.

7 (a) Jazdzewski, B. A.; Holland, P. L.; Pink, M.; Young, V. G., Jr.; Spencer, D. J. E.; Tolman, W. B. *Inorg. Chem.* **2001**, *40*, 6097. (b) Holland, P. L.; Tolman, W. B. *J. Am. Chem. Soc.* **1999**, *121*, 7270.

8 A subset of the β-diketiminato copper(II) system studied by Tolman does access reversible 1-electron chemistry by cyclic voltammetry, but syntheses of the corresponding copper(I) complexes have not been reported. See ref 7.

9 Harkins, S. B.; Peters, J. C. *J. Am. Chem. Soc.* **2004**, *126*, 2885.

10 (a) Gamelin, D. R.; Randall, D. W.; Hay, M. T.; Houser, R. P.; Mulder, T. C.; Canters, G. W.; de Vries, S.; Tolman, W. B.; Lu, Y.; Solomon, E. I. *J. Am. Chem. Soc.* **1998**, *120*, 5246. (b) DeBeer-George, S.; Metz, M.; Szilagyi, R. K.; Wang, J.; Cramer, S. P.; Lu, Y.; Tolman, W. B.; Hedman, B.; Hodgson, K. O.; Solomon, E. I. *J. Am. Chem. Soc.* **2001**, *123*, 5757.

11 (a) Solomon, E. I.; Randall, D. W.; Glaser, T; *Coord. Chem. Rev.* **2000**, *200-202*, 595. (b) Szilagyi, R. K.; Solomon, E. I.; *Curr. Opin. Chem. Biol.* **2002**, *6*, 250.

12 Harkins, S. B.; Mankad, N. P.; Miller, A. J. M.; Szilagyi, R. K.; Peters, J. C. *J. Am. Chem. Soc.* **2008**, *130*, 3478.

13 Büttner, T.; Geier, J.; Frison, G.; Harmer, J.; Calle, C.; Schweiger, A.; Schönberg, H.; Grützmacher, H. *Science* **2005**, *307*, 235.

14 For a brief review, see Hicks, R. G. *Angew. Chem., Int. Ed.* **2008**, *47*, 2. Also see Miyazato, Y.; Wada, T.; Muckerman, J. T.; Fujita, E.; Tanaka, K. *Angew Chem. Int. Ed.* **2007**, 46, 5728.

15 Kau, L. S.; Spira-Solomon, D. J.; Pennerhahn, J. E.; Hodgson, K. O.; Solomon, E. I. *J. Am. Chem. Soc.* **1987**, *109*, 6433.

16 The small features (* in Figure 2) at 930.3 and 930.7 eV for CuCl and complex **1**, respectively, are due to contamination from oxidation during shipping and handling.

17 The B(38HF)P86 functional and GT 6-311+G(d) basis set were employed. Spin densities were estimated using Mulliken population analysis.

18 Libertint, L. J.; Griffith, O. H. *J. Chem. Phys.* **1970**, *53*, 1359.

19 Lockwood, M. A.; Blubaugh, T. J.; Collier, A. M.; Lovell, S.; Mayer, J. M. *Angew. Chem., Int. Ed.* **1999**, *38*, 225.

20 Selected examples: (a) Thomas, F.; Gellon, G.; Gautier-Luneau, I.; Saint-Aman, E.; Pierre, J.-L. *Angew. Chem., Int. Ed.* **2002**, *41*, 3047. (b) Chaudhuri, P.; Hess, M.; Weyhermüller, T.; Wieghardt, K. *Angew. Chem., Int. Ed.* **1999**, *38*, 1095. (c) Wang, Y.; DuBois, J. L.; Hedman, B.; Hodgson, K. O.; Stack, T. D. P. *Science* **1998**, *279*, 537.

21 Mankad, N. P.; Peters, J. C. *Chem. Commun.* **2008**, 1061.

22 Chavez, I.; *J. Organomet. Chem.* **2000**, *601*, 126.

23 Sheldrick, G. M. *Acta Cryst.* **2008**, *A64*, 112.

24 (a) Goodwin, J. A.; Stanbury, D. M.; Wilson, L. J.; Eigenbrot, C. W.; Scheidt, W. R. *J. Am. Chem. Soc.* **1987**, *109*, 2979. (b) Pulliam, E. J.; McMillin, D. R. *Inorg. Chem.* **1984**, *23*, 1172. (c) McConnell, H. M.; Berger, S. B. *J. Chem. Phys.* **1957**, *27*, 230.

25 Frisch, M. J.; Trucks, G. W.; Schlegel, H. B.; Scuseria, G. E.; Robb, M. A.; Cheeseman, J. R.; Montgomery, J. A. J.; Vreven, T.; Kudin, K. N.; Burant, J. C.; Millam, J. M.; Iyengar, S. S.; Tomasi, J.; Barone, V.; Mennucci, B.; Cossi, M.; Scalmani, G.; Rega, N.; Petersson, G. A.; Nakatsuji, H.; Hada, M.; Ehara, M.; Toyota, K.; Fukuda, R.; Hasegawa, J.; Ishida, M.; Nakajima, T.; Honda, Y.; Kitao, O.; Nakai, H.; Klene, M.; Li, X.; Knox, J. E.; Hratchian, H. P.; Cross, J. B.; Adamo, C.; Jaramillo, J.; Gomperts, R.; Stratmann, R. E.; Yazyev, O.; Austin, A. J.; Cammi, R.; Pomelli, C.; Ochterski, J. W.; Ayala, P. Y.; Morokuma, K.; Voth, G. A.; Salvador, P.; Dannenberg, J. J.; Zakrzewski, V. G.; Dapprich, S.; Daniels, A. D.; Strain, M. C.; Farkas, O.; Malick, D. K.; Rabuck, A. D.; Raghavachari, K.; Foresman, J. B.; Ortiz, J.

V.; Cui, Q.; Baboul, A. G.; Clifford, S.; Cioslowski, J.; Stefanov, B. B.; Liu, G.; Liashenko, A.; Piskorz, P.; Komaromi, I.; Martin, R. L.; Fox, D. J.; Keith, T.; Al-Laham, M. A.; Peng, C. Y.; Nanayakkara, A.; Challacombe, M.; Gill, P. M. W.; Johnson, B.; Chen, W.; Wong, M. W.; Gonzalez, C.; Pople, J. A. Gaussian03, Rev. C02; Gaussian, Inc.: Pittsburgh PA, 2004.

26 (a) Feller, D., *J. Comp. Chem.* **1996**, 17, 1571-1586. (b) Schuchardt, K.L., Didier, B.T., Elsethagen, T., Sun, L., Gurumoorthi, V., Chase, J., Li, J., and Windus, T.L. *J. Chem. Inf. Model.* **2007**, 47, 1045-1052. (c) Becke, A. D. *Phys. Rev. A: Gen. Phys.* **1988**, 38, 3098. (d) Perdew, J. P. *Phys. Rev. B: Condens. Matter Mater. Phys.* **1986**, 33, 8822. (e) Wachters, A. J. H. *J. Chem. Phys.* **1970**, 52, 1033. (f) Hay, P. J. *J. Chem. Phys.* **1977**, 66, 4377. (g) Raghavachari, K. Trucks, G. W. *J. Chem. Phys.* **1989**, 91, 1062.

27 Szilagyi, R. K.; Metz, M.; Solomon, E. I., *J. Chem. Phys. A* **2002**, 106, 2994-3007.

28 Szilagyi, R. K.; Winslow, M. *J. Comput. Chem.* **2006**, 27, 1385.

29 GaussView, Version 4.1; Roy Dennington II, Todd Keith and John Millam, Semichem, Inc., Shawnee Mission, KS, 2007.

30 EXAFSPAK: A suite of computer Programs for Analysis of X-ray Absorption Spectra. G.N. George, I.J. Pickering, June 2000 (http://www-ssrl.slac.stanford.edu/~george/exafspak/)

31 Hedman, B.; Hodgson, K.O.; Solomon, E.I. *J. Am. Chem. Soc.* **1992**, 112, 1643-1645

32 Froncisz, W.; Hyde, J. S. *J. Magn. Reson.* **1982**, *47*, 515.

33 Hyde, J. S.; Newton, M. E.; Strangeway, R. A.; Camenisch, T. G.; Froncisz, W. *Rev. Sci. Instrum.* **1991**, *62*, 2969.

34 Neese, F. *QCPE Bull*. **1995**, *15*, 5.

Chapter 4: Terminal Fe^{I}-N_2 and Fe^{II}···H-C Interactions Supported by Tris(phosphino)silyl Ligands

Reproduced in part with permission from

Mankad, N. P., Whited, M. W., and Peters, J. C. *Angewandte Chemie, International Edition* **2007**, *46*, 5768-5771.

4.1 Introduction

Dinitrogen complexes of iron have been the targets of numerous synthetic studies in recent years.[1] An unusual and intriguing formal oxidation state to explore in such systems is iron(I), especially in the context of a Chatt-type[2] $Fe^{I/IV}$ N_2 fixation cycle (i.e., Fe^{I}-N_2 + 3 H → Fe^{IV}≡N + NH_3; Fe^{IV}≡N + 3H → Fe^{I}-N_2 + NH_3). Schrock's recent work has provided impetus for such studies by establishing the synthetic viability of a conceptually related $Mo^{III/VI}$ N_2 fixation cycle.[3] Both iron and molybdenum are present in the FeMo-cofactor of MoFe nitrogenases,[4] and pseudotetrahedral Fe^{IV}≡N species, hypothetical intermediates of an $Fe^{I/IV}$ N_2 fixation mechanism, have recently been characterized.[5] Both Holland's group and our own have reported examples of 3- and 4-coordinate N_2 adducts of iron in the formal +1 oxidation state, but in neither case were terminally bonded N_2 species identified or isolated; dinuclear end-on Fe-NN-Fe species were inevitably obtained.[6] For the Schrock tris(amido)amine Mo-N_2 systems, it proved necessary to use a high degree of steric bulk to prevent bimetallic adduct formation before the N_2 fixation chemistry of interest could be exposed. We have attempted to retrofit the [$PhBP^{R}_3$]Fe scaffolds ([$PhBP^{R}_3$] = [$PhBP(CH_2PR_2)_3$]$^-$) with bulky substituents at phosphorus to prevent dinuclear reaction pathways, but have thus far been unable to obtain terminally bonded Fe^{I}-N_2 adducts using [$PhBP^{R}_3$] ligands.

Recently we began to turn our attention to new derivatives of the classic Sacconi-type NP_3 ligands (e.g., $N(CH_2CH_2PR_2)_3$) to achieve access to a terminally bonded Fe^{I}-N_2 synthon.[7] While $Fe^{II}(N_2)(H)^+$ species are readily accessible using ligands of these types,[7] N_2 adducts of iron(I) have yet to be obtained. We find, however, that replacement of the apical neutral N-atom donor of a tetradentate NP_3 ligand by an anionic Si-atom donor

achieves the intended goal. Herein we describe our efforts to prepare the monoanionic [SiP^R_3] ligands ([SiP^R_3] = (2-$R_2PC_6H_4)_3Si$, R = Ph and iPr) and to exploit them in the preparation of 5-coordinate, [SiP^R_3]Fe^I-N_2 complexes.

Scheme 4.1

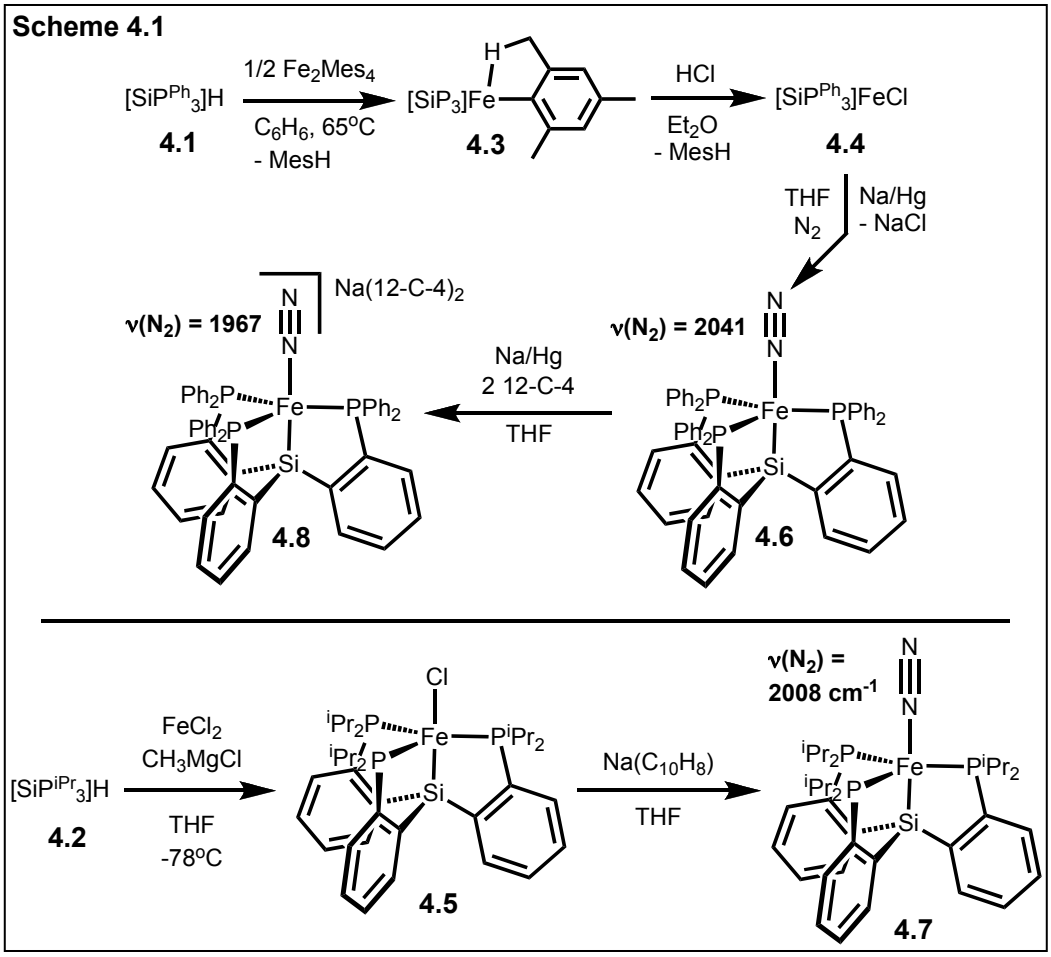

4.2 Results and Discussion

The tris(phosphino)silane precursors [SiP^R_3]H (R = Ph (**4.1**) and iPr (**4.2**)) are prepared by *ortho*-lithiation of 2-$R_2PC_6H_4Br$ reagents with *n*-butyllithium, followed by addition of 1/3 equiv of trichlorosilane. Heating a benzene solution of **4.1** and mesityliron(II) to 65 °C results in Si-H activation and extrusion of mesitylene, producing

red [SiP$^{Ph}_3$]FeMes (**4.3**, Mes = 2,4,6- trimethylphenyl) (Scheme 4.1).[8] Complex **4.3** has an interesting solid-state structure (Figure 4.1) and is nominally 6-coordinate; the [SiP$^{Ph}_3$] ligand and the mesityl *ipso*-carbon together occupy five of the coordination sites, while the sixth site (*trans* to the silyl donor) is occupied by an agostic C-H interaction with a mesityl *ortho*-methyl group. Two molecules are found in the asymmetric unit, and both feature very short distances from the iron center to the carbon participating in the agostic interaction (2.564(4) and 2.569(4) Å).[9] It is plausible to attribute the structure of **4.3** to the presence of strongly *trans*-influencing aryl and silyl donors that do not favor a *trans* configuration.

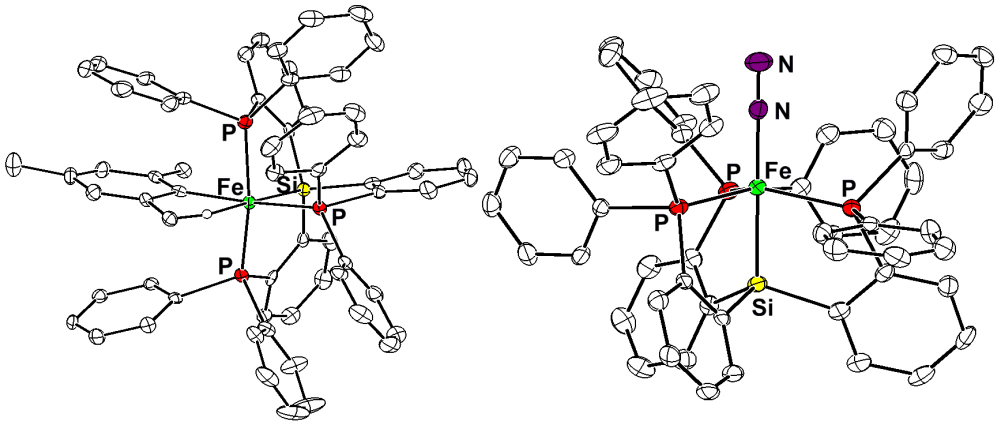

Figure 4.1. (*left*) Solid-state structure of [SiP$^{Ph}_3$]FeMes (**4.3**) (only one molecule from the asymmetric unit shown, agostic hydrogen shown in calcd position). (*right*) Solid-state structure of [SiP$^{Ph}_3$]FeN$_2$ (**4.6**). Selected bond distances (Å) and angles (°) for one molecule of **4.3**: Fe-Si, 2.1988(14); for others see text. For **4.6**: Fe-N, 1.819(2); N-N, 1.106(3); Fe-Si, 2.2682(8); Si-Fe-N, 179.00(7); Fe-N-N, 178.5(2).

Solution NMR spectra of **4.3** are also interesting (Figure 4.2). The room-temperature ^{1}H NMR spectrum (C_6D_6) of diamagnetic **4.3** features a sharp resonance at δ 1.84 ppm corresponding to the mesityl *para*-methyl group and two broad resonances at δ 5.33 and 0.58 ppm corresponding to the two *ortho*-methyl groups, which are inequivalent on the NMR time scale due to restricted Fe-C_{ipso} rotation. The ^{1}H NMR spectrum at -60°C (toluene-d_8) instead features *three* broad resonances for the *ortho*-methyl groups (δ 4.59, 1.10, and -0.24 ppm) in addition to the sharp *para*-methyl singlet at δ 1.88 ppm, indicating that at low temperature even the exchange of C-H bonds on the same methyl group is slower than the NMR timescale due to restricted C-C rotation. In addition, the ^{31}P{^{1}H} NMR spectrum of **3** at -60°C resolves the inequivalent phosphines into a doublet (2P) and a triplet (1P) with $^{2}J_{PP}$ = 11 Hz. While iron(II) species that exhibit C-H agostic interactions are known,[9] complexes in which a C-H agostic interaction is stable enough to freeze rotation between the three C-H positions of a methyl group are quite rare.[10]

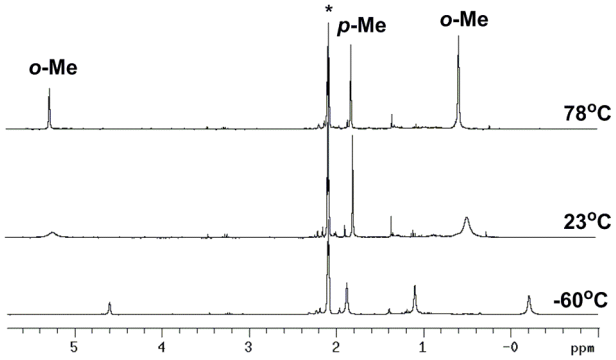

Figure 4.2. ^{1}H NMR spectroscopy of [SiP$^{Ph}_{3}$]FeMes (**4.3**) as a function of temperature (* = residual NMR solvent peak).

Protonolysis of ethereal solutions of **4.3** with HCl cleanly produces mesitylene and paramagnetic, light orange [SiP^{Ph}_3]FeCl (**4.4**) (Scheme 4.1). Though reaction between **4.2** and mesityliron(II) does not produce a tractable reaction mixture, light orange [SiP^{iPr}_3]FeCl (**4.5**) can be accessed by addition of CH_3MgCl to a mixture of **4.2** and $FeCl_2$ (Scheme 4.1).[11] The crystal structures of **4.4** and **4.5** feature iron centers with trigonal bipyramidal coordination geometries (Figure 4.3), and solution magnetic data indicate triplet ground states for both (μ_{eff} = 2.9 μ_B (**4.4**) and 3.3 μ_B (**4.5**)). The cyclic voltammogram (CV) of **4.4** in THF features two reversible redox events, an Fe(III/II) couple at $E^{0'}$ = -0.40 V and an Fe(II/I) couple at $E^{0'}$ = -2.10 V (vs Fc^+/Fc). The corresponding redox events for **4.5** are shifted to more negative potentials by approximately 300 mV each due to the more strongly electron-donating phosphine substituents. The Fe(II/I) couple in **4.5** is irreversible at 500 mV/s scan rates, presumably due to the enhanced lability of the chloride ligand in the more electron-rich system.

Na/Hg reduction of **4.3** in THF produces the target terminal iron(I) dinitrogen adduct [SiP^{Ph}_3]FeN_2 (**4.6**) (Scheme 4.1). The closely related dinitrogen complex [SiP^{iPr}_3]FeN_2 (**4.7**) is synthesized by Na($C_{10}H_8$) reduction of **4.5** (Scheme 4.1). Solution magnetic data indicate S = 1/2 spin states for these iron(I) complexes **4.6** (μ_{eff} = 1.8 μ_B) and **4.7** (μ_{eff} = 2.2 μ_B). Accordingly, the X-band EPR spectrum of **4.6** at 4 K (2-MeTHF glass) features an intense rhombic signal with g_1 = 2.013, g_2 = 2.051, g_3 = 2.187 that is coupled to three P-atoms (A_1 = 58.0 MHz, A_2 = 55.0 MHz, A_3 = 5.8 MHz) (See section 4.3.6). The solid-state structures of these red-orange complexes (Figure 4.1) confirm their identities as terminally bonded N_2 adducts of iron(I). Complex **4.6** has an Fe-N distance of 1.819(2) Å and a short N-N distance of 1.106(3) Å consistent with the weak N_2

activation implied by the relatively high- energy N-N stretching vibrations observed by IR spectroscopy (2041 cm^{-1} for **6** and 2008 cm^{-1} for **7**).[12] For comparison, tetrakis(phosphine)iron(0) dinitrogen complexes have N-N vibrations ranging from 1955 cm^{-1} in $Fe(N_2)(depe)_2$[13] to 2068 cm^{-1} in $Fe(N_2)(dppe)_2$.[14] As expected, the N_2 ligands in **4.6** and **4.7** are in positions *trans* to the silyl donors. This structural feature is unusual; transition metal N_2 complexes that also feature silyl donors are rare,[15] especially where the ligands are *trans* disposed. Such an arrangement of ligands might be expected to labilize the N_2 ligand. Indeed, prolonged exposure of **4.6** to vacuum results in loss of some of the N_2 adduct species (determined by ^1H NMR, Toepler pump analysis, and combustion analysis). The N_2 ligand of **4.7** is similarly labile. Hence, while each complex can be generated cleanly in solution and crystallographically characterized, neither provides satisfactory combustion analysis data upon rigorous solvent removal.

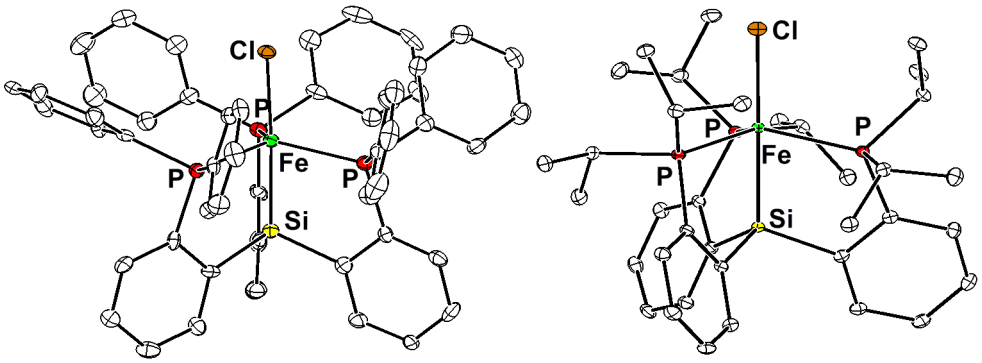

Figure 4.3. Solid-state structures of $[SiP^{Ph}_3]FeCl$ (**4.4**) (*left*) and $[SiP^{iPr}_3]FeCl$ (**4.5**) (*right*). Selected bond distances (Å) and angles (°) for **4.4**: Fe-Cl, 2.2623(12); Fe-Si, 2.3062(14); avg Fe-P, 2.289(4); Si-Fe-Cl, 177.28(5). For **4.5**: Fe-Cl, 2.2820(9); Fe-Si, 2.3046(10); avg Fe-P, 2.352(2); Si-Fe-Cl, 178.532(17).

Comparative examination of the respective solid-state structures of **4.6** and **4.7** provides insight as to why dinuclear complex formation is observed for $\{[PhBP^{iPr}_3]Fe\}_2(\mu\text{-}N_2)$, but not in the case of **4.6** and **4.7**. Figure 4.4 shows space-filling models of the hypothetical '$[PhBP^{iPr}_3]Fe\text{-}N_2$' fragment, derived from the X-ray structure of $\{[PhBP^{iPr}_3]Fe\}_2(\mu\text{-}N_2)$ after stripping away one of the $[PhBP^{iPr}_3]Fe$ units, alongside its 5-coordinate relative **4.7**. As can be seen, the N_2 ligand of '$[PhBP^{iPr}_3]Fe\text{-}N_2$' extends well beyond the protective pocket provided by the isopropyl substituents of the phosphine donors, whereas even the β-N atom of the N_2 ligand of **4.7** is nicely shrouded by the isopropyl substituents. Energetically unfavorable interactions can be anticipated for **4.7** under the approach of another '$[SiP^{iPr}_3]Fe$' unit, precluding formation of the dinuclear species. A similar analysis holds for $[SiP^{Ph}]Fe(N_2)$ (**4.6**), where the terminal N_2 ligand is buried even more deeply in the protective pocket than for the case of **4.7** (Figure 4.4).

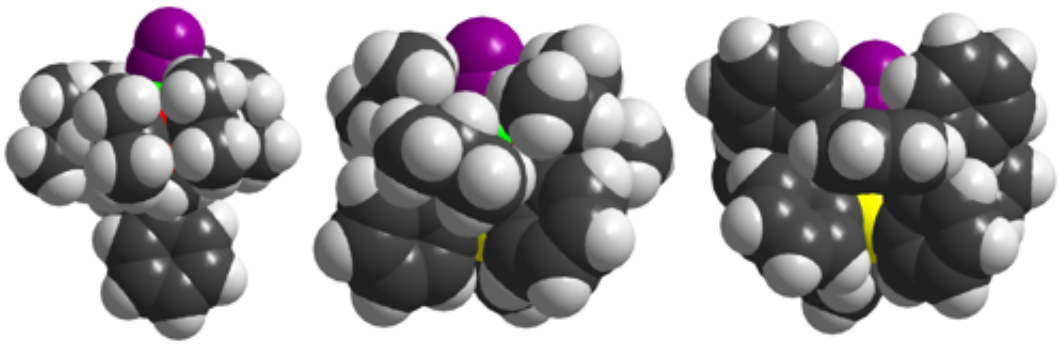

Figure 4.4. Space-filling models of $\{[PhBP^{iPr}_3]Fe\}_2(\mu\text{-}N_2)$ (*left*, one $[PhBP^{iPr}_3]Fe$ fragment omitted), $[SiP^{iPr}_3]FeN_2$ (**4.7**) (*center*), and $[SiP^{Ph}_3]FeN_2$ (**4.6**) (*right*).

Reversible 1-electron reduction events at $E^{0'}$ = -1.93 V for **4.6** and $E^{0'}$ = -2.72 V for **4.7** (vs Fc^{+}/Fc) are observed by CV, along with irreversible oxidations at higher potentials. Chemical reduction of **4.6** with an additional equiv of Na/Hg in the presence of 12-crown-4 affords the dark purple formally iron(0) species assigned as $\{[SiP^{Ph}_3]FeN_2\}\{Na(12\text{-crown-}4)_2\}$ (**4.8**) on the basis of a strong N_2 vibration at 1967 cm^{-1} in its IR spectrum, its diamagnetic ^1H and $^{31}P\{^1H\}$ (δ 84.3 ppm) NMR spectra, and combustion analysis (Scheme 4.1). On the other hand, one-electron oxidation of **4.6** with $[FeCp_2][BAr^F_4]$ releases N_2 and produces the high-spin solvento species $\{[SiP^{Ph}_3]Fe(thf)\}\{BAr^F_4\}$ (**4.9**) (Ar^F = 3,5-$(F_3C)_2C_6H_4$).[16] Note that anion **4.8** features a less labile N_2 ligand than its neutral precursor **4.6** (*vide supra*) due to stronger backbonding from the more electron-rich Fe center, and it therefore gives satisfactory combustion analysis data.

The N_2 ligand in **4.6** can be displaced by CO (1 atm) to provide $[SiP^{Ph}_3]Fe(CO)$ (**4.10**) (ν_{CO} = 1881 cm^{-1}). The ν_{CO} stretching frequency for **4.10** is virtually identical to that for the structurally related but cationic Fe(I) carbonyl complex $[\{N(2\text{-diisopropylphosphino-4-methylphenyl})_3\}Fe(CO)][BPh_4]$, where isopropyl rather than phenyl substituents decorate the phosphine donors.[7a] No reaction, however, is observed between **4.6** and excess PMe_3 or NH_3. The Fe(I) site *trans* to the silyl ligand therefore appears preferentially disposed to coordination of π-acidic ligands, whereas Fe(II) accommodates pure σ-donors, as for the THF-adduct complex **4.9**.

Previously characterized iron dinitrogen complexes have been reported to release low yields (<15% per Fe) of hydrazine and/or ammonia under strongly protolytic conditions.[17] However, the addition of protic sources to either of the previously reported

diiron(I) systems $\{[PhBP^{iPr}_3]Fe\}_2(\mu\text{-}N_2)$ or β-diketiminato $L^RFeNNFeL^R$ [6a] did not lead to any detectable production of either NH_3 or N_2H_4. Therefore, our observation of low yields of hydrazine upon addition of acids HX to **4.6** (17% per Fe for X = BF_4; 7% per Fe for X = Cl) represents a promising initial lead for the $[SiP^R]Fe$ systems. More interesting is the observation that performing such protonations in the presence of CrX'_2 as a sacrificial 1-electron reductant increases yields of hydrazine significantly (47% per Fe for X' = Cl; 42% per Fe for X' = Cp*). The addition of similar protic sources to **4.8** rapidly and cleanly regenerates **4.6** with no evidence for protonation at the N_2 ligand. Analogous conditions result in substantially lower yields of hydrazine for **4.7** (9% per Fe) even in the presence of $CrCp^*_2$, presumably because the more reducing nature of **4.7** causes direct H^+ reduction to H_2 to vastly outcompete N_2 reduction. Complex **4.7** is more basic than **4.6**, and therefore weaker acids that fail to react with **4.6** instead provide low yields of hydrazine with **4.6** (e.g., 13% per Fe for HX = $[HN^iPr_2Et][BPh_4]$). One key to advancing this N_2 reduction chemistry further will be to more carefully control the delivery of protons and electrons so that N_2 reduction is favored over H_2 evolution.

4.3 Experimental Section

4.3.1 General Considerations

All manipulations were carried out using standard Schlenk or glovebox techniques under a dinitrogen atmosphere. Unless otherwise noted, solvents were deoxygenated and dried by thoroughly sparging with N_2 gas followed by passage through

an activated alumina column. Nonhalogenated solvents were tested with a standard purple solution of sodium benzophenone ketyl in tetrahydrofuran in order to confirm effective oxygen and moisture removal. All reagents were purchased from commercial vendors and used without further purification unless otherwise stated. 2-(diphenylphosphino)phenyl bromide,[18] 2-(diisopropylphosphino)phenyl bromide,[19] and mesityliron(II)[20] were prepared according to literature procedures. Elemental analyses were performed by Desert Analytics, Tucson, AZ. Deuterated solvents were purchased from Cambridge Isotope Laboratories (Cambridge, MA), degassed, and dried over activated 3 Å molecular sieves prior to use.

4.3.2 X-ray Crystallography Procedures

X-ray diffraction studies were carried out at the Beckman Institute Crystallography Facility on a Brüker Smart 1000 CCD diffractometer and solved using SHELX v. 6.14.[21] X-ray quality crystals were grown as indicated in the experimental procedures per individual complex. The crystals were mounted on a glass fiber with Paratone N oil. Structures were determined using direct methods with standard Fourier techniques using the Bruker AXS software package. Special refinement details used for the disordered solvent region in **4.3** and for the entire data set in **4.9** are specified in the comments sections of the cif files.

4.3.3 Spectroscopic Measurements

Varian Mercury-300 and Inova-500 spectrometer was used to record ^{1}H, ^{13}C, ^{29}Si, and ^{31}P NMR spectra at ambient temperature unless otherwise indicated. ^{1}H and ^{13}C chemical shifts were referenced to the residual solvent peaks. ^{31}P chemical shifts were referenced to external phosphoric acid (δ = 0 ppm). ^{29}Si chemical shifts were referenced to external tetramethylsilane (δ = 0 ppm). Optical spectroscopy measurements were taken on a Cary 50 UV/Vis Spectrophotometer using a 1 cm quartz cell sealed with a Teflon stopper.

4.3.4 Synthesis

Synthesis of tris(2-(diphenylphosphino)phenyl)silane ([SiP$^{Ph}_3$]H, 4.1). Under a dinitrogen atmosphere, 2-(diphenylphosphino)phenyl bromide (6.65 g, 19.5 mmol) was dissolved in diethyl ether (100 mL) and cooled to -78°C. *n*-Butyllithium (8.30 g of a 1.6 M solution in hexanes, 19.5 mmol) was added slowly, giving a light orange solution with a tan-colored precipitate. This mixture was allowed to warm gradually to room temperature and then stirred for 1 h, after which the volatiles were removed *in vacuo*. Toluene (100 mL) was added, and the cloudy orange solution was cooled back to -78°C. Trichlorosilane (0.660 mL, 6.54 mmol) was added in one portion, and the resulting mixture was warmed to room temperature gradually. After stirring for 0.5 h at room temperature, the reaction was heated in a sealed reaction bomb to 110°C for 15 h. The resulting yellow solution and white precipitate were cooled to room temperature and filtered through Celite, and the filtrate was concentrated to white solids. Petroleum ether

(60 mL) was added and the resulting mixture was stirred vigorously for 20 min, at which point tan solids were collected on a sintered glass frit and washed with additional petroleum ether (2 x 10 mL) to afford [SiP^{Ph}_3]H as a fine tan powder (4.59 g, 87%). ^{1}H NMR (C_6D_6, δ): 7.63 (dm, *J* = 1.5 and 6.3 Hz, 3H), 7.34 (ddm, *J* = 1.0, 3.9, and 7.8 Hz, 3H), 7.25-7.20 (m, 12H), 7.05 (td, *J* = 1.5 and 7.3 Hz, 6H), 7.02-6.95 (m, 19H). ^{13}C{^{1}H} NMR (C_6D_6, δ): 145.5 (d, *J* = 11.4 Hz), 144.3 (t, *J* = 4.0 Hz), 144.0 (t, *J* = 4.0 Hz), 138.8 (d, *J* = 14.6 Hz), 138.5 (d, *J* = 12.8 Hz), 134.7, 134.5 (d, *J* = 19.2 Hz), 130.4, 128.8, 128.6 (d, *J* = 17.3 Hz). ^{29}Si{^{1}H} NMR (C_6D_6, δ): -33.8 (q, $^3J_{Si\text{-}P}$ = 24.4 Hz). ^{31}P{^{1}H} NMR (C_6D_6, δ): -10.4 (s). IR (KBr, cm^{-1}): 3044, 2170 (ν[Si-H]), 1580, 1478, 1429, 1109, 795. Anal. Calcd for $C_{54}H_{43}P_3Si$: C, 79.78; H, 5.33. Found: C, 79.39; H, 5.61.

Synthesis of tris(2-(diisopropylphosphino)phenyl)silane ([SiP^{iPr}_3]H, 4.2). (2-bromophenyl)diisopropylphosphine (4.1429 g, 15.164 mmol) was dissolved in 100 mL of diethyl ether and chilled to -78 °C, and *n*-butyllithium (1.60 M solution in hexanes, 9.50 mL, 15.2 mmol) was added dropwise, causing a darkening of the solution and gradual precipitation of solids. After 15 min, the slurry was brought to room temperature and stirred for 2 h, after which volatiles were removed *in vacuo* to yield a pale-red powder. The powder was redissolved in toluene (80 mL), chilled to -35 °C, and trichlorosilane (511 μL, 5.06 mmol) was added in one portion, resulting in the immediate precipitation of white solids and lightening of the solution. The mixture was stirred at room temperature for 30 min, then at 90 °C for 15 h, and filtered through Celite to give a clear, light orange solution. Solvents were removed *in vacuo* to give an orange oil, and the addition of petroleum ether (20 mL) caused the precipitation of white solids. These were isolated on a frit and washed with petroleum ether (2 x 5 mL) to yield **4.2** as a white

powder. Subsequent crops could be isolated by crystallization from concentrated petroleum ether solutions at -35 °C (0.5439 g, 18%). ^{1}H NMR (C_6D_6): δ 7.46 – 7.34 (m, 3H, Ar-*H*). 7.30 – 7.20 (m, 3H, Ar-*H*), 7.20 – 7.10 (td, *J* = 1.2 and 7.2 Hz, 3H, Ar-*H*), 7.02 – 6.92 (tt, *J* = 1.5 and 7.5 Hz, 3H, Ar-*H*), 2.05 – 1.85 (doublet of septets, $^{2}J_{HP}$ = 6.9 Hz, $^{3}J_{HH}$ = 3.0 Hz, 6H, -C*H*(CH_3)$_2$), 1.20 – 1.02 (m, 18H, -CH(C*H*$_3$)$_2$), 1.00 – 0.88 (m, 18H, -CH(C*H*$_3$)$_2$). ^{31}P NMR (C_6D_6): δ 1.7 (s). IR (THF, cm^{-1}): ν(Si-H): 2218. Anal. Calcd. for $C_{36}H_{55}P_3Si$: C, 71.02; H, 9.11. Found: C, 71.09; H, 9.38.

Synthesis of [SiP$^{Ph}_3$]Fe(Mes) (4.3). [SiP$^{Ph}_3$]H (3.06 g, 3.77 mmol) and mesityliron(II) (1.11 g, 3.77 mmol) were combined in benzene (40 mL) and heated to 65°C for 14 h. Volatiles were removed *in vacuo*, petroleum ether (100 mL) was added, and the mixture was stirred for 30 min. Filtration through Celite afforded a strawberry red filtrate that was concentrated to oily red solids. Benzene (15 mL) was added, and the clear red solution was lyophilized to give a fine red powder (1.70 g, 46%). Though this material was typically utilized without further purification, analytically pure material could be obtained by cooling a saturated petroleum ether solution to -30°C for 16 h. Crystals suitable for X-ray diffraction were obtained by diffusion of hexamethyldisiloxane vapors into a saturated petroleum ether solution at -30°C. ^{1}H NMR (C_6D_6, δ): 8.50 (d, *J* = 7.2 Hz, 6H), 7.6-6.8 (m, 29H), 6.7-6.5 (m, 18H), 5.33 (br, *ortho*-C$\underline{H}_3$), 1.84 (s, 3H, *para*-C$\underline{H}_3$), 0.58 (br, *ortho*-C$\underline{H}_3$). ^{1}H NMR (toluene-d_8, -60°C, δ): 8.48 (d, *J* = 7.2 Hz, 2H), 8.33 (d, *J* = 7.8 Hz, 1H), 7.6-6.9 (m, 29H), 6.8-6.6 (m, 15H), 6.52 (t, *J* = 7.5 Hz, 1H), 6.36 (t, *J* = 7.8 Hz, 2H), 4.60 (*ortho*-C$\underline{H}_3$), 1.88 (s, 3H, *para*-C$\underline{H}_3$), 1.10 (*ortho*-C$\underline{H}_3$), -0.24 (*ortho*-C$\underline{H}_3$). ^{13}C{^{1}H} NMR (C_6D_6, δ): 157.4 (br), 150.0 (br), 139.5 (br), 134.7, 134.5 (d, *J* = 19.2 Hz), 132.7, 132.5, 131.7 (br), 130.9, 130.4, 128.9, 128.8,

127.3, 127.2, 104.9 (br, mesityl *ipso*-C), 23.1 (s, *ortho*-$\underline{C}H_3$), 20.5 (s, *para*-$\underline{C}H_3$), 14.6 (s, *ortho*-$\underline{C}H_2$-H-Fe). $^{31}P\{^1H\}$ (C_6D_6, δ): 72.0 (br). $^{31}P\{^1H\}$ (toluene-d_8, -60°C, δ): 76.0 (t, 1P, $^2J_{PP}$ = 10.7 Hz), 73.3 (d, 2P, $^2J_{PP}$ = 10.7 Hz). UV-Vis (toluene, nm($M^{-1}cm^{-1}$)): 367(5000), 508(3800). IR (KBr, cm^{-1}): 3049, 2956, 2910, 1584, 1479, 1429, 1100, 838. Anal. Calcd for $C_{63}H_{53}FeP_3Si$: C, 76.67; H, 5.41. Found: C, 77.50; H, 5.37.

Synthesis of [SiP$^{Ph}_3$]FeCl (4.4). [SiP$^{Ph}_3$]Fe(Mes) (1.02 g, 1.03 mmol) was dissolved in diethyl ether (40 mL) and cooled to -78°C. Hydrogen chloride (1.0 mL of a 1.0 M solution in diethyl ether, 1.0 mmol) was added in one portion by syringe. The solution was allowed to warm to room temperature with stirring, resulting in gradual precipitation of an orange solid. After stirring the reaction at room temperature for 1.5 h, the orange solid was collected on a sintered glass frit and washed with additional portions of diethyl ether (2 x 10 mL), affording an analytically pure sample of [SiP$^{Ph}_3$]FeCl (0.555 g, 60%). Crystals suitable for X-ray diffraction were obtained by slow diffusion of petroleum ether vapors into a dichloromethane solution. ^1H NMR (C_6D_6, δ): 12.32, 7.61, 6.99, 4.67, 3.29, -2.09, -5.03. μ_{eff} (C_6D_6, Evans' method, 23°C): 2.9 μ_B. UV-Vis (toluene, nm($M^{-1}cm^{-1}$)): 426(4700), 479(5700). IR (KBr, cm^{-1}): 2363, 1482, 1433, 1103. Anal. Calcd for $C_{54}H_{42}ClFeP_3Si$: C, 71.81; H, 4.69. Found: C, 71.82; H, 4.41.

Alternative synthesis of 4.4. To a THF-suspension (30 mL) of **4.1** (1.43 g, 1.76 mmol) and $FeCl_2$ (0.224 g, 1.76 mmol) was added 1,4-dioxane (3 mL). The entire mixture was cooled to -78°C, and CH_3MgBr (1.17 mL of a 3.0 M solution in Et_2O, 3.51 mmol) was added by syringe with stirring. The solution was kept stirring at -78°C for 0.5 h, and then was stirred at room temperature for 12 h, resulting in a cloudy brown mixture.

Volatiles were removed *in vacuo*. Diethyl ether (50 mL) was added and the mixture was filtered through Celite. The resulting red filtrate was cooled to -78°C, and HCl (1.75 mL of a 1.0 M solution in Et_2O, 1.75 mmol) was added, forming a light orange precipitate. After stirring at room temperature for 0.5 h, this precipitate was collected on a sintered glass frit, washed with additional portions of diethyl ether, and dried. ^{1}H NMR confirmed the product's identity as **4.4**. Yield: 0.381 g, 24%.

Synthesis of [SiP$^{i\mathrm{Pr}}_3$]FeCl (4.5). To a stirring slurry of ferrous chloride (30.6 mg, 0.241 mmol) in THF (10 mL) was added a solution of H[SiP$^{i\mathrm{Pr}}_3$] (147.2 mg, 0.2418 mmol) in THF (5 mL), causing a color change to yellow. The resulting solution was chilled to -78 °C, and MeMgCl (3.0 M in THF, 81 μL, 0.24 mmol) was diluted in THF (1 mL) and added dropwise, causing an immediate darkening of the solution. The reaction was stirred at -78 °C for 1 h, then warmed to room temperature and stirred 3 h to give a dark orange solution. The solution was filtered through Celite and concentrated to an orange film *in vacuo*. The residues were extracted into benzene, filtered, lyophilized, and washed with petroleum ether (3 x 3 mL) to yield **4.5** as an orange powder (72.5 mg, 43%). Crystals suitable for X-ray diffraction were obtained by slow evaporation of benzene from a concentrated solution. ^{1}H NMR (C_6D_6): δ 6.3, 5.9, 5.4, 4.7, 3.7, 3.2, 2.5, 2.0, 1.4, 1.1, 0.9, 0.3, -2.5. UV-vis (THF, λ_{max}, nm (ε, M^{-1} cm^{-1})): 471 (990), 379 (2100). Evans Method (C_6D_6): 3.3 μ_B. Anal. Calcd. for $C_{36}H_{54}ClFeP_3Si$: C, 61.85; H, 7.79. Found: C, 62.34; H, 7.96.

Synthesis of [SiP$^{\mathrm{Ph}}_3$]Fe(N$_2$) (4.6). Sodium (8.3 mg, 0.36 mmol) and mercury (0.714 g) were combined in THF (1 mL). Solid [SiP$^{\mathrm{Ph}}_3$]FeCl (0.322 g, 0.357 mmol) was

added, and the total volume was brought up to 15 mL. After vigorous stirring for 6 h at room temperature, a brown supernatant was decanted off the Na/Hg amalgam and concentrated *in vacuo* to brown solids. Benzene (10 mL) was added, and the resulting cloudy solution was filtered through Celite. The resulting red-orange filtrate was lyophilized, providing spectroscopically pure [SiP^{Ph}_3]Fe(N_2) as a fluffy red-orange solid (0.278 g, 87%). Crystals suitable for x-ray diffraction were obtained by slow diffusion of petroleum ether vapors into a THF solution. ^{1}H NMR (C_6D_6, δ): 10.48, 7.98, 7.42, 6.17, 4.46, -1.6 – -2.1 (br), -1.86. μ_{eff} (C_6D_6, Evans' method, 23°C): 1.8 μ_B. UV-Vis (toluene, nm($M^{-1}cm^{-1}$)): 347(9400). IR (KBr, cm^{-1}): 3048, 2041 (ν_{NN}), 1578, 1477, 1432, 1096. Note: Though all solution data we have collected indicates the presence of **4.6** in pure form, the lability of the dinitrogen ligand complicated isolation of analytically pure solid samples. As a result, combustion analysis and Toepler pump analysis indicated low levels of nitrogen. To probe this instability, we note that after repeated lyophilization of **4.6** from benzene over several hours, a new paramagnetic species is observed as **4.6** decays. This unidentified paramagnetic species subsequently decomposes at temperatures as low as -30ºC to cleanly generate [SiP^{Ph}_3]H in benzene solution.

[SiP^{iPr}_3]Fe(N_2) (4.7). A dark-green solution of sodium naphthalide was prepared by stirring a colorless solution of naphthalene (8.6 mg, 0.067 mmol) in THF (3 mL) over excess sodium metal (8.0 mg, 0.35 mmol) for 3 h. The resulting naphthalide solution was filtered away from sodium and added dropwise to an orange solution of **4.5** (46.8 mg, 0.0669 mmol) in THF (5 mL), causing the color of the solution to change to dark orange over a period of several minutes. The reaction was allowed to proceed overnight, filtered, and volatiles removed *in vacuo* to give an orange-red film. The residues were extracted

into benzene (5 mL), filtered and dried. The residues were triturated with petroleum ether (1 x 5 mL) to give a red powder that was washed with petroleum ether (2 x 3 mL) to yield spectroscopically pure **4.7** (10.5 mg, 23%). Crystals suitable for X-ray diffraction were obtained by slow evaporation of benzene from a concentrated solution. ^{1}H NMR (C_6D_6): δ 10.0, 5.9, 5.5, 4.8, 3.8, 3.3, 0.3. Evans Method (C_6D_6): 2.2 μ_B. IR (THF, cm^{-1}): $\nu(N_2)$: 2008. UV-vis (THF, λ_{max}, nm (ε, M^{-1} cm^{-1})): 468 (1800), 380 (3500).

Synthesis of {[SiP$^{Ph}_3$]Fe(N$_2$)}{Na(12-crown-4)$_2$} (4.8). Sodium (2.3 mg, 0.10 mmol) and mercury (0.552 g) were combined in THF (1 mL). A THF solution (8 mL) of [SiP$^{Ph}_3$]Fe(N_2) (73.5 mg, 0.0821 mmol) and then 12-crown-4 (40.0 mL, 0.247 mmol) were added, resulting in a red-purple solution. The reaction was stirred vigorously for 6.5 h, then the deep purple supernatant was decanted off the Na/Ha amalgam, filtered through Celite, and concentrated *in vacuo* to purple solids. The residue was triturated with diethyl ether (10 mL), and a purple microcrystalline solid was collected on a sintered glass frit. Additional diethyl ether washes (2 x 10 mL) yielded analytically pure {[SiP$^{Ph}_3$]Fe(N_2)}{Na(12-crown-4)$_2$} (63.5 mg, 71%). ^{1}H NMR (THF-d_8, δ): 8.22 (d, J = 10.5 Hz, 3H), 7.4-6.4 (m, 39H), 3.55 (s, 32H, 12-crown-4). ^{31}P{^{1}H} NMR (THF-d_8, δ): 84.3 (s). UV-Vis (THF, nm($M^{-1}cm^{-1}$)): 415(6100), 460(6300). IR (KBr, cm^{-1}): 3042, 2963, 2911, 2866, 1967 (ν_{NN}), 1578, 1476, 1431, 1364, 1289, 1244, 1134, 1096, 1023, 916. Anal. Calcd for $C_{70}H_{74}FeN_2O_8P_3Si$: C, 66.14; H, 5.87; N, 2.20. Found: C, 66.35; H, 5.85; N, 1.77.

Synthesis of {[SiP$^{Ph}_3$]Fe(thf)}{BAr$^F_4$} (4.9). A THF solution (1 mL) of [$FeCp_2$][BAr$^F_4$] (48.6 mg, 0.0463 mmol) was added slowly to a stirring THF solution (2

mL) of **4.6** (42.2 mg, 0.0471 mmol) at room temperature. After stirring for 2 h, the volatiles were removed and **4.9** was recrystallized from Et_2O/petroleum ether (-30°C). Yield: 54.5 mg (65%). ^{1}H NMR (10:1 C_6D_6/THF-d_8, δ): 8.22, 7.63, 7.09, 6.99, 3.32, 0.82. μ_{eff} (10:1 C_6D_6/THF-d_8, Evans' method, 23°C): 5.6 μ_B. ^{19}F NMR (10:1 C_6D_6/THF-d_8, δ): -60 (s). IR (KBr, cm^{-1}): 3055, 2961, 1611, 1439, 1356, 1280, 1125, 867, 839. Anal. Calcd for $C_{90}H_{62}BF_{24}FeOP_3Si$: C, 59.95; H, 3.47; N, 0.00. Found: C, 55.28; H, 3.72; N, <0.05. Note: Satisfactory combustion analysis for this complex was not obtained, possibly due to lability of the thf ligand. However, an analogous preparation was used to access {[SiP$^{Ph}_3$]Fe(thf)}{BPh_4}, whose x-ray quality crystals were grown by diffusion of Et_2O vapors into a THF solution.

Synthesis of [SiP$^{Ph}_3$]Fe(CO) (4.10). Sodium (4.2 mg, 0.18 mmol) and mercury (0.982 g) were combined in THF (1 mL). Solid [SiP$^{Ph}_3$]FeCl (0.153 g, 0.169 mmol) was added, and the total volume was brought up to 5 mL. After vigorous stirring for 3.5 h at room temperature, a brown supernatant was decanted off the Na/Hg amalgam and concentrated *in vacuo* to brown solids. Benzene (10 mL) was added, and the resulting cloudy solution was filtered through Celite into a resealable Schlenk tube. The resulting red-orange filtrate was frozen, evacuated, and backfilled with CO (1 atm). After stirring at room temperature for 1 h, the solution was filtered through Celite and concentrated to brown solids. Trituration with petroleum ether (10 mL) provided a brown powder that was collected on a sintered glass frit and washed with additional portions of petroleum ether, providing [SiP$^{Ph}_3$]Fe(CO) (0.062 g, 41%). ^{1}H NMR (C_6D_6, δ): 10.37, 7.62, 7.01, 6.15, 5.29, -1.02, -1.52. μ_{eff} (C_6D_6, Evans' method, 23°C): 2.1 μ_B. UV-Vis (toluene,

nm($M^{-1}cm^{-1}$)): 335(2400), 411(1600). IR (C_6H_6, cm^{-1}): 1881 (ν_{CO}). Anal. Calcd for $C_{55}H_{42}FeOP_3Si$: C, 73.75; H, 4.73; N, 0,00. Found: C, 73.22; H, 4.68; N, 0.28.

Reaction of 4.6 and 4.7 with acids. $[SiP^R_3]FeN_2$ (approx 10 mg), and in some cases a sacrificial Cr(II) reagent (10 equiv per Fe), were dissolved in THF (3 mL) in a 2-neck 25 mL round-bottom flask and sealed with septa. An ethereal solution of the acid (10 equiv per Fe) was added via syringe, and the resulting solution was stirred overnight under septum seal. Volatiles were then vacuum-transferred onto a frozen HCl solution (5 mL, 1.0 M in Et_2O). A solution of NaO^{t}Bu (>15 equiv) in THF (5 mL) was then added to the source flask via syringe through the second neck, and the mixture was stirred vigorously for 30 min. The volatiles were again vacuum-transferred into the same receiving flask. The combined distillates were concentrated to white solids by rotary evaporation and analyzed by ^{1}H NMR (DMSO-d_6) with mesitylene added as an internal integration standard. $[N_2H_6]Cl_2$ was detected[22] in modest yields based on ^{1}H NMR integration. The results of these experiments are summarized in Table 4.1.

Table 4.1. Summary of protolytic hydrazine formation experiments

Phosphine substituent	H^+	e^-	Solvent	Yield of N_2H_4 per Fe
Ph	HCl	None	THF	7%
Ph	HBF_4	None	THF	17%
Ph	HBF_4	$CrCl_2$	THF	47%
Ph	HBF_4	$CrCp^*_2$	THF	42%
Ph	HBF_4	$CrCp^*_2$	THF, 0°C	28%
Ph	HBF_4	$CrCp^*_2$	THF, add H^+ dropwise	23%
Ph	HBF_4	$CrCp^*_2$	Et_2O	15%
Ph	HBF_4	$CrCp^*_2$	C_6H_6	<5%
Ph	$[LutH]BPh_4$	$CrCp^*_2$	THF	0%
Ph	$[LutH]BPh_4$	$CrCp^*_2$	C_6H_6	0%
iPr	HBF_4	$CrCp^*_2$	THF	9%
iPr	$[HNiPr_2Et]BPh_4$	$CrCp^*_2$	THF	13%
iPr	$[HNiPr_2Et]BPh_4$	$CrCp^*_2$	C_6H_6	0%
iPr	$[LutH]BPh_4$	$CrCp^*_2$	C_6H_6	0%

Lut = 2,6-lutidine, Cp* = pentamethylcyclopentadienyl

4.3.5 Electrochemistry

Electrochemical measurements were carried out in a glovebox under a dinitrogen atmosphere in a one-compartment cell using a CH Instruments 600B electrochemical analyzer. A glassy carbon electrode was used as the working electrode and platinum wire was used as the auxillary electrode. The reference electrode was $Ag/AgNO_3$ in THF. The ferrocene couple Fc^+/Fc was used as an external reference. Solutions (THF) of

electrolyte (0.3 M tetra-*n*-butylammonium hexafluorophosphate) and analyte were also prepared under an inert atmosphere.

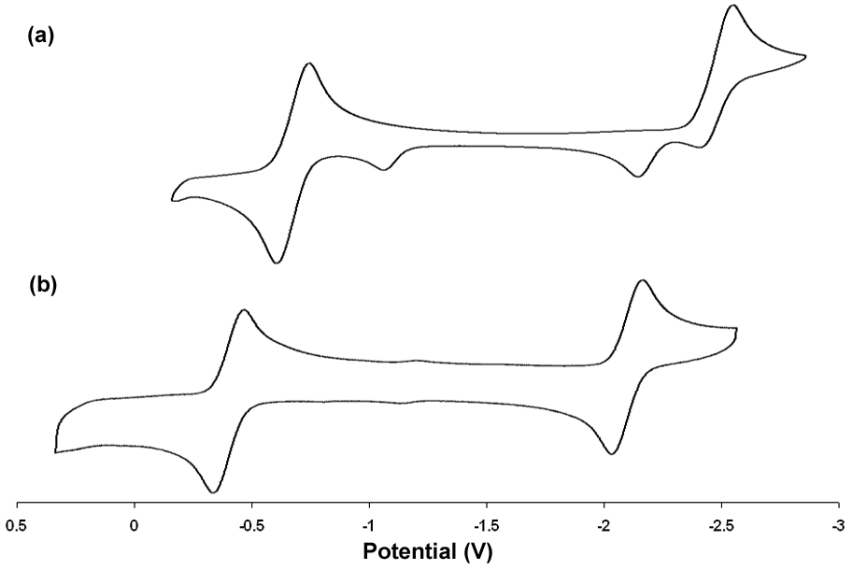

Figure 4.5. Cyclic voltammograms of (a) [SiP^{iPr}_3]FeCl and (b) [SiP^{Ph}_3]FeCl. The potential scale is vs $FeCp_2^+/FeCp_2$.

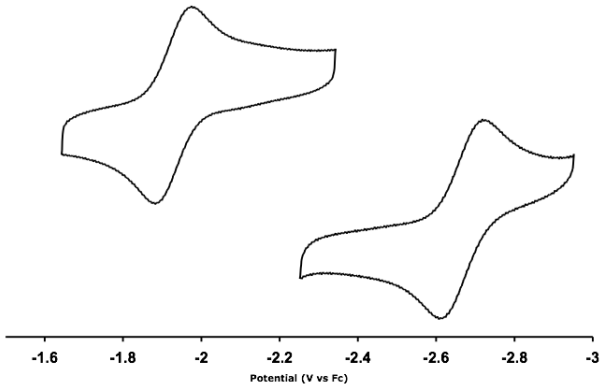

Figure 4.6. Cyclic voltammograms for [SiP^{Ph}_3]Fe(N_2) (*top*) and [SiP^{iPr}_3]Fe(N_2) (*bottom*).

4.3.6 EPR Spectroscopy

X-band EPR spectra were obtained on a Bruker EMX spectrometer (controlled by Bruker Win EPR software v. 3.0) equipped with a rectangular cavity working in the TE_{102} mode and an Oxford continuous-flow helium cryostat (temperature range 3.6-300 K). Accurate EPR frequency values were provided by a frequency counter built into the microwave bridge. EPR spectra were simulated using the W95EPR program.[23]

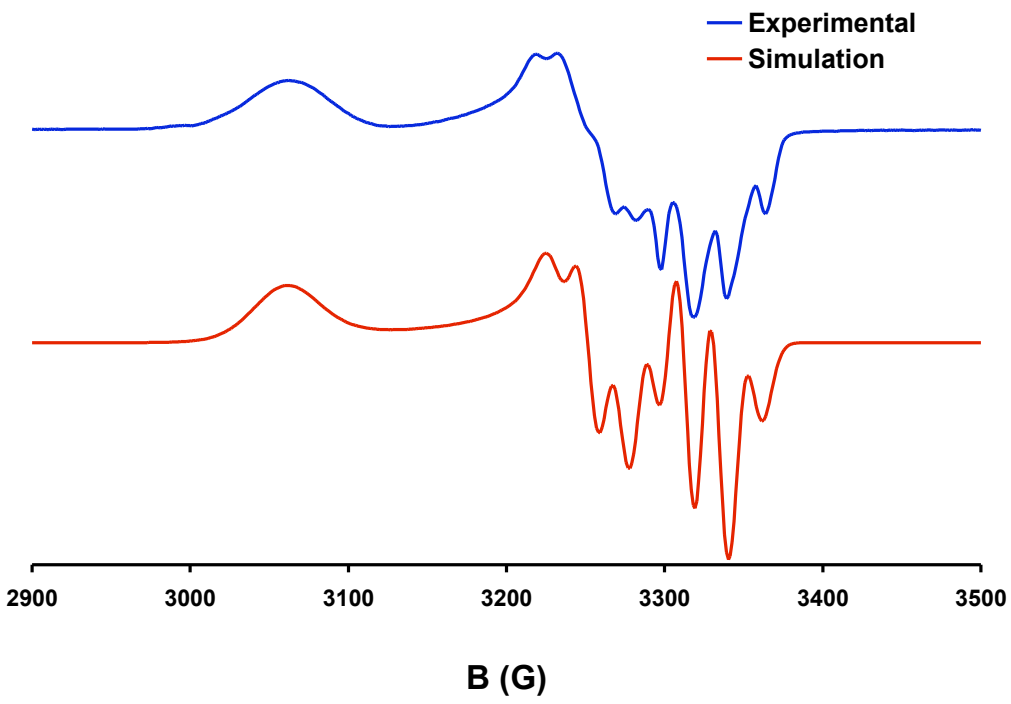

Figure 4.7. X-band EPR spectrum of $[SiP^{Ph}_3]FeN_2$ (**4.6**) (*blue*) and simulation (*red*) in a 2-methyltetrahydrofuran glass at 4 K. ***Simulation parameters:*** ν = 9.3743 GHz; g_1 = 2.013, g_2 = 2.051, g_3 = 2.187; for 3 equivalent P atoms: A_1 = 58 MHz, A_2 = 55 MHz, A_3 = 5.8 MHz; line widths: W_1 = 8.0 G, W_2 = 9.5 G, W_3 = 26.0 G.

References Cited

1 (a) B. A. MacKay, M. D. Fryzuk, *Chem. Rev.* **2004**, *104*, 385. (b) J. C. Peters, M. P. Mehn, In *Activation of Small Molecules*, W. B. Tolman (ed.), Wiley, New York, **2006**, p. 81.

2 J. Chatt, J. R. Dilworth, R. L. Richards, *Chem. Rev.* **1978**, *78*, 589.

3 D. V. Yandulov, R. R. Schrock, *Science* **2003**, *301*, 76.

4 (a) L. C. Seefeldt, I. G. Dance, D. R. Dean, *Biochemistry* **2004**, *43*, 1401. (b) O. Einsle, F. A. Tezcan, S. L. A. Andrade, B. Schmid, M. Yoshida, J. B. Howard, D. C. Rees, *Science* **2002**, *297*, 1696.

5 (a) T. A. Betley, J. C. Peters, *J. Am. Chem. Soc.* **2004**, *126*, 6252. (b) M. P. Hendrich, W. Gunderson, R. K. Behan, M. T. Green, M. P. Mehn, T. A. Betley, C. C. Lu, J. C. Peters, *Proc. Nat. Acad. Sci.* **2006**, *103*, 17107. (c) C. Vogel, F. W. Heinemann, J. Sutter, C. Anthon, K. Meyer, *Angew. Chem., Int. Ed.* **2008**, *47*, 2681. (d) J. J. Scepaniak, M. D. Fulton, R. P. Bontchev, E. N. Duesler, M. L. Kirk, J. M. Smith, *J. Am. Chem. Soc.* **2008**, *130*, 10515.

6 (a) J. M. Smith, A. R. Sadique, T. R. Cundari, K. R. Rodgers, G. Lukat-Rodgers, R. J. Lachicotte, C. J. Flaschenriem, J. Vela, P. L. Holland, *J. Am. Chem. Soc.* **2006**, *128*, 756. (b) T. A. Betley, J. C. Peters, *J. Am. Chem. Soc.* **2003**, *125*, 10782.

7 (a) C. E. MacBeth, S. B. Harkins, J. C. Peters, *Can. J. Chem.* **2005**, *83*, 332. (b) P. Stoppioni, F. Mani, L. Sacconi, *Inorg. Chim. Acta* **1974**, *11*, 227.

8 Rh complexes of the related ligand $[(R_3PCH_2CH_2)_3Si]$- have been reported: F. L. Joslin, S. R. Stobart, *J. Chem. Soc., Chem. Commun.*, **1989**, 504.

9 Similar Fe···C distances have been observed in other systems for which C-H agostic interactions have been assigned. Recent examples: (a) S. W. Kohl, F. W. Heinemann, M. Hummert, W. Bauer, A. Grohmann, *Chem. Eur. J.* **2006**, *12*, 4313. (b) N. A. Eckert, J. M. Smith, R. J. Lachicotte, P. L. Holland, *Inorg. Chem.* **2004**, *43*, 3306. (c) K. Rachlewicz, S.-L. Wang, C.-H. Peng, C.-H. Hung, L. Latos-Grazynski, *Inorg. Chem.* **2003**, *42*, 7348.

10 Selected examples: (a) M. D. Leatherman, S. A. Svejda, L. K. Johnson, M. Brookhart, *J. Am. Chem. Soc.* **2003**, *125*, 3068. (b) F. M. Conroy-Lewis, L. Mole, A. D. Redhouse, S. A. Litser, J. L. Spencer, *J. Chem. Soc., Chem. Commun.* **1991**, 1601.

11 Pre-complexation of **4.2** with $FeCl_2$ is observed upon mixing, and the L_2FeCl_2 (L_2 = κ^2-[SiP^{iPr}_3]H) intermediate has been characterized by X-ray crystallography (see Appendix 3). Though no reaction is observed between **4.1** and $FeCl_2$, adding CH_3MgCl to the mixture does produce **4.4** in modest yields.

12 In the X-ray structure of **4.7**, a Cl ligand is present in place of the N_2 ligand with approx 3% occupancy. As a result, Fe-N and N-N bond lengths are not discussed here.

13 S. Komiya, M. Akita, A. Yoza, N. Kasuga, A. Fukuoka, Y. Kai, *J. Chem. Soc., Chem. Comm.* **1993**, 787.

14 R. A. Cable, M. Green, R. E. Mackenzie, P. L. Timms, T. W. Turney, *J. Chem. Soc., Chem. Commun.* **1976**, 270.

15 (a) R. J. Trovitch, E. Lobkovsky, P. J. Chirik, *Inorg. Chem.* **2006**, *45*, 7252. (b) V. K. Dioumaev, K. Plossl, P. J. Carroll, D. H. Berry, *J. Am. Chem. Soc.* **1999**, *121*, 8391.

(c) D. G. Gusev, F. G. Fontaine, A. J. Lough, D. Zargarian, *Angew. Chem.*, **2003**, *115*, 226; *Angew. Chem., Int. Ed.,* **2003**, *42*, 216.

16 The related complex $\{[SiP^{Ph}_3]Fe(thf)\}\{BPh_4\}$ has been identified by X-ray crystallography. See Appendix 3.

17 (a) J. D. Gilbertson, N. K. Szymczak, D. R. Tyler, *J. Am. Chem. Soc.* **2005**, *127*, 10184. (b) T. A. George, D. J. Rose, Y. Chang, Q. Chen, J. Zubieta, *Inorg. Chem.,* **1995**, *34*, 1295. (c) G. J. Leigh, *Acc. Chem. Res.* **1992**, *25*, 177.

18 M. T. Whited, E. Rivard, J. C. Peters, *Chem. Commun.*, **2006**, 1613.

19 (a) R. Talay, D. Rehder, *Zeit. f. Natur, B: Anorg. Chem.*, **1981**, *36*, 451. (b) M. Tamm, B. Drebel, K. Baum, T. Lügger, T. Pape, *J. Organomet. Chem.*, **2003**, *677*, 1.

20 A. Klose, E. Solari, R. Ferguson, C. Floriani, A. Chiesi-Villa, C. Rizzoli, *Organometallics*, **1993**, *12*, 2414.

21 G. M. Sheldrick, *Acta Cryst.* **2008**, *A64*, 112.

22 Identical spectra were obtained by exposing hydrazine (anhydrous) to a large excess of HCl (1.0 M in Et_2O), followed by concentration and dissolution in DMSO-d_6.

23 F. Neese, *QCPE Bull.* **1995**, *15*, 5.

Chapter 5: Catalytic N-N Coupling of Aryl Azides to Yield Azoarenes via Trigonal Bipyramidal Fe-Nitrene Intermediates

Reproduced in part from

Mankad, N. P., Müller, P., and Peters, J. C. *Manuscript submitted*.

5.1 Introduction

Organoazides (N_3R) are desirable reagents for nitrene transfer reactions.[1] Generally, organoazides interact with transition metal catalysts to form transient M-N_3R adduct species that in many cases subsequently extrude N_2 to yield metal-imido/nitrene (MNR) complexes as the key reactive intermediates for substrate activation.[1] Understanding the properties of metal-organoazide and metal-imido/nitrene complexes is fundamentally important in this context. Several iron-imido/nitrene intermediates that are unstable toward hydrogen atom abstraction and/or intramolecular ligand oxidation pathways have been proposed for various coordination geometries.[2] We[3] and others[4] have shown that iron-imido complexes formed from organoazides can be stabilized in pseudotetrahedral coordination environments. Subsequently, stable iron-imido complexes with distorted square planar geometries,[5] as well as a trigonal planar bis(imido)iron complex,[6] also have been structurally characterized.

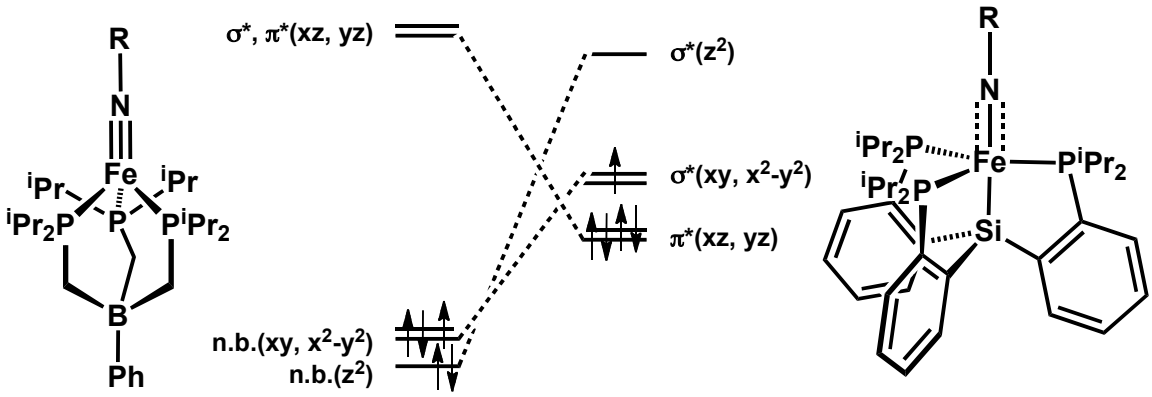

Figure 5.1. Qualitative d-orbital splitting diagrams for pseudotetrahedral and trigonal bipyramidal iron-imido/nitrene complexes.

An interesting geometry to consider for an FeNR unit is the trigonal bipyramid (TBP). The well-studied pseudotetrahedral $L_3Fe^{III}NR$ complexes feature bona fide Fe-N

triple bonds resulting from two highly destabilized, unoccupied π^*_{FeN} orbitals (Figure 5.1, *left*).[3] Introducing a ligand *trans* to the imido group and shifting the Fe into the L_3 plane in a TBP leads in principle to population of the π^*_{FeN} set (Figure 5.1, *right*), thereby obliterating a significant degree of the Fe-N multiple bonding character presumed responsible for the stability of pseudotetrahedral $L_3Fe^{III}NR$ species.[3,4a] Accordingly, until recently[7] metal-ligand multiply bonded species in TBP configurations had been isolated only for d-electron counts of 0 or 1.[8] TBP systems with higher d-electron counts often dissociate the apical ligand and distort towards the more stable pseudotetrahedral geometry when accommodating an axial metal-ligand multiple bond.[9] In this context, we sought to examine the ramifications of placing a FeNR linkage in a TBP environment. Our recent work[10] with low-valent TBP Fe complexes supported by anionic tris(phosphino)silyl ligands $(2\text{-}R_2PC_6H_4)_3Si^-$ ($[SiP^R_3]^-$) provided a convenient entry point for such studies (Figure 5.1).

5.2 Results and Discussion

5.2.1 Coordination of 1-Adamantylazide

Addition of 1-adamantylazide to red-colored $[SiP^{iPr}_3]Fe(N_2)$ (**5.1**) produced dark-brown solutions from which the organoazide adduct $[SiP^{iPr}_3]Fe(\eta^1\text{-}N_3Ad)$ (**5.2**) was crystallized. A characteristic optical band for **5.2** appears at 679 nm (ε = 1100 M^{-1} cm^{-1}). The solution magnetic moment of **5.2** is μ_{eff} = 2.2 μ_B, consistent with an S = 1/2 ground state similar to **5.1** and in accord with its intense EPR signal with $g_{average}$ = 2.086.

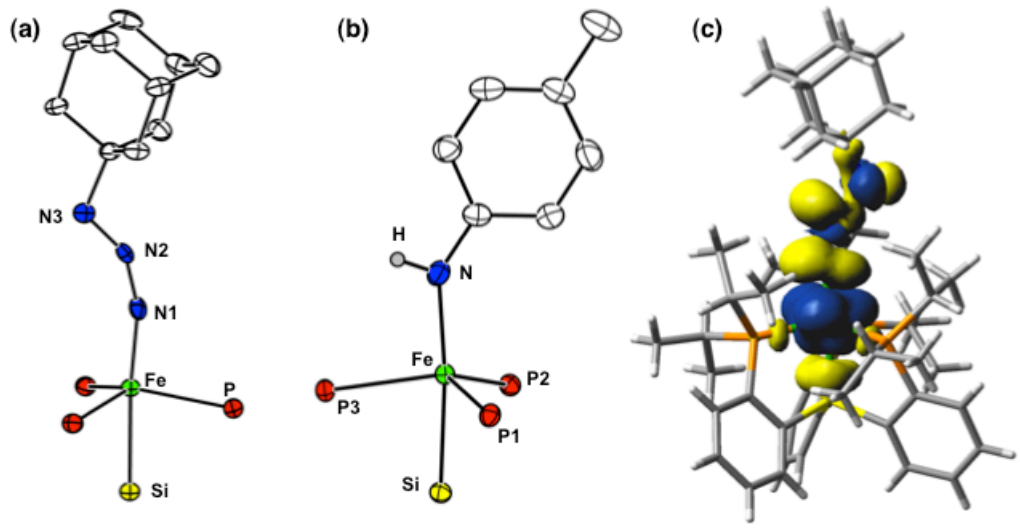

Figure 5.2. Core structures of (a) **5.2** and (b) **5.6** as 50% probability ellipsoids. The N-H hydrogen in **5.6** was located on the Fourier difference map and refined semifreely. (c) Spin density plot of **5.2** (0.002 isocontour). Selected bond lengths (Å) and angles (°) for **5.2**: Fe-N1, 1.769(5); N1-N2, 1.269(13); N2-N3, 1.25(3); Fe-N1-N2, 162(3); N1-N2-N3, 147(4); N2-N3-C, 111.5(15). For **5.6**: Fe-N, 1.963(2).

The solid-state structure of **5.2** (Figure 5.2a) is noteworthy because isolable metal-organoazide complexes are unknown for Fe and rare in general.[11] The η^1-N_γ binding exhibited in **5.2** is the most common binding mode represented in the literature.[11a-f] The diazenylimido(2-) resonance structure (M=N-N=NR) is descriptive of many of these complexes[11a-e] and results in bent N-N-N angles (114°-117°) and redshifted $\nu(N_3)$ IR bands. A recent copper(I) 1-adamantylazide complex,[11f] on the other hand, is best formulated as a redox-innocent $RN_3 \rightarrow M$ adduct and exhibits a linear N-N-N angle of 173.1(3)° and a blueshifted $\nu(N_3)$ IR band. Complex **5.2** has an N-N-N angle of 147(4)°, and its N_3 vibration occurs at an energy that is indistinguishable from free 1-

adamantylazide. Also noteworthy is the Fe-N distance in **5.2** (1.769(5) Å), which is significantly shorter than that of **5.1** (1.817(4) Å).[10] These data collectively indicate that the electronic structure of **5.2** lies somewhere between the above two limiting resonance structures. DFT calculations[12] are consistent with this hypothesis, as the calculated spin densities (molecular sum 1.00) on the P_3Fe and N_3 units are 1.81 and -0.77, respectively (Figure 5.2c). This electronic structure is distinct from metalloradical **5.1**, for which 92% of the calculated spin density resides on Fe.[12]

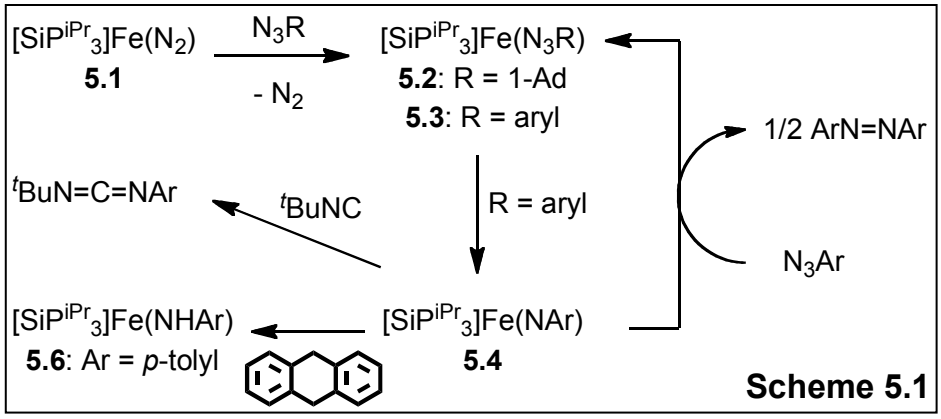

Scheme 5.1

5.2.2 Stoichiometric and Catalytic Aryl Azide Coupling

Stoichiometric reactions of **5.1** with aryl azides (N_3Ar) gave green-colored solutions that decayed gradually to yield red solutions containing **5.1** and the corresponding azoarene (ArN=NAr) products (Scheme 5.1). Complex **5.1** also was found to be a catalyst for this unusual N-N coupling reaction (Table 5.1). With 5% catalyst loading in C_6D_6 solutions at 70°C, various aryl azides (Ar = Ph, *p*-tolyl, *p*-C_6H_4OMe, Mes) were converted to the corresponding azoarenes in moderate yields (44%-57%). The only other spectroscopically detectable species were the corresponding anilines ($ArNH_2$) as minor by-products (8%-24%).[13] To our knowledge, the only previous example of

catalytic N-N coupling to yield diazenes from organoazides was reported as a side reaction during the catalytic amination of C-H bonds by Co porphyrins.[14] Thus, we became interested in understanding the mechanism of this unusual process.

Table 5.1. Results from the catalytic decomposition of aryl azides (N_3Ar) by catalyst **1**

Entry	Ar	Temp. (°C)	Solvent	Catalyst Loading (%)	Reaction Time (h)	Yield ArNNAr (%)	Yield $ArNH_2$ (%)
1	*p*-tolyl	23	Benzene	10	48	46	5
2	*p*-tolyl	45	Benzene	5	17	52	11
3	*p*-tolyl	70	Benzene	5	3	57	8
4	*p*-tolyl	70	Benzene	0	17	0	0
5	*p*-tolyl	70	C_7H_{14}	5	18[a]	25	< 2
6	*p*-tolyl	70	THF	5	18[a]	10	< 2
7	Ph	70	Benzene	5	18[a]	44	24
8	*p*-anisyl	70	Benzene	5	18[a]	50	16
9	Mes	70	Benzene	5	18[a]	50	22

[a] Separate *in situ* NMR experiments established that reaction times of <3 h were sufficient for these conditions.

The green intermediates observed during the reactions between **5.1** and aryl azides were assigned as the aryl azide complexes $[SiP^{iPr}_3]Fe(N_3Ar)$ (**5.3**, Ar = Ph, *p*-tolyl, *p*-C_6H_4OMe, Mes, 2,6-$Et_2C_6H_3$) on the basis of *in situ* spectroscopic characterization and comparison to stable organoazide complex **5.2**. Characteristic $\nu(N_3)$ IR bands were observed at energies deviating by ≤3 cm^{-1} from the corresponding free aryl azides, implying the presence of coordinated azide ligands. Complexes **5.3** are paramagnetic, and the *p*-tolyl derivative $[SiP^{iPr}_3]Fe(N_3Tol)$ (**5.3-Tol**, Tol = *p*-tolyl) exhibited an intense EPR

signal with $g_{average}$ = 2.106. Characteristic optical bands for **5.3** were evident at λ_{max} = 608 – 617 nm (ε = (est.) 1400 M^{-1} cm^{-1}) and ca. 775 nm (Table 5.2).

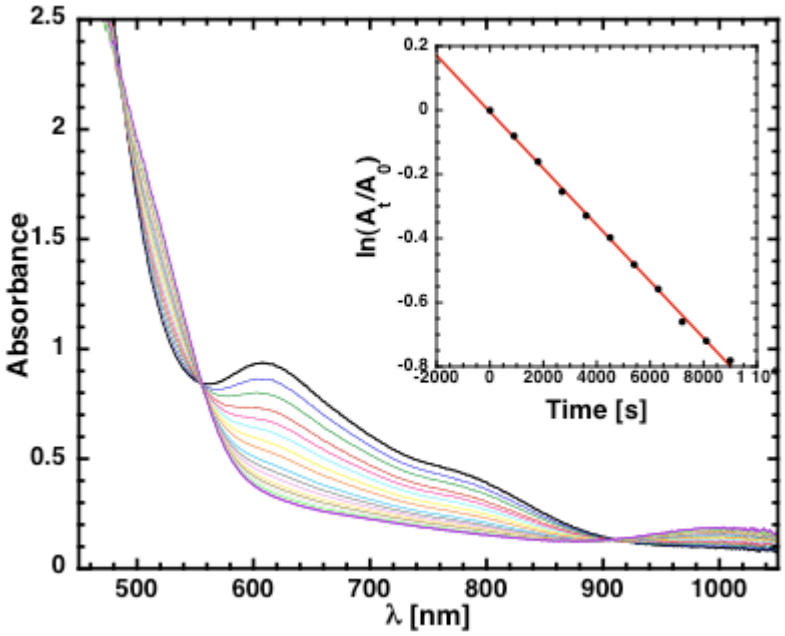

Figure 5.3. Changes in the UV-Vis spectrum during the decay of [SiP^{iPr}_3]Fe(N_3Ph) (*inset*: first-order plot of absorbance at 611 nm).

The decay profiles of **5.3** were followed by UV-vis spectroscopy at room temperature. In all cases studied, clean isosbestic behavior was observed (Figure 5.3), indicating that no intermediates were accumulating during the conversion of **5.3** to ArN=NAr and **5.1**. The decay of **5.3** was found to be clean and first order (Figure 5.3). The rate of decay of the aryl azide complexes was relatively insensitive to the identity of the aryl substituent, as the $t_{1/2}$ of the complexes spanned a relatively small range (1.2 – 3.2 h at 23°C) even as the electronics (Ar = Ph, *p*-tolyl, *p*-C_6H_4OMe) and sterics (Ar = Mes, 2,6-$Et_2C_6H_3$) were varied.

Table 5.2. λ_{max} and half-life data for [SiP$^{iPr}_3$]Fe(N_3R) at 23°C in C_6H_6 solution

R	λ_{max} (nm)	$t_{1/2}$ (h)
Ph	608	1.3
p-tolyl	614	1.8
p-C_6H_4OMe	617	3.2
Mes	609	1.2
2,6-$Et_2C_6H_3$	617	2.2
1-adamantyl	679	N/A

5.2.3 Experimental Evidence for N-N Coupling of Iron-Nitrene Intermediates

It is likely that complexes **5.3** decayed to yield reactive [SiP$^{iPr}_3$]Fe(NAr) intermediates (**5.4**) prior to N-N coupling, akin to first-order conversions of Cp_2Ta(Me)(N_3Ar) complexes to Cp_2Ta(Me)(NAr) studied by Bergman.[11a,b] Important to note is our recent isolation and structural characterization of the Ru analogues of **5.4**, [SiP$^{iPr}_3$]Ru(NAr).[15] Though the corresponding Fe complexes **5.4** are too reactive to permit isolation and thorough characterization, it appears that the *p*-tolyl derivative [SiP$^{iPr}_3$]Fe(NTol) (**5.4-Tol**) can be observed by EPR spectroscopy in a frozen glass. Photolysis of **5.3-Tol** in frozen 2-methyltetrahydofuran over 1 h at 77 K resulted in a color change from green to red-brown. The disappearance of the EPR signal for **5.3-Tol** (Figure 5.4b) was accompanied by the appearance of a new EPR signal (Figure 5.4c) that we presume to correspond to **5.4-Tol**. A simulation of this signal was obtained with the parameters (g_x, g_y, g_z) = (1.990, 2.032, 2.098) and (A^P_x, A^P_y, A^P_z) = (55, 40, 50 MHz) (Figure 5.4d), suggesting that imido complex **5.4-Tol** possesses an S = 1/2 ground state.

Intermediate **5.4-Tol** rapidly converted to **5.1** upon thawing of the glass, as judged by EPR spectroscopy (Figure 5.4e).

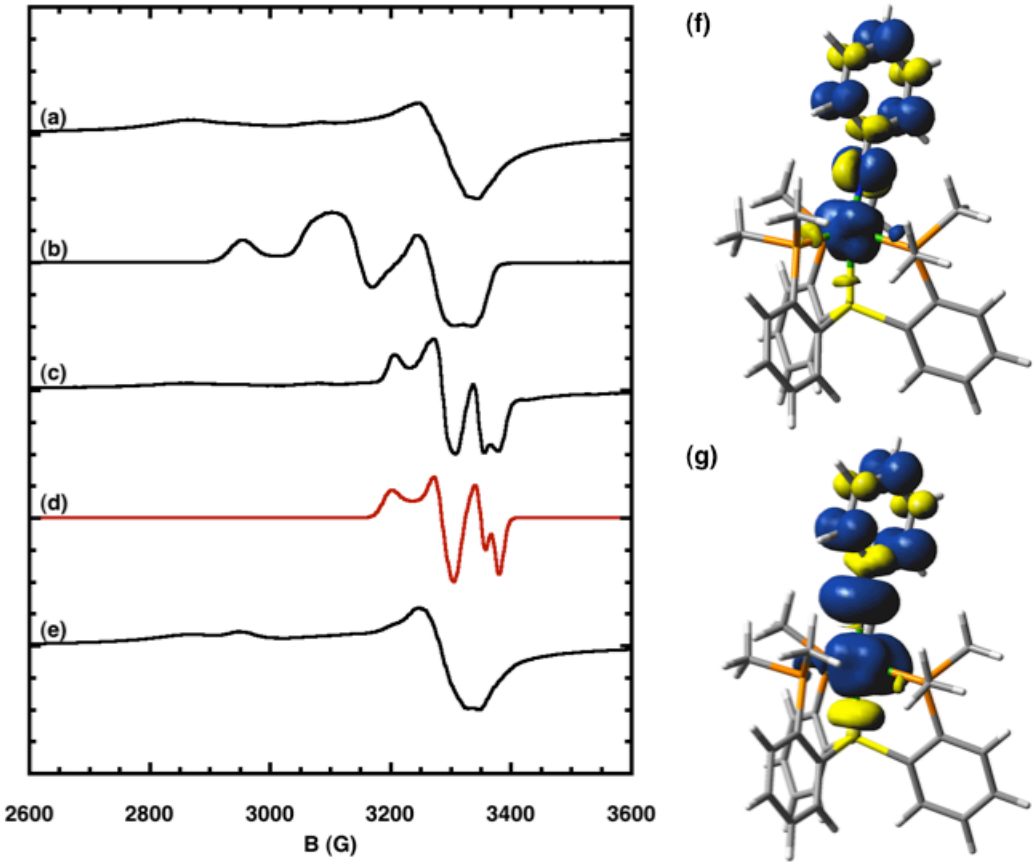

Figure 5.4. X-band EPR spectra (77 K, 2-methyltetrahydrofuran) of (a) **5.1**, (b) **5.3-Tol**, (c) **5.4-Tol** produced by photolysis of a frozen glass of **5.3-Tol**, (d) simulated spectrum of **5.4-Tol**, and (e) **5.1** produced upon warming and re-freezing **5.4-Tol**. Spin density plots (0.002 isocontours) of (f) **5.7-LS** and (g) **5.7-IS**.[12]

Two chemical transformations further support the existence of the proposed FeNAr intermediates (Scheme 5.1). First, when **5.3-Tol** was generated in the presence of ^{t}BuNC, the resulting product mixture contained TolN=NTol, **5.1**, ^{t}BuN=C=NTol, and

[SiP^{iPr}_3]Fe(CN^{t}Bu) (**5.5**). Stoichiometric[16] and catalytic[17] reactions with isocyanides to yield carbodiimide products are diagnostic of isolable FeNR species. Second, when **5.3-Tol** was generated in the presence of 9,10-dihydroanthracene (DHA), the resulting product mixture contained a new paramagnetic product (**5.6**), identified crystallographically (Figure 5.1b) as [SiP^{iPr}_3]Fe(NHTol) after independent synthesis from [SiP^{iPr}_3]Fe(OTf) and LiNHTol. For comparison, adamantylazide adduct **5.2**, which does not decay at a measureable rate under analogous conditions, was found to be unreactive towards DHA and underwent ligand substitution with ^{t}BuNC to yield **5.5** and free N_3Ad.

Careful analysis of product distributions in these trapping experiments proved informative with regard to the mechanism of N-N bond formation. The ratio of azotoluene to anthracene decreased linearly when decreasing the concentration of **5.1** while holding the concentrations of N_3Tol and DHA constant (Table 5.3). If one assumes that only one Fe center is involved in the hydrogen atom transfer (HAT) reaction with DHA, this result implyies the involvement of two Fe centers in the N-N bond-forming step. On the other hand, the azotoluene:anthracene ratio was insensitive to varying the concentration of N_3Tol while holding the concentrations of **5.1** and DHA constant (Table 5.3). Though mechanisms involving the reactions of metal-imido species with excess organoazides have been discovered for stoichiometric generation of diazenes,[18] we propose for the present system that the mechanism most consistent with these product distributions is the bimolecular coupling of Fe-nitrene species **5.4**. Stoichiometric imido-imido coupling has been observed recently.[19]

Table 5.3. Product distributions as a function of reagent concentration

Entry	[Fe] (mM)	[$TolN_3$] (mM)	[DHA] (mM)	Product ratio (TolN=NTol/anthracene)
1	13.7	13.7	11	2.5
2	13.7	13.7	25	1.2
3	13.7	13.7	68.8	0.8
4	20.0	20.0	10	4.2
5	9.0	20.0	10	2.6
6	4.2	20.0	10	1.6
7	20.0	25.0	10	4.1
8	20.0	20.0	10	4.6
9	20.0	6.7	10	4.2
10	10.6	10.7	5.2	3.1
11	10.6	7.1	5.2	3.1
12	10.6	3.6	5.2	2.6

5.2.4 DFT Studies of a Hypothetical Trigonal Bipyramidal Iron-Imido

This finding is significant not only in the context of catalytic nitrene transfer reactions, but also because nitrene-nitrene coupling is related conceptually to oxo-oxo coupling, which may be relevant to O-O bond forming processes for some water splitting catalysts.[20] It has been suggested that oxygen-centered radical character is crucial for such reactions to proceed.[20] We hence chose to examine the model complex [SiP^{Me}_3]Fe(NPh) (**5.7**) by DFT methods[12] to explore the degree of spin character carried by the NPh moeity.

The low spin, $S = 1/2$ state (**5.7-LS**) was calculated to be the ground state of **5.7**, consistent with the EPR spectroscopy of **5.4-Tol** and the observed ground state of

$[SiP^{iPr}_3]Ru[N(p\text{-}C_6H_4CF_3)]$.[15] The optimized geometry of **5.7-LS** falls intermediate between TBP and square pyramidal ($\tau = 0.49$)[21] and is similar to the crystallographically determined structure of $[SiP^{iPr}_3]Ru[N(p\text{-}C_6H_4CF_3)]$ ($\tau = 0.54$). The optimized Fe-N distance in **5.7-LS** (1.703 Å) is much shorter than that of anilido complex **5.6** (1.963(2) Å). Structurally characterized Fe-NR bond distances range from 1.61-1.66 Å for tetrahedral systems[3,4] to 1.70-1.72 Å for distorted square planar systems.[5] Low-spin $[SiP^{iPr}_3]Ru[N(p\text{-}C_6H_4CF_3)]$ has experimental and computational characteristics implying significant radical delocalization through the RuNAr π-system.[15] Such delocalization is less obvious for **5.7-LS** (Figure 5.4f, Table 5.4), which has calculated spin densities (molecular sum 1.00) on the Fe center and NPh unit of 0.89 and 0.16, respectively, with very little spin density on the N atom itself (0.01). Noteworthy, however, are the short N-C (1.341 Å) and alternating C-C bond lengths in the calculated NPh unit of **7-LS** that suggest a significant quinoidal resonance contributor (see Figure 5.17).

Table 5.4. Mülliken spin densities of complexes **5.7-LS** and **5.7-IS**

Atom(s)	Spin density, 5.7-LS	Spin density, 5.7-IS
Fe	0.89	2.00
N	0.01	0.82
C,H (Ph)	0.15	0.15
P	-0.07	0.04
Si	-0.06	-0.18
C,H (SiP^{Me}_3)	0.08	0.17
total	1.00	3.00

Interestingly, the intermediate spin, S = 3/2 state (**5.7-IS**) of **5.7** was higher in energy than **5.7-LS** by only 2.8 kcal/mol. The calculated spin densities for **5.7-IS** (molecular sum 3.00) on the Fe, N, and Ph units are 2.00 and 0.82, and 0.15 (Table 5.4), respectively, indicating some radical character for the imido ligand (Figure 5.4g). Considering the likelihood that, based on our DFT studies of **5.7**, the [SiP$^{iPr}_3$]Fe(NAr) intermediates **5.4** also possess low-lying excited states, the possibility of two-state reactivity[22] for **5.4** could account for the strikingly rich redox chemistry that enables 1-electron (HAT), 2-electron (nitrene transfer), and 4-electron (bimolecular coupling) redox processes and merits further study.

5.3 Experimental Section

5.3.1 General Considerations

All manipulations were carried out using standard Schlenk or glovebox techniques under a N_2 atmosphere unless otherwise indicated. Unless otherwise noted, solvents were deoxygenated and dried by thoroughly sparging with Ar gas followed by passage through an activated alumina column in the solvent purification system by SG Water, USA LLC. Non-halogenated solvents were tested with a standard purple solution of sodium benzophenone ketyl in tetrahydrofuran in order to confirm effective oxygen and moisture removal. [SiP$^{iPr}_3$]Fe(N_2) (**5.1**) was prepared according to literature procedures.[10] LiNHTol was prepared from NH_2Tol and *n*BuLi in *n*-pentane. All aryl azides were prepared according to literature procedures.[23] All azoarene and carbodiimide products were synthesized independently by literature methods to compare

characterization data.[24,25] All other reagents were purchased from commercial vendors and used without further purification. Elemental analyses were performed by Midwest Microlab, LLC, Indianapolis, IN. Deuterated solvents were purchased from Cambridge Isotope Laboratories (Cambridge, MA), degassed, and dried over activated 3 Å molecular sieves prior to use. Photolysis was conducted with a Blak-Ray long-wave UV, medium skirted Hg spot lamp (100 W).

5.3.2 X-ray Crystallography Procedures

Low-temperature diffraction data were collected on a Siemens Platform three-circle diffractometer coupled to a Bruker-AXS Smart Apex CCD detector with graphite-monochromated Mo Kα radiation (λ = 0.71073 Å), performing ϕ-and ω-scans. The structures were solved by direct methods using SHELXS[26] and refined against F^2 on all data by full-matrix least squares with SHELXL-97[27] using established methods.[28] All non-hydrogen atoms were refined anisotropically. All hydrogen atoms (except the hydrogen on nitrogen atom N in the structure of **5.6**, which was taken from the difference Fourier synthesis and refined semifreely with the help of distance restraints) were included into the model at geometrically calculated positions and refined using a riding model. The isotropic displacement parameters of all hydrogen atoms were fixed to 1.2 times the *U* value of the atoms they are linked to (1.5 times for methyl groups). Details of the data quality and a summary of the residual values of the refinements are listed in Appendix 4.

Compound **5.6** crystallizes in the orthorhombic space group $P2_12_12_1$ with one molecule per asymmetric unit. Structure solution and refinement were straightforward

and routine. Compound **5.2** crystallizes in the rhombohedral space group *R*-3*c* (hexagonal setting) with one-third of **5.2** plus one-half of an *n*-pentane molecule per asymmetric unit. Only parts of the molecule of **5.2** show threefold symmetry, which results in a threefold disorder of the 1-adamantylazide moiety about the crystallographic threefold axis. The half solvent molecule is disordered over four positions involving a crystallographic twofold axis; hence only two of the four positions are crystallographically independent, corresponding to one half pentane molecule in the asymmetric unit. The ratio between the two independent components of the solvent disorder was refined freely and converged at 0.710(8). Similarity restraints on 1-2 and 1-3 distances and displacement parameters as well as rigid bond restraints for anisotropic displacement parameters were applied to all atoms of the solvent molecule and also of the adamantly moiety. The fact that the asymmetric unit contains one third of **5.2** but one half pentane molecule results in a non-integer number for the element C in the empirical formula.

5.3.3 Spectroscopic Measurements

Varian Mercury-300 and Inova-500 spectrometers were used to record ^{1}H, ^{19}F, and ^{31}P NMR spectra at ambient temperature unless otherwise indicated. ^{1}H chemical shifts were referenced to the residual solvent peaks. ^{19}F chemical shifts were referenced to external hexafluorobenzene (δ = –165 ppm). ^{31}P chemical shifts were referenced to external phosphoric acid (δ = 0 ppm). Solution magnetic moments were determined by the method of Evans.[29,30] Optical spectroscopy measurements were taken on a Cary 50 UV-Vis spectrophotometer using either a 1 cm or 2 mm two-window quartz cell sealed

with a standard closed cap purchased from Starna Cells, Inc. Infrared spectra were recorded on a BioRad FTS 3000 EXCALIBUR series FT-IR spectrometer. An Agilent 5973N Gas Chromatograph/Mass Spectrometer was used for GC-MS analysis. X-band EPR measurements were recorded using a Brüker EMX spectrometer at 77 K in 2-methyltetrahydrofuran glasses. EPR samples were prepared in a glovebox under N_2 in quartz EPR tubes equipped with J. Young caps. X-band microwave frequencies: [SiP$^{iPr}_3$]Fe(N_2), ν = 9.3368 GHz; [SiP$^{iPr}_3$]Fe(η^1-N_3Ad), ν = 9.3367 GHz; [SiP$^{iPr}_3$]Fe(N_3Tol), ν = 9.3379 GHz, [SiP$^{iPr}_3$]Fe(NTol), ν = 9.3764 GHz. EPR spectra were simulated using the W95EPR program.[31]

5.3.4 Synthetic Procedures

Synthesis of [SiP$^{iPr}_3$]Fe(η^1-N_3Ad) (5.2). A solution of 1-adamantylazide (31.6 mg, 0.178 mmol) in benzene (3 mL) was added to solid **5.1** (78.0 mg, 0.113 mmol), resulting in effervescence and a darkening of the solution. The brown solution was stirred for 6 days, and then volatiles were removed *in vacuo*. *n*-Pentane (1 mL) was added, and the resulting brown insoluble material was collected on a sintered glass frit and washed with additional *n*-pentane (2 x 1 mL). The solids were then lyophilized from benzene to give **5.2** as a brown powder (54.3 mg, 57%). X-ray quality crystals were grown by diffusion of hexamethyldisiloxane vapors into a pentane solution of **5.2**. In the absence of excess 1-adamantylazide, a trace equilibrium amount of **5.1** was consistently evident by ^{1}H NMR spectroscopy. Therefore, combustion analysis was not obtained. ^{1}H NMR (C_6D_6, δ): 11.4, 7.3, 7.0, 6.8, 3.9, 2.0, 1.8-1.0 (multiple overlapping peaks), 0.4, 0.3, -6.6. IR (KBr pellet, cm^{-1}): 2086 (ν_{N3}). μ_{eff} (C_6D_6, room temp): 2.2 μ_B. UV-Vis (C_6H_6,

nm($M^{-1}cm^{-1}$)): 298(37000), 406(11000), 679(1100).

Synthesis of [SiP$^{iPr}_3$]Fe(CN^{t}Bu) (5.5). Addition of *tert*-butylisocyanide (2.03 μL, 0.0179 mmol) to a solution of **5.1** (12.4 mg, 0.0179 mmol) in benzene-d_6 (~0.7 mL) provided **5.5** *in situ* after stirring for 18 h. In the absence of excess isocyanide, complex **5.1** was consistently a minor impurity in the product mixtures. Moreover, prolonged exposure of these solutions to vacuum caused the majority of the material to revert to **5.1** upon reexposure to an N_2 atmosphere, as judged by ^{1}H NMR. Therefore, complex **5.5** was not isolated in pure form; characterization data for **5.5** generated *in situ* is provided here and match the data obtained from the competitive trapping experiments (*vide infra*). ^{1}H NMR (C_6D_6, δ): 10.3, 6.8, 4.9, 4.3, 1.6, 0.9. IR (C_6D_6 solution, cm^{-1}): 1977 (ν_{CN}).

Synthesis of [SiP$^{iPr}_3$]Fe(OTf). Complex **5.1** (0.565 g, 0.817 mmol) was dissolved in THF (10 mL) and frozen in a cold well bathed in liquid N_2. Silver triflate (0.211 g, 0.821 mmol) was dissolved in THF (5 mL) and likewise frozen. As the silver triflate solution thawed, it was added dropwise to the still-frozen solution of **5.1**. The entire mixture was then allowed to thaw and warm to room temperature, resulting in a darkening of the solution and precipitation of black solids. After stirring at room temperature for 2 h, the mixture was filtered through Celite and evaporated to dryness. A toluene/*n*-pentane mixture (1:1, 10 mL) was added, the resulting solution was filtered once again, and the dark orange filtrate was placed in a -35°C freezer overnight, resulting in light orange crystals of [SiP$^{iPr}_3$]Fe(OTf) (0.397 g, 60%). ^{1}H NMR (C_6D_6, δ): 31.7, 6.8, 6.6, 5.4, 1.8, 1.0, -0.4, -4.8. ^{19}F NMR (C_6D_6, δ): -55.6 (br). IR (KBr pellet, cm^{-1}): 3039, 2956, 2922, 2870, 1496, 1424, 1383, 1367, 1315, 1226, 1207, 1174, 1106, 1019. μ_{eff} (C_6D_6, room temp): 2.8 μ_B. UV-Vis (C_6H_6, nm($M^{-1}cm^{-1}$)): 367(4700), 427(5400),

486(6900). Anal. Calcd for $C_{37}H_{54}F_3FeO_3P_3SSi \cdot C_7H_8$ ([SiP$^{iPr}_3$]Fe(OTf)·toluene): C, 58.40; H, 6.91. Found: 58.49, 6.68.

Synthesis of [SiP$^{iPr}_3$]Fe(NHTol) (5.6). A thawing solution of LiNHTol (21.5 mg, 0.190 mmol) in THF (1 mL) was added to a frozen solution of [SiP$^{iPr}_3$]Fe(OTf) (0.149 g, 0.183 mmol). The mixture was allowed to warm to room temperature gradually, resulting a color change to an intense cherry red. After stirring for 18 h at room temperature, volatiles were removed *in vacuo*. *n*-Pentane (10 mL) was added, and the resulting solution was filtered. The cherry-red filtrate was concentrated *in vacuo* to red solids (93.3 mg, 66%). ^{1}H NMR of this material indicates that the product contains **5.1** and NH_2Tol as minor impurities. Recrystallization from *n*-pentane (-35°C or by slow evaporation) gave red crystals of co-crystallized **5.6** and **5.1**, and these complexes could not be separated in our hands by repeated crystallization. X-ray quality crystals were grown by diffusion of hexamethyldisiloxane vapors into a pentane solution of crude **5.6**, and a crystal of **5.6** rather than **5.1** was selected based upon color. Crude characterization with only spectral data attributed to **5.6** is presented here. ^{1}H NMR (C_6D_6, δ): 87, 38, 5.6, -0.6, -1.5, -2.7. IR (C_6H_6 solution, cm^{-1}): 3380 (ν_{NH}).

5.3.5 Catalytic Conversion of Aryl Azides to Azoarenes

General procedure. Catalyst **5.1** was dissolved in a solvent (approx 1 mL) in a resealable Schlenk tube equipped with a stirbar. The aryl azide and an internal integration standard (mesitylene) were added, and the resulting solution was sealed and stirred as indicated in Table 5.1. The solution color progressed from red to brown to green to brown to red, at which point the reaction was complete as judged by full consumption of

starting azide based on separate *in situ* NMR experiments. Yields of azoarene and aniline were determined by ^{1}H NMR analysis (integration against the internal standard). IR spectroscopy of the solutions confirmed the presence of **5.1**. Filtration through silica gel under air followed by analysis by GC-MS confirmed the product assignments. ^{1}H NMR and GC-MS characterization of the azoarene products were reproduced with authentic samples prepared by literature methods.[24] A representative NMR spectrum is shown in Figure 5.5. Tabulated results are presented in Table 5.1.

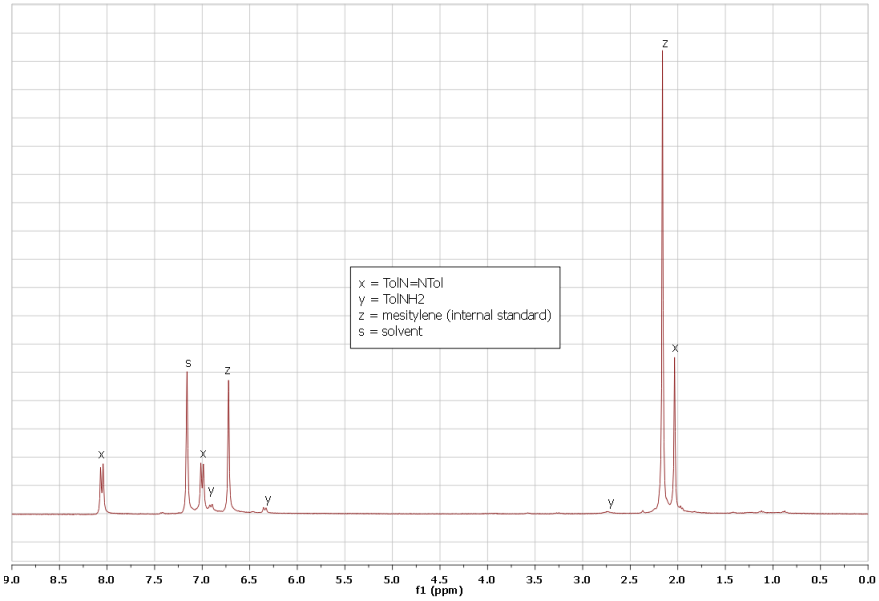

Figure 5.5. ^{1}H NMR spectrum from the catalytic decomposition of N_3Tol by catalyst **5.1**.

5.3.6 IR Data for [SiP$^{iPr}_3$]Fe(N_3Ar)

General procedure. [SiP$^{iPr}_3$]Fe(N_2) was dissolved in benzene, and an aryl azide (1 equiv) was added. Periodically, aliquots were transferred to a solution IR cell and analyzed by IR spectroscopy. Representative spectra are presented in Figure 5.6. In all

cases, the difference between free and coordinated azide was found to be $\Delta\nu(N_3) \leq 2$ cm^{-1} (see Table 5.5).

Table 5.5. IR data for various [SiP$^{iPr}_3$]Fe(N_3Ar) derivatives in benzene solution

Ar	$\nu(N_3)$ (cm^{-1})	$\nu(N_3)$ (cm^{-1}) (free azide)
Ph	2127	2127
p-tolyl	2105	2103
p-C_6H_4OMe	2104	2104
Mes	2120	2119
2,6-$Et_2C_6H_3$	2098	2098

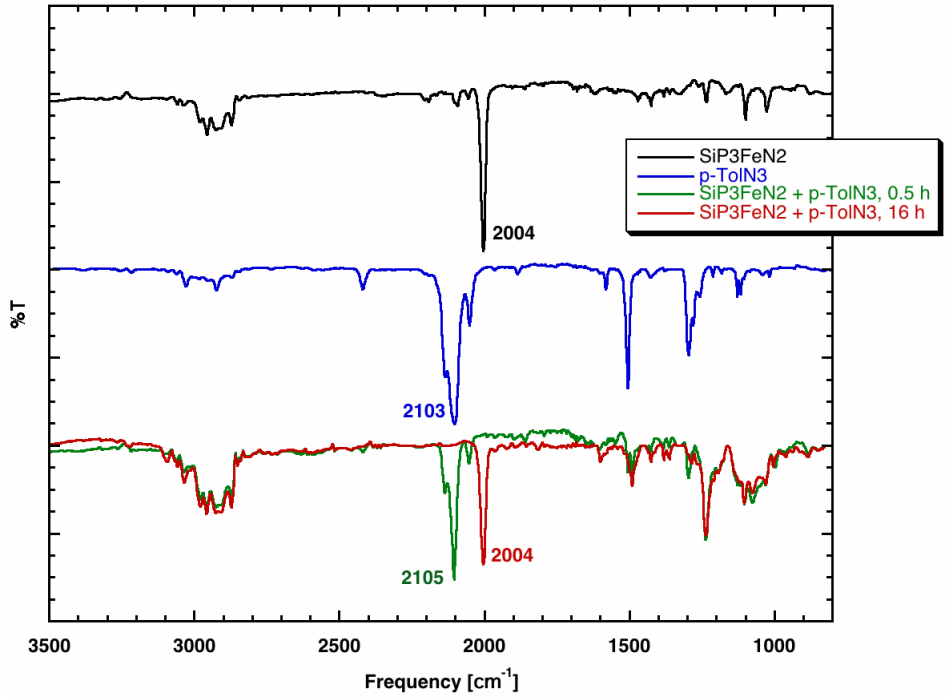

Figure 5.6. IR spectra (benzene solutions) of **5.1**, TolN_3, and initial and final time points for the reaction between **5.1** and TolN_3.

5.3.7 UV-Vis Spectroscopy and Kinetics

General procedures. All UV-Vis spectra were recorded in benzene solution. Figure 5.7 shows spectra for the various [SiP$^{iPr}_3$]Fe(N$_3$Ar) derivatives as well as complexes **5.1** and **5.2** recorded at arbitrary concentrations in a 1 cm path length cell.

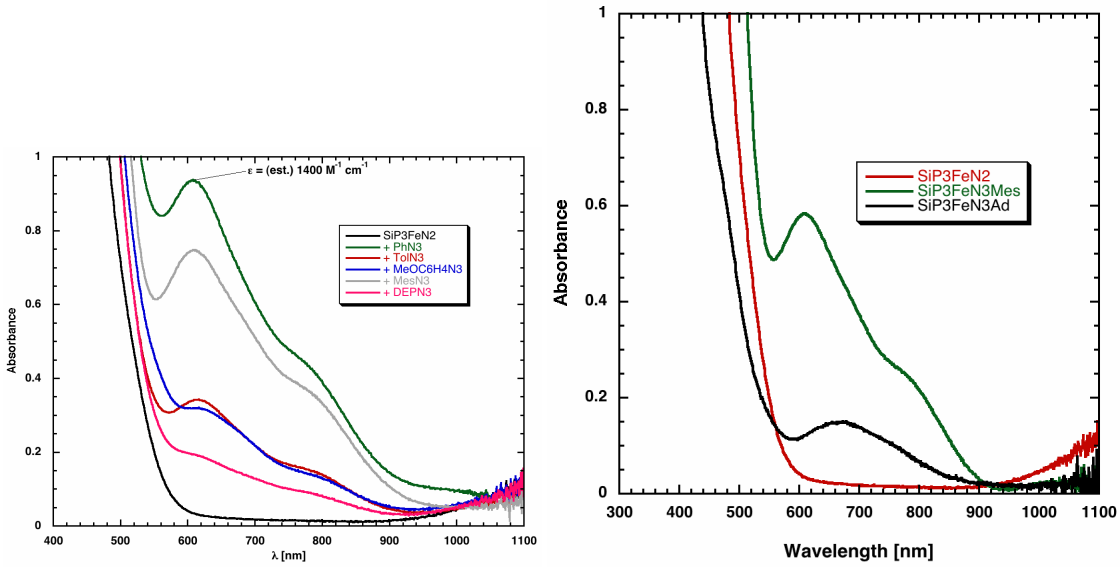

Figure 5.7. (*left*) UV-Vis spectra of various [SiP$^{iPr}_3$]Fe(N$_3$Ar) derivatives at arbitrary concentrations in benzene solutions. (*right*) Overlaid UV-Vis spectra of [SiP$^{iPr}_3$]Fe(N$_2$) (**5.1**), [SiP$^{iPr}_3$]Fe(η^1-N$_3$Ad) (**5.2**), and [SiP$^{iPr}_3$]Fe(N$_3$Mes).

UV-Vis Kinetics. The decay rates of the various [SiP$^{iPr}_3$]Fe(N$_3$Ar) species were monitored at room temperature in 2 mm path length cells. In each experiment, a stock solution of complex **5.1** (3.3 mM) was loaded into the cell, and then 1 equiv of the aryl azide was added. Data points were taken every 15 min. Over the earliest data points, the peaks corresponding to the green intermediate species (see Figure 5.7) were observed to be growing in. During the many subsequent data points, these peaks proceeded to decay.

The kinetic analysis of the disappearance of the green intermediates was based on the latter set of points. An example of this decaying absorbance is shown in Figure 5.2. Isosbestic points are evident in Figure 5.2 and were evident in for all aryl groups canvassed. Plots of $\ln(A_t/A_0)$ versus time revealed linear relationships ($R > 0.99$) in all cases, indicating first order processes. An example of such a plot is shown in Figure 5.2. The first-order rate constants were extracted from the slopes of these linear plots, and the half-lives tabulated in Table 5.2 are based upon those rate constants. The linearities and slopes of the lines were independent of wavelength, and the half-lives in Table 5.2 are based upon decay at the λ_{max} of each species that is near 610 nm (Table 5.2).

5.3.8 EPR Spectroscopy.

General procedures. EPR spectra were recorded in 2-methyltetrahydrofuran glasses (~5-10 mM) at 77 K. In the cases of **5.1** and **5.2**, isolated material was utilized to record the spectra. In the case of $[SiP^{iPr}_3]Fe(N_3Tol)$, complex **5.1** was incubated with N_3Tol in 2-methyltetrahydrofuran for 0.5 h prior to freezing. Optical spectroscopy was used to determine that this was the optimal amount of time to maximize concentration of **5.3-Tol** and minimize the concentration of residual **1**. Figures 5.8 – 5.11 present EPR data and fits, and Table 5.6 summarizes the resulting EPR parameters.

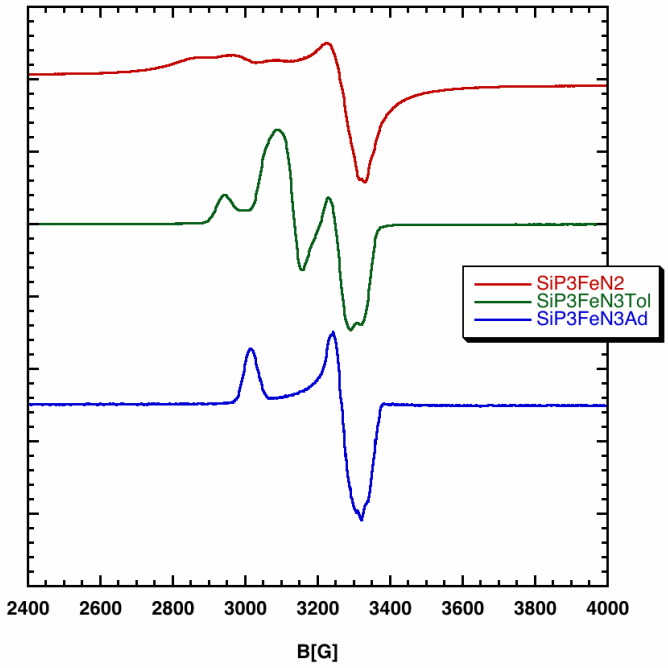

Figure 5.8. X-band EPR spectra (2-methyltetrahydrofuran glass, 77 K) of isolated **1** and **2**, as well as [SiP$^{iPr}_3$]Fe(N_3Tol) generated *in situ*.

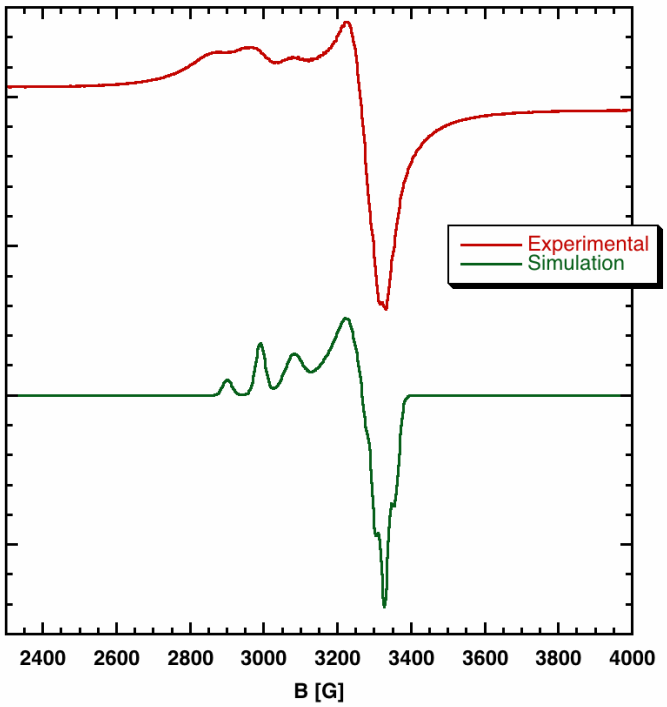

Figure 5.9. Experimental (red) and simulated (green) EPR spectra for complex **1**.

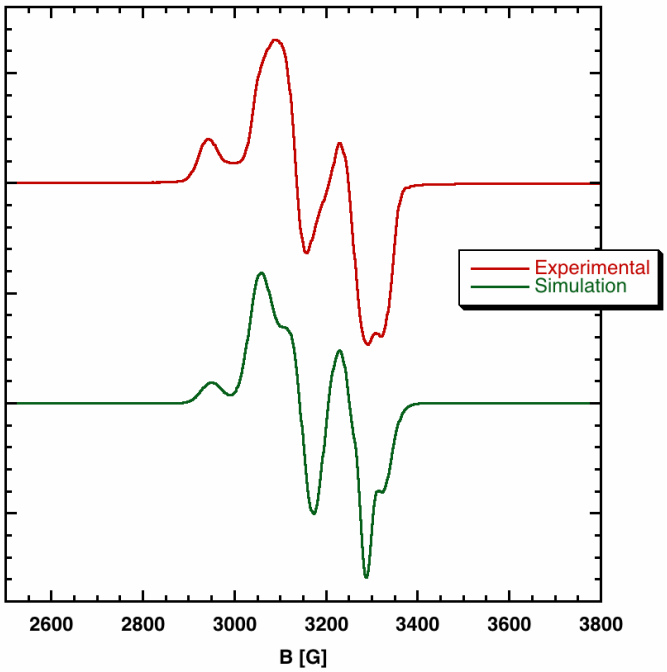

Figure 5.10. Experimental (red) and simulated (green) EPR spectra for *in situ* generated [SiP^{iPr}_3]Fe(N_3Tol).

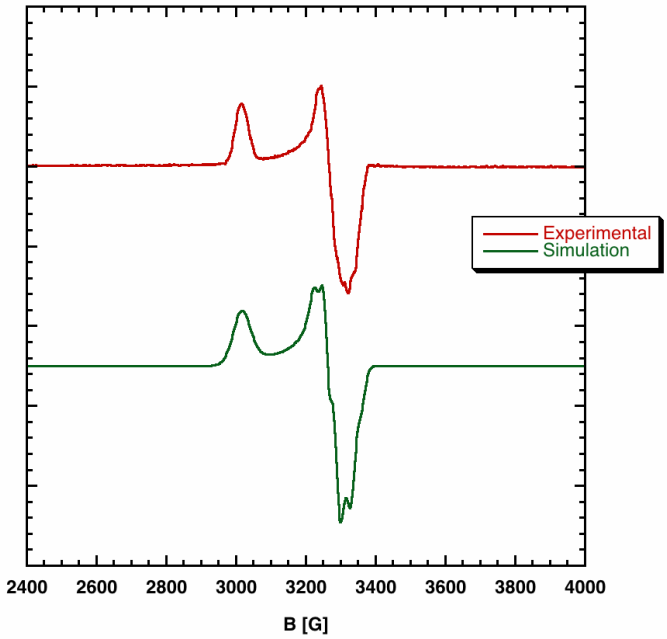

Figure 5.11. Experimental (red) and simulated (green) EPR spectra for complex **2**.

Observation of the EPR spectrum for [SiP$^{iPr}_3$]Fe(NTol). Complex **5.1** (15.6 mg, 0.0226 mmol) was dissolved in 2-methyltetrahydrofuran (1.00 mL) and split into two equal solutions (A and B). To solution A was added *p*-tolylazide (1.27 μL, 0.0113 mmol). After 1 h the resulting deep green Solution A as well as Solution B were diluted to 7.5 mM and frozen into a glasses at 77 K in EPR tubes equipped with a J. Young cap. Both samples were photolyzed while constantly bathed in liquid nitrogen. Solution A changed from green to brown over the first 1 h, at which point the spectra shown in Figure 5.3 were collected. Solution B was treated as a control and exhibited a clean EPR spectrum corresponding to **5.1** that did not change upon prolonged photolysis side by side with Solution A. After photolyzing the solutions for 2 h, the solutions were allowed to stand at room temperature for 5 min before being frozen in liquid nitrogen once again. EPR spectra of both samples displayed complex **5.1** at this point. Simulation parameters are listed in Table 5.6. A separate control was run with 7.5 mM N_3Tol and no Fe complex in solution. A weak signal similar to that previously reported for the free NTol nitrene[32] was observed in this case and did not align with the spectrum shown in Figure 5.3.

Table 5.6. EPR parameters implied from computer simulations of spectra

Complex	g_x	g_y	g_z	A_x (MHz)[a]	A_y (MHz)[a]	A_z (MHz)[a]
[SiP$^{iPr}_3$]Fe(N_2)	2.013	2.041	2.196	6.0	3.7	25.4
[SiP$^{iPr}_3$]Fe(η^1-N_3Ad)	2.013	2.036	2.210	6.7	6.5	0
[SiP$^{iPr}_3$]Fe(N_3Tol)	2.041	2.130	2.146	6.9	4.0	28.9
[SiP$^{iPr}_3$]Fe(NTol)	1.990	2.032	2.087	55.0	40.0	50.0

[a] *A* values correspond to hyperfine splitting from 3 equivalent I = 1/2 (i.e., phosphorus) nuclei, except in the case of [SiP$^{iPr}_3$]FeNTol, where only 1 P nucleus was included.

5.3.9 Competitive Trapping Experiments

Reactions with *tert*-butylisocyanide. To solutions of **5.1** in C_6D_6 was added 1 equiv each of N_3Tol and ^{t}BuNC, resulting in a dark-brown color. After stirring for 2 days at room temperature, the solutions had become red colored. Analysis by ^{1}H NMR revealed the presence of the following products: TolN=NTol, ^{t}BuN=C=NTol, **5.1**, and **5.5**. The presence of **5.1** and **5.5** was also confirmed by IR spectroscopy of the solution. Characterization data for **5.5** matched that of a sample prepared independently from **5.1** and ^{t}BuNC (*vide supra*). The ratio of azotoluene to carbodiimide was typically approximately 2:1. Under air, the solutions were filtered through silica gel and analyzed by GC-MS, confirming the presence of TolN=NTol and ^{t}BuN=C=NTol. The characterization data for ^{t}BuN=C=NTol matched that of authentic samples prepared by literature methods.[25]

Reactions with 9,10-dihydroanthracene. In a typical experiment, a C_6D_6 solution containing **5.1** and N_3Tol (1:1) was added to 0.5 equiv of 9,10-dihydroanthracene. After stirring for 18 h, the red solution was analyzed by ^{1}H NMR. Two paramagnetic products were evident: **5.1** and **5.6**. ^{1}H NMR data for **5.6** matched that of material synthesized independently from [SiP$^{iPr}_3$]Fe(OTf) and LiNHTol (*vide supra*). Three diamagnetic products were also evident (in addition to unreacted 9,10-dihydroanthracene): TolN=NTol, NH_2Tol, and anthracene. Under air, the solution was filtered through silica gel and analyzed by GC-MS, confirming the assignments of the diamagnetic components.

For utilization of GC-MS for quantitative measurements, calibration curves were made over the range 0-50 ppm with triphenylamine as an internal standard. These

calibration curves are shown in Figure 5.14.

Table 5.3 was constructed as follows. For Entries 1-3, a freshly prepared stock solution of **5.1** and N_3Tol was immediately added to various amounts of 9,10-dihydroanthracene. For Entries 4-6, a freshly prepared stock solution of N_3Tol and 9,10-dihydroanthracene was added to varying amounts of **5.1**. For Entries 7-9, a freshly prepared stock solution of **5.1** and 9,10-dihydroanthracene was split into three equal parts, and various amounts of N_3Tol were added to each one. (*Note*: Control experiments established that under analogous reaction conditions, no reactions are observed between 9,10-dihydroanthracene and either **5.1** or N_3Tol individually, and so the order of addition is not important.) For all Entries 1-9, the solutions were stirred for 18 h prior to opening them to the air, filtering them through silica gel, and analyzing them by GC-MS. A sample GC trace is shown in Figure 5.15. Concentrations of 9,10-dihydroanthracene, azotoluene, and anthracene were quantitated using the Agilent data analysis software and the calibration curves described above. Table 5.3 summarizes the results, and Figure 5.16 plots the azotoluene/anthracene ratio against Fe concentration, implying that two Fe centers are involved in the N-N bond-forming step.

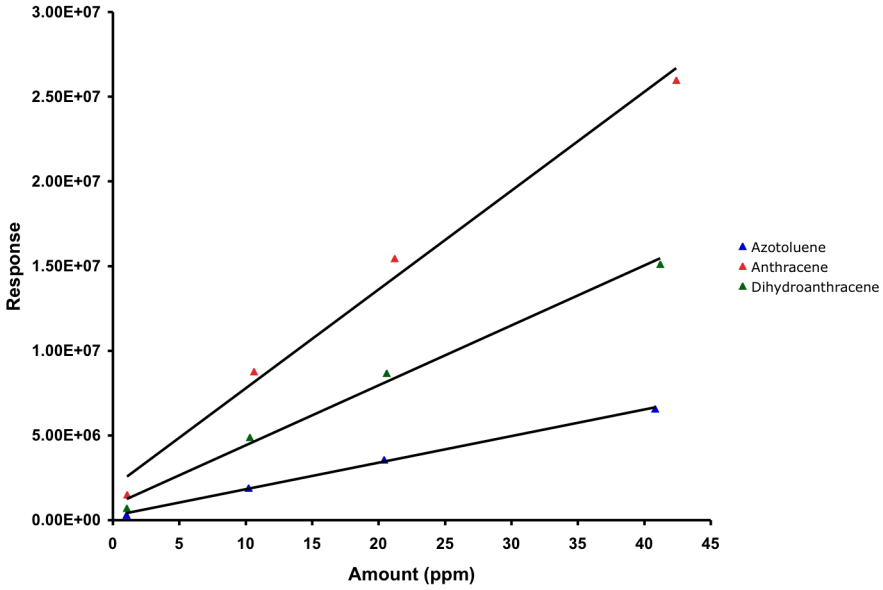

Figure 5.12. GC-MS calibration curves for azotoluene, anthracene, and 9,10-dihydroanthracene using triphenylamine as an internal standard.

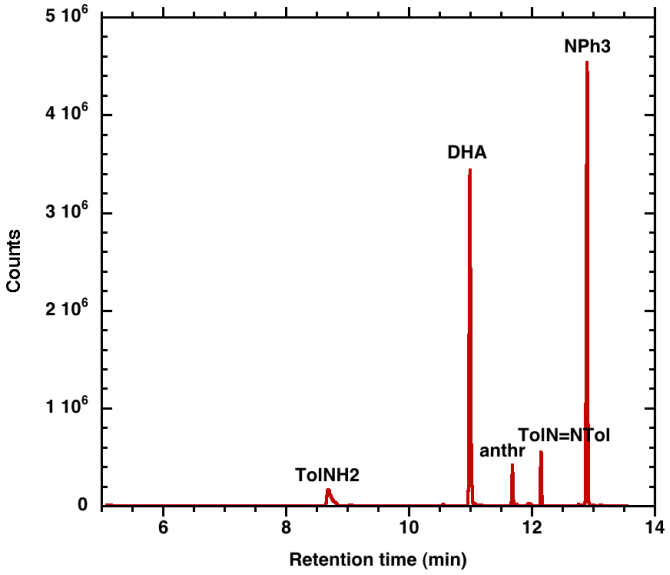

Figure 5.13. Sample GC trace (in this case from Table 5.3, Entry 4) showing the compounds quantitated and the internal standard (NPh_3).

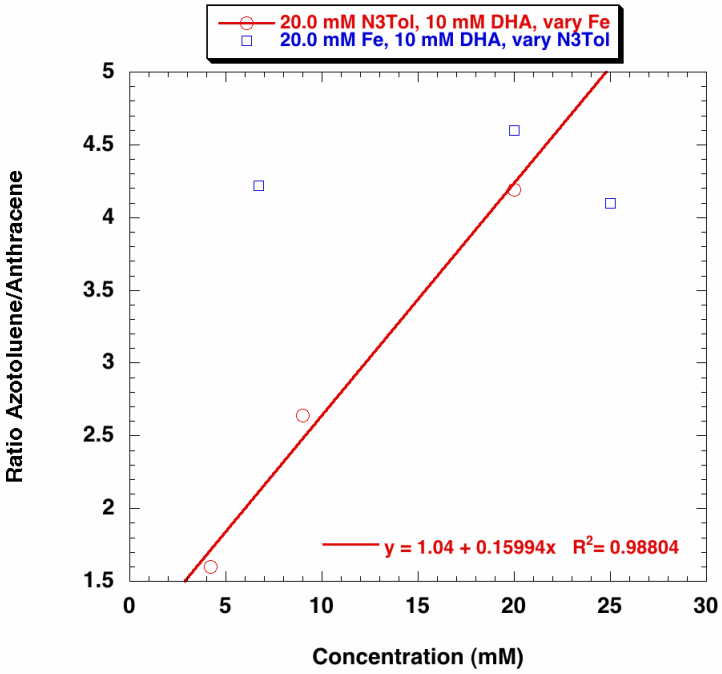

Figure 5.14. Plot of the azotoluene/anthracene ratio versus reagent concentrations (as indicated in legend).

5.3.10 DFT Calculations

Density functional calculations were carried out using the Gaussian03 suite[33] using the unrestricted B3LYP functional. For complexes **5.1** and **5.2**, the 6-311++G** basis set was utilized to do single-point energy calculations using crystallographic coordinates. Initial coordinates for **5.7** were generated by taking crystallographic coordinates of complex **5.6**, removing the N-H hydrogen, truncating the *p*-tolyl group to a phenyl group, and truncating the *iso*-propyl groups to methyl groups. The 6-31+G* basis set was used for obtaining minimized structures for **5.7-LS** and **5.7-IS**, and subsequently the final electronic structure calculations used the 6-311++G** basis set. Mülliken population analysis was used to examine spin density. The molecular orbital and spin

density contour plots were generated using GaussView 4.1.[34] Spin density data and optimized structures are presented below; frontier orbitals are presented in Appendix 4.

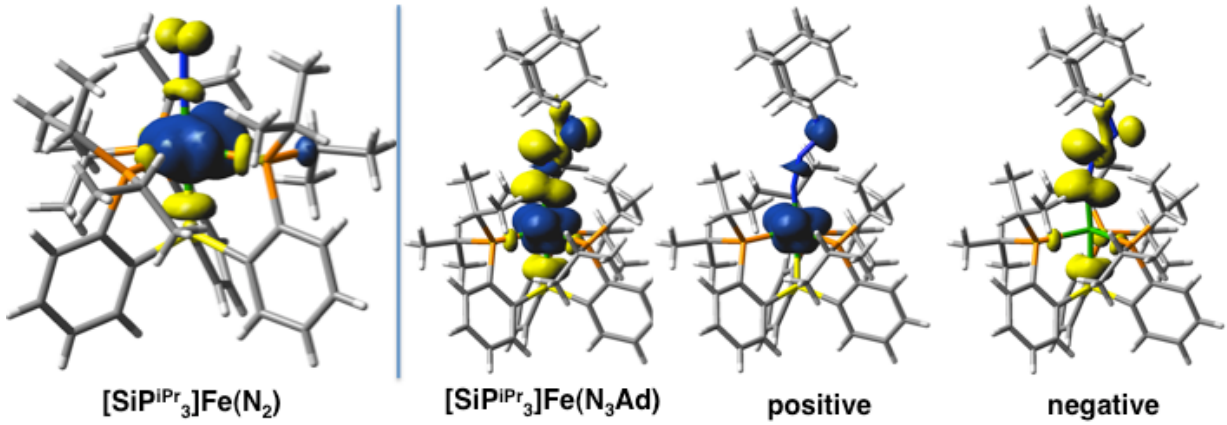

Figure 5.15. Spin density plots (0.002 isocontours). (*left*) Complex **5.1**. (*right*) Combined, positive phase, and negative phase spin density of **5.2**.

Table 5.7. Mülliken spin densities of complexes **5.1** and **5.2**

Atom(s)	Spin density, $[SiP^{iPr}_3]Fe(N_2)$	Spin density, $[SiP^{iPr}_3]Fe(N_3Ad)$
Fe	0.92	1.59
N_α	0.03	-0.53
N_β	-0.09	-0.47
N_γ	N/A	0.23
P	0.01	0.22
Si	-0.01	-0.05
C,H	0.14	0.01
total	1.00	1.00

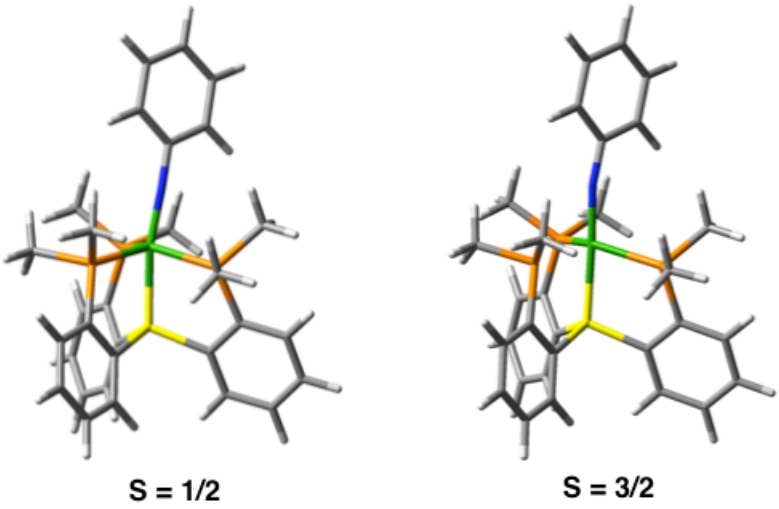

Figure 5.16. Optimized structures of [SiP$^{Me}_3$]Fe(NPh) (**5.7**): (*left*) low spin, **5.7-LS**; (*right*) intermediate spin, **5.7-IS**.

Table 5.8. Metric parameters for the optimized structures of **5.7-LS** and **5.7-IS**

Metric	5.7-LS	5.7-IS
Fe-N (Å)	1.70322	1.76669
Fe-Si (Å)	2.35284	2.37279
Fe-P (Å)	2.21410, 2.27132, 2.24227	2.28779, 2.38238, 2.32360
N-C (Å)	1.34087	1.34208
P-Fe-P (deg)	107.414, 134.782, 109.263	109.093, 108.123, 135.880
Si-Fe-N (deg)	164.46463	177.82614
Fe-N-C (deg)	174.41771	161.98101
τ	0.49	0.70

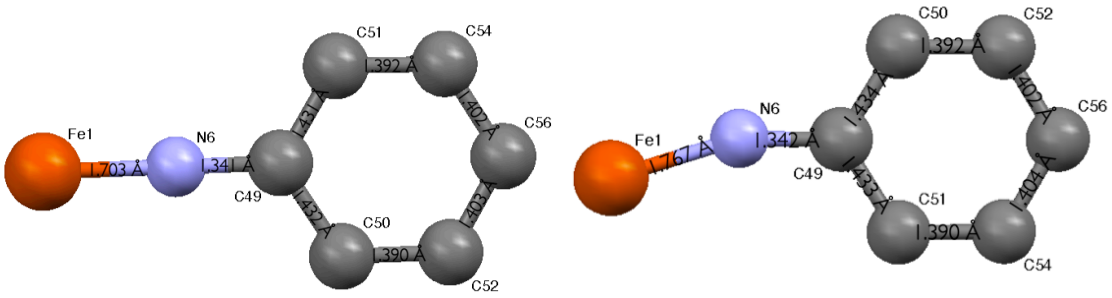

Figure 5.17. Bond lengths within the FeNPh groups of **5.7-LS** (*left*) and **5.7-IS** (*right*).

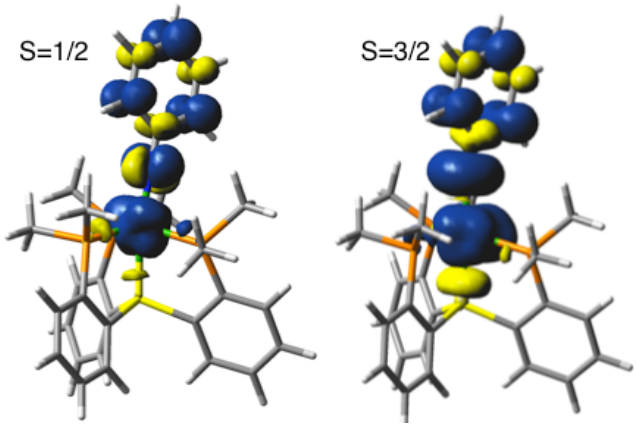

Figure 5.18. Spin density plots (0.002 isocontours) of (*left*) **5.7-LS** and (*left*) **5.7-IS**.

Table 5.9. Mülliken spin densities of complexes **5.7-LS** and **5.7-IS**

Atom(s)	Spin density, 5.7-LS	Spin density, 5.7-IS
Fe	0.89	2.00
N	0.01	0.82
C,H (Ph)	0.15	0.15
P	-0.07	0.04
Si	-0.06	-0.18
C,H (SiP^{Me}_3)	0.08	0.17
total	1.00	3.00

References Cited

1 Cenini, S.; Gallo, E.; Caselli, A.; Ragaini, F.; Fantauzzi, S.; Piangiolino, C. *Coord. Chem. Rev.* **2006**, *250*, 1234.

2 (a) Eckert, N. A.; Vaddadi, S.; Stoian, S.; Flaschenriem, C. J.; Cundari, T. R.; Holland, P. L. *Angew. Chem., Int. Ed. Engl.* **2006**, *45*, 6868. (b) Lucas, R. L.; Powell, D. R.; Borovik, A. S. *J. Am. Chem. Soc.* **2005**, *127*, 11596. (c) Jensen, M. P.; Mehn, M. P.; Que, L., Jr. *Angew. Chem., Int. Ed.* **2003**, *42*, 4357. (d) King, E. R.; Betley, T. A. *Inorg. Chem.* **2009**, *48*, 2361.

3 (a) Brown, S. D.; Betley, T. A.; Peters, J. C. *J. Am. Chem. Soc.* **2003**, *125*, 322. (b) Brown, S. D.; Peters, J. C. *J. Am. Chem. Soc.* **2005**, *127*, 1913. (c) Thomas, C. M.; Mankad, N. P.; Peters, J. C. *J. Am. Chem. Soc.* **2006**, *128*, 4956.

4 (a) Nieto, I.; Ding, F.; Bontchev, R. P.; Wang, H.; Smith, J. M. *J. Am. Chem. Soc.*, **2008**, *130*, 2716. (b) Verma, A. K.; Nazif, T. N.; Achim, C.; Lee, S. C. *J. Am. Chem. Soc.* **2000**, *122*, 11013.

5 Bart, S. C.; Lobkovsky, E.; Bill, E.; Chirik, P. J. *J. Am. Chem. Soc.* **2006**, *128*, 5302.

6 Ni, C.; Fettinger, J. C.; Long, G. J.; Brynda, M.; Power, P. P. *Chem. Commun.* **2008**, *45*, 6045.

7 England, J.; Martinho, M.; Farquhar, E. R.; Frisch, J. R.; Bominaar, E. L.; Münck, E.; Que, L., Jr. *Angew. Chem., Int. Ed.* **2009**, *48*, 3622.

8 Betley, T. A.; Wu, Q.; Van Voorhis, T.; Nocera, D. G. *Inorg. Chem.* **2008**, *47*, 1849.

9 (a) Hu, X.; Meyer, K. *J. Am. Chem. Soc.*, **2004**, *126*, 16322. (b) Vogel, C.; Heinemann, F. W.; Sutter, J.; Anthon, C.; Meyer, K. *Angew. Chem., Int. Ed.* **2008**, *47*, 2681.

10 Mankad, N. P.; Whited, M. T.; Peters, J. C. *Angew. Chem., Int. Ed.* **2007**, *46*, 5768.

11 (a) Proulx, G.; Bergman, R. G. *J. Am. Chem. Soc.* **1995**, 117, 6382. (b) Proulx, G.; Bergman, R. G. *Organometallics* **1996**, 15, 684. (c) Fickes, M. G.; Davis, W. M.; Cummins, C. C. *J. Am. Chem. Soc.* **1995**, 117, 6384. (d) Guillemot, G.; Solari, E.; Floriani, C.; Rozzoli, C. *Organometallics* **2001**, 20, 607. (e) Hanna, T. A.; Baranger, A. M.; Bergman, R. G. *Angew. Chem., Int. Ed. Engl.* **1996**, 35, 653. (f) Dias, H. V. R.; Polach, S. A.; Goh, S.-K.; Archibong, D. F.; Marynick, D. S. *Inorg. Chem.* **2000**, 39, 3894. (g) Barz, M.; Herdtweck, E.; Thiel, W. R. *Angew. Chem., Int. Ed. Engl.* **1998**, 37, 2262. (h) Albertin, G.; Antoniutti, S.; Baldan, D.; Castro, J.; Garcia-Fontan, S. *Inorg. Chem.* **2008**, 47, 742. (i) Waterman, R.; Hillhouse, G. L. *J. Am. Chem. Soc.* **2008**, 130, 12628.

12 B3LYP, 6-31+G* for minimizations, 6-311++G** for final energy calculations. Spin densities were calculated using Mülliken population analyses. See Supporting Information for further details.

13 Though the complete mass balance was not accounted for in these product mixtures, we note that dark insoluble material was evident upon scale-up, implying the production of oligomeric or polymeric material.

14 Ragaini, F.; Penoni, A.; Gallo, E.; Tollari, S.; Gotti, C. L.; Lapadula, M.; Mangioni, E.; Cenini, S. *Chem. Eur. J.* **2003**, 9, 249.

15 Takaoka, A.; Gerber, L. C. H.; Peters, J. C., **2009**, *Manuscript submitted*.

16 Brown, S. D. Ph.D. Thesis, California Institute of Technology, May 2005.

17 (a) Cowley, R. E.; Eckert, N. A.; Elhaïk, J.; Holland, P. L. *Chem. Commun.*, **2009**, 1760. (b) Laskowski, C. A.; Hillhouse, G. L. *Organometallics*, **2009**, *28*, 6114.

18 (a) Hansert, B.; Vahrenkamp, H. *J. Organomet. Chem.* **1993**, *459*, 265. (b) Harrold, N. D.; Waterman, R.; Hillhouse, G. L.; Cundari, T. R. *J. Am. Chem. Soc.*, **2009**, *131*, 12872.

19 (a) Yiu, S.-M.; Lam, W. W. Y.; Ho, C.-M.; Lau, T.-C. *J. Am. Chem. Soc.* **2007**, *129*, 803. (b) Zarkesh, R. A.; Ziller, J. W.; Heyduk, A. F. *Angew. Chem., Int. Ed.* **2008**, *47*, 4715. (c) Mansuy, D.; Battioni, P.; Mahy, J. P. *J. Am. Chem. Soc.* **1982**, *104*, 4487.

20 Yang, X.; Baik, M.-H. *J. Am. Chem. Soc.* **2006**, *128*, 7476.

21 $\tau = 0$ for an ideal square pyramid and 1 for an ideal trigonal bipyramid: Addison, A. W.; Rao, T. N.; Reedijk, J.; van Rijn, J.; Verschoor, G. C. *J. Chem. Soc. Dalton Trans.* **1984**, 1349.

22 (a) Klinker, E. J.; Shaik, S.; Hirao, H.; Que, L., Jr. *Angew. Chem., Int. Ed.* **2009**, *48*, 1291. (b) Hirao, H.; Kumar, D.; Que, L., Jr.; Shaik, S. *J. Am. Chem. Soc.* **2006**, *128*, 8590. (c) Dhuri, S. N.; Seo, M. S.; Lee, Y.-M.; Hirao, H.; Wang, Y.; Nam, W.; Shaik, S. *Angew. Chem., Int. Ed.* **2008**, *47*, 3356.

23 Kitamura, Y.; Taniguchi, K.; Maegawa, T.; Monguchi, Y.; Kitade, Y.; Sajiki, H. *Heterocycles* **2009**, *77*, 521-532.

24 For azoarenes: Lu, W.; Xi, C. *Tetrahdron Lett.* **2008**, *49*, 4011-4015.

25 For carbodiimides: Ito, Y.; Hirao, T.; Saegusa, T. *J. Org. Chem.* **1975**, *40*, 2981-2982.

26 Sheldrick, G. M. *Acta Cryst.* **1990**, *A46*, 467-473.

27 Sheldrick, G. M.. *Acta Cryst.* **2008**, *A64*, 112–122.

28 Müller, P. *Crystallography Reviews* **2009**, *15*, 57-83.

29 Evans, D. F. *J. Chem. Soc*, **1959**, 2003-2005.

30 Sur, S. K. *J. Magn. Reson.* **1989**, *82*, 169-173.

31 Neese, F. *QCPE Bull*. **1995**, *15*, 5.

32 Hall, J. H.; Fargher, J. M.; Gisler, M. R. *J. Am. Chem. Soc*. **1978**, *100*, 2029.

33 Frisch, M. J.; Trucks, G. W.; Schlegel, H. B.; Scuseria, G. E.; Robb, M. A.; Cheeseman, J. R.; Montgomery, J. A. J.; Vreven, T.; Kudin, K. N.; Burant, J. C.; Millam, J. M.; Iyengar, S. S.; Tomasi, J.; Barone, V.; Mennucci, B.; Cossi, M.; Scalmani, G.; Rega, N.; Petersson, G. A.; Nakatsuji, H.; Hada, M.; Ehara, M.; Toyota, K.; Fukuda, R.; Hasegawa, J.; Ishida, M.; Nakajima, T.; Honda, Y.; Kitao, O.; Nakai, H.; Klene, M.; Li, X.; Knox, J. E.; Hratchian, H. P.; Cross, J. B.; Adamo, C.; Jaramillo, J.; Gomperts, R.; Stratmann, R. E.; Yazyev, O.; Austin, A. J.; Cammi, R.; Pomelli, C.; Ochterski, J. W.; Ayala, P. Y.; Morokuma, K.; Voth, G. A.; Salvador, P.; Dannenberg, J. J.; Zakrzewski, V. G.; Dapprich, S.; Daniels, A. D.; Strain, M. C.; Farkas, O.; Malick, D. K.; Rabuck, A. D.; Raghavachari, K.; Foresman, J. B.; Ortiz, J. V.; Cui, Q.; Baboul, A. G.; Clifford, S.; Cioslowski, J.; Stefanov, B. B.; Liu, G.; Liashenko, A.; Piskorz, P.; Komaromi, I.; Martin, R. L.; Fox, D. J.; Keith, T.; Al-Laham, M. A.; Peng, C. Y.; Nanayakkara, A.; Challacombe, M.; Gill, P. M. W.; Johnson, B.; Chen, W.; Wong, M. W.; Gonzalez, C.; Pople, J. A. Gaussian03, Rev. C02; Gaussian, Inc.: Pittsburgh PA, 2004.

34 GaussView, Version 4.1; Roy Dennington II, Todd Keith and John Millam, Semichem, Inc., Shawnee Mission, KS, 2007.

Chapter 6: Exploratory Studies with Tris(phosphino)silyl Platinum Complexes

Reproduced in part from

Tsay, C., Mankad, N. P., and Peters, J. C. *Manuscript in preparation*.

6.1 Introduction

Electrophilic platinum(II) complexes have been studied extensively due to their ability to activate C-H bonds such as those in methane and other cheap hydrocarbons.[1,2] As these species are almost always square planar,[3] it is of interest to consider how other geometries might impact the electrophilicity and reactivity of Pt(II) centers. Using the tris(phosphino)silyl scaffold $[SiP^{R}_{3}]^{-}$ (where $[SiP^{R}_{3}]^{-}$ = $[(2\text{-}R_2PC_6H_4)_3Si]^{-}$, R = Ph or ^{i}Pr),[4] we sought to access trigonal bipyramidal (TBP) platinum(II) synthons that could allow access to 4-coordinate, trigonal pyramidal (TP) species. In general, isolable d^8 complexes with non-planar 4-coordinate geometries are extremely rare and require stabilization by strongly π-accepting, non-innocent ligands.[5] However, targeting such a species seems reasonable considering the recent report from Maron, Ozerov, Bourissou, and co-workers of the first divalent TP platinum complex, $[(2\text{-}^{i}Pr_2PC_6H_4)_3B]Pt$.[6] Replacing the apical boron atom in that complex with the silicon atom featured in the $[SiP^{R}_{3}]$ framework would render the complex cationic (Figure 6.1), and therefore presumably more reactive as an electrophile. We report herein the characterization of TBP $[SiP^{Ph}_{3}]Pt(L)^{+}$ cations, with weak solvent ligands bound in the axial site, as candidate precursors to the TP target compounds.

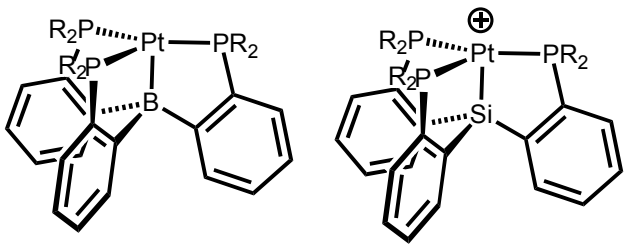

Figure 6.1. (*left*) Neutral trigonal planar Pt complex reported by Maron, Ozerov, Bourissou, and coworkers; (*right*) Cationic trigonal planar Pt complex targeted herein.

6.2 Results and Discussion

Neutral Pt(II) complexes are readily accessible by reaction of $[SiP^{Ph}_3]H$ with appropriate commercially available platinum reagents (Scheme 6.1). Specifically, reaction of $[SiP^{Ph}_3]H$ with $(COD)PtCl_2$ (COD = cyclooctadiene), $(COD)PtMe_2$, and $(Ph_3P)_4Pt$ provided $[SiP^{Ph}_3]PtCl$ (**6.1**), $[SiP^{Ph}_3]PtMe$ (**6.2**), and $[SiP^{Ph}_3]PtH$ (**6.3**), respectively.

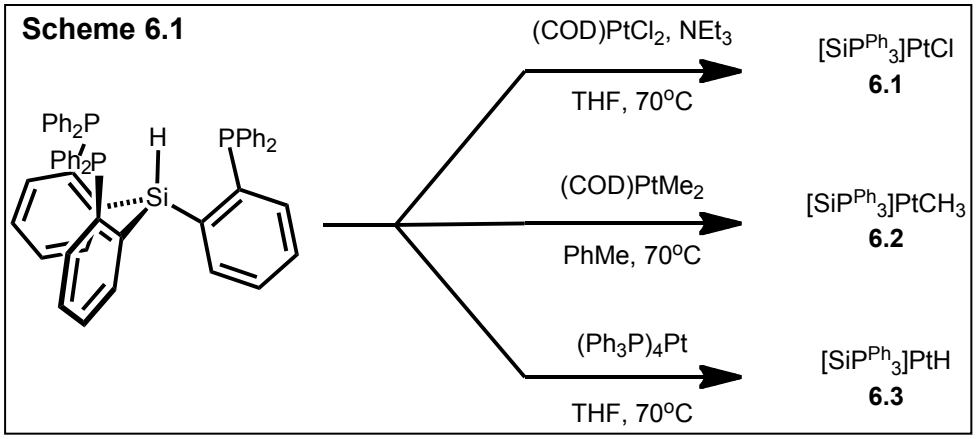

Complexes **6.1** – **6.3** are yellow, air-stable solids that exhibit single peaks in their $^{31}P\{^1H\}$ NMR spectra ranging from 22.6 to 34.0 ppm, indicative of threefold symmetry in solution. ^{195}Pt satellites are observed with an average $^1J_{PtP}$ of 3086 Hz. Complex **6.2** displays characteristic methyl resonances in the ^1H NMR (0.34 ppm, $^3J_{PH}$ = 6.9 Hz, $^2J_{PtH}$ = 49.6 Hz) and $^{13}C\{^1H\}$ NMR spectra (-35.4 ppm, $^2J_{PC}$ = 9.7 Hz, $^1J_{PtC}$ = 458 Hz). Complex **6.3** possesses a characteristic hydride ^1H NMR resonance at -6.27 ppm with $^2J_{PH}$ = 19.8 Hz and $^1J_{PtH}$ = 782 Hz (Figure 6.2a), and the Pt-H vibration occurs at ν_{PtH} = 1803 cm^{-1} in the solid-state IR spectrum. The TBP geometry is retained in the solid state as confirmed

by single crystal X-ray diffraction (Figure 6.3). Further discussion of the metrical parameters is provided below.

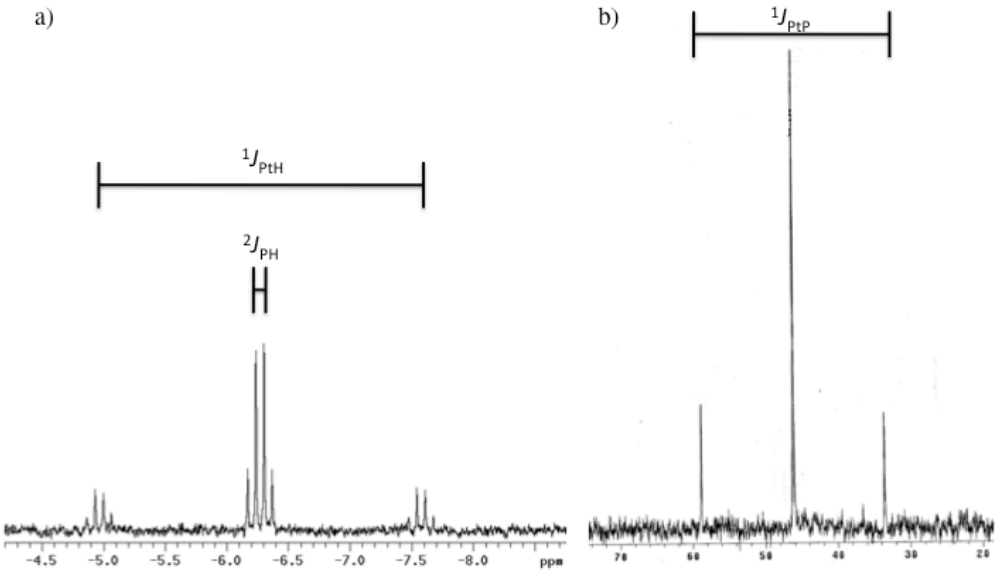

Figure 6.2. a) ^{1}H NMR spectrum of [SiP$^{Ph}_3$]PtH (**6.3**), b) ^{31}P{^{1}H} NMR spectrum of {[SiP$^{Ph}_3$]Pt(CD$_2$Cl$_2$)}{BAr$^F_4$} (**6.5**).

Complexes **6.2** and **6.3** are structurally unusual. Transition metal complexes featuring both a silyl ligand and either a hydride or alkyl ligand are rare,[7] especially when the alkyl or hydride ligand is *trans* to the silyl group.[7b] Accordingly, complexes **6.2** and **6.3** are useful synthons for access to cationic species via protonolysis reactions. The Brønsted basicity of methyl complex **6.2** was examined by the addition of various acidic reagents. Complex **6.2** was unreactive towards phenol but was easily converted to the acetate derivative [SiP$^{Ph}_3$]PtOAc (**6.4**) using acetic acid. Thus, the basicity of **6.2** can be bracketed by considering the relative pKa values of PhOH (18.0 in DMSO)[8] and AcOH (12.6 in DMSO).[9]

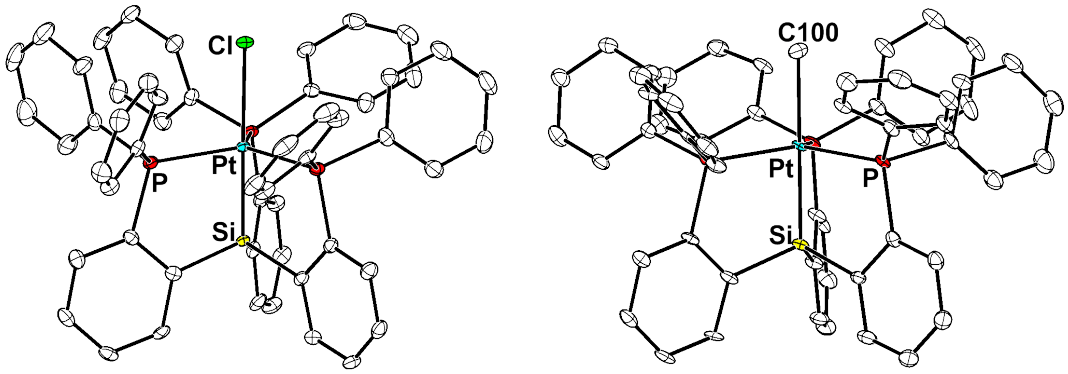

Figure 6.3. Solid-state structures of (*left*) [SiP$^{Ph}_3$]PtCl (**6.1**) and (*right*) [SiP$^{Ph}_3$]PtCH$_3$ (**6.2**) as 50% ellipsoids. Hydrogen atoms have been omitted for clarity. Selected bond lengths (Å) for **6.1**: Pt-Cl, 2.4975(10). For **6.2**: Pt-C(100), 2.229(6). Further parameters are in Table 6.1.

Cationic species were accessed by using the non-coordinating borate anion BAr$^F_4$$^-$ (Ar^F = 3,5-(F$_3$C)$_2$C$_6$H$_3$). As shown in Scheme 6.2, protonolysis of **6.2** with H(OEt$_2$)$_2$BAr$^F_4$ resulted in methane evolution and generation of stable, cationic solvento species {[SiP$^{Ph}_3$]Pt(L)}{BAr$^F_4$} (**6.5**) dependent on the reaction solvent. Analogous species were generated by methide abstraction from **6.2** with B(C$_6$F$_5$)$_3$, but the resulting compounds were found to decay to unidentified products over the course of several days. The cationic species **6.5** retained threefold symmetry as evidenced by their single resonances (with ^{195}Pt satellites) in the ^{31}P{^{1}H} NMR spectra (Figure 6.2b). The ^{31}P NMR peaks were shifted downfield significantly (46.3 ppm in CD$_2$Cl$_2$, 54.5 ppm in C$_6$D$_6$) compared to the neutral counterparts **6.1** – **6.3**; apparently this feature is diagnostic of cationic, electron-deficient Pt centers in this system. Variable temperature ^{1}H and ^{31}P{^{1}H} NMR spectroscopy, both of CD$_2$Cl$_2$ and toluene-d_8 solutions, indicated that threefold symmetry

was maintained even at temperatures as low as -90°C, and no features in the ^{1}H NMR spectra indicative of intramolecular interactions between the Pt center and the SiP^{Ph}_3 ligand were detected.

Scheme 6.2

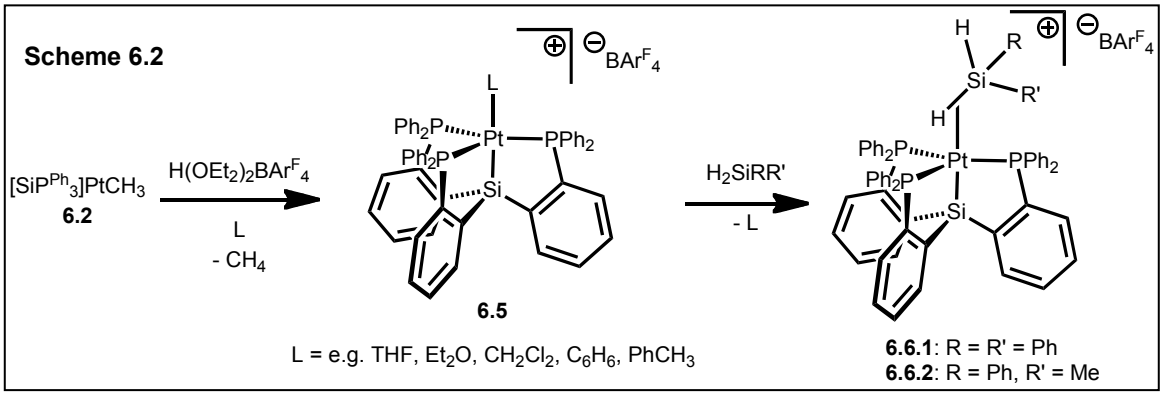

It is likely that the cationic complexes **6.5** take on the L ligands corresponding to the solvent in which the compound is dissolved. One set of observations consistent with this hypothesis is the solvent-dependent color of **6.5**. In coordinating solvents such as THF or CH_3CN, **6.5** appears yellow. In poorly coordinating solvents such as benzene or toluene, cations **6.5** appears red. Instead, **6.5** appears orange in diethyl ether or dichloromethane solutions. Accordingly, a dominant band in the visible region of the UV-Vis spectra of **6.5** was found to be highly solvent dependent (Figure 6.4), moving to higher energy in strong donor solvents and to lower energy is poorly coordinating solvents. All of these observations are consistent with dative solvent ligands coordinating to the axial position of a TBP geometry and thus modulating the energy of the lowest-energy unoccupied orbital of dz^2 parentage.

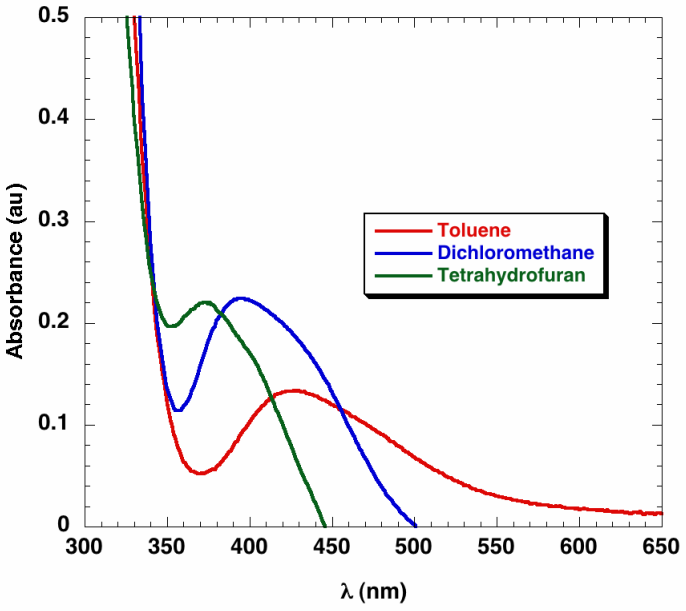

Figure 6.4. UV-Vis spectra of **6.5** in toluene (red), dicholoromethane (blue), and tetrahydrofuran (green) solutions.

The assignment of **6.5** as a solvento species in dichloromethane solution was confirmed by X-ray crystallography (Figure 6.5). Four dichloromethane solvent molecules were found in the asymmetric unit of crystals of **6.5** grown from dichloromethane; one CH_2Cl_2 unit was coordinated to the Pt center via one of its chlorine atoms, while the others showed no interactions with the Pt center. The Pt-Cl distance of 2.6236(16) Å, though well within the sum of the covalent radii of Pt and Cl, is indicative of a weak dative interaction, especially when compared to the Pt-Cl distance of 2.4975(10) Å in the neutral chloride complex **6.1**. Further metrics are presented below. Crystals of **6.5** grown from benzene solutions were consistently of rhombohedral symmetry and suffered from significant disorder about a threefold axis of crystallographic symmetry as well as whole-molecule disorder, precluding its characterization by X-ray crystallography. However, subsequent unpublished work in the

Peters group has since shown that crystals of **6.5** grown from toluene solutions do indeed feature a toluene solvent molecule coordinated to the cationic Pt center via the *para*-C-H bond.[10]

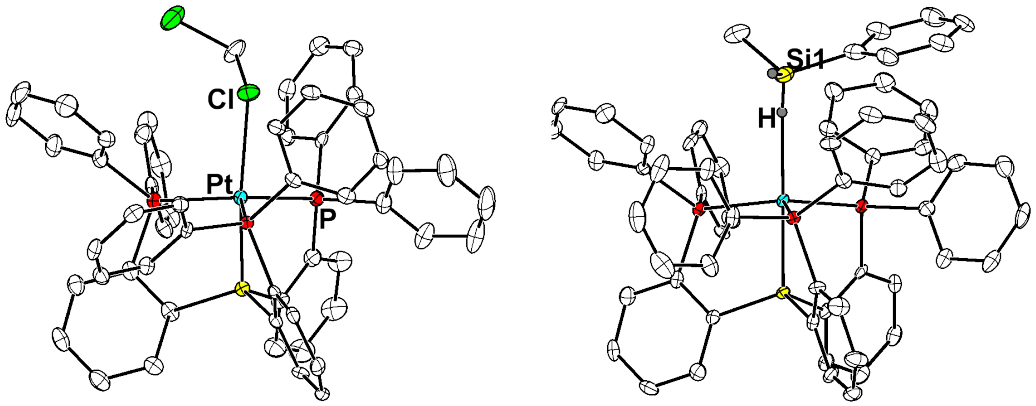

Figure 6.5. Solid-state structures of the cationic portions of (*left*) {[SiP$^{Ph}_3$]Pt(CH$_2$Cl$_2$)}{BAr$^F_4$} (**6.5**) and (*right*) {[SiP$^{Ph}_3$]Pt(η^2-H$_2$SiMePh)}{BAr$^F_4$} (**6.6.2**) as 50% ellipsoids. Hydrogen atoms in **6.6.2** are placed in calculated positions. Selected bond lengths (Å) for **6.5**: Pt-Cl, 2.6236(16). For **6.6.2**: Pt-H, 2.1821; Pt-Si1, 2.290(2). Further parameters are in Table 6.1.

According to all available data, a solvent molecule coordinates the axial site of **6.5** *trans* to the silyl ligand for any solvent that dissolves **6.5**. Thus, the target TP cation {[SiP$^{Ph}_3$]Pt}{BAr$^F_4$} could not be observed directly either by solution methods or by X-ray crystallography, and in fact no evidence of its existence has yet been gained. Nonetheless, it is of interest to consider whether some equilibrium between **6.5** and such a "naked" cation exists and thus can provide access to interesting solution reactivity.

Along these lines, attempts at inducing C-H activation reactions by thermolysis of **6.5** in the presence of various potential substrates and a base did not prove fruitful. A noteworthy control experiment showed that prolonged exposure of **6.5** to triethylamine resulted in significant decomposition, a major product of which was hydride species **6.3**. Presumably, this product is the result of NEt_3 coordination followed by β-hydride elimination.

In attempts to induce Si-H activation, cationic **6.5** was exposed to various silanes. Rather than succumbing to Si-H activation, however, secondary silanes H_2SiPh_2 and $H_2SiMePh$ were found to displace the solvent ligand of **6.5** to rapidly form yellow σ_{SiH} adduct species $\{[SiP^{Ph}_3]Pt(\eta^2\text{-}H_2SiRR')\}\{BAr^F_4\}$ (**6.6.1** and **6.6.2**, respectively; see Scheme 6.2). No reaction was observed with the tertiary silane $HSiPh_3$. Thermolysis of **6.6.1** and **6.6.2** at 90°C led to partial conversion to **6.3** with no evidence of an observable Si-H activation intermediate, and the fate of the silyl moiety is unknown.

Simple electron-counting considerations dictate that only one Si-H σ-bond can coordinate a Pt center at a time to generate 18-electron complexes. At room temperature, the ^{1}H NMR spectra of **6.6.1** and **6.6.2** reveal broad silane Si-H resonances (5.19 ppm for **6.6.1** and 4.32 ppm for **6.6.2**; *cf*. 5.13 ppm and 4.48 ppm for free H_2SiPh_2 and $H_2SiMePh$, respectively), indicative of rapid exchange of the two available Si-H σ-bonds. Complex **6.6.2** was studied by variable temperature ^{1}H NMR. At -60°C in CD_2Cl_2 solution, distinct Si-H peaks were found to decoalesce, with the free Si-H proton appearing as a broad resonance at 4.89 ppm and the bound Si-H proton appearing at -5.01 ppm as a broad peak with Pt satellites (J_{PtH} = 346 Hz, intermediate between $^1J_{PtH}$ = 782 of **6.3** and $^2J_{PtH}$ = 49.6 of **6.2**). The timescale of an IR experiment is much faster than that of an NMR

experiment, and accordingly at room temperature in benzene solution the IR spectra exhibited Si-H vibrations at ν_{SiH} = 2187 and 2140 cm^{-1} for **6.6.1** and ν_{SiH} = 2136 and 1900 cm^{-1} for **6.6.2** (*cf*. 2158 cm^{-1} for free H_2SiPh_2; 2158 and 2117 cm^{-1} for free $H_2SiMePh$).

The solid-state structure of **6.6.2** was investigated using X-ray crystallography (Figure 6.5). The Si-H hydrogens could not be located on the difference map and were placed in calculated positions. The calculated Pt-H distance in **6.6.2** is 2.1821 Å, indicative of significant Pt-silane interaction in the solid state. The Pt-Si_{silane} distance (3.148(3) Å) is quite long in comparison to the Pt-Si_{silyl} distance (2.290(2) Å). Silane complexes of transition metals are relatively well known and span a wide variety of binding modes and electronic structures.[11] However, it is noteworthy that 1:1 Pt-silane complexes have not been structurally characterized previous to **6.6.2** despite their proposed role in Pt-catalyzed hydrosilylation reactions.[12,13]

Table 6.1. Structural data for $[SiP^{Ph}_3]Pt^{II}X$ complexes

X	**Si-Pt-X (°)**	**τ**[c]	**Si_{silyl}-Pt (Å)**
Cl^- (**6.1**)	178.17(3)	0.88	2.2689(11)
CH_3^- (**6.2**)	178.15(16)	0.87	2.3076(15)
H^- (**6.3**)	n.d.[a]	n.d.[a]	2.3136(13)
CH_2Cl_2 (**6.5**)	178.48(5)	0.89	2.2805(16)
$H_2SiMePh$ (**6.6.2**)	177.6(5)[b]	0.93	2.290(2)

[a] Not determined because the hydride ligand could not be located on the Fourier difference map. [b] Estimated by averaging the Si_{silyl}-Pt-Si_{silane} and Si_{silyl}-Pt-H angles. [c] τ = 0 for a square pyramid and 1 for a trigonal bipyramid.[14]

When considering the collection of $[SiP^{Ph}_3]PtX$ structures presented herein, the Pt-silyl distances provide a convenient indicator of the *trans* influence. Table 6.1

summarizes representative structural data for complexes **6.1** – **6.3**, **6.5**, and **6.6.2**. The τ values all indicate close to idealized TBP geometries, and the Si-Pt-X angles are all extremely close to 180°. The Pt-Si_{silyl} distances increase as a function of the *trans* ligand X in the order $CH_2Cl_2 < Cl^- < H_2SiMePh < CH_3^- < H^-$.

6.3 Conclusions

The neutral, trigonal bipyramidal Pt(II) compounds $[SiP^{Ph}_3]PtX$ (X = Cl (**6.1**), CH_3 (**6.2**), H (**6.3**)) were prepared and thoroughly characterized by solution spectroscopy and solid-state X-ray crystallography. The methyl and hydride compounds are structurally unusual by virtue of placing extremely strong σ-donors *trans* to a silyl ligand. Protonolysis of these precursors was examined in order to target trigonal pyramidal geometries achieved by leaving the axial site *trans* to the silyl donor empty. Though such a trigonal pyramidal species was never detected directly, various labile solvento species $[SiP^{Ph}_3]Pt(L)^+$ (**6.5**, L = e.g., THF, Et_2O, CH_2Cl_2, C_6H_6, PhMe) were observed. Apparently, the Lewis acidity of the cationic Pt(II) center in this system precludes access to a "naked" cation with an empty coordination site in any solvent that can dissolve the compound. This fact is noteworthy when making a comparison to the neutral analogue prepared by Maron, Ozerov, Bourrisou, and co-workers (Figure 6.1). Future studies already underway will entail extending this chemistry to the $[SiP^{iPr}_3]^-$ scaffold to access a bona fide trigonal pyramidal Pt(II) complex, as well as studying the reactivity of these and related Pd(II) and Ni(II) complexes.[10]

6.4 Experimental Section

6.4.1 General Considerations

Unless otherwise noted, all manipulations were carried out using standard Schlenk or glovebox techniques under a dinitrogen atmosphere. Unless otherwise noted, solvents were deoxygenated and dried by thoroughly sparging with N_2 gas followed by passage through an activated alumina column. Non-halogenated solvents were tested with a standard purple solution of sodium benzophenone ketyl in tetrahydrofuran in order to confirm effective oxygen and moisture removal. All reagents were purchased from commercial vendors and used without further purification unless otherwise stated. $[SiP^{Ph}_3]H$[4] and $H(OEt_2)_2BAr^F_4$[15] were prepared according to literature methods. Elemental analyses were performed by Desert Analytics, Tucson, AZ. Deuterated solvents were purchased from Cambridge Isotope Laboratories (Cambridge, MA), degassed, and dried over activated 3 Å molecular sieves prior to use.

6.4.2 Spectroscopic Measurements

A Varian Mercury-300 spectrometer was used to record ^1H, ^{13}C, ^{19}F, and ^{31}P NMR spectra at ambient temperature (unless otherwise indicated). ^1H and ^{13}C chemical shifts were referenced to the residual solvent peaks. ^{19}F and ^{31}P chemical shifts were referenced to external hexafluorobenzene (δ = -165 ppm) and phosphoric acid (δ = 0 ppm) respectively. Optical spectroscopy measurements were taken on a Cary 50 UV/Vis Spectrophotometer using a 1 cm quartz cell.

6.4.3 X-ray Crystallography Procedures

X-ray diffraction studies were carried out at the Beckman Institute Crystallography Facility on a Brüker Smart 1000 CCD diffractometer and solved using SHELX v. 6.14.[16] X-ray quality crystals were grown as indicated in the experimental procedures per individual complex. The crystals were mounted on a glass fiber with Paratone N oil. Structures were determined using direct methods with standard Fourier techniques using the Bruker AXS software package. Spatial refinement details: Refinement of F^2 against ALL reflections. The weighted R-factor (*w*R) and goodness of fit (S) are based on F^2, conventional R-factors (R) are based on F, with F set to zero for negative F^2. The threshold expression of $F^2 > 2\sigma(F^2)$ is used only for calculating R-factors(gt) etc. and is not relevant to the choice of reflections for refinement. R-factors based on F^2 are statistically about twice as large as those based on F, and R-factors based on ALL data will be even larger. All esds (except the esd in the dihedral angle between two l.s. planes) are estimated using the full covariance matrix. The cell esds are taken into account individually in the estimation of esds in distances, angles, and torsion angles; correlations between esds in cell parameters are only used when they are defined by crystal symmetry. An approximate (isotropic) treatment of cell esds is used for estimating esds involving l.s. planes. Crystallographic details have been placed in Appendix 5.

6.4.4 Synthesis

Preparation of [SiP$^{Ph}_3$]PtCl (6.1). Under a dinitrogen atmosphere, [SiP$^{Ph}_3$]H (0.631 g, 0.776 mmol) and (COD)$PtCl_2$ (0.290 g, 0.775 mmol) were placed in a

resealable Schlenk tube with THF (20 mL) and triethylamine (1.5 mL). The tube was sealed and heated to 70°C for 1.5 h, resulting in a yellow solution with bright yellow precipitate. This mixture was poured under air into a 250 mL separatory funnel with dichloromethane (75 mL). The combined organic fraction was then washed with water (150 mL), sodium bicarbonate (saturated aqueous solution, 2 x 150 mL), and water (150 mL). The cloudy yellow organic fraction was dried over anhydrous magnesium sulfate, filtered through Celite, and evaporated to dryness by rotary evaporation. Diethyl ether (50 mL) was added with stirring, and a bright yellow powder was collected on a sintered glass frit and washed with several portions of diethyl ether to yield spectroscopically pure [SiP^{Ph}_3]PtCl (0.571 g, 71%). Analytically pure material was obtained by recrystallization from dichloromethane/petroleum ether. The complex is stable to air and moisture indefinitely. Crystals suitable for X-ray diffraction were grown by layering a dichloromethane solution with petroleum ether. ^{1}H NMR (CD_2Cl_2, δ): 8.46 (d, 3H, J = 7.2 Hz), 7.56 (t, 3H, J = 7.1 Hz), 7.32 (m, 6H), 7.11 (m, 18H), 6.91 (t, 12H, J = 7.7 Hz). ^{13}C{^{1}H} NMR (CD_2Cl_2, δ): 150.2 (m), 144.1 (m), 137.6 (m), 134.3 (t, J_{PtC} = 15.3 Hz), 133.2 (q, J = 8.0 Hz), 132.8 (q, J = 4.2 Hz), 130.8 (s), 129.6 (s), 129.1 (s), 128.2 (q, J = 3.1 Hz). ^{31}P{^{1}H} NMR (CD_2Cl_2, δ): 29.3 ($^1J_{PtP}$ = 3064 Hz). IR (KBr, cm^{-1}): 3051, 2874, 2864, 1582, 1479, 1429, 1255, 1186, 1105, 1065, 1028, 999, 910. Anal. Calcd. for $C_{54}H_{42}ClP_3PtSi$: C, 62.22; H, 4.06. Found: C, 62.02; H, 3.88.

Preparation of [SiP^{Ph}_3]$PtCH_3$ (6.2). Under a dinitrogen atmosphere, [SiP^{Ph}_3]H (0.941 g, 1.16 mmol) and (COD)$PtMe_2$ (0.386 g, 1.16 mmol) were placed in a resealable Schlenk tube with toluene (40 mL). The tube was sealed and heated to 70°C for 18 h, resulting in a golden yellow solution with some yellow precipitate. The solvent was

removed *in vacuo*. To the residues was added diethyl ether (50 mL) under air, and an off-white powder was collected on a frit and washed with additional portions of diethyl ether to yield analytically pure [SiP^{Ph}_3]$PtCH_3$ (0.997 g, 84%). The complex is stable to air and moisture indefinitely. Crystals suitable for X-ray diffraction were grown by diffusion of petroleum ether vapors into a THF solution. ^{1}H NMR (CD_2Cl_2, δ): 8.51 (d, J = 7.5 Hz, 3H), 7.48 (t, 3H, J = 6.8 Hz), 7.23 (m, 6H), 7.06 (m, 6H), 6.88 (m, 24H), 0.34 (3H, $^3J_{PH}$ = 6.9 Hz, $^2J_{PtH}$ = 49.6 Hz, PtCH_3). ^{13}C{^{1}H} NMR (CD_2Cl_2, δ): 153.3 (m), 149.4 (m), 139.1 (m), 133.5 (t, J = 11.3 Hz), 133.1 (m), 132.5 (q, J = 4.3 Hz), 129.9 (s), 128.8 (s), 128.4 (s), 128.1 (q, J = 2.9 Hz), -35.4 ($^2J_{PC}$ = 9.7 Hz, $^1J_{PtC}$ = 458 Hz, Pt-CH_3). ^{31}P{^{1}H} NMR (CD_2Cl_2, δ): 23.2 ($^1J_{PtP}$ = 3104 Hz). IR (KBr, cm^{-1}): 3051, 2974, 2864, 1580, 1477, 1429, 1304, 1248, 1182, 1126, 1089, 1065, 1027, 907. Anal. Calcd. for $C_{55}H_{45}P_3PtSi$: C, 64.63; H, 4.44. Found: C, 64.82; H, 5.35.

Preparation of [SiP^{Ph}_3]PtH (6.3). [SiP^{Ph}_3]H (76.7 mg, 94.4 μmol) and tetrakis(triphenylphosphine)platinum(0) (117 mg, 94.4 μmol) were dissolved in THF (5 mL) in a resealable Schlenk tube under a dinitrogen atmosphere and heated to 70˚C for 17 h. Volitiles were removed, and the residues were triturated with diethyl ether (20 mL) under air. An off-white solid was then collected on a sintered glass frit and washed with diethyl ether (2 x 25 mL) to yield analytically pure [SiP^{Ph}_3]PtH (54.9 mg, 58%). The complex is stable to air and moisture indefinitely. Crystals suitable for X-ray diffraction were grown by diffusion of petroleum vapors into a THF solution. ^{1}H NMR (C_6D_6, δ): 8.60 (d, J = 7.5 Hz, 3H), 7.41 (d, J = 9.0 Hz, 3H), 7.27 (m, 15H), 6.97 (t, J = 7.6 Hz, 3H), 6.78 (t, J = 7.3 Hz, 6H), 6.63 (t, J = 7.5 Hz, 12H), -6.27 ($^2J_{PH}$ = 19.8 Hz, $^1J_{PtH}$ = 782 Hz, 1H). ^{13}C{^{1}H} NMR (C_6D_6, δ): 154.3 (dd, J = 19.7 Hz and 37.1 Hz), 150.3 (m), 140.0 (m),

134.7 (s), 133.6 (m), 132.9 (d, J = 4.1 Hz), 130.0 (s). $^{31}P\{^{1}H\}$ NMR (C_6D_6, δ): 34.0 ($^{1}J_{PtP}$ = 3092 Hz). IR (KBr, cm^{-1}): 3046, 2974, 2858, 1803 (n_{PtH}), 1582, 1479, 1431, 1304, 1248, 1184, 1093, 1065, 1028, 910. Anal. Calcd. for $C_{54}H_{43}P_3PtSi$: C, 64.34; H, 4.30. Found: C, 64.44; H, 4.21.

Preparation of [SiP$^{Ph}_3$]PtOAc (6.4). Under air, [SiP$^{Ph}_3$]PtCH$_3$ (0.216 g, 0.211 mmol) was suspended in dichloromethane (25 mL) in a 100 mL round-bottom flask. Acetic acid (0.5 mL) was added by pipet with stirring. Over the first 5 min of the reaction, the solution changed from cloudy off-white to clear yellow. After 0.5 h, the solution was evaporated to dryness on a rotovap. Diethyl ether (25 mL) was added, and bright yellow flakes of analytically pure [SiP$^{Ph}_3$]PtOAc were collected on a frit (0.148 g, 66%). The complex is stable to air and moisture indefinitely. ^{1}H NMR (CD_2Cl_2, δ): 8.31 (d, J = 7.2 Hz, 3H), 7.49 (t, J = 6.7 Hz, 3H), 7.31 (m, 6H), 7.12 (m, 18H), 6.93 (t, J = 7.5 Hz, 12H), 1.72 (s, 3H, Pt-CO_2CH_3). $^{13}C\{^{1}H\}$ NMR (CD_2Cl_2, δ): 175.6 (Pt-CO_2CH_3, *Note*: Multiplicity could not be determined due to a poor signal-to-noise ratio), 148.8 (m), 145.4 (m), 138.1 (m), 133.4 (t, J = 8.4 Hz), 132.9 (m), 130.3 (s), 129.6 (s), 129.0 (s), 128.1 (t, J = 4.7 Hz), 23.6 (s, Pt-CO_2CH_3). $^{31}P\{^{1}H\}$ NMR (CD_2Cl_2, δ): 35.5 ($^{1}J_{PtP}$ = 3152 Hz). IR (KBr, cm^{-1}): 3050, 2919, 1614 (n_{CO}), 1584, 1482, 1431, 1363, 1320, 1186, 1157, 1108, 1027, 916. Anal. Calcd. for $C_{56}H_{45}O_2P_3PtSi$: C, 63.09; H, 4.25. Found: C, 62.97; H, 4.33.

Preparation of 6.5. Under a dinitrogen atmosphere, [SiP$^{Ph}_3$]PtCH$_3$ (0.108 g, 0.106 mmol) was suspended in dichloromethane (2 mL). A dichloromethane solution (2 mL) of $H(OEt_2)_2BAr^F_4$ (0.107 g, 0.106 mmol) was added in one portion. The solution immediately went clear and became red-orange. After stirring for 2 min, volitiles were

removed *in vacuo*. The residues were recrystallized from diethyl ether/petroleum ether (-30°C). The resulting yellow-orange crystals were crushed and dried under vacuum for 18 h, giving analytically pure **6.5** as a red powder (0.171 g, 86%). The complex is stable under a dinitrogen atmosphere indefinitely. Crystals suitable for X-ray diffraction were grown by diffusion of petroleum ether vapors into a concentrated dichloromethane solution. ^{1}H NMR (C_6D_6, δ): 8.42 (br, 8H, BAr^F_4 *o*-C*H*), 7.63 (m, 7H, overlapping BAr^F_4 *p*-C*H* and a SiP_3 Ar*H* peak), 7.04 (t, J = 7.2 Hz, 3H), 6.9 – 6.7 (m, 36H). ^{13}C{^{1}H} NMR (C_6D_6, δ): 163.2 (q, $^{1}J_{BC}$ = 49.4 Hz, B-*C*), 135.8 (s), 133.0 (s), 131.2 (q, $^{1}J_{CF}$ = 35.4 Hz, Ar*C*F_3), 130.2 (q, $^{1}J_{CF}$ = 34.3 Hz, Ar*C*F_3), 129.3 (s), 126.7 (s), 124.5 (s), 122.4 (s), 118.4 (s) (*Note*: Some peaks are likely obscured by the C_6D_6 peak). ^{19}F NMR (C_6D_6, δ): -62.9 (s). ^{31}P{^{1}H} NMR (C_6D_6, δ): 54.5 ($^{1}J_{PtP}$ = 3064 Hz). IR (KBr, cm^{-1}): 3059, 2984, 1610, 1481, 1435, 1355, 1278, 1130, 1000. Anal. Calcd. for $C_{86}H_{54}BF_{24}P_3PtSi$ (i.e., {[SiP^{Ph}_3]Pt}{BAr^F_4}): C, 55.23; H, 2.91. Calcd. for $C_{90}H_{64}BF_{24}OP_3PtSi$ (i.e., {[SiP^{Ph}_3]Pt(OEt_2)}{BAr^F_4}): C, 55.60; H, 3.32. Calcd. for $C_{87}H_{56}BF_{24}P_3PtSi$ (i.e., {[SiP^{Ph}_3]Pt(CH_2Cl_2)}{BAr^F_4}): C, 53.45; H, 2.89. Found: C, 55.56; H, 3.01.

Preparation of {[SiP^{Ph}_3]Pt(η^2-H_2SiMePh)}{BAr^F_4} (6.6.2). Under a dinitrogen atmosphere, **6.5** (15.2 mg, 8.13 μmol) was dissolved in either C_6H_6, C_6D_6 or CD_2Cl_2 (ca. 0.7 mL), giving a red-orange solution. H_2SiMePh (1.00 μL, 8.1 μmol) was added in one portion, resulting in an immediate color change to bright yellow. Diffusion of petroleum ether vapors into such a solution gave X-ray quality crystals. However, either exposing the crystals to vacuum or evaporating a solution to dryness results in reversion to **6.5**. Therefore, satisfactory combustion analysis data could not be obtained. ^{1}H NMR (CD_2Cl_2, 20°C, δ): 8.14 (d, J = 7.2 Hz, 3H), 7.74 (br, 4H, BAr^F_4 *p*-C*H*), 7.57 (m, 6H),

7.40 – 7.28 (m, 29H), 7.20 (m, 3H), 7.09 (t, J = 7.6 Hz, 6H), 6.84 (br, 8H, BAr^F_4 *o*-C*H*), 4.32 (br, 2H, H_2SiMePh), 0.41 (br, 3H, $H_2SiPhCH_3$). ^{19}F NMR (CD_2Cl_2, 20°C, δ): -63.2 (s). $^{31}P\{^1H\}$ NMR (CD_2Cl_2, 20°C, δ): 37.9 ($^1J_{PtP}$ = 3022 Hz). ^{1}H NMR (CD_2Cl_2, -60°C, δ): 8.13 (d, J = 7.2 Hz, 3H), 7.74 (br, 4H, BAr^F_4 *p*-C*H*), 7.57 – 7.51 (m, 11H), 7.39 – 7.21 (m, 26H), 7.07 – 6.97 (m, 6H), 6.79 – 6.70 (m, 6H), 6.23 (d, J = 7.2 Hz, 3H), 4.89 (br, 1H, unbound H_2SiPhMe), 0.12 (br, 3H, $H_2SiPhCH_3$), -5.01 (br, J_{PtH} = 346 Hz, 1H, bound H_2SiPhMe). ^{19}F NMR (CD_2Cl_2, -60°C, δ): -63.2 (s). $^{31}P\{^1H\}$ NMR (CD_2Cl_2, -60°C, δ): 37.9 ($^1J_{PtP}$ = 3022 Hz). IR (C_6H_6, cm^{-1}): 2136, 1900.

References Cited

1 (a) Crabtree, R. H. *Chem. Rev.* **1985**, *85*, 245. (b) Lersch, M.; Tilset, M. *Chem. Rev.* **2005**, *105*, 2471.

2 Shilov, A. E. *Activation of Saturated Hydrocarbons by Transition Metal Complexes*; D. Reidel: Dordrecht, The Netherlands, **1984**.

3 Crabtree, R. H. *The Organometallic Chemistry of the Transition Metals*; 3rd edition; Wiley-Interscience: New York, **2001**.

4 (a) Mankad, N. P.; Whited, M. T.; Peters, J. C. *Angew. Chem., Int. Ed.* **2007**, *46*, 5768. (b) Whited, M. T.; Mankad, N. P.; Lee, Y.; Oblad, P. F.; Peters, J. C. *Inorg. Chem.*; **2009**; *48*; 2507.

5 (a) Ostendorf, D.; Landis, C.; Grützmacher, H. *Angew. Chem., Int. Ed.* **2006**, *45*, 5169. (b) Douvris, C.; Reed, C. A. *Organometallics* **2008**, *27*, 807. (c) Ogasaware, M.; Macgregor, S. A.; Streib, W. E.; Folting, K.; Eisenstein, O.; Caulton, K. G. *J. Am. Chem. Soc.* **1995**, *117*, 8869.

6 Bontemps, S.; Bouhadir, G.; Gu, W.; Mercy, M.; Chen, C.-H.; Foxman, B. M.; Maron, L.; Ozerov, O. V.; Bourissou, D. *Angew. Chem., Int. Ed.* **2008**, *47*, 1481.

7 Selected references: (a) Sangtrirutnugul, P.; Stradiotto, M.; Tilley, T. D. *Organometallics* **2006**, *25*, 1607. (b) Mitton, S. J.; McDonald, R.; Turculet, L. *Organometallics* **2009**, *28*, 5122.

8 Bordwell, F. G.; McCallum, R. J.; Olmstead, W. N. *J. Org. Chem.* **1984**, *49*, 1424.

9 Bordwell, F. G.; Algrim, D. *J. Org. Chem.* **1976**, *41*, 2507.

10 Tsay, C.; Mankad, N. P.; Peters, J. C. *Manuscript in preparation*.

11 (a) Alcaraz, G.; Sabo-Etienne, S. *Coord. Chem. Rev.* **2008**, *252*, 2395. (b) Lin, Z. *Chem. Soc. Rev.* **2002**, *31*, 239.

12 For recent examples, see (a) Marchand, D.; Martinez, J.; Cavelier, F. *Eur. J. Org. Chem.* **2008**, *18*, 3107. (b) Hamze, A.; Provot, O.; Brion, J.-D.; Alami, M. *Tetrahedron Lett.* **2008**, *49*, 2429.

13 Dinuclear structures featuring silane ligands bridging two Pt centers or Pt and another transition metal are known. Selected references: (a) Tanabe, M.; Yamada, T.; Osakada, K. *Organometallics* **2003**, *22*, 2190. (b) Levchinsky, Y.; Rath, N. P.; Braddock-Wilking, J.; *Organometallics* **1999**, *18*, 2583.

14 Addison, A. W.; Rao, T. N.; Reedijk, J.; van Rijn, J.; Verschoor, G. C. *J. Chem. Soc. Dalton Trans.* **1984**, 1349.

15 Brookhart, M.; Grant, B.; Volpe, Jr., A. F. *Organometallics* **1992**, *11*, 3920.

16 Sheldrick, G. M. *Acta Cryst.* **2008**, *A64*, 112.

Appendix 1: Supplementary Data for Chapter 2

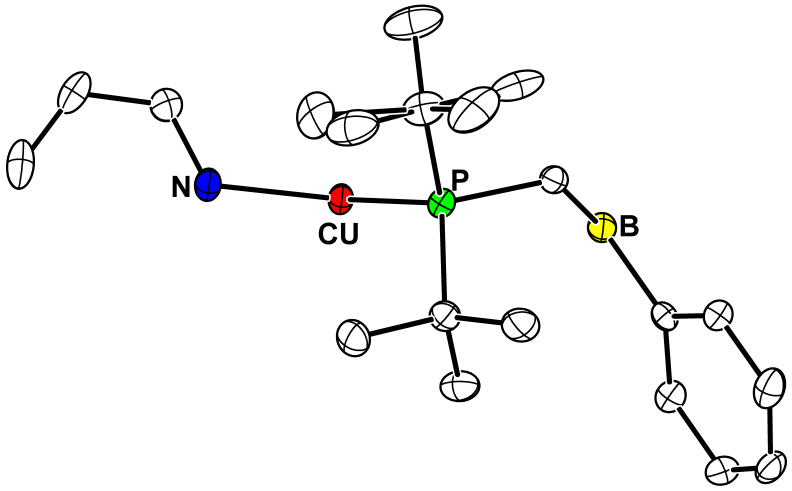

Figure A1.1. Diagram of $[Ph_2BP^{tBu}_2]Cu(pyridine)$ (**2.1**). Half of the molecule (not shown) was generated by symmetry operations. Disorder in the *tert*-butyl group was modeled as shown. Note: The Flack parameter refined to 0.009(12) in this structure. Ellipsoids are plotted at 50% probability. Hydrogen atoms have been omitted for clarity.

Table A1.1. Crystal data and structure refinement for $[Ph_2BP^{tBu}_2]Cu(pyridine)$ (**2.1**).

Empirical formula	$C_{18}H_{28}BCuNP_2$	
Formula weight	394.70	
Temperature	100(2) K	
Wavelength	0.71073 Å	
Crystal system	Orthorhombic	
Space group	*Fdd*2	
Unit cell dimensions	a = 16.5848(13) Å	α = 90°
	b = 30.917(2) Å	β = 90°
	c = 13.3863(10) Å	γ = 90°
Volume	6863.8(9) $Å^3$	
Z	8	
Density (calculated)	0.764 g/cm^3	
Absorption coefficient	0.729 mm^{-1}	
F(000)	1656	
Crystal size	0.33 x 0.15 x 0.11 mm^3	
θ range for data collection	2.06 to 23.27°	
Index ranges	$-18 \le h \le 18$, $-34 \le k \le 34$, $-14 \le l \le 14$	
Reflections collected	8664	
Independent reflections	2460 [R(int) = 0.0409]	
Completeness to θ = 23.27°	99.9 %	
Absorption correction	None	
Refinement method	Full-matrix least-squares on F^2	
Data / restraints / parameters	2460 / 1 / 210	
Goodness-of-fit on F^2	0.973	
Final R indices [$I>2\sigma(I)$]	R1 = 0.0273, wR2 = 0.0674	
R indices (all data)	R1 = 0.0297, wR2 = 0.0691	
Absolute structure parameter	0.009(12)	
Largest diff. peak and hole	0.316 and -0.318 $e.Å^{-3}$	

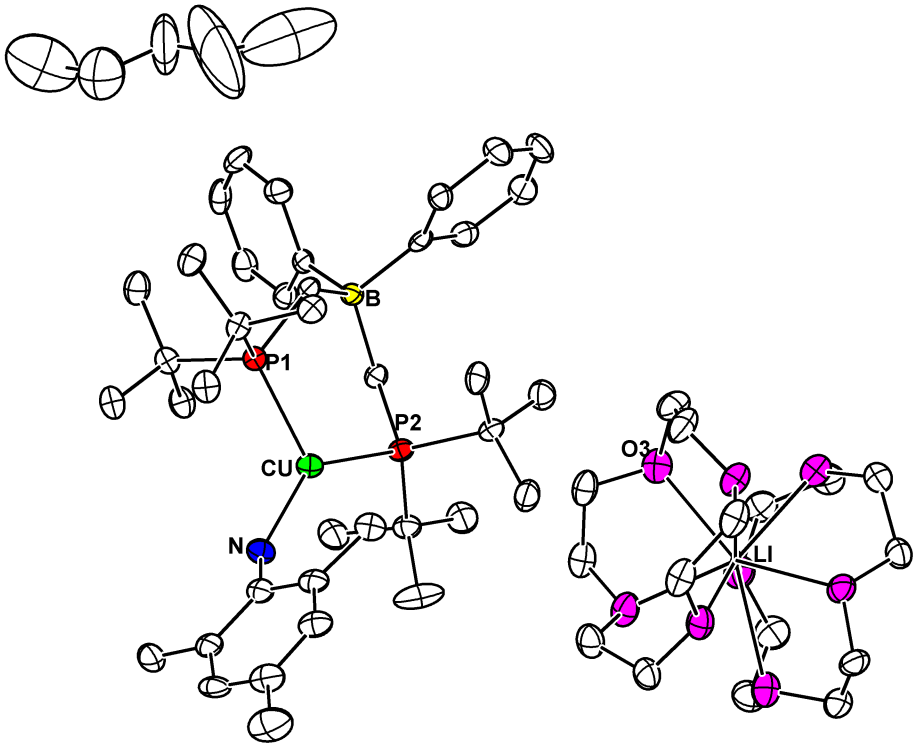

Figure A1.2. Diagrams of {[$Ph_2BP^{tBu}{}_2$]Cu(NHMes)}{Li(12-crown-$4)_2$} (**2.2**) and a cocrystallized pentane molecule. Ellipsoids are plotted at 50% probability. Hydrogen atoms have been omitted for clarity.

Table A1.2. Crystal data and structure refinement for {[$Ph_2BP^{tBu}{}_2$]Cu(NHMes)}{Li(12-crown-$4)_2$} (**2.2**).

Empirical formula	$C_{60}H_{106}BCuLiNO_8P_2$	
Formula weight	1112.69	
Temperature	100(2) K	
Wavelength	0.71073 Å	
Crystal system	Monoclinic	
Space group	$P2_1/c$	
Unit cell dimensions	a = 11.9146(9) Å	α = 90°
	b = 21.3858(16) Å	β = 92.5560(10)°
	c = 24.4619(18) Å	γ = 90°
Volume	6226.8(8) $Å^3$	
Z	8	
Density (calculated)	2.374 g/cm^3	
Absorption coefficient	0.905 mm^{-1}	
F(000)	4832	
Crystal size	0.42 x 0.15 x 0.14 mm^3	
θ range for data collection	1.71 to 33.18°	
Index ranges	$-18 \le h \le 15$, $-27 \le k \le 27$, $-32 \le l \le 32$	
Reflections collected	72625	
Independent reflections	14800 [R(int) = 0.0841]	
Completeness to θ = 33.18°	62.1 %	
Refinement method	Full-matrix least-squares on F^2	
Data / restraints / parameters	14800 / 0 / 684	
Goodness-of-fit on F^2	2.234	
Final R indices [$I>2\sigma(I)$]	R1 = 0.0715, wR2 = 0.1193	
R indices (all data)	R1 = 0.1280, wR2 = 0.1242	
Largest diff. peak and hole	1.631 and -0.989 $e.Å^{-3}$	

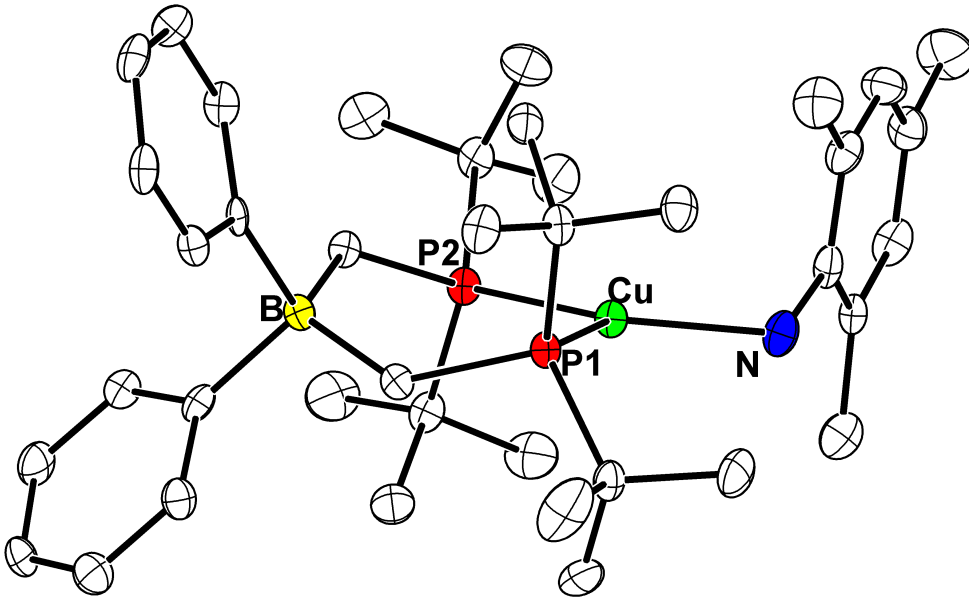

Figure A1.3. Diagram of $[Ph_2BP^{tBu}_2]Cu(NH_2Mes)$ (**2.3**). Ellipsoids are plotted at 50% probability. Hydrogen atoms have been omitted for clarity.

Table A1.3. Crystal data and structure refinement for $[Ph_2BP^{tBu}{}_2]Cu(NH_2Mes)$ (**2.3**).

Empirical formula	$C_{39}H_{63}BCuNP_2$	
Formula weight	682.19	
Temperature	293(2) K	
Wavelength	0.71073 Å	
Crystal system	Monoclinic	
Space group	$P2_1/n$	
Unit cell dimensions	a = 10.186(5) Å	α = 90°
	b = 17.079(8) Å	β = 98.24(4)°
	c = 22.083(7) Å	γ = 90°
Volume	3802(3) Å^3	
Z	4	
Density (calculated)	1.192 g/cm^3	
Absorption coefficient	0.685 mm^{-1}	
F(000)	1472	
Crystal size	0.22 x 0.17 x 0.11 mm^3	
θ range for data collection	1.51 to 28.38°	
Index ranges	$-12 \le h \le 13$, $-19 \le k \le 19$, $-28 \le l \le 22$	
Reflections collected	31590	
Independent reflections	7306 [R(int) = 0.0990]	
Completeness to θ = 28.38°	76.6 %	
Refinement method	Full-matrix least-squares on F^2	
Data / restraints / parameters	7306 / 0 / 412	
Goodness-of-fit on F^2	1.288	
Final R indices [$I>2\sigma(I)$]	R1 = 0.0473, wR2 = 0.0746	
R indices (all data)	R1 = 0.1049, wR2 = 0.0834	
Largest diff. peak and hole	0.640 and -0.498 e.Å^{-3}	

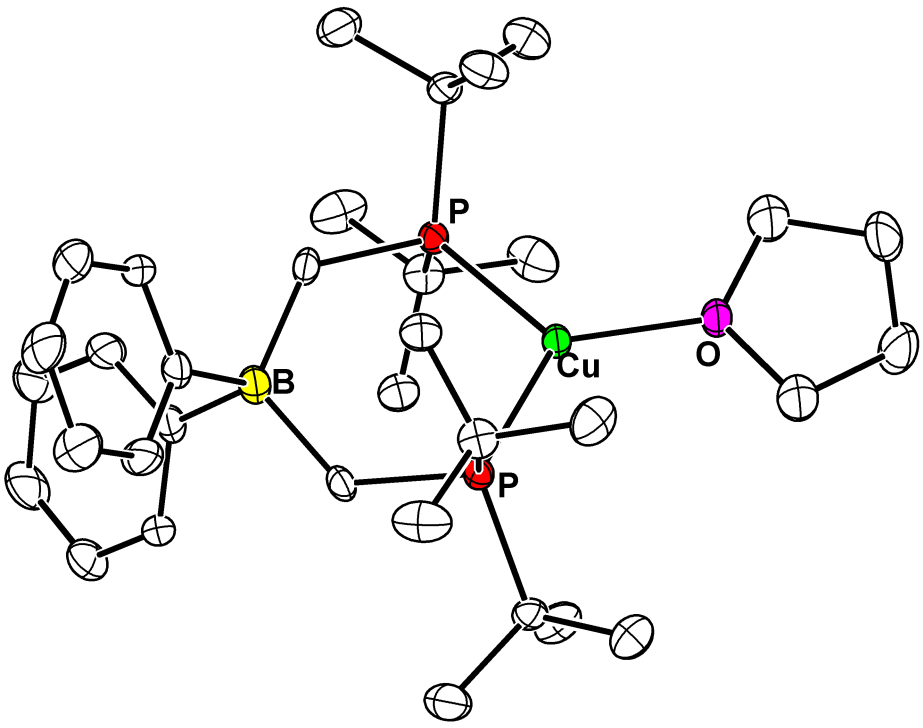

Figure A1.4. Diagram of $[Ph_2BP^{tBu}_2]Cu(THF)$ (**2.4**), which sits on a crystallographic twofold axis of symmetry. Ellipsoids are plotted at 50% probability. Hydrogen atoms have been omitted for clarity.

Table A1.4. Crystal data and structure refinement for $[Ph_2BP^{tBu}_2]Cu(THF)$ (**2.4**).

Empirical formula	$C_{34}H_{58}BCuOP_2$	
Formula weight	619.09	
Temperature	100(2) K	
Wavelength	0.71073 Å	
Crystal system	Orthorhombic	
Space group	*Fdd*2	
Unit cell dimensions	a = 17.548(3) Å	α = 90°
	b = 30.333(5) Å	β = 90°
	c = 12.818(3) Å	γ = 90°
Volume	6823(2) $Å^3$	
Z	8	
Density (calculated)	1.205 g/cm^3	
Absorption coefficient	0.758 mm^{-1}	
F(000)	2672	
Crystal size	0.59 x 0.33 x 0.30 mm^3	
θ range for data collection	2.08 to 28.45°	
Index ranges	$-15 \le h \le 12$, $-40 \le k \le 11$, $-16 \le l \le 9$	
Reflections collected	3639	
Independent reflections	2005 [R(int) = 0.0358]	
Completeness to θ = 28.45°	70.7 %	
Refinement method	Full-matrix least-squares on F^2	
Data / restraints / parameters	2005 / 1 / 185	
Goodness-of-fit on F^2	2.106	
Final R indices [$I>2\sigma(I)$]	R1 = 0.0345, wR2 = 0.0646	
R indices (all data)	R1 = 0.0388, wR2 = 0.0653	
Absolute structure parameter	1.01(3)	
Largest diff. peak and hole	0.548 and -0.324 e.$Å^{-3}$	

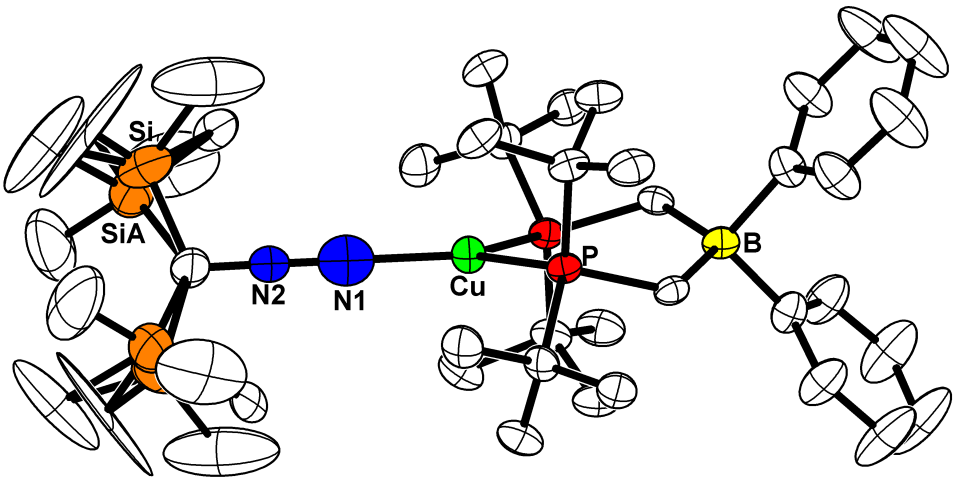

Figure A1.5. Diagram of $[Ph_2BP^{tBu}_2]Cu(N_2C(SiMe_3)_2)$ (**2.5**), which sits on a crystallographic twofold axis of symmetry. Disorder in the $SiMe_3$ group was modeled as indicated in the diagram. Ellipsoids are plotted at 50% probability. Hydrogen atoms have been omitted for clarity.

Table A1.5. Crystal data and structure refinement for $[Ph_2BP^{tBu}{}_2]Cu(N_2C(SiMe_3)_2$ (**2.5**).

Empirical formula	$C_{34}H_{59}BCuN_2P_2Si_2$	
Formula weight	688.30	
Temperature	100(2) K	
Wavelength	0.71073 Å	
Crystal system	Rhombohedral	
Space group	*R*-3*c*	
Unit cell dimensions	a = 21.4508(13) Å	α = 90°
	b = 21.4508(13) Å	β = 90°
	c = 47.633(3) Å	γ = 120.
Volume	18981(2) $Å^3$	
Z	15	
Density (calculated)	0.903 g/cm^3	
Absorption coefficient	0.561 mm^{-1}	
F(000)	5535	
Crystal size	0.41 x 0.22 x 0.09 mm^3	
θ range for data collection	1.90 to 23.33°	
Index ranges	$-23 \le h \le 23$, $-23 \le k \le 23$, $-52 \le l \le 52$	
Reflections collected	37667	
Independent reflections	3067 [R(int) = 0.0834]	
Completeness to theta = 23.33°	99.9 %	
Absorption correction	None	
Refinement method	Full-matrix least-squares on F^2	
Data / restraints / parameters	3067 / 0 / 254	
Goodness-of-fit on F^2	1.121	
Final R indices [$I>2\sigma(I)$]	R1 = 0.0453, wR2 = 0.1020	
R indices (all data)	R1 = 0.0720, wR2 = 0.1224	
Largest diff. peak and hole	0.579 and -0.362 e.$Å^{-3}$	

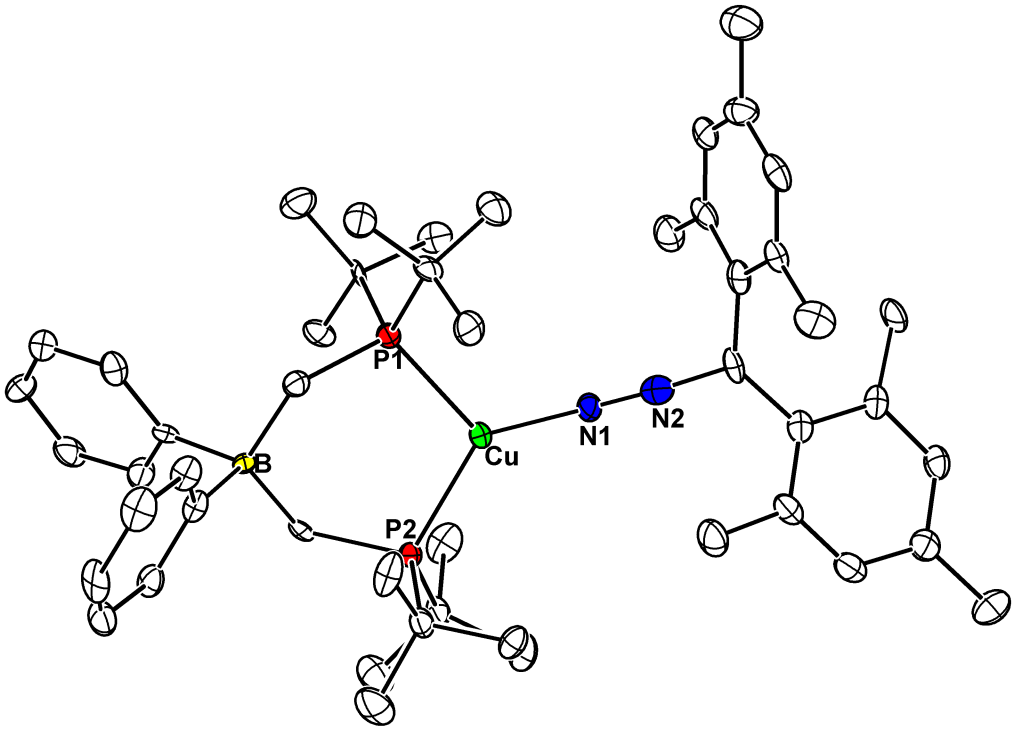

Figure A1.6. Diagram of $[Ph_2BP^{tBu}_2]Cu(N_2CMes_2)$ (**2.6**). Ellipsoids are plotted at 50% probability. Hydrogen atoms have been omitted for clarity.

Table A1.6. Crystal data and structure refinement for $[Ph_2BP^{tBu}{}_2]Cu(N_2CMes_2)$ (**2.6**).

Empirical formula	$C_{49}H_{72}BCuN_2P_2$	
Formula weight	825.38	
Temperature	100(2) K	
Wavelength	0.71073 Å	
Crystal system	Monoclinic	
Space group	$P2_1/c$	
Unit cell dimensions	a = 11.6975(16) Å	α = 90°
	b = 17.955(2) Å	β = 91.707(4)°
	c = 23.035(3) Å	γ = 90°
Volume	4836.1(12) Å^3	
Z	4	
Density (calculated)	1.134 g/cm^3	
Absorption coefficient	0.550 mm^{-1}	
F(000)	1776	
Crystal size	0.15 x 0.13 x 0.11 mm^3	
θ range for data collection	1.44 to 24.16°	
Index ranges	$-12 \le h \le 13$, $-20 \le k \le 20$, $-25 \le l \le 25$	
Reflections collected	22763	
Independent reflections	6798 [R(int) = 0.1309]	
Completeness to θ = 24.16°	87.7 %	
Refinement method	Full-matrix least-squares on F^2	
Data / restraints / parameters	6798 / 6 / 514	
Goodness-of-fit on F^2	0.910	
Final R indices [$I>2\theta(I)$]	R1 = 0.0571, wR2 = 0.1168	
R indices (all data)	R1 = 0.1360, wR2 = 0.1425	
Largest diff. peak and hole	0.505 and -0.465 e.Å^{-3}	

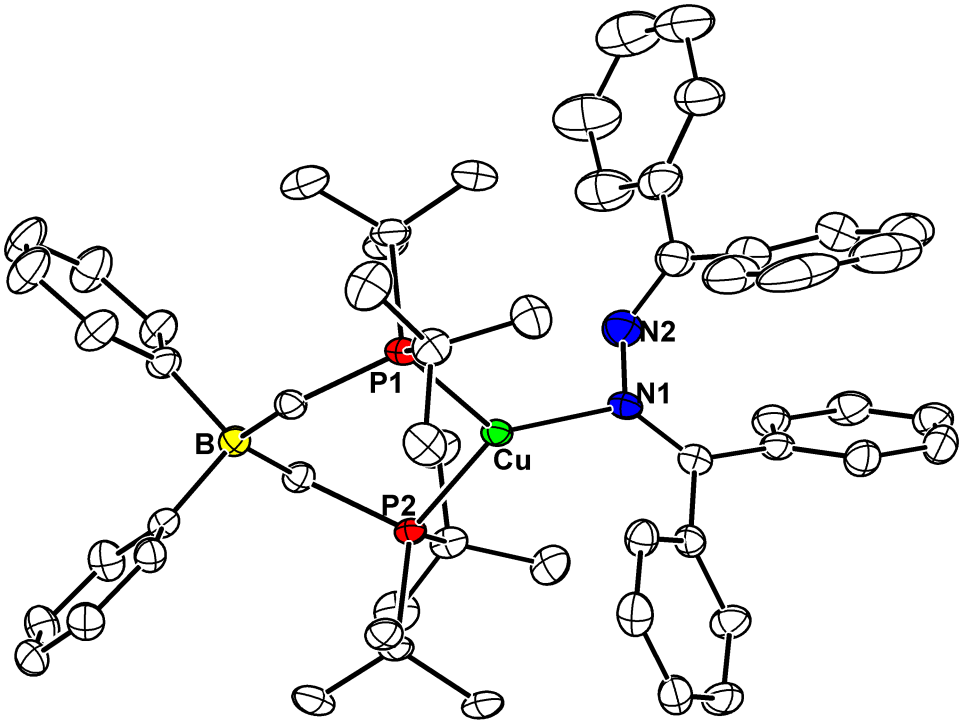

Figure A1.7. Diagram of $[Ph_2BP^{tBu}_2]Cu(N(=CPh_2)NCPh_2)$ (**2.7**). Ellipsoids are plotted at 50% probability. Hydrogen atoms have been omitted for clarity.

Table A1.7. Crystal data and structure refinement for $[Ph_2BP^{tBu}{}_2]Cu(N(=CPh_2)NCPh_2)$ (**2.7**).

Empirical formula	$C_{56}H_{70}BCuN_2P_2$	
Formula weight	907.43	
Temperature	100(2) K	
Wavelength	0.71073 Å	
Crystal system	Monoclinic	
Space group	$P2_1/c$	
Unit cell dimensions	a = 12.0749(11) Å	α = 90°
	b = 22.347(2) Å	β = 104.625(2)°
	c = 19.2412(18) Å	γ = 90°
Volume	5023.8(8) $Å^3$	
Z	4	
Density (calculated)	1.200 g/cm^3	
Absorption coefficient	0.536 mm^{-1}	
F(000)	1936	
Crystal size	0.31 x 0.30 x 0.11 mm^3	
θ range for data collection	1.74 to 28.46°	
Index ranges	$-15 \le h \le 15$, $-28 \le k \le 28$, $-24 \le l \le 24$	
Reflections collected	42567	
Independent reflections	11402 [R(int) = 0.0617]	
Completeness to θ = 28.46°	90.0 %	
Refinement method	Full-matrix least-squares on F^2	
Data / restraints / parameters	11402 / 0 / 571	
Goodness-of-fit on F^2	2.064	
Final R indices [$I>2\sigma(I)$]	R1 = 0.0574, wR2 = 0.0940	
R indices (all data)	R1 = 0.0967, wR2 = 0.0978	
Largest diff. peak and hole	1.112 and -0.744 $e.Å^{-3}$	

Appendix 2: Supplementary Data for Chapter 3

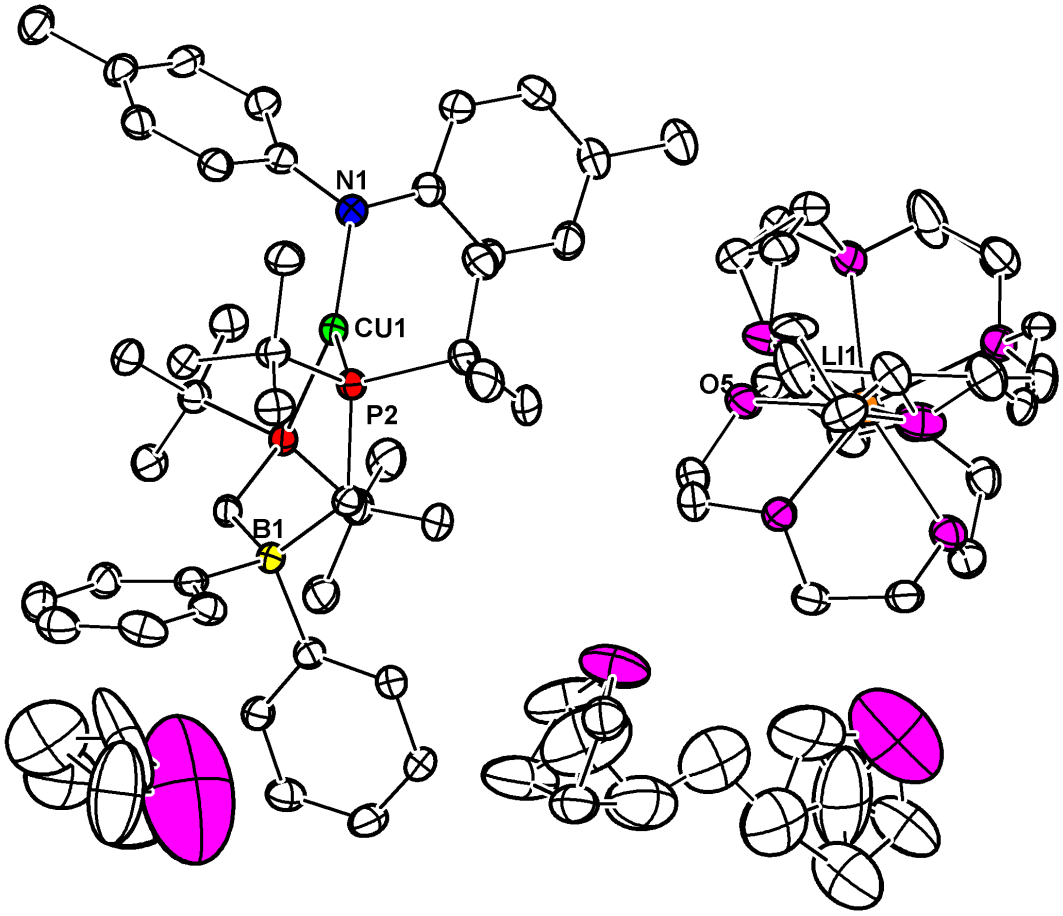

Figure A2.1. Solid-state structure of {[$Ph_2BP^{tBu}_2$]Cu($NTol_2$)}{Li(12-crown-4)$_2$} (**3.1**, 50% ellipsoids). Hydrogen atoms have been omitted for clarity. Conformational disorder in the 12-crown-4 and solvent regions were modeled as depicted in the diagram.

Table A2.1. Crystal data and structure refinement for **3.1**.

Empirical formula	$C_{70.57}H_{118.12}BCuLiNO_{10.02}P_2$	
Formula weight	1284.14	
Temperature	100(2) K	
Wavelength	0.71073 Å	
Crystal system	Triclinic	
Space group	*P*-1	
Unit cell dimensions	a = 12.9114(9) Å	α = 79.4810(10)°
	b = 16.8578(12) Å	β = 74.3230(10)°
	c = 17.6005(12) Å	γ = 80.2250(10)°
Volume	3596.9(4) $Å^3$	
Z	4	
Density (calculated)	1.186 g/cm^3	
Absorption coefficient	0.403 mm^{-1}	
F(000)	2092	
Crystal size	0.35 x 0.30 x 0.15 mm^3	
θ range for data collection	1.21 to 29.13°	
Index ranges	$-17 \le h \le 17$, $-23 \le k \le 23$, $-24 \le l \le 23$	
Reflections collected	78924	
Independent reflections	19261 [R(int) = 0.0564]	
Completeness to θ= 29.13°	99.4 %	
Absorption correction	None	
Refinement method	Full-matrix least-squares on F^2	
Data / restraints / parameters	19261 / 304 / 932	
Goodness-of-fit on F^2	1.015	
Final R indices [$I>2\sigma(I)$]	R1 = 0.0518, wR2 = 0.1274	
R indices (all data)	R1 = 0.0820, wR2 = 0.1458	
Largest diff. peak and hole	0.664 and -0.559 e.$Å^{-3}$	

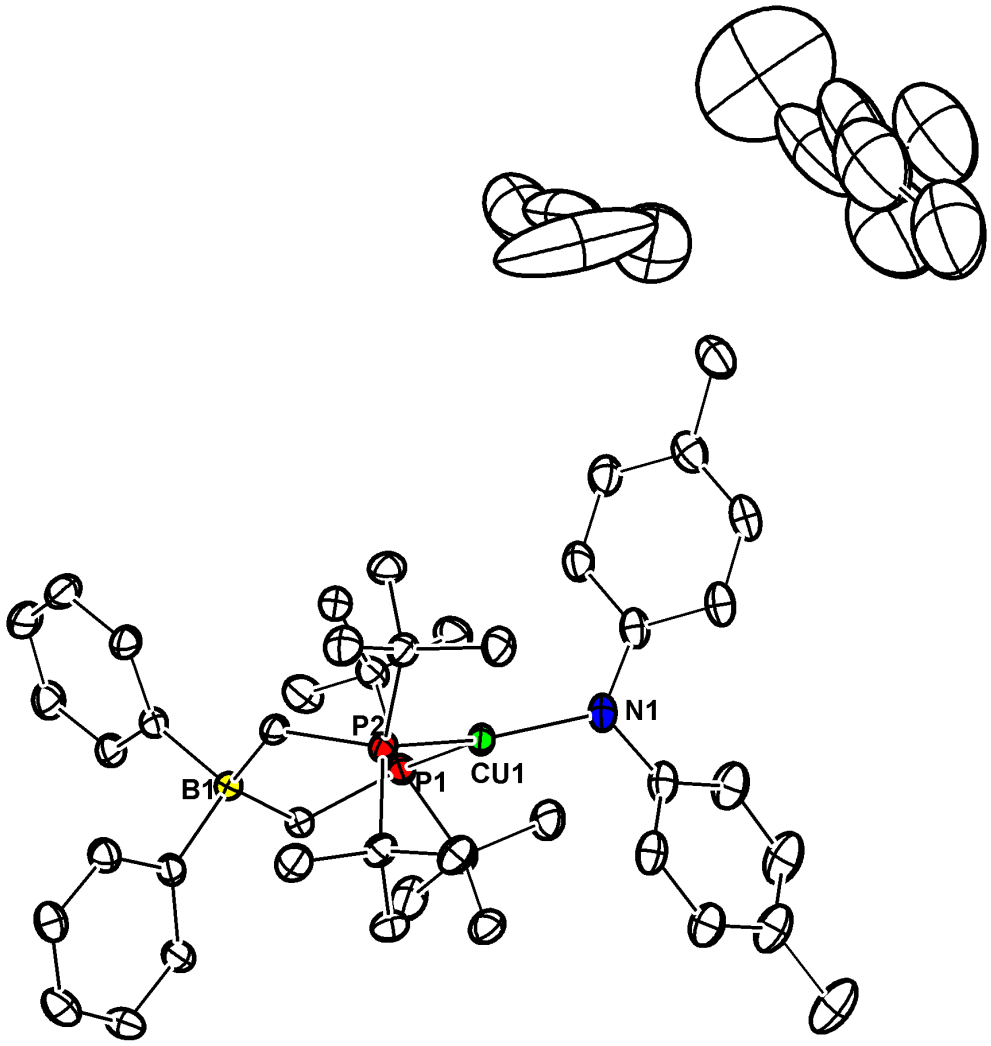

Figure A2.2. Solid-state structure of $[Ph_2BP^{tBu}_2]Cu(NTol_2)$ (**3.2**, 50% ellipsoids), including disordered solvent regions. Hydrogen atoms have been omitted for clarity.

Table A2.2. Crystal data and structure refinement for **3.2**.

Empirical formula	$C_{52.42}H_{80.84}BCuNP_2$	
Formula weight	861.36	
Temperature	100(2) K	
Wavelength	0.71073 Å	
Crystal system	Monoclinic	
Space group	$P2_1/n$	
Unit cell dimensions	a = 16.3201(18) Å	α = 90°
	b = 16.3538(18) Å	β = 91.277(2)°
	c = 18.849(2) Å	γ = 90°
Volume	5029.4(10) Å^3	
Z	4	
Density (calculated)	1.137 g/cm^3	
Absorption coefficient	0.531 mm^{-1}	
F(000)	2488	
Crystal size	0.65 x 0.35 x 0.20 mm^3	
θ range for data collection	1.63 to 29.57°	
Index ranges	$-22 \le h \le 22$, $-22 \le k \le 22$, $-26 \le l \le 26$	
Reflections collected	132059	
Independent reflections	14110 [R(int) = 0.0613]	
Completeness to θ = 29.57°	100.0 %	
Absorption correction	None	
Refinement method	Full-matrix least-squares on F^2	
Data / restraints / parameters	14110 / 105 / 562	
Goodness-of-fit on F^2	1.282	
Final R indices [$I>2\sigma(I)$]	R1 = 0.0606, wR2 = 0.1667	
R indices (all data)	R1 = 0.0807, wR2 = 0.1813	
Largest diff. peak and hole	2.930 and -1.964 e.Å^{-3}	

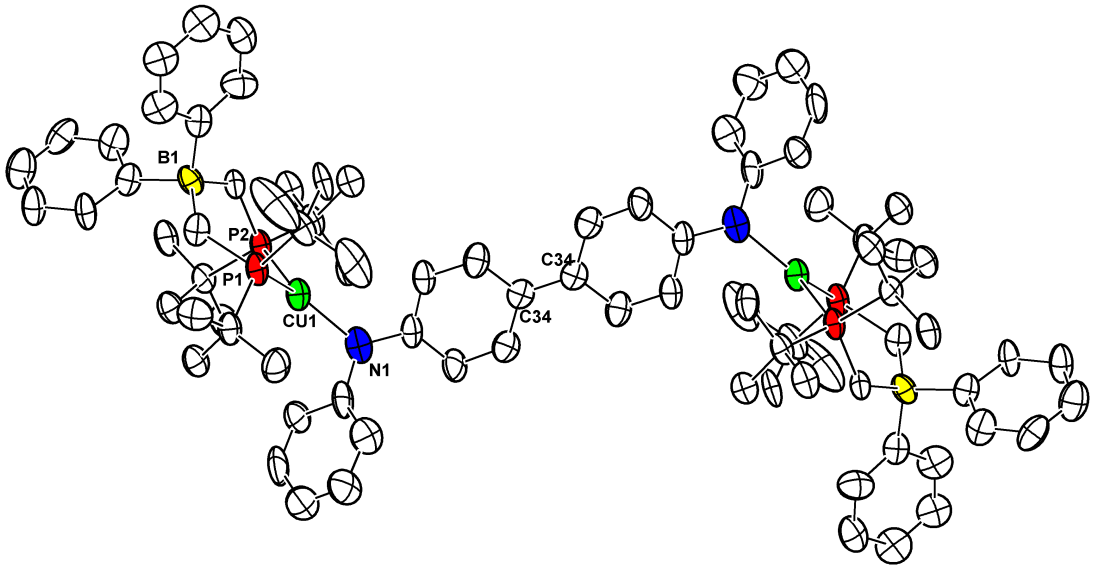

Figure A2.3. Solid-state structure of **3.5** as 50% ellipsoids. Hydrogen atoms have been omitted for clarity. Half of the molecule was generated by symmetry operations.

Table A2.3. Crystal data and structure refinement for **3.5**.

Empirical formula	$C_{42}H_{59}BCuNP_2$	
Formula weight	714.25	
Temperature	100(2) K	
Wavelength	0.71073 Å	
Crystal system	Monoclinic	
Space group	$P2_1/n$	
Unit cell dimensions	a = 10.575(15) Å	α = 90°
	b = 21.60(3) Å	β = 96.41(2)°
	c = 16.50(2) Å	γ = 90°
Volume	3745(9) $Å^3$	
Z	4	
Density (calculated)	1.297 g/cm^3	
Absorption coefficient	0.702 mm^{-1}	
F(000)	1524	
Crystal size	0.45 x 0.10 x 0.10 mm^3	
θ range for data collection	1.56 to 23.25°	
Index ranges	$-11 \le h \le 11$, $-24 \le k \le 24$, $-18 \le l \le 18$	
Reflections collected	50483	
Independent reflections	5387 [R(int) = 0.3278]	
Completeness to θ = 23.25°	100.0 %	
Absorption correction	None	
Refinement method	Full-matrix least-squares on F^2	
Data / restraints / parameters	5387 / 0 / 436	
Goodness-of-fit on F^2	1.021	
Final R indices [$I>2\sigma(I)$]	R1 = 0.1187, wR2 = 0.2839	
R indices (all data)	R1 = 0.2077, wR2 = 0.3511	
Largest diff. peak and hole	1.193 and -1.281 $e.Å^{-3}$	

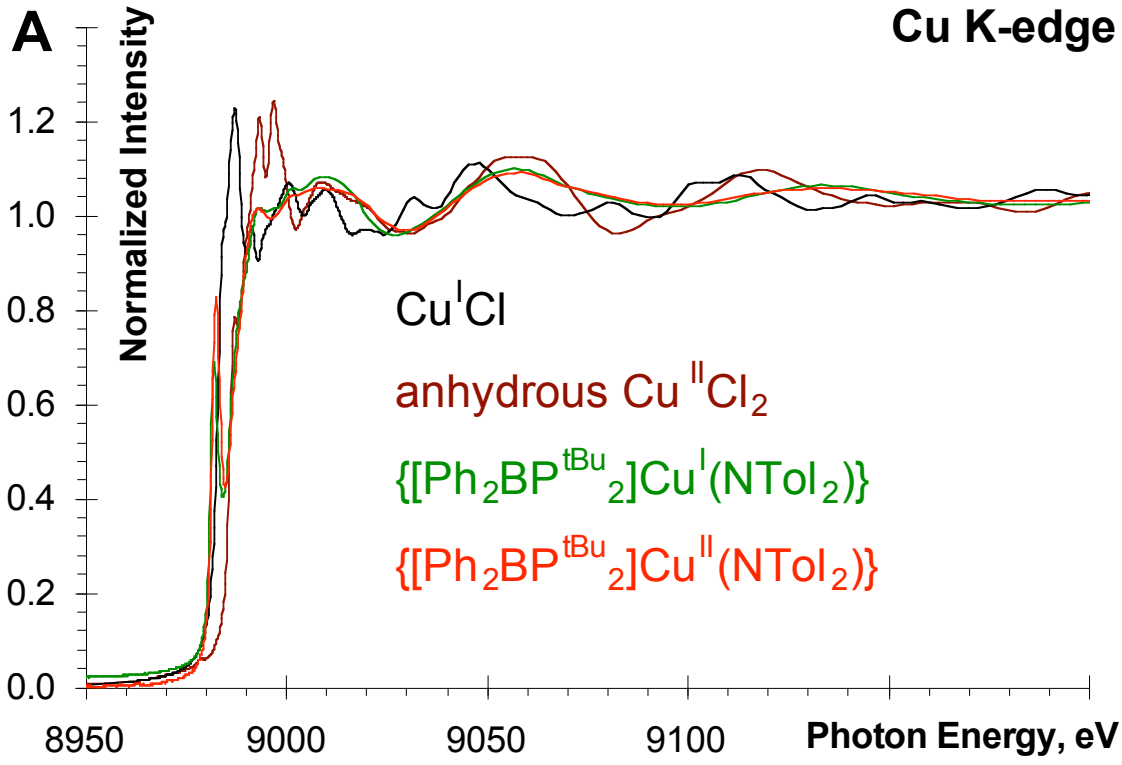

Figure A2.4. Background corrected and normalized Cu K-edge spectra for CuCl (black), anhydrous $CuCl_2$ (brown), **3.1** (green), and **3.2** (red).

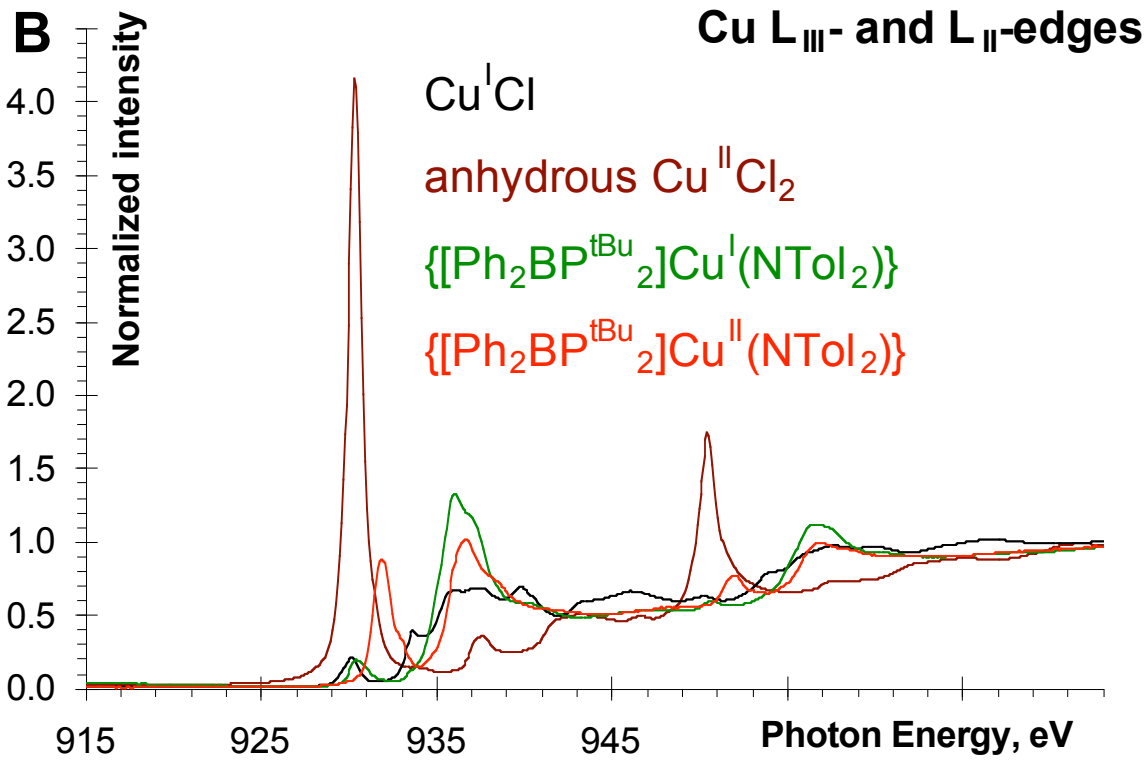

Figure A2.5. Background corrected and normalized Cu L-edge spectra for CuCl (black), anhydrous $CuCl_2$ (brown), **3.1** (green), and **3.2** (red).

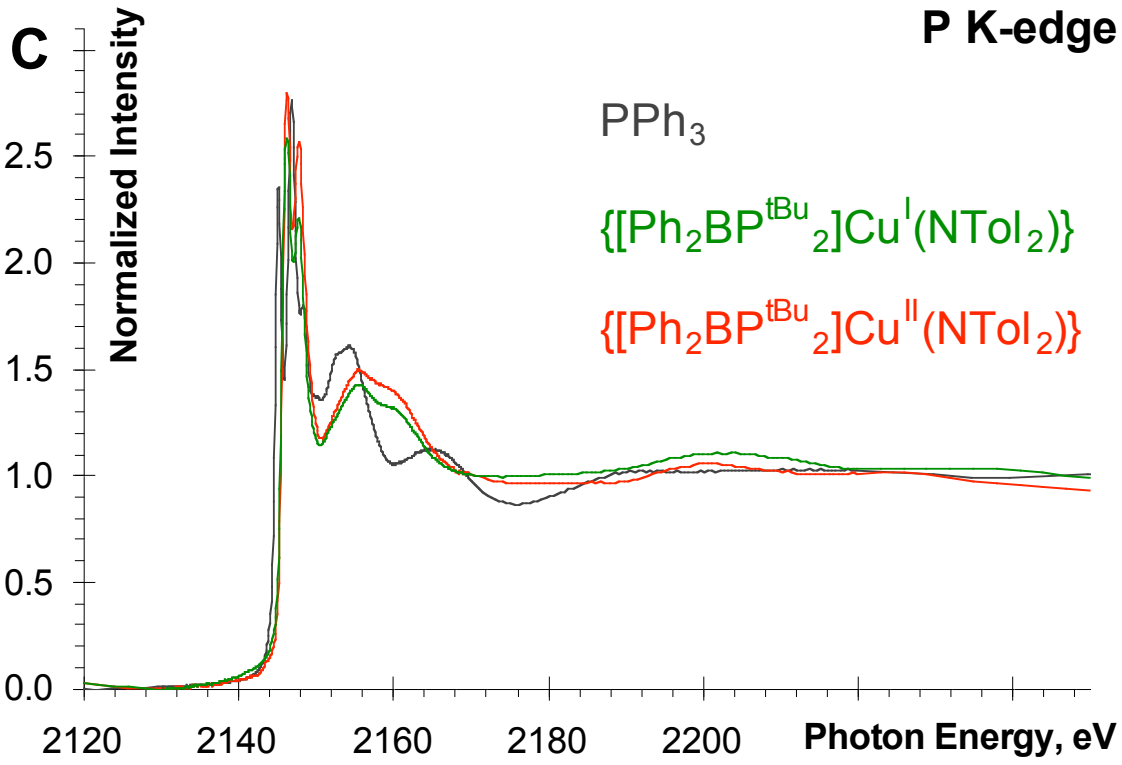

Figure A2.6. Background corrected and normalized P K-edge spectra for PPh_3 (black), **3.1** (green), and **3.2** (red).

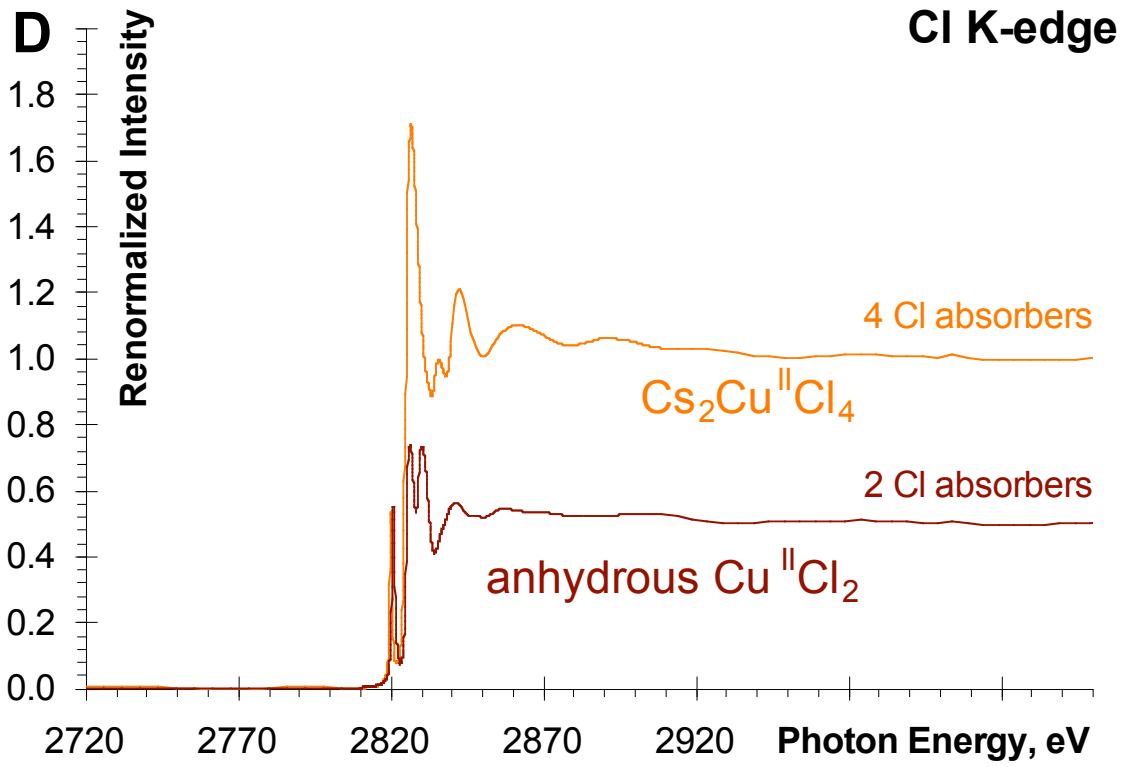

Figure A2.7. Background corrected and renormalized Cl K-edge spectra for D_{2d} $Cs_2Cu^{II}Cl_4$ (orange) and anhydrous $Cu^{II}Cl_2$.

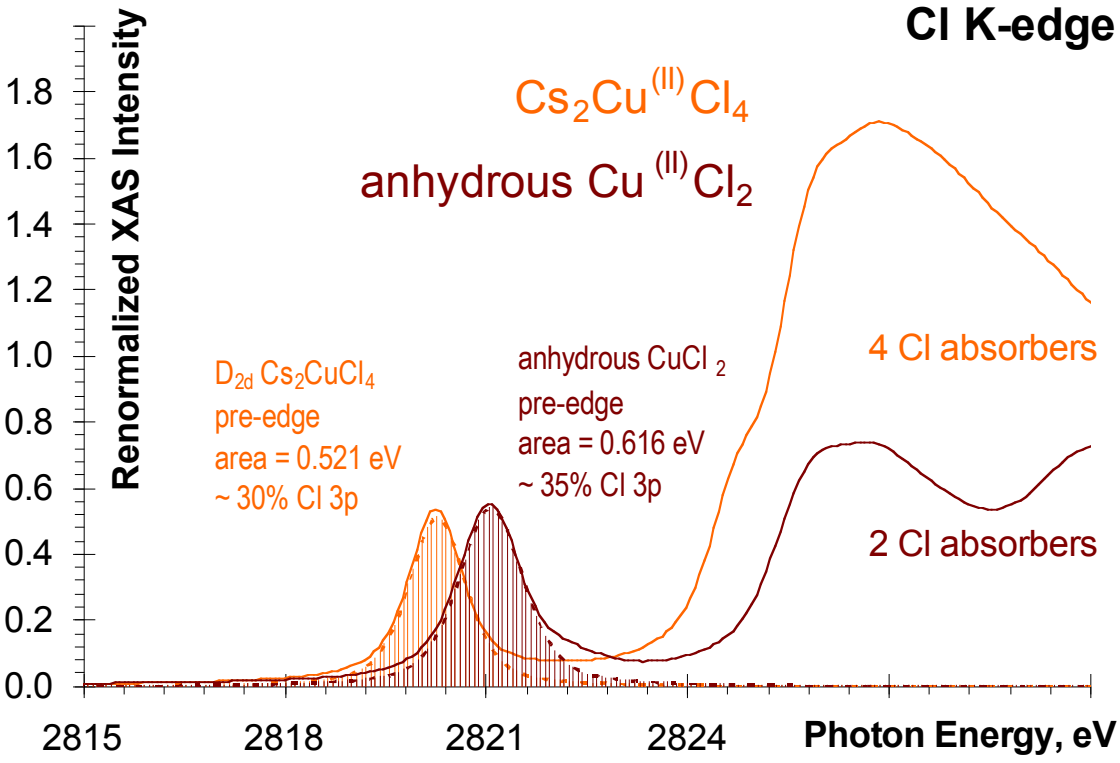

Figure A2.8. Fitted Cl K-edge XANES spectra for D_{2d} $Cs_2Cu^{II}Cl_4$ (orange) and anhydrous $Cu^{II}Cl_2$ to generate transition dipole integrals for quantifying the Cu L-edge pre-edge features.

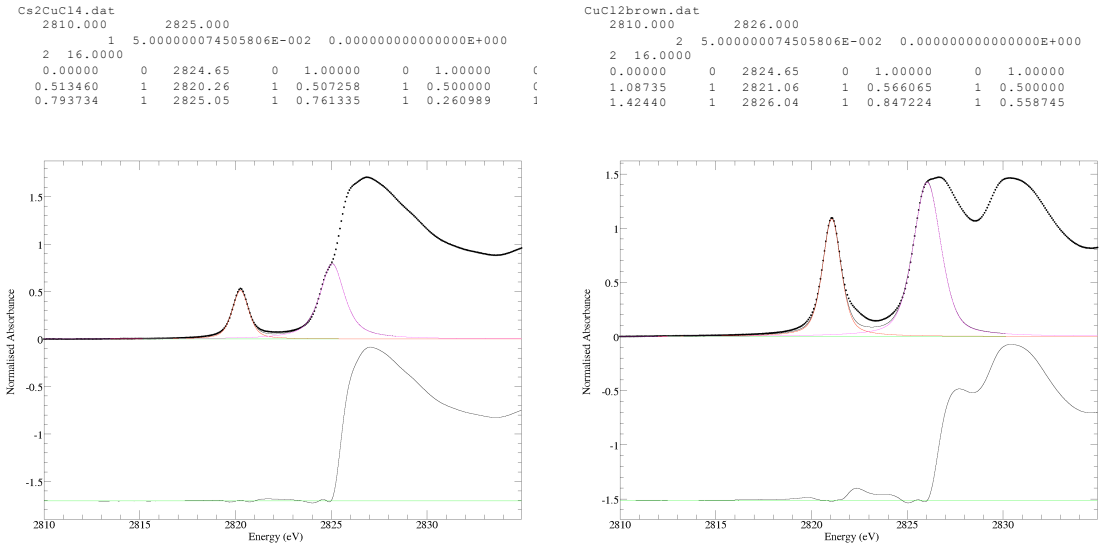

Figure A2.9. Representative fits to the pre-edge features at the Cl K-edge spectra.

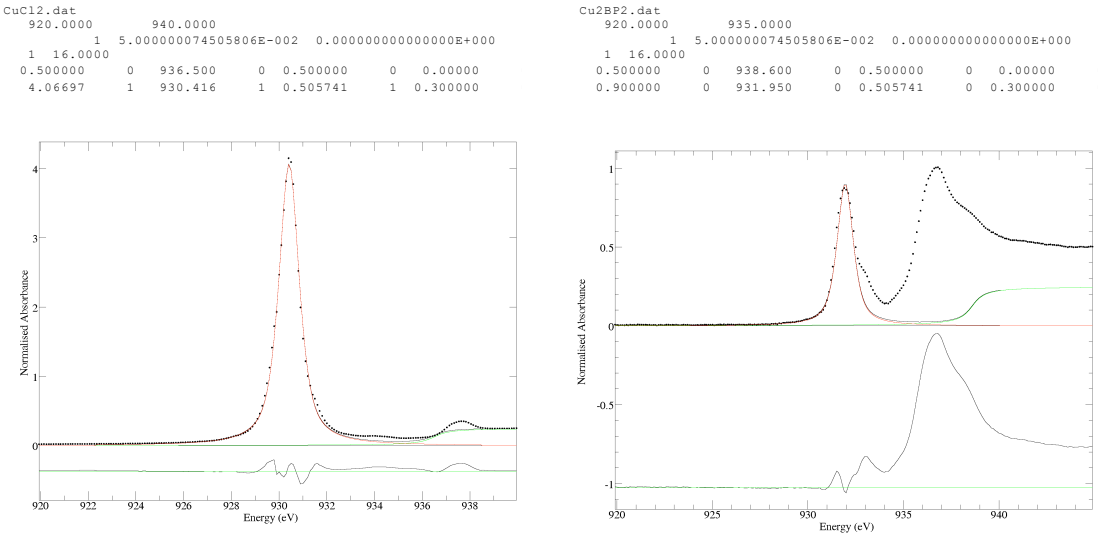

Figure A2.10. Representative fits to the pre-edge features at the Cu L_3-edge spectra.

```
Cu1BP2.dat
  2140.  2150.
 1  0.0500000007  0.
   2  16.0000
   1.00000      0   2148.50      1   1.17571      1  0.869465
   2.04091      1   2146.29      1  0.544170      1   1.00000
   2.29790      1   2147.81      1   1.06906      1  0.308965
```

```
Cu2BP2.dat
  2140.  2150.
 2  0.0500000007  0.
   3  16.0000
   1.00000      0   2148.80      1   1.17571      0  0.869465
   1.59780      0   2146.45      0  0.544170      0  0.500000
   1.89920      0   2147.85      0   1.06906      0  0.308965
  0.780000      0   2145.93      0  0.450000      0  0.500000
```

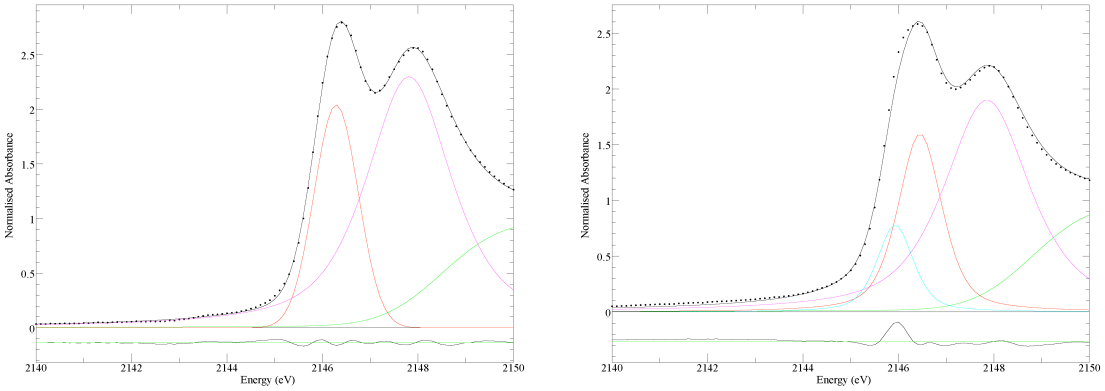

Figure A2.11. Representative fits to the pre-edge features at the P K-edge spectra.

Appendix 3: Supplementary Data for Chapter 4

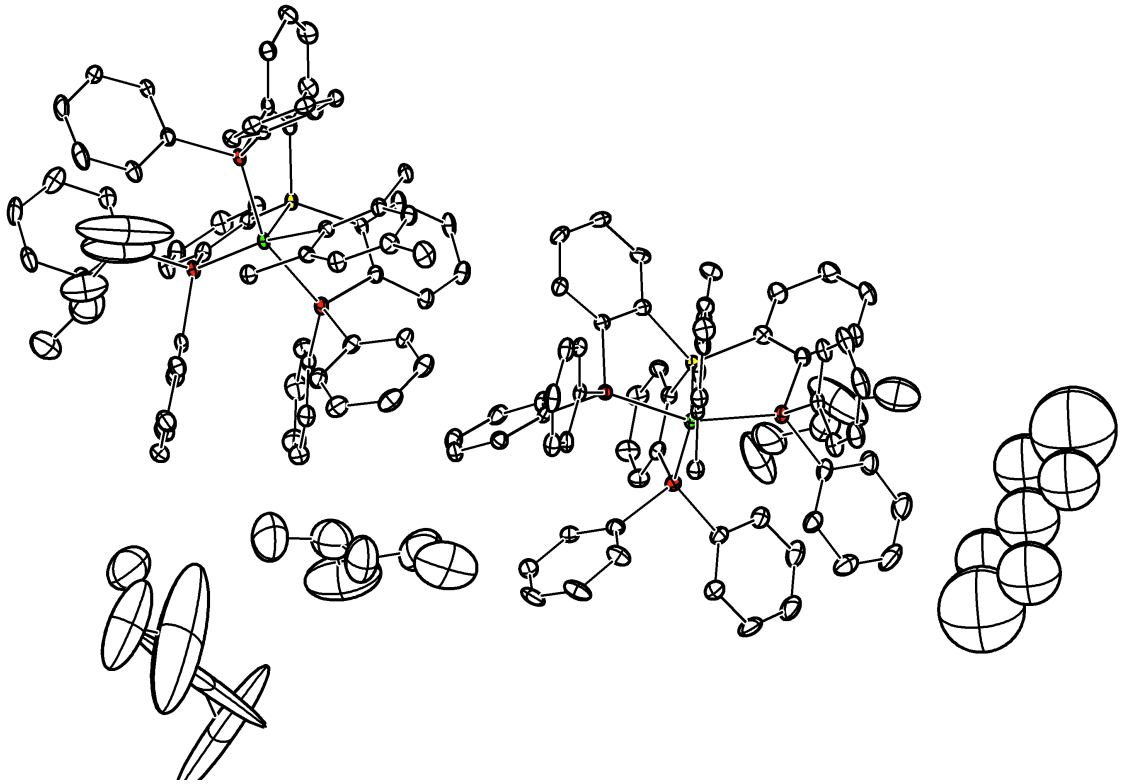

Figure A3.1. Solid-state structure of [SiP$^{Ph}_{3}$]FeMes (**4.3**, 50% ellipsoids) and cocrystallized alkane solvent molecules. Hydrogen atoms have been omitted for clarity.

Table A3.1. Crystal data and structure refinement for **4.3**.

Empirical formula	$C_{149.5}H_{162}Fe_2P_6Si_2$	
Formula weight	2312.49	
Temperature	100(2) K	
Wavelength	0.71073 Å	
Crystal system	Triclinic	
Space group	*P*-1	
Unit cell dimensions	a = 10.966(5) Å	α = 101.547(16)°
	b = 21.469(12) Å	β = 93.092(18)°
	c = 27.269(13) Å	γ = 100.968(10)°
Volume	6147(5) $Å^3$	
Z	2	
Density (calculated)	1.249 g/cm^3	
Absorption coefficient	0.387 mm^{-1}	
F(000)	2458	
Crystal size	0.37 x 0.35 x 0.13 mm^3	
θ range for data collection	1.37 to 35.99°	
Index ranges	$-14 \le h \le 16$, $-35 \le k \le 27$, $-33 \le l \le 42$	
Reflections collected	69138	
Independent reflections	33909 [R(int) = 0.0738]	
Completeness to θ = 35.99°	58.2 %	
Absorption correction	None	
Refinement method	Full-matrix least-squares on F^2	
Data / restraints / parameters	33909 / 10 / 1442	
Goodness-of-fit on F^2	0.952	
Final R indices [$I>2\sigma(I)$]	R1 = 0.0656, wR2 = 0.1590	
R indices (all data)	R1 = 0.1357, wR2 = 0.1894	
Largest diff. peak and hole	1.213 and -0.662 $e.Å^{-3}$	

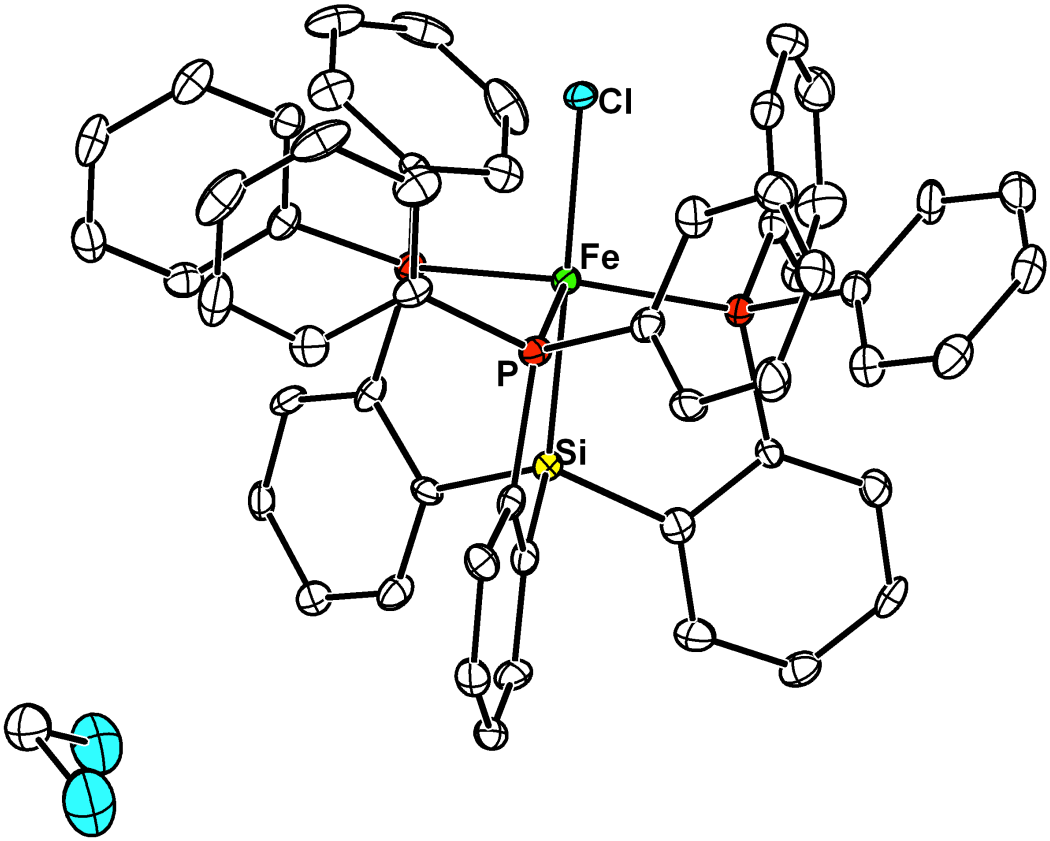

Figure A3.2. Solid-state structure of [SiP^{Ph}_3]FeCl (**4.4**, 50% ellipsoids) and aco-crystallized dichloromethane solvent molecule. Hydrogen atoms have been omitted for clarity.

Table A3.2. Crystal data and structure refinement for **4.4**.

Empirical formula	$C_{55}H_{44}Cl_2FeP_3Si$	
Formula weight	952.65	
Temperature	100(2) K	
Wavelength	0.71073 Å	
Crystal system	Triclinic	
Space group	*P*-1	
Unit cell dimensions	a = 11.1583(15) Å	α = 87.973(2)°
	b = 13.2714(18) Å	β = 84.822(2)°
	c = 15.689(2) Å	γ = 86.423(2)°
Volume	2308.3(5) Å^3	
Z	2	
Density (calculated)	1.371 g/cm^3	
Absorption coefficient	0.610 mm^{-1}	
F(000)	986	
Crystal size	0.18 x 0.067 x 0.041 mm^3	
θ range for data collection	1.54 to 26.05°	
Index ranges	$-13 \le h \le 13$, $-15 \le k \le 15$, $-11 \le l \le 18$	
Reflections collected	13098	
Independent reflections	7641 [R(int) = 0.0671]	
Completeness to θ = 26.05°	83.8 %	
Absorption correction	None	
Refinement method	Full-matrix least-squares on F^2	
Data / restraints / parameters	7641 / 0 / 569	
Goodness-of-fit on F^2	0.956	
Final R indices [$I>2\sigma(I)$]	R1 = 0.0504, wR2 = 0.0786	
R indices (all data)	R1 = 0.0975, wR2 = 0.0886	
Largest diff. peak and hole	0.587 and -0.466 e.Å^{-3}	

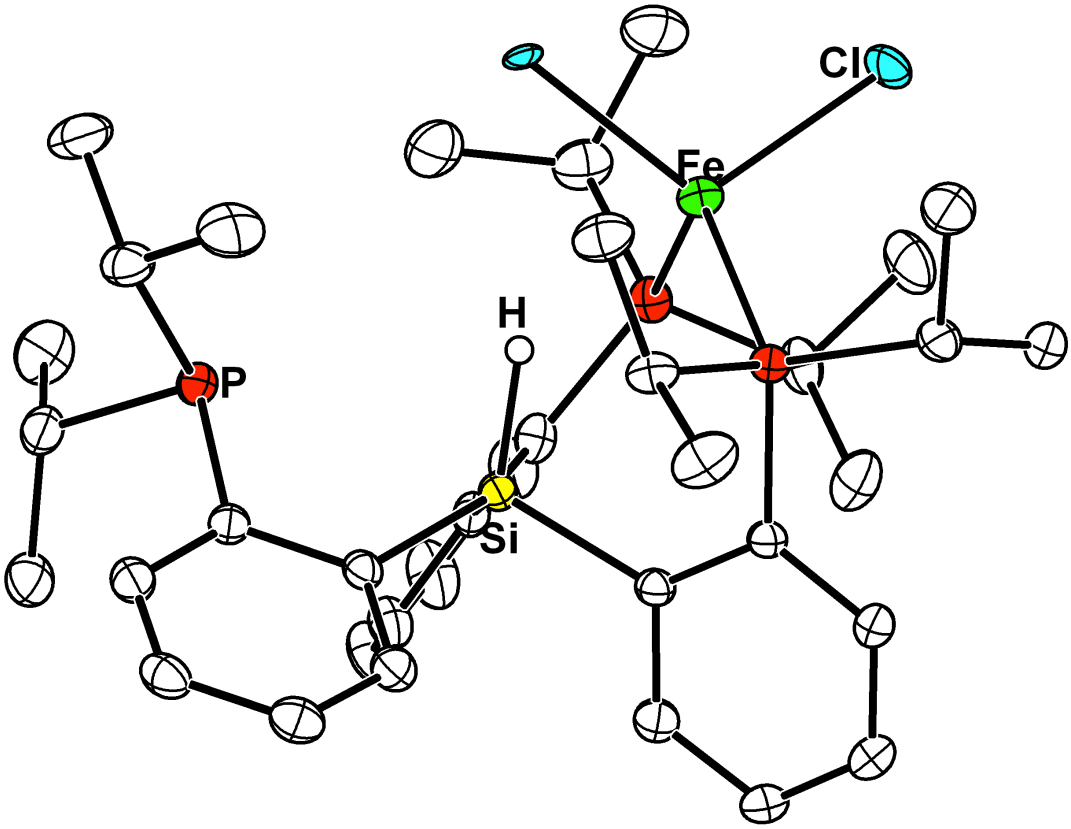

Figure A3.3. Solid-state structure of $\{\kappa^2\text{-}[SiP^{iPr}_3]H\}FeCl_2$ (50% ellipsoids). C-H hydrogen atoms have been omitted for clarity. The silicon hydride was located on the Fourier difference map and refined freely.

Table A3.3. Crystal data and structure refinement for (κ^2-[SiP$^{iPr}_3$]H)FeCl$_2$.

Empirical formula	$C_{36}H_{55}Cl_2FeP_3Si$	
Formula weight	735.55	
Temperature	100(2) K	
Wavelength	0.71073 Å	
Crystal system	Monoclinic	
Space group	$P2_1/n$	
Unit cell dimensions	a = 13.0548(19) Å	α = 90°
	b = 13.718(3) Å	β = 104.102(11)°
	c = 22.356(6) Å	γ = 90°
Volume	3883.0(13) Å^3	
Z	4	
Density (calculated)	1.258 g/cm^3	
Absorption coefficient	0.704 mm^{-1}	
F(000)	1560	
Crystal size	0.34 x 0.29 x 0.19 mm^3	
θ range for data collection	1.88 to 35.37°	
Index ranges	$-20 \le h \le 17$, $-22 \le k \le 21$, $-35 \le l \le 33$	
Reflections collected	62610	
Independent reflections	15058 [R(int) = 0.0954]	
Completeness to θ = 35.37°	85.6 %	
Absorption correction	None	
Refinement method	Full-matrix least-squares on F^2	
Data / restraints / parameters	15058 / 0 / 404	
Goodness-of-fit on F^2	1.091	
Final R indices [$I>2\sigma(I)$]	R1 = 0.0688, wR2 = 0.2048	
R indices (all data)	R1 = 0.1255, wR2 = 0.2406	
Largest diff. peak and hole	3.615 and -0.796 e.Å^{-3}	

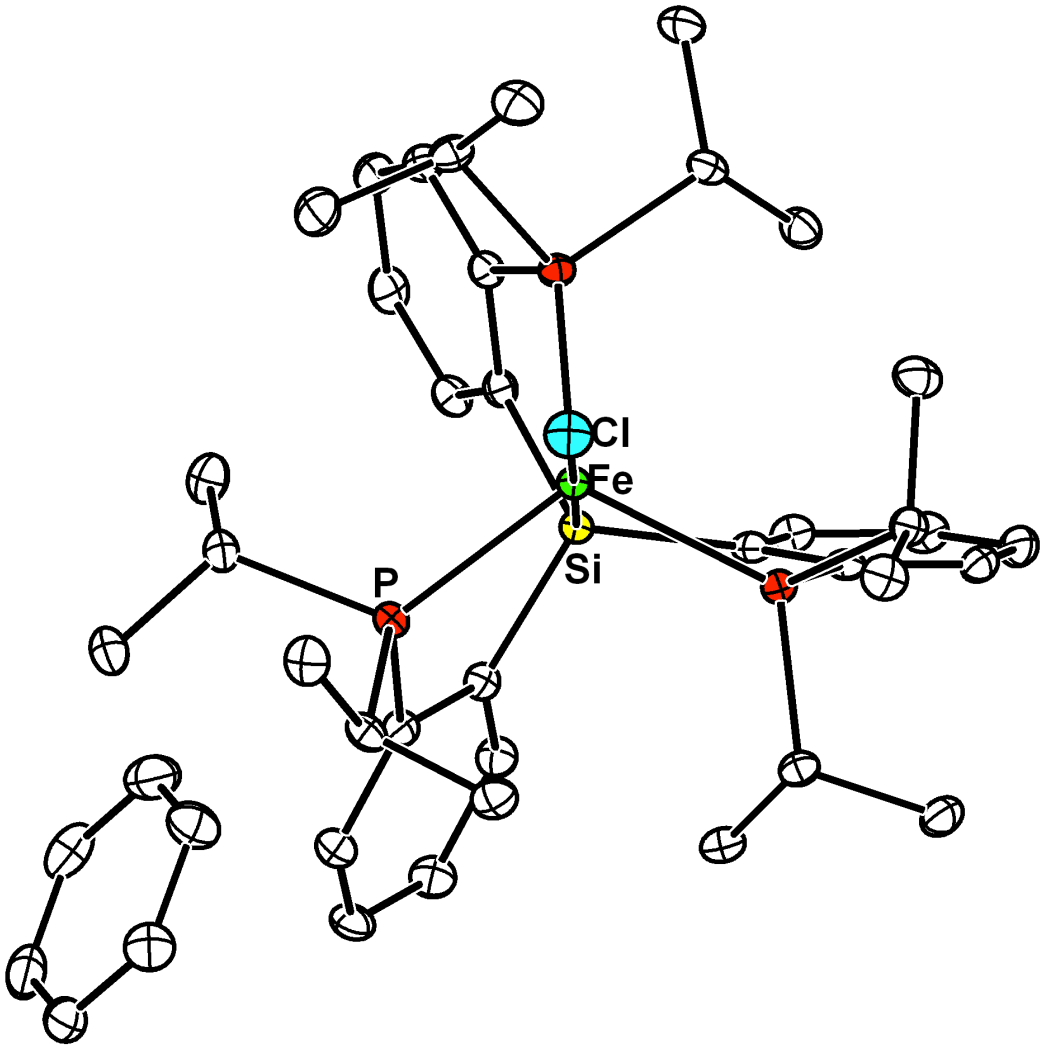

Figure A3.4. Solid-state structure of [SiP$^{iPr}_3$]FeCl (**4.5**, 50% ellipsoids) and a cocrystallized benzene solvent molecule. Hydrogen atoms have been omitted for clarity.

Table A3.4. Crystal data and structure refinement for **4.5**.

Empirical formula	$C_{42}H_{60}ClFeP_3Si$	
Formula weight	777.20	
Temperature	100(2) K	
Wavelength	0.71073 Å	
Crystal system	Monoclinic	
Space group	$P2_1/c$	
Unit cell dimensions	a = 12.913(4) Å	α = 90°
	b = 15.513(4) Å	β = 92.33(3)°
	c = 20.296(8) Å	γ = 90°
Volume	4062(2) Å^3	
Z	4	
Density (calculated)	1.271 g/cm^3	
Absorption coefficient	0.613 mm^{-1}	
F(000)	1656	
Crystal size	0.37 x 0.26 x 0.21 mm^3	
Theta range for data collection	1.58 to 38.63°	
Index ranges	$-22 \le h \le 22$, $-27 \le k \le 27$, $-34 \le l \le 34$	
Reflections collected	77474	
Independent reflections	20057 [R(int) = 0.0936]	
Completeness to θ = 38.63°	86.9 %	
Absorption correction	None	
Refinement method	Full-matrix least-squares on F^2	
Data / restraints / parameters	20057 / 0 / 445	
Goodness-of-fit on F^2	1.367	
Final R indices [$I>2\sigma(I)$]	R1 = 0.0510, wR2 = 0.0872	
R indices (all data)	R1 = 0.1009, wR2 = 0.0956	
Largest diff. peak and hole	1.302 and -0.731 e.Å^{-3}	

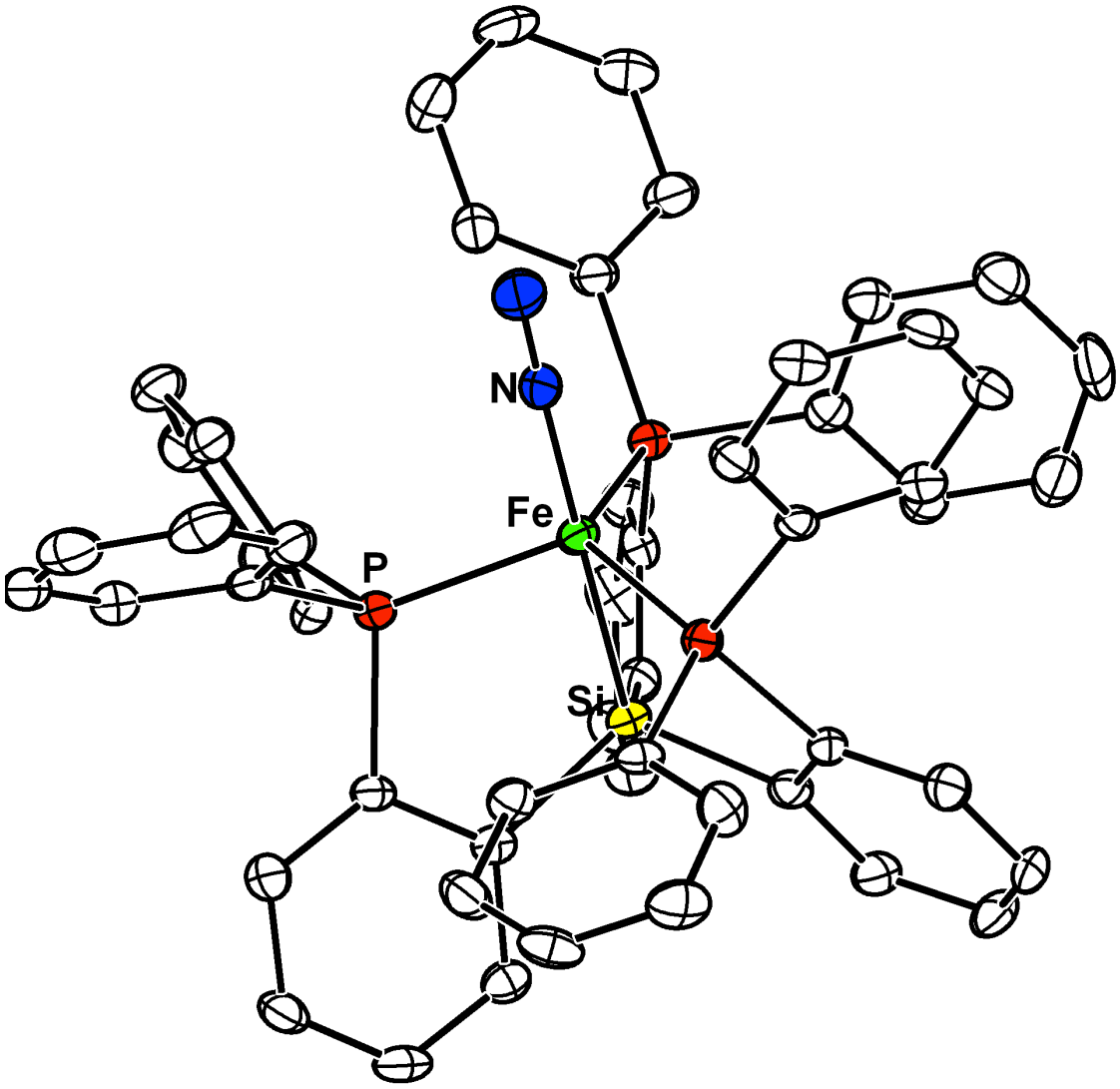

Figure A3.5. Solid-state structure of [SiP^{Ph}_3]FeN_2 (**4.6**, 50% ellipsoids). Hydrogen atoms have been omitted for clarity.

Table A3.5. Crystal data and structure refinement for **4.6**.

Empirical formula	$C_{54}H_{42}FeN_2P_3Si$	
Formula weight	895.75	
Temperature	100(2) K	
Wavelength	0.71073 Å	
Crystal system	Monoclinic	
Space group	$P2_1/c$	
Unit cell dimensions	a = 12.7101(9) Å	α = 90°
	b = 17.4799(12) Å	β = 99.0290(10)°
	c = 19.7248(14) Å	γ = 90°
Volume	4328.0(5) Å ^{3}	
Z	4	
Density (calculated)	1.375 g/cm^3	
Absorption coefficient	0.528 mm^{-1}	
F(000)	1860	
Crystal size	0.18 x 0.16 x 0.14 mm^3	
θ range for data collection	1.57 to 28.45°	
Index ranges	$-16 \le h \le 16$, $-22 \le k \le 23$, $-26 \le l \le 24$	
Reflections collected	34641	
Independent reflections	9873 [R(int) = 0.0732]	
Completeness to θ = 28.45°	90.6 %	
Absorption correction	None	
Refinement method	Full-matrix least-squares on F^2	
Data / restraints / parameters	9873 / 0 / 550	
Goodness-of-fit on F^2	1.343	
Final R indices [$I>2\sigma(I)$]	R1 = 0.0481, wR2 = 0.0745	
R indices (all data)	R1 = 0.0882, wR2 = 0.0796	
Largest diff. peak and hole	0.954 and -0.577 e. Å $^{-3}$	

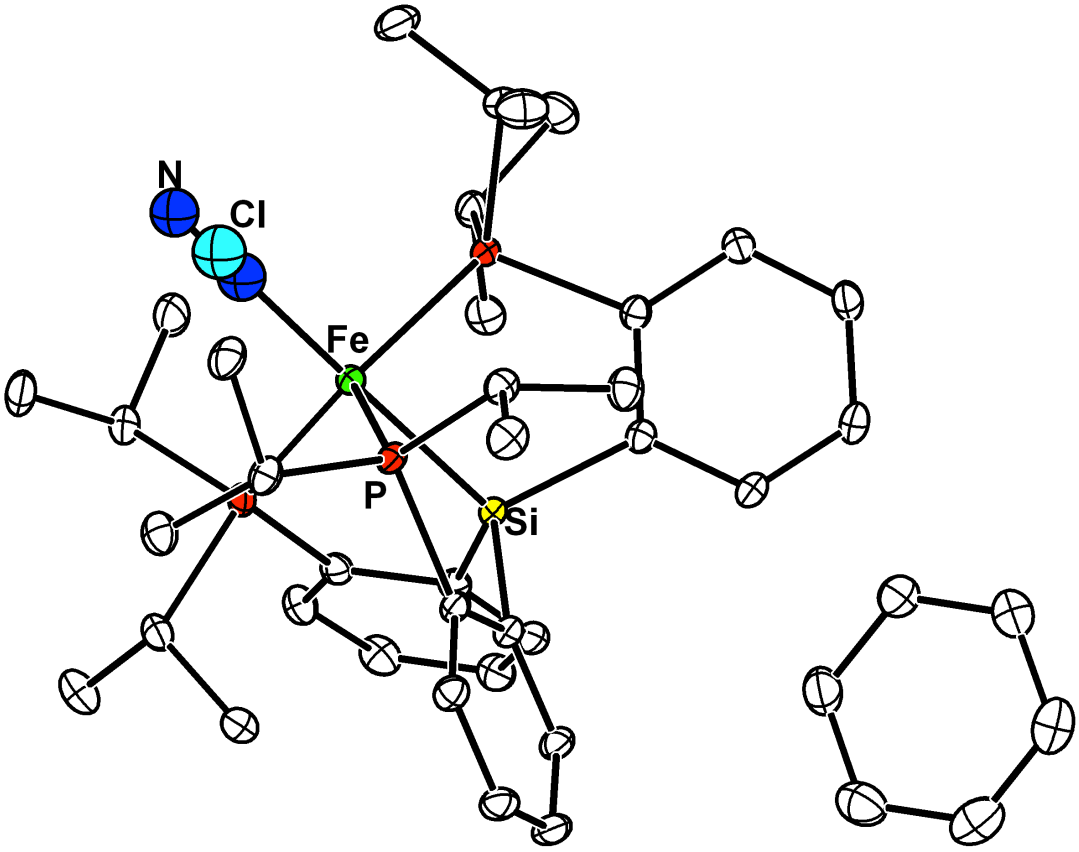

Figure A3.6. Solid-state structure of [SiP$^{iPr}_3$]FeN$_2$ (**4.7**, 50% ellipsoids) and a cocrystallized benzene solvent molecule. As shown in the figure, the N$_2$ site had partial chloride occupancy; for this reason, bond lengths and angles are not discussed in Chapter 4. The N and Cl atoms were refined isotropically; all other atoms were refined anistotropically. The occupancies of the two N atoms refined to approximately 0.97, and the occupancy of the Cl atom refined to approximately 0.03.

Table A3.6. Crystal data and structure refinement for **4.7**.

Empirical formula	$C_{42}H_{60}Cl_{0.03}FeN_{1.94}P_3Si$	
Formula weight	765.45	
Temperature	100(2) K	
Wavelength	0.71073 Å	
Crystal system	Monoclinic	
Space group	$P2_1/c$	
Unit cell dimensions	a = 12.759(2) Å	α = 90°.
	b = 15.4865(19) Å	β = 92.006(16)°.
	c = 20.561(4) Å	γ = 90°.
Volume	4060.1(11) Å^3	
Z	4	
Density (calculated)	1.317 g/cm^3	
Absorption coefficient	0.617 mm^{-1}	
F(000)	1712	
Crystal size	0.35 x 0.33 x 0.17 mm^3	
θ range for data collection	1.60 to 40.85°	
Index ranges	$-22 \le h \le 23$, $-28 \le k \le 25$, $-37 \le l \le 35$	
Reflections collected	79596	
Independent reflections	24271 [R(int) = 0.0828]	
Completeness to θ = 40.85°	91.5 %	
Absorption correction	None	
Refinement method	Full-matrix least-squares on F^2	
Data / restraints / parameters	24271 / 0 / 452	
Goodness-of-fit on F^2	1.431	
Final R indices [$I>2\sigma(I)$]	R1 = 0.0512, wR2 = 0.0892	
R indices (all data)	R1 = 0.0993, wR2 = 0.0966	
Largest diff. peak and hole	1.409 and -0.750 e.Å^{-3}	

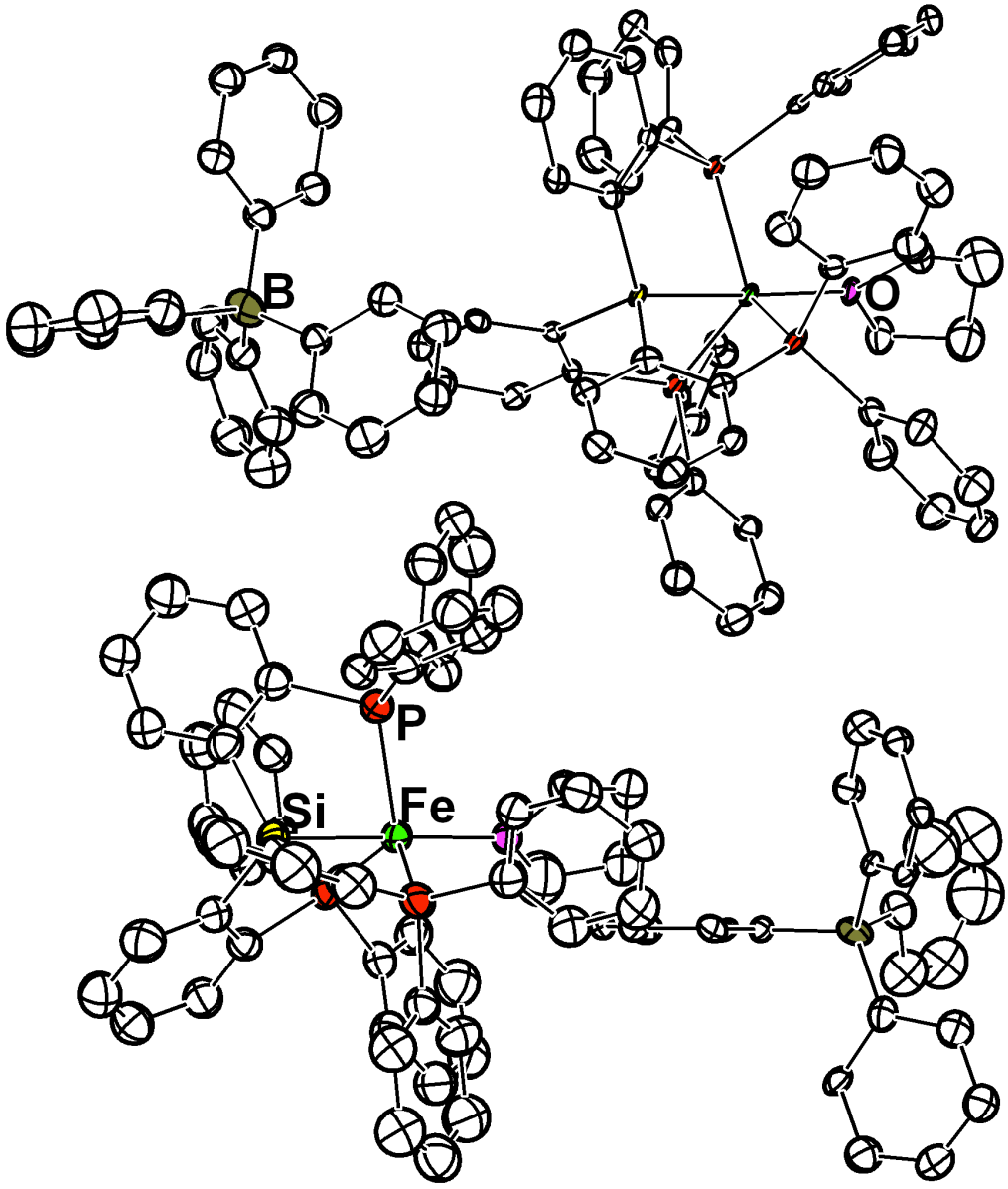

Figure A3.7. Solid-state structure of the two molecules of {[SiP$^{Ph}_3$]Fe(THF)}{BPh$_4$} (**4.9**, 50% ellipsoids) found in the assymmetric unit. Hydrogen atoms and cocrystallized THF solvent molecules have been omitted for clarity.

Table A3.7. Crystal data and structure refinement for **4.9**.

Empirical formula	$C_{300}H_{182}B_2Fe_2O_9P_6Si_2$	
Formula weight	4305.78	
Temperature	293(2) K	
Wavelength	0.71073 Å	
Crystal system	Monoclinic	
Space group	*C*2/*c*	
Unit cell dimensions	a = 79.786(5) Å	α = 90°
	b = 15.5571(9) Å	β = 99.316(2)°
	c = 23.7631(14) Å	γ = 90°
Volume	29107(3) Å^3	
Z	20	
Density (calculated)	4.913 g/cm^3	
Absorption coefficient	0.957 mm^{-1}	
F(000)	44680	
Crystal size	0.30 x 0.24 x 0.06 mm^3	
θ range for data collection	1.52 to 21.85°	
Index ranges	$-78 \le h \le 83$, $-16 \le k \le 15$, $-23 \le l \le 23$	
Reflections collected	62552	
Independent reflections	14763 [R(int) = 0.1781]	
Completeness to θ = 21.85°	84.2 %	
Absorption correction	None	
Refinement method	Full-matrix least-squares on F^2	
Data / restraints / parameters	14763 / 1128 / 1802	
Goodness-of-fit on F^2	1.026	
Final R indices [$I>2\sigma(I)$]	R1 = 0.1128, wR2 = 0.2673	
R indices (all data)	R1 = 0.2064, wR2 = 0.3108	
Largest diff. peak and hole	0.987 and -0.636 e.Å^{-3}	

Appendix 4: Supplementary Data for Chapter 5

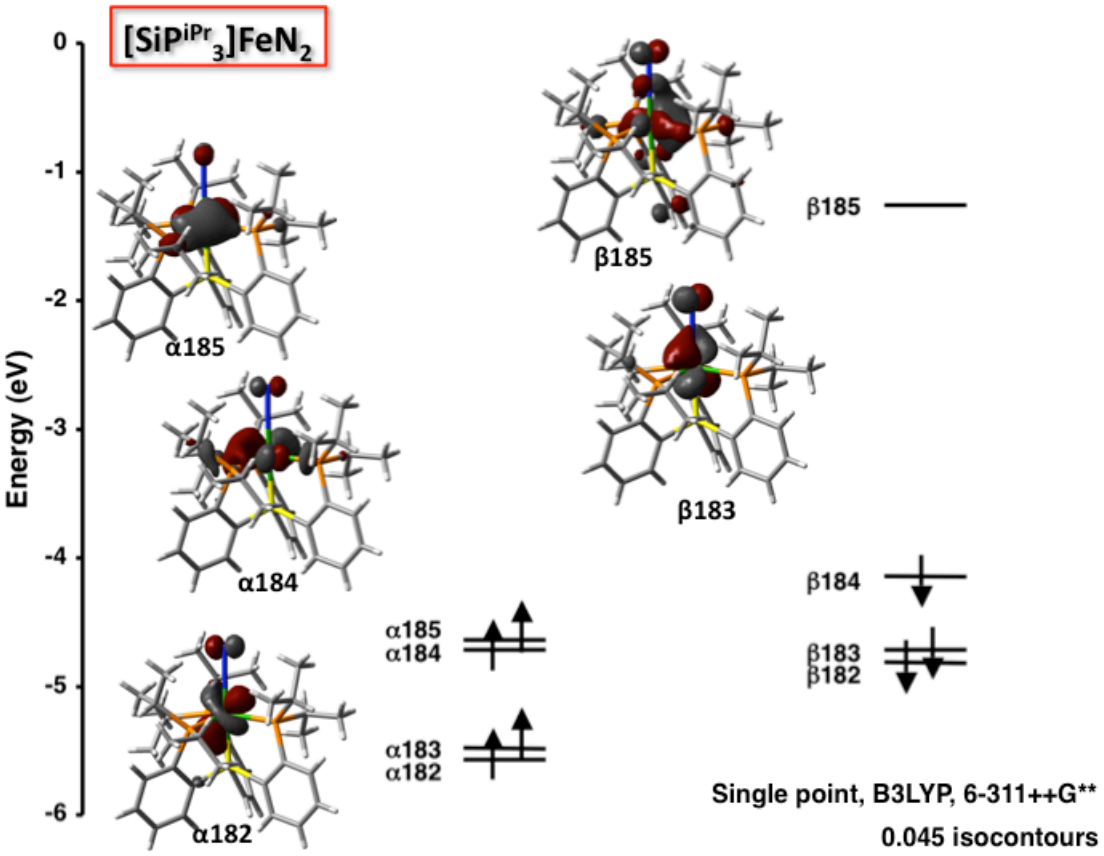

Figure A4.1. Calculated frontier molecular orbitals for [SiP$^{iPr}_3$]Fe(N_2) (**5.1**).

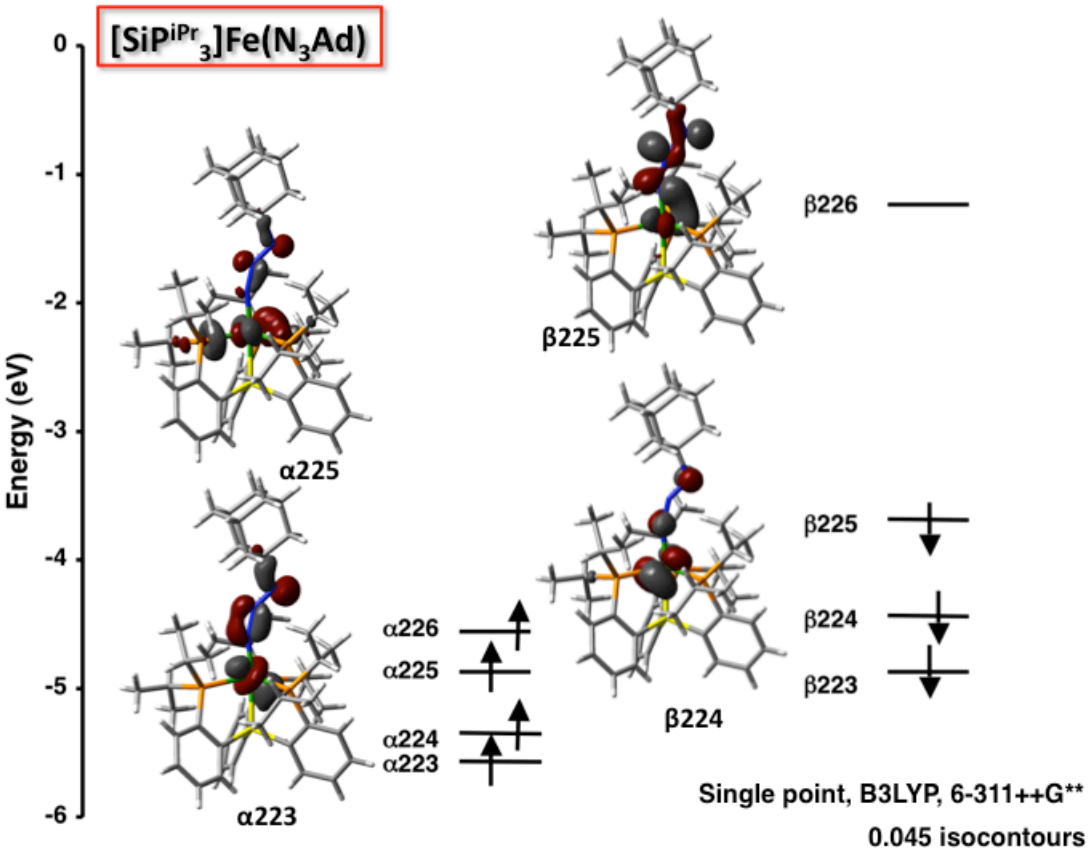

Figure A4.2. Calculated frontier molecular orbitals for [SiP$^{iPr}_3$]Fe(η^1-N$_3$Ad) (**5.2**).

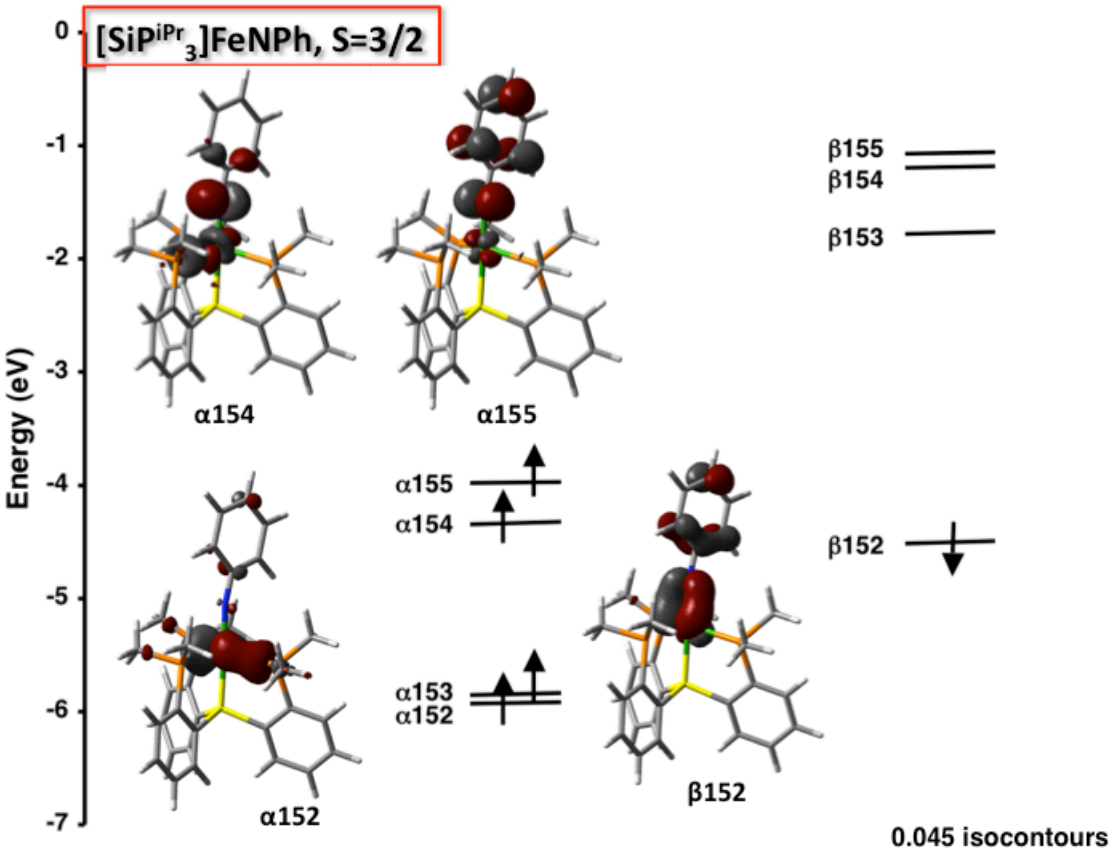

Figure A4.3. Calculated frontier molecular orbitals for the S=3/2 state of [SiP$^{Me}_3$]Fe(NPh) (**7-IS**).

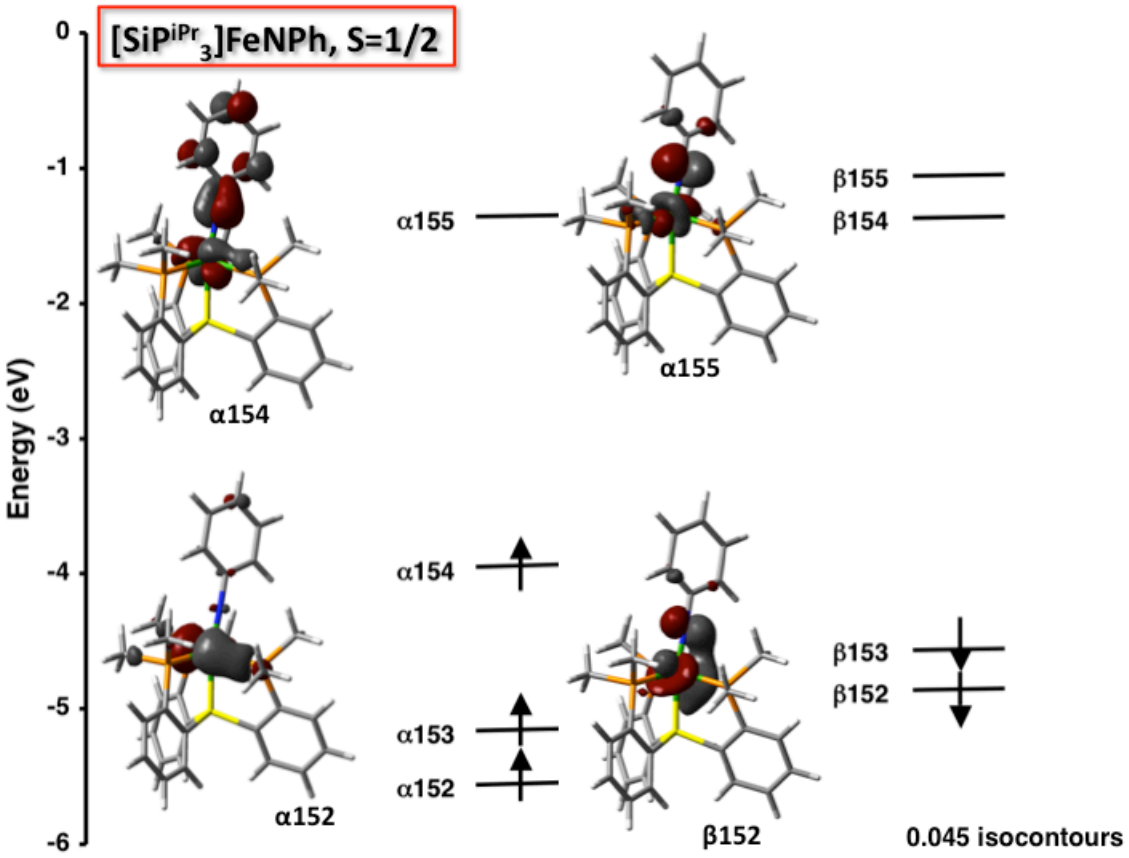

Figure A4.4. Calculated frontier molecular orbitals for the S=1/2 state of [SiP$^{Me}_{3}$]Fe(NPh) (**7-LS**).

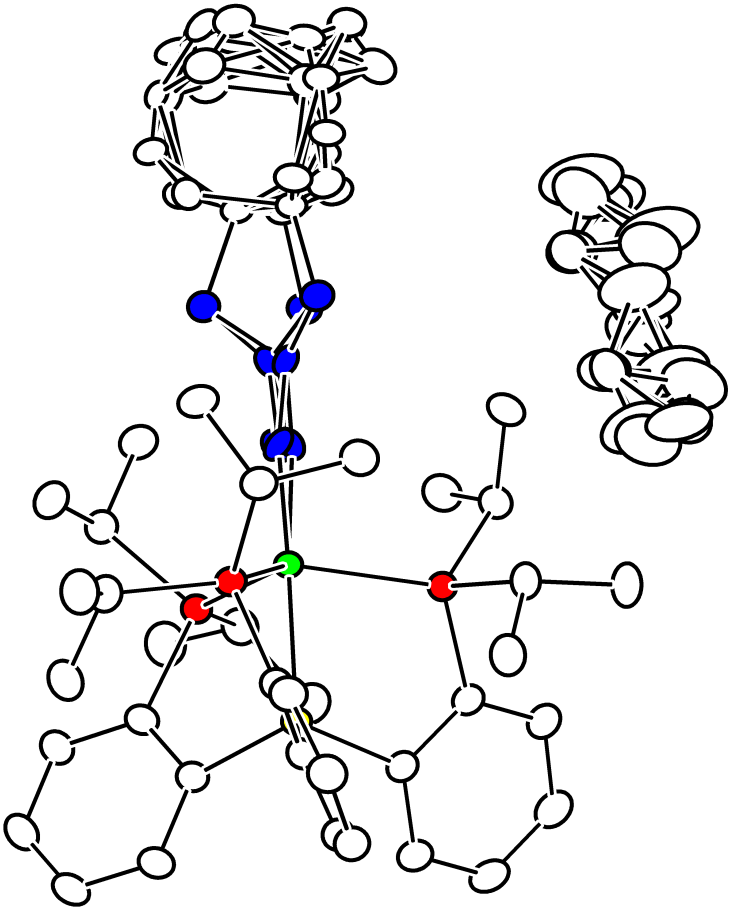

Figure A4.5. Solid-state structure of [SiP$^{iPr}_3$]Fe(N_3Ad) (**5.2**) and a disordered *n*-pentane solvent molecule as 50% ellipsoids. All parts are shown, and hydrogen atoms have been omitted. Details about the disorder and refinement details are found in Section 5.3.2.

Table A4.1. Crystal data and structure refinement for compound **5.2**.

Empirical formula	$C_{53.50}H_{87}FeN_3P_3Si$	
Formula weight	949.11	
Temperature	100(2) K	
Wavelength	0.71073 Å	
Crystal system	Rhombohedral	
Space group	*R*-3*c*	
Unit cell dimensions	*a* = 15.0449(8) Å	α = 90°
	b = 15.0449(8) Å	β = 90°
	c = 81.101(6) Å	γ = 120°
Volume	15897.8(17) $Å^3$	
Z	12	
Density (calculated)	1.190 g/cm^3	
Absorption coefficient	0.435 mm^{-1}	
F(000)	6168	
Crystal size	0.50 x 0.50 x 0.45 mm^3	
θ range for data collection	1.51 to 30.50°.	
Index ranges	$-21 \le h \le 21, -21 \le k \le 21, -115 \le l \le 115$	
Reflections collected	136582	
Independent reflections	5406 [R(int) = 0.0557]	
Completeness to θ = 30.50°	99.8 %	
Absorption correction	Semi-empirical from equivalents	
Max. and min. transmission	0.8284 and 0.8120	
Refinement method	Full-matrix least-squares on F^2	
Data / restraints / parameters	5406 / 331 / 336	
Goodness-of-fit on F^2	1.210	
Final R indices [$I>2\sigma(I)$]	R1 = 0.0516, wR2 = 0.1168	
R indices (all data)	R1 = 0.0588, wR2 = 0.1200	
Largest diff. peak and hole	0.429 and -0.375 e.$Å^{-3}$	

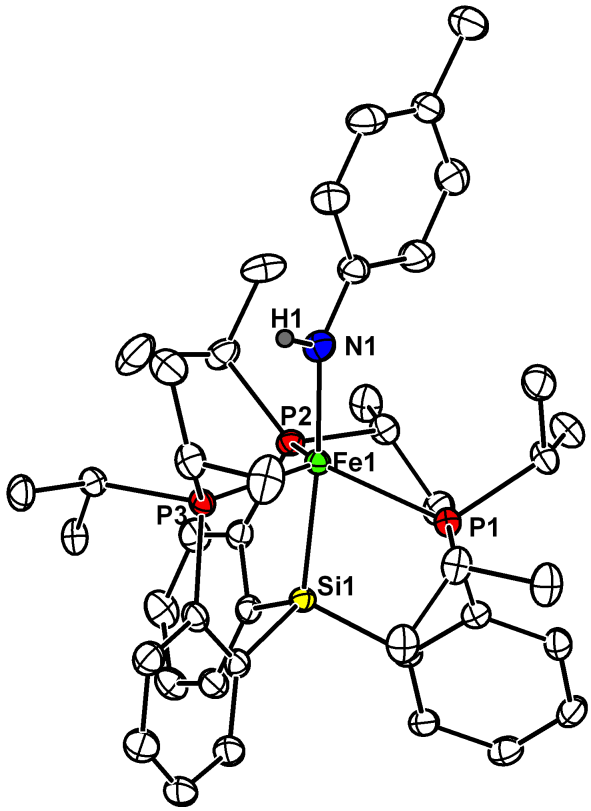

Figure A4.6. Solid-state structure of [SiP$^{iPr}_{3}$]Fe(NHTol) (**5.6**) as 50% ellipsoids. C-H hydrogens have been omitted. H1 was located on the Fourier difference map and refined semifreely.

Table A4.2. Crystal data and structure refinement for compound **5.6**.

Empirical formula	$C_{43}H_{62}FeNP_3Si$	
Formula weight	769.79	
Temperature	100(2) K	
Wavelength	0.71073 Å	
Crystal system	Orthorhombic	
Space group	$P2_12_12_1$	
Unit cell dimensions	a = 13.4209(18) Å	α = 90°
	b = 14.619(2) Å	β = 90°
	c = 21.192(3) Å	γ = 90°
Volume	4157.8(10) Å^3	
Z	4	
Density (calculated)	1.230 g/cm^3	
Absorption coefficient	0.537 mm^{-1}	
F(000)	1648	
Crystal size	0.30 x 0.20 x 0.10 mm^3	
Theta range for data collection	1.69 to 30.03°.	
Index ranges	$-18 \le h \le 18$, $-20 \le k \le 20$, $-29 \le l \le 29$	
Reflections collected	93936	
Independent reflections	12149 [R(int) = 0.0903]	
Completeness to θ = 30.03°	100.0 %	
Absorption correction	Semi-empirical from equivalents	
Max. and min. transmission	0.9482 and 0.8555	
Refinement method	Full-matrix least-squares on F^2	
Data / restraints / parameters	12149 / 1 / 459	
Goodness-of-fit on F^2	1.011	
Final R indices [$I>2\sigma(I)$]	R1 = 0.0419, wR2 = 0.0820	
R indices (all data)	R1 = 0.0587, wR2 = 0.0899	
Absolute structure parameter	-0.016(11)	
Largest diff. peak and hole	0.363 and -0.239 e.Å^{-3}	

Appendix 5: Supplementary Data for Chapter 6

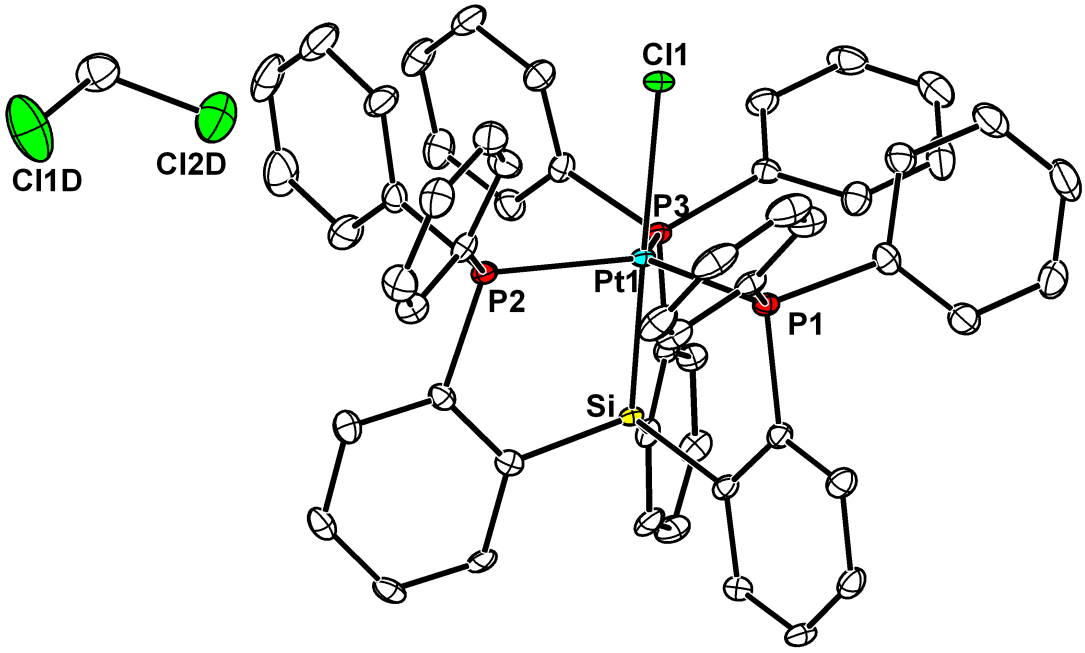

Figure A5.1. Solid-state structure of [SiP^{Ph}_3]PtCl (**6.1**, 50% ellipsoids) and a cocrystallized dichloromethane solvent molecule. C-H hydrogen atoms have been omitted for clarity.

Table A5.1. Crystal data and structure refinement for **6.1**.

Empirical formula	$C_{55}H_{44}Cl_3P_3PtSi$	
Formula weight	1127.34	
Temperature	100(2) K	
Wavelength	0.71073 Å	
Crystal system	Triclinic	
Space group	*P*-1	
Unit cell dimensions	a = 11.1768(12) Å	α = 87.699(2)°
	b = 13.3695(14) Å	β = 84.961(2)°
	c = 15.7387(16) Å	γ = 86.359(2)°
Volume	2336.6(4) $Å^3$	
Z	2	
Density (calculated)	1.602 g/cm^3	
Absorption coefficient	3.341 mm^{-1}	
F(000)	1124	
Crystal size	0.19 x 0.10 x 0.08 mm^3	
θ range for data collection	1.53 to 29.15°	
Index ranges	$-15 \le h \le 14$, $-17 \le k \le 17$, $-20 \le l \le 21$	
Reflections collected	40452	
Independent reflections	11408 [R(int) = 0.0562]	
Completeness to θ = 25.00°	99.7 %	
Absorption correction	Semi-empirical from equivalents	
Max. and min. transmission	0.7759 and 0.5693	
Refinement method	Full-matrix least-squares on F^2	
Data / restraints / parameters	11408 / 510 / 568	
Goodness-of-fit on F^2	1.082	
Final R indices [$I>2\sigma(I)$]	R1 = 0.0422, wR2 = 0.1040	
R indices (all data)	R1 = 0.0489, wR2 = 0.1081	
Largest diff. peak and hole	3.382 and -2.062 $e.Å^{-3}$	

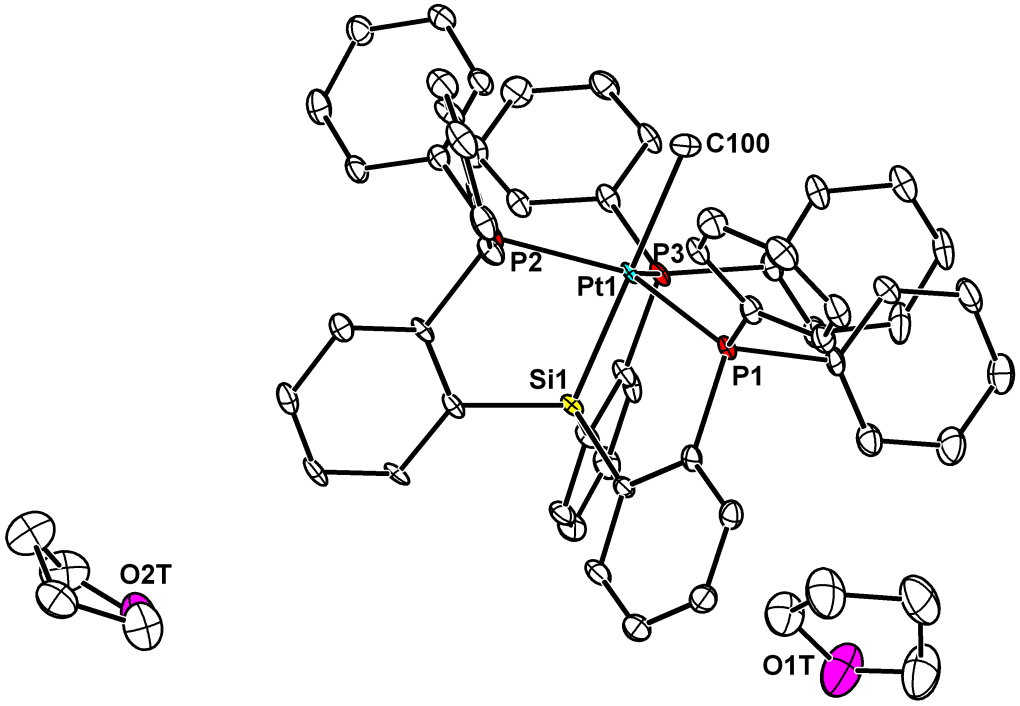

Figure A5.2. Solid-state structure of [SiP^{Ph}_3]$PtCH_3$ (**6.2**, 50% ellipsoids) and cocrystallized THF solvent molecules. C-H hydrogen atoms have been omitted for clarity.

Table A5.2. Crystal data and structure refinement for **6.2**.

Empirical formula	$C_{63}H_{61}O_2P_3PtSi$	
Formula weight	1166.21	
Temperature	100(2) K	
Wavelength	0.71073 Å	
Crystal system	Monoclinic	
Space group	$P2_1/c$	
Unit cell dimensions	a = 18.745(2) Å	α = 90°
	b = 16.1454(18) Å	β = 94.181(4)°
	c = 16.911(2) Å	γ = 90°
Volume	5104.4(10) Å^3	
Z	4	
Density (calculated)	1.518 g/cm^3	
Absorption coefficient	2.913 mm^{-1}	
F(000)	2368	
Crystal size	0.30 x 0.08 x 0.05 mm^3	
θ range for data collection	1.67 to 29.13°	
Index ranges	$-25 \le h \le 24$, $-21 \le k \le 22$, $-23 \le l \le 21$	
Reflections collected	75418	
Independent reflections	13406 [R(int) = 0.1465]	
Completeness to θ = 29.13°	97.7 %	
Absorption correction	Semi-empirical from equivalents	
Max. and min. transmission	0.8680 and 0.4753	
Refinement method	Full-matrix least-squares on F^2	
Data / restraints / parameters	13406 / 613 / 632	
Goodness-of-fit on F^2	1.091	
Final R indices [$I>2\sigma(I)$]	R1 = 0.0506, wR2 = 0.1189	
R indices (all data)	R1 = 0.0844, wR2 = 0.1457	
Largest diff. peak and hole	5.837 and -2.011 e.Å^{-3}	

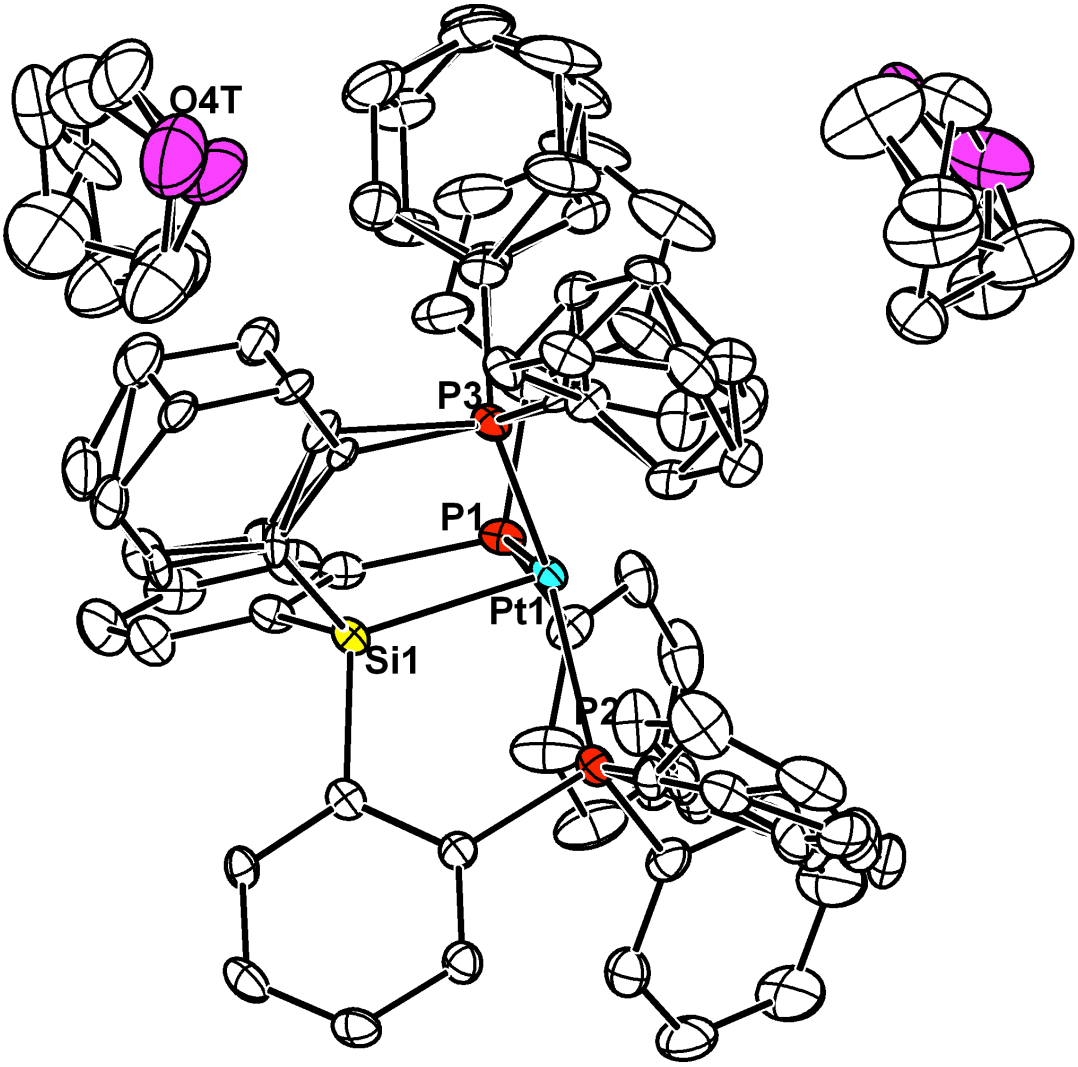

Figure A5.3. Solid-state structure of [SiP$^{Ph}_{3}$]PtH (**6.3**, 50% ellipsoids) and cocrystallized THF solvent molecules. C-H hydrogen atoms have been omitted for clarity. Disorder was modeled as indicated in the figure.

Table A5.3. Crystal data and structure refinement for **6.3**.

Empirical formula	$C_{62}H_{58}O_2P_3PtSi$	
Formula weight	1151.17	
Temperature	100(2) K	
Wavelength	0.71073 Å	
Crystal system	Monoclinic	
Space group	$P2_1/c$	
Unit cell dimensions	a = 18.572(3) Å	α = 90°
	b = 16.157(3) Å	β = 96.473(3)°
	c = 16.968(3) Å	β = 90°
Volume	5059.0(15) Å^3	
Z	4	
Density (calculated)	1.511 g/cm^3	
Absorption coefficient	2.938 mm^{-1}	
F(000)	2332	
Crystal size	0.19 x 0.07 x 0.07 mm^3	
θ range for data collection	1.10 to 28.70°	
Index ranges	$-24 \le h \le 22$, $-21 \le k \le 19$, $-22 \le l \le 22$	
Reflections collected	30622	
Independent reflections	11907 [R(int) = 0.0651]	
Completeness to θ = 25.00°	99.3 %	
Absorption correction	Semi-empirical from equivalents	
Max. and min. transmission	0.8208 and 0.6053	
Refinement method	Full-matrix least-squares on F^2	
Data / restraints / parameters	11907 / 1625 / 889	
Goodness-of-fit on F^2	1.030	
Final R indices [$I>2\sigma(I)$]	R1 = 0.0437, wR2 = 0.0879	
R indices (all data)	R1 = 0.0778, wR2 = 0.1041	
Largest diff. peak and hole	2.285 and -1.598 e.Å^{-3}	

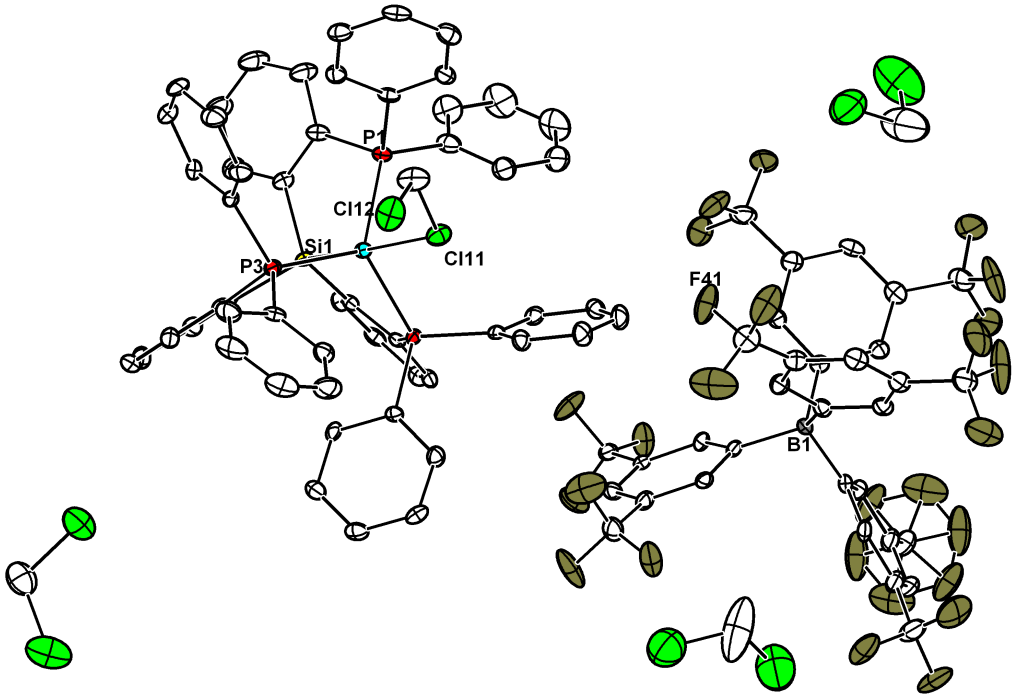

Figure A5.3. Solid-state structure of {[SiP^{Ph}_3]Pt(CH_2Cl_2)}{BAr^F_4} (**6.5**, 50% ellipsoids) and cocrystallized dichloromethane solvent molecules. C-H hydrogen atoms have been omitted for clarity. Trifluoromethyl disorder was modeled as indicated in the figure.

Table A5.4. Crystal data and structure refinement for **6.5**.

Empirical formula	$C_{90}H_{62}BCl_8F_{24}P_3PtSi$	
Formula weight	1104.95	
Temperature	100(2) K	
Wavelength	0.71073 Å	
Crystal system	Triclinic	
Space group	*P*-1	
Unit cell dimensions	a = 12.6057(11) Å	α = 84.459(2)°
	b = 17.5913(16) Å	β = 84.435(2)°
	c = 20.2306(18) Å	γ = 86.795(2)°
Volume	4439.2(7) Å^3	
Z	2	
Density (calculated)	1.653 g/cm^3	
Absorption coefficient	1.986 mm^{-1}	
F(000)	2192	
Crystal size	0.38 x 0.09 x 0.05 mm^3	
θ range for data collection	1.61 to 27.87°	
Index ranges	$-15 \le h \le 16$, $-23 \le k \le 23$, $-26 \le l \le 25$	
Reflections collected	54713	
Independent reflections	19579 [R(int) = 0.0645]	
Completeness to θ = 25.00°	99.6 %	
Absorption correction	Semi-empirical from equivalents	
Max. and min. transmission	0.9072 and 0.5191	
Refinement method	Full-matrix least-squares on F^2	
Data / restraints / parameters	19579 / 1727 / 1163	
Goodness-of-fit on F^2	1.050	
Final R indices [$I>2\sigma(I)$]	R1 = 0.0635, wR2 = 0.1600	
R indices (all data)	R1 = 0.0840, wR2 = 0.1736	
Largest diff. peak and hole	3.246 and -2.506 e.Å^{-3}	

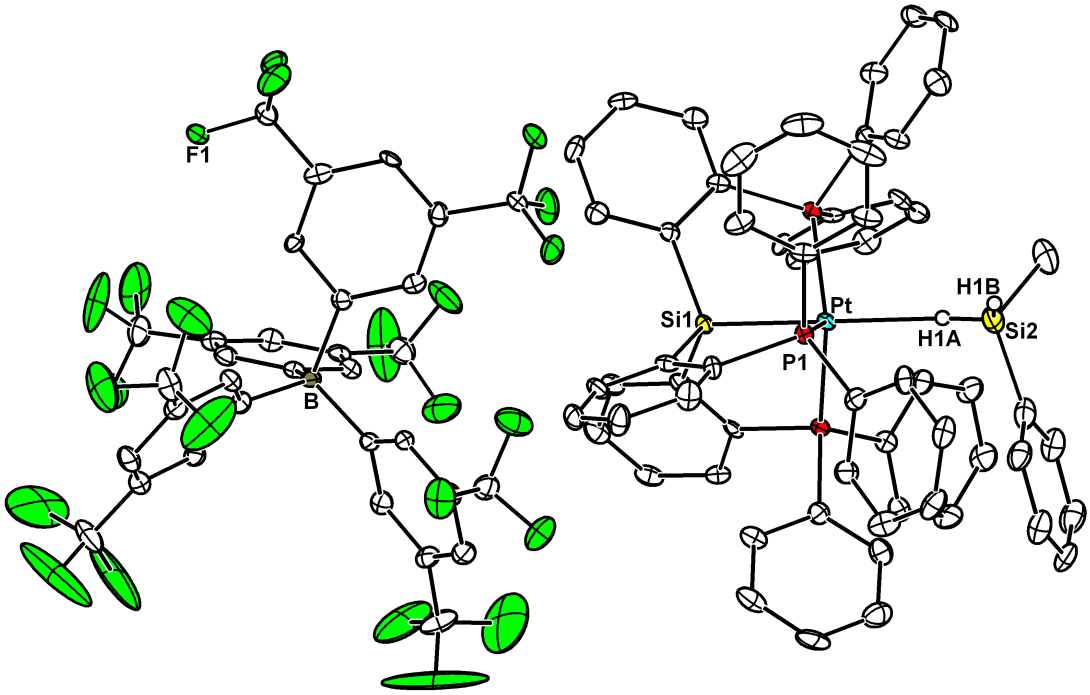

Figure A5.5. Solid-state structure of {[SiP$^{Ph}_3$]Pt(η^2-H_2SiMePh)}{BAr$^F_4$} (**6.6.2**, 50% ellipsoids). C-H hydrogen atoms have been omitted for clarity. Si-H hydrogens are shown in calculated positions. This structure has not been published and is not currently part of a manuscript in preparation; thus, full tables of coordinates, anisotropic displacement parameters, and bond metrics are included below.

Table A5.5. Crystal data and structure refinement for **6.6.2**.

Empirical formula	$C_{93}H_{64}BF_{24}P_3PtSi$	
Formula weight	1992.43	
Temperature	100(2) K	
Wavelength	0.71073 Å	
Crystal system	Triclinic	
Space group	*P*-1	
Unit cell dimensions	a = 13.192(14) Å	α = 68.45(4)°
	b = 17.568(17) Å	β = 78.88(7)°
	c = 19.961(15) Å	γ = 87.26(8)°
Volume	4220(7) $Å^3$	
Z	2	
Density (calculated)	1.568 g/cm^3	
Absorption coefficient	1.848 mm^{-1}	
F(000)	1988	
Crystal size	0.26 x 0.09 x 0.07 mm^3	
θ range for data collection	1.75 to 26.38°.	
Index ranges	$-16 \le h \le 16$, $-21 \le k \le 21$, $-24 \le l \le 24$	
Reflections collected	45339	
Independent reflections	17025 [R(int) = 0.0630]	
Completeness to θ = 26.38°	98.5 %	
Absorption correction	Multi-scan	
Refinement method	Full-matrix least-squares on F^2	
Data / restraints / parameters	17025 / 0 / 1118	
Goodness-of-fit on F^2	1.057	
Final R indices [$I>2\sigma(I)$]	R1 = 0.0556, wR2 = 0.1301	
R indices (all data)	R1 = 0.0721, wR2 = 0.1409	
Largest diff. peak and hole	3.217 and -2.210 $e.Å^{-3}$	

Table A5.6. Atomic coordinates (x 10^4) and equivalent isotropic displacement parameters ($Å^2$x 10^3) for **6.6.2**. U(eq) is defined as one third of the trace of the orthogonalized U^{ij} tensor.

	x	y	z	U(eq)
Pt	8848(1)	6915(1)	7065(1)	10(1)
P(1)	7101(1)	7229(1)	6963(1)	11(1)
P(2)	10139(1)	7943(1)	6715(1)	11(1)
P(3)	9383(1)	5594(1)	7094(1)	11(1)
Si(1)	9081(1)	7227(1)	5825(1)	11(1)
Si(2)	8378(1)	6498(1)	8770(1)	24(1)
C(1)	7789(4)	7181(3)	5577(3)	14(1)
C(2)	6903(4)	7182(4)	6090(3)	15(1)
C(3)	5928(5)	7154(4)	5942(3)	25(1)
C(4)	5824(5)	7120(4)	5276(3)	26(2)
C(5)	6690(5)	7108(4)	4763(3)	22(1)
C(6)	7654(5)	7145(4)	4914(3)	19(1)
C(7)	9777(4)	8247(3)	5327(3)	11(1)
C(8)	10323(4)	8529(3)	5728(3)	12(1)
C(9)	10988(4)	9204(4)	5378(3)	18(1)
C(10)	11121(5)	9608(4)	4623(3)	20(1)
C(11)	10565(5)	9338(4)	4223(3)	20(1)
C(12)	9898(4)	8674(4)	4566(3)	17(1)
C(13)	9940(4)	6434(4)	5604(3)	13(1)
C(14)	10089(4)	5700(3)	6177(3)	12(1)
C(15)	10699(4)	5089(4)	6040(3)	16(1)
C(16)	11150(4)	5201(4)	5321(3)	19(1)
C(17)	11017(4)	5911(4)	4752(3)	22(1)
C(18)	10413(4)	6529(4)	4894(3)	17(1)
C(19)	6062(4)	6539(4)	7620(3)	16(1)
C(20)	5991(4)	5744(4)	7617(3)	19(1)
C(21)	5236(5)	5194(4)	8103(4)	26(1)
C(22)	4546(5)	5409(4)	8619(3)	24(1)
C(23)	4623(5)	6190(4)	8634(3)	22(1)
C(24)	5359(4)	6756(4)	8134(3)	19(1)
C(25)	6673(4)	8262(4)	6892(3)	16(1)

C(26)	6526(5)	8850(4)	6217(4)	23(1)
C(27)	6254(5)	9637(5)	6158(4)	34(2)
C(28)	6111(5)	9864(4)	6760(4)	32(2)
C(29)	6255(5)	9293(4)	7434(4)	32(2)
C(30)	6539(4)	8499(4)	7494(4)	20(1)
C(31)	9963(4)	8687(3)	7168(3)	13(1)
C(32)	10774(4)	9193(4)	7139(3)	18(1)
C(33)	10603(5)	9755(4)	7486(3)	21(1)
C(34)	9627(5)	9809(4)	7873(3)	21(1)
C(35)	8815(5)	9316(4)	7907(3)	23(1)
C(36)	8994(5)	8751(4)	7553(3)	19(1)
C(37)	11427(4)	7548(3)	6840(3)	12(1)
C(38)	12009(4)	7249(3)	6331(3)	15(1)
C(39)	12908(4)	6851(4)	6464(3)	19(1)
C(40)	13260(4)	6734(4)	7108(3)	20(1)
C(41)	12689(5)	7026(4)	7616(3)	21(1)
C(42)	11775(4)	7430(4)	7487(3)	17(1)
C(43)	10238(4)	5025(4)	7721(3)	14(1)
C(44)	10823(4)	5465(4)	7977(3)	19(1)
C(45)	11527(5)	5064(4)	8427(3)	24(1)
C(46)	11635(5)	4222(4)	8635(4)	25(1)
C(91)	5116(4)	7740(4)	3181(3)	14(1)
C(47)	11057(5)	3779(4)	8383(4)	24(1)
C(48)	10362(4)	4181(4)	7923(3)	18(1)
C(49)	8375(4)	4832(4)	7241(3)	16(1)
C(50)	7958(4)	4280(4)	7935(3)	20(1)
C(51)	7163(5)	3741(4)	8020(4)	27(1)
C(52)	6753(5)	3754(4)	7427(4)	27(2)
C(53)	7145(5)	4328(4)	6739(4)	25(1)
C(54)	7949(4)	4857(4)	6640(3)	18(1)
C(55)	9332(7)	6842(5)	9166(4)	44(2)
C(56)	8016(5)	5389(4)	9223(3)	26(1)
C(57)	8723(5)	4782(4)	9498(3)	29(2)
C(58)	8419(5)	3958(4)	9797(4)	30(2)
C(59)	7416(6)	3737(4)	9835(3)	29(2)
C(60)	6695(5)	4328(4)	9582(3)	28(2)

C(61)	7004(5)	5148(4)	9278(3)	25(1)
B	6631(5)	8415(4)	2076(4)	15(1)
C(62)	6604(4)	9236(3)	2295(3)	13(1)
C(63)	6755(4)	10012(3)	1742(3)	13(1)
C(64)	6796(4)	10716(4)	1905(3)	16(1)
C(65)	6687(4)	10681(3)	2616(3)	13(1)
C(66)	6575(4)	9912(4)	3170(3)	16(1)
C(67)	6543(4)	9199(4)	3011(3)	14(1)
C(68)	6979(4)	11537(4)	1299(3)	16(1)
C(69)	6518(5)	9815(4)	3953(3)	21(1)
C(70)	7866(4)	8301(3)	1821(3)	15(1)
C(71)	8363(4)	8576(4)	1088(3)	18(1)
C(72)	9440(5)	8546(4)	884(3)	20(1)
C(73)	10056(4)	8237(4)	1419(3)	19(1)
C(74)	9579(4)	7966(3)	2154(3)	16(1)
C(75)	8499(4)	7992(4)	2348(3)	16(1)
C(76)	9921(5)	8797(4)	92(3)	28(2)
C(77)	10210(5)	7654(4)	2740(4)	24(1)
C(78)	5955(4)	8518(4)	1440(3)	16(1)
C(79)	6134(4)	8020(4)	1026(3)	16(1)
C(80)	5497(5)	8025(4)	542(3)	20(1)
C(81)	4645(5)	8522(4)	459(3)	23(1)
C(82)	4431(5)	9006(4)	886(3)	20(1)
C(83)	5077(4)	9001(4)	1366(3)	16(1)
C(84)	5764(6)	7513(5)	82(4)	35(2)
C(85)	3483(5)	9508(5)	847(4)	29(2)
C(86)	6064(4)	7626(3)	2774(3)	14(1)
C(87)	6379(4)	6816(4)	2947(3)	17(1)
C(88)	5807(5)	6166(4)	3508(3)	18(1)
C(89)	4895(4)	6299(4)	3922(3)	20(1)
C(90)	4545(4)	7096(4)	3749(3)	15(1)
C(92)	6166(5)	5304(4)	3672(4)	31(2)
C(93)	3536(5)	7283(4)	4155(3)	22(1)
F(1)	7021(3)	11516(2)	627(2)	23(1)
F(2)	7869(3)	11905(2)	1262(2)	26(1)
F(3)	6234(3)	12068(2)	1383(2)	34(1)

F(4)	6424(4)	10531(2)	4059(2)	39(1)
F(5)	5734(3)	9322(2)	4409(2)	28(1)
F(6)	7377(3)	9474(3)	4208(2)	33(1)
F(7)	9428(4)	9376(4)	-341(2)	67(2)
F(8)	9983(6)	8181(3)	-132(3)	84(2)
F(9)	10882(4)	9092(4)	-59(2)	63(2)
F(10)	11179(4)	7563(5)	2500(3)	86(2)
F(11)	9870(4)	6933(3)	3229(3)	59(2)
F(12)	10177(4)	8137(3)	3118(2)	48(1)
F(13)	6215(8)	6864(5)	360(4)	145(4)
F(14)	6398(10)	7880(5)	-516(5)	183(6)
F(15)	5020(6)	7346(6)	-164(6)	136(4)
F(16)	3200(4)	9757(3)	195(3)	57(2)
F(17)	2671(3)	9112(4)	1338(3)	77(2)
F(18)	3586(3)	10199(3)	965(3)	52(1)
F(19)	7019(5)	5231(3)	3258(4)	84(2)
F(20)	6460(6)	5010(4)	4326(4)	105(3)
F(21)	5486(5)	4795(3)	3745(7)	160(5)
F(22)	2809(3)	7467(3)	3747(2)	37(1)
F(23)	3635(3)	7925(3)	4350(2)	37(1)
F(24)	3179(3)	6657(3)	4772(2)	35(1)

Table A5.7. Bond lengths [Å] and angles [°] for **6.6.2**.

Pt-H(1A)	2.1821
Pt-Si(1)	2.290(2)
Pt-P(2)	2.358(3)
Pt-P(1)	2.374(3)
Pt-P(3)	2.376(3)
Pt-Si(2)	3.148(3)
P(1)-C(19)	1.834(6)
P(1)-C(25)	1.839(6)
P(1)-C(2)	1.842(6)
P(2)-C(31)	1.827(5)
P(2)-C(8)	1.830(6)
P(2)-C(37)	1.831(5)
P(3)-C(43)	1.832(6)
P(3)-C(14)	1.833(6)
P(3)-C(49)	1.838(6)
Si(1)-C(1)	1.877(6)
Si(1)-C(13)	1.879(6)
Si(1)-C(7)	1.881(6)
Si(2)-C(55)	1.839(8)
Si(2)-C(56)	1.862(8)
Si(2)-H(1A)	0.9900
Si(2)-H(1B)	0.9900
C(1)-C(6)	1.395(8)
C(1)-C(2)	1.398(8)
C(2)-C(3)	1.380(8)
C(3)-C(4)	1.387(9)
C(3)-H(3)	0.9500
C(4)-C(5)	1.385(9)
C(4)-H(4)	0.9500
C(5)-C(6)	1.372(8)
C(5)-H(5)	0.9500
C(6)-H(6)	0.9500
C(7)-C(8)	1.398(7)
C(7)-C(12)	1.406(8)

C(8)-C(9)	1.385(8)
C(9)-C(10)	1.389(9)
C(9)-H(9)	0.9500
C(10)-C(11)	1.394(8)
C(10)-H(10)	0.9500
C(11)-C(12)	1.371(9)
C(11)-H(11)	0.9500
C(12)-H(12)	0.9500
C(13)-C(18)	1.385(8)
C(13)-C(14)	1.411(8)
C(14)-C(15)	1.387(8)
C(15)-C(16)	1.388(8)
C(15)-H(15)	0.9500
C(16)-C(17)	1.375(9)
C(16)-H(16)	0.9500
C(17)-C(18)	1.398(8)
C(17)-H(17)	0.9500
C(18)-H(18)	0.9500
C(19)-C(24)	1.396(8)
C(19)-C(20)	1.406(8)
C(20)-C(21)	1.377(9)
C(20)-H(20)	0.9500
C(21)-C(22)	1.387(9)
C(21)-H(21)	0.9500
C(22)-C(23)	1.393(9)
C(22)-H(22)	0.9500
C(23)-C(24)	1.385(9)
C(23)-H(23)	0.9500
C(24)-H(24)	0.9500
C(25)-C(30)	1.387(8)
C(25)-C(26)	1.407(9)
C(26)-C(27)	1.381(10)
C(26)-H(26)	0.9500
C(27)-C(28)	1.377(11)
C(27)-H(27)	0.9500
C(28)-C(29)	1.393(11)

C(28)-H(28)	0.9500
C(29)-C(30)	1.394(9)
C(29)-H(29)	0.9500
C(30)-H(30)	0.9500
C(31)-C(36)	1.382(8)
C(31)-C(32)	1.402(8)
C(32)-C(33)	1.388(8)
C(32)-H(32)	0.9500
C(33)-C(34)	1.387(9)
C(33)-H(33)	0.9500
C(34)-C(35)	1.385(9)
C(34)-H(34)	0.9500
C(35)-C(36)	1.403(8)
C(35)-H(35)	0.9500
C(36)-H(36)	0.9500
C(37)-C(42)	1.395(7)
C(37)-C(38)	1.396(8)
C(38)-C(39)	1.369(8)
C(38)-H(38)	0.9500
C(39)-C(40)	1.391(8)
C(39)-H(39)	0.9500
C(40)-C(41)	1.383(8)
C(40)-H(40)	0.9500
C(41)-C(42)	1.389(8)
C(41)-H(41)	0.9500
C(42)-H(42)	0.9500
C(43)-C(48)	1.396(8)
C(43)-C(44)	1.397(8)
C(44)-C(45)	1.400(8)
C(44)-H(44)	0.9500
C(45)-C(46)	1.389(9)
C(45)-H(45)	0.9500
C(46)-C(47)	1.391(9)
C(46)-H(46)	0.9500
C(91)-C(90)	1.394(8)
C(91)-C(86)	1.403(8)

C(91)-H(91)	0.9500
C(47)-C(48)	1.403(8)
C(47)-H(47)	0.9500
C(48)-H(48)	0.9500
C(49)-C(50)	1.390(9)
C(49)-C(54)	1.406(8)
C(50)-C(51)	1.391(9)
C(50)-H(50)	0.9500
C(51)-C(52)	1.385(9)
C(51)-H(51)	0.9500
C(52)-C(53)	1.389(10)
C(52)-H(52)	0.9500
C(53)-C(54)	1.381(9)
C(53)-H(53)	0.9500
C(54)-H(54)	0.9500
C(55)-H(55A)	0.9800
C(55)-H(55B)	0.9800
C(55)-H(55C)	0.9800
C(56)-C(61)	1.392(9)
C(56)-C(57)	1.408(9)
C(57)-C(58)	1.393(10)
C(57)-H(57)	0.9500
C(58)-C(59)	1.378(10)
C(58)-H(58)	0.9500
C(59)-C(60)	1.393(10)
C(59)-H(59)	0.9500
C(60)-C(61)	1.389(10)
C(60)-H(60)	0.9500
C(61)-H(61)	0.9500
B-C(70)	1.637(9)
B-C(78)	1.641(8)
B-C(86)	1.644(9)
B-C(62)	1.651(8)
C(62)-C(67)	1.393(8)
C(62)-C(63)	1.397(8)
C(63)-C(64)	1.394(8)

C(63)-H(63)	0.9500
C(64)-C(65)	1.378(8)
C(64)-C(68)	1.496(8)
C(65)-C(66)	1.389(8)
C(65)-H(65)	0.9500
C(66)-C(67)	1.405(8)
C(66)-C(69)	1.496(8)
C(67)-H(67)	0.9500
C(68)-F(2)	1.344(7)
C(68)-F(1)	1.346(6)
C(68)-F(3)	1.351(6)
C(69)-F(5)	1.339(7)
C(69)-F(4)	1.346(7)
C(69)-F(6)	1.355(7)
C(70)-C(71)	1.394(8)
C(70)-C(75)	1.404(8)
C(71)-C(72)	1.405(8)
C(71)-H(71)	0.9500
C(72)-C(73)	1.401(8)
C(72)-C(76)	1.490(9)
C(73)-C(74)	1.390(8)
C(73)-H(73)	0.9500
C(74)-C(75)	1.406(8)
C(74)-C(77)	1.491(8)
C(75)-H(75)	0.9500
C(76)-F(7)	1.309(8)
C(76)-F(8)	1.309(8)
C(76)-F(9)	1.330(8)
C(77)-F(10)	1.300(8)
C(77)-F(11)	1.319(8)
C(77)-F(12)	1.322(7)
C(78)-C(79)	1.392(8)
C(78)-C(83)	1.402(8)
C(79)-C(80)	1.395(8)
C(79)-H(79)	0.9500
C(80)-C(81)	1.387(9)

C(80)-C(84)	1.492(8)
C(81)-C(82)	1.396(8)
C(81)-H(81)	0.9500
C(82)-C(83)	1.397(8)
C(82)-C(85)	1.493(9)
C(83)-H(83)	0.9500
C(84)-F(13)	1.250(9)
C(84)-F(15)	1.269(9)
C(84)-F(14)	1.280(11)
C(85)-F(17)	1.325(9)
C(85)-F(16)	1.333(7)
C(85)-F(18)	1.336(8)
C(86)-C(87)	1.398(8)
C(87)-C(88)	1.395(8)
C(87)-H(87)	0.9500
C(88)-C(89)	1.385(8)
C(88)-C(92)	1.499(9)
C(89)-C(90)	1.392(9)
C(89)-H(89)	0.9500
C(90)-C(93)	1.508(8)
C(92)-F(21)	1.248(9)
C(92)-F(19)	1.293(8)
C(92)-F(20)	1.343(10)
C(93)-F(22)	1.329(7)
C(93)-F(24)	1.334(7)
C(93)-F(23)	1.340(7)

H(1A)-Pt-Si(1)	178.9
H(1A)-Pt-P(2)	96.4
Si(1)-Pt-P(2)	82.81(8)
H(1A)-Pt-P(1)	97.3
Si(1)-Pt-P(1)	83.77(9)
P(2)-Pt-P(1)	122.10(9)
H(1A)-Pt-P(3)	95.7
Si(1)-Pt-P(3)	83.97(7)
P(2)-Pt-P(3)	117.64(9)

P(1)-Pt-P(3)	116.47(8)
H(1A)-Pt-Si(2)	4.7
Si(1)-Pt-Si(2)	176.40(5)
P(2)-Pt-Si(2)	99.47(8)
P(1)-Pt-Si(2)	92.64(9)
P(3)-Pt-Si(2)	97.35(7)
C(19)-P(1)-C(25)	104.9(3)
C(19)-P(1)-C(2)	101.5(3)
C(25)-P(1)-C(2)	102.6(3)
C(19)-P(1)-Pt	119.54(19)
C(25)-P(1)-Pt	117.84(19)
C(2)-P(1)-Pt	108.00(19)
C(31)-P(2)-C(8)	106.7(3)
C(31)-P(2)-C(37)	103.6(2)
C(8)-P(2)-C(37)	103.0(3)
C(31)-P(2)-Pt	117.9(2)
C(8)-P(2)-Pt	110.35(19)
C(37)-P(2)-Pt	113.9(2)
C(43)-P(3)-C(14)	105.1(3)
C(43)-P(3)-C(49)	103.4(3)
C(14)-P(3)-C(49)	101.2(3)
C(43)-P(3)-Pt	119.24(19)
C(14)-P(3)-Pt	108.0(2)
C(49)-P(3)-Pt	117.76(19)
C(1)-Si(1)-C(13)	109.7(2)
C(1)-Si(1)-C(7)	113.8(3)
C(13)-Si(1)-C(7)	107.4(3)
C(1)-Si(1)-Pt	108.5(2)
C(13)-Si(1)-Pt	107.57(19)
C(7)-Si(1)-Pt	109.69(18)
C(55)-Si(2)-C(56)	114.4(4)
C(55)-Si(2)-Pt	117.6(3)
C(56)-Si(2)-Pt	107.6(2)
C(55)-Si(2)-H(1A)	108.7
C(56)-Si(2)-H(1A)	108.7
Pt-Si(2)-H(1A)	10.5

C(55)-Si(2)-H(1B)	108.7
C(56)-Si(2)-H(1B)	108.7
Pt-Si(2)-H(1B)	98.6
H(1A)-Si(2)-H(1B)	107.6
C(6)-C(1)-C(2)	117.6(5)
C(6)-C(1)-Si(1)	124.2(4)
C(2)-C(1)-Si(1)	118.1(4)
C(3)-C(2)-C(1)	121.2(5)
C(3)-C(2)-P(1)	122.0(4)
C(1)-C(2)-P(1)	116.8(4)
C(2)-C(3)-C(4)	119.5(6)
C(2)-C(3)-H(3)	120.2
C(4)-C(3)-H(3)	120.2
C(5)-C(4)-C(3)	120.4(6)
C(5)-C(4)-H(4)	119.8
C(3)-C(4)-H(4)	119.8
C(6)-C(5)-C(4)	119.4(5)
C(6)-C(5)-H(5)	120.3
C(4)-C(5)-H(5)	120.3
C(5)-C(6)-C(1)	121.8(6)
C(5)-C(6)-H(6)	119.1
C(1)-C(6)-H(6)	119.1
C(8)-C(7)-C(12)	118.6(5)
C(8)-C(7)-Si(1)	116.8(4)
C(12)-C(7)-Si(1)	123.9(4)
C(9)-C(8)-C(7)	120.5(5)
C(9)-C(8)-P(2)	122.9(4)
C(7)-C(8)-P(2)	116.6(4)
C(8)-C(9)-C(10)	120.3(5)
C(8)-C(9)-H(9)	119.9
C(10)-C(9)-H(9)	119.9
C(9)-C(10)-C(11)	119.4(6)
C(9)-C(10)-H(10)	120.3
C(11)-C(10)-H(10)	120.3
C(12)-C(11)-C(10)	120.7(6)
C(12)-C(11)-H(11)	119.7

C(10)-C(11)-H(11)	119.7
C(11)-C(12)-C(7)	120.5(5)
C(11)-C(12)-H(12)	119.8
C(7)-C(12)-H(12)	119.8
C(18)-C(13)-C(14)	118.3(5)
C(18)-C(13)-Si(1)	122.6(5)
C(14)-C(13)-Si(1)	119.0(4)
C(15)-C(14)-C(13)	121.2(5)
C(15)-C(14)-P(3)	122.9(5)
C(13)-C(14)-P(3)	115.8(4)
C(14)-C(15)-C(16)	118.9(5)
C(14)-C(15)-H(15)	120.6
C(16)-C(15)-H(15)	120.6
C(17)-C(16)-C(15)	121.1(5)
C(17)-C(16)-H(16)	119.5
C(15)-C(16)-H(16)	119.5
C(16)-C(17)-C(18)	119.8(6)
C(16)-C(17)-H(17)	120.1
C(18)-C(17)-H(17)	120.1
C(13)-C(18)-C(17)	120.7(6)
C(13)-C(18)-H(18)	119.6
C(17)-C(18)-H(18)	119.6
C(24)-C(19)-C(20)	118.5(6)
C(24)-C(19)-P(1)	123.2(5)
C(20)-C(19)-P(1)	118.2(4)
C(21)-C(20)-C(19)	121.0(6)
C(21)-C(20)-H(20)	119.5
C(19)-C(20)-H(20)	119.5
C(20)-C(21)-C(22)	120.4(6)
C(20)-C(21)-H(21)	119.8
C(22)-C(21)-H(21)	119.8
C(21)-C(22)-C(23)	119.0(6)
C(21)-C(22)-H(22)	120.5
C(23)-C(22)-H(22)	120.5
C(24)-C(23)-C(22)	121.1(6)
C(24)-C(23)-H(23)	119.5

C(22)-C(23)-H(23)	119.5
C(23)-C(24)-C(19)	120.0(6)
C(23)-C(24)-H(24)	120.0
C(19)-C(24)-H(24)	120.0
C(30)-C(25)-C(26)	118.1(6)
C(30)-C(25)-P(1)	121.0(5)
C(26)-C(25)-P(1)	120.9(5)
C(27)-C(26)-C(25)	120.7(6)
C(27)-C(26)-H(26)	119.7
C(25)-C(26)-H(26)	119.7
C(28)-C(27)-C(26)	120.8(7)
C(28)-C(27)-H(27)	119.6
C(26)-C(27)-H(27)	119.6
C(27)-C(28)-C(29)	119.5(6)
C(27)-C(28)-H(28)	120.3
C(29)-C(28)-H(28)	120.3
C(28)-C(29)-C(30)	119.9(6)
C(28)-C(29)-H(29)	120.0
C(30)-C(29)-H(29)	120.0
C(25)-C(30)-C(29)	121.1(6)
C(25)-C(30)-H(30)	119.5
C(29)-C(30)-H(30)	119.5
C(36)-C(31)-C(32)	119.0(5)
C(36)-C(31)-P(2)	118.6(4)
C(32)-C(31)-P(2)	122.4(4)
C(33)-C(32)-C(31)	120.5(5)
C(33)-C(32)-H(32)	119.8
C(31)-C(32)-H(32)	119.8
C(34)-C(33)-C(32)	119.8(6)
C(34)-C(33)-H(33)	120.1
C(32)-C(33)-H(33)	120.1
C(35)-C(34)-C(33)	120.6(5)
C(35)-C(34)-H(34)	119.7
C(33)-C(34)-H(34)	119.7
C(34)-C(35)-C(36)	119.2(6)
C(34)-C(35)-H(35)	120.4

C(36)-C(35)-H(35)	120.4
C(31)-C(36)-C(35)	121.0(6)
C(31)-C(36)-H(36)	119.5
C(35)-C(36)-H(36)	119.5
C(42)-C(37)-C(38)	118.9(5)
C(42)-C(37)-P(2)	120.9(4)
C(38)-C(37)-P(2)	119.6(4)
C(39)-C(38)-C(37)	120.5(5)
C(39)-C(38)-H(38)	119.7
C(37)-C(38)-H(38)	119.7
C(38)-C(39)-C(40)	120.8(5)
C(38)-C(39)-H(39)	119.6
C(40)-C(39)-H(39)	119.6
C(41)-C(40)-C(39)	119.2(5)
C(41)-C(40)-H(40)	120.4
C(39)-C(40)-H(40)	120.4
C(40)-C(41)-C(42)	120.4(5)
C(40)-C(41)-H(41)	119.8
C(42)-C(41)-H(41)	119.8
C(41)-C(42)-C(37)	120.2(5)
C(41)-C(42)-H(42)	119.9
C(37)-C(42)-H(42)	119.9
C(48)-C(43)-C(44)	119.2(5)
C(48)-C(43)-P(3)	122.7(4)
C(44)-C(43)-P(3)	118.1(4)
C(43)-C(44)-C(45)	120.2(6)
C(43)-C(44)-H(44)	119.9
C(45)-C(44)-H(44)	119.9
C(46)-C(45)-C(44)	120.3(6)
C(46)-C(45)-H(45)	119.8
C(44)-C(45)-H(45)	119.8
C(45)-C(46)-C(47)	119.8(6)
C(45)-C(46)-H(46)	120.1
C(47)-C(46)-H(46)	120.1
C(90)-C(91)-C(86)	122.6(5)
C(90)-C(91)-H(91)	118.7

C(86)-C(91)-H(91)	118.7
C(46)-C(47)-C(48)	119.9(6)
C(46)-C(47)-H(47)	120.0
C(48)-C(47)-H(47)	120.0
C(43)-C(48)-C(47)	120.4(5)
C(43)-C(48)-H(48)	119.8
C(47)-C(48)-H(48)	119.8
C(50)-C(49)-C(54)	118.9(6)
C(50)-C(49)-P(3)	122.2(4)
C(54)-C(49)-P(3)	118.7(5)
C(49)-C(50)-C(51)	119.9(6)
C(49)-C(50)-H(50)	120.1
C(51)-C(50)-H(50)	120.1
C(52)-C(51)-C(50)	121.3(6)
C(52)-C(51)-H(51)	119.3
C(50)-C(51)-H(51)	119.3
C(51)-C(52)-C(53)	118.6(6)
C(51)-C(52)-H(52)	120.7
C(53)-C(52)-H(52)	120.7
C(54)-C(53)-C(52)	121.0(6)
C(54)-C(53)-H(53)	119.5
C(52)-C(53)-H(53)	119.5
C(53)-C(54)-C(49)	120.3(6)
C(53)-C(54)-H(54)	119.9
C(49)-C(54)-H(54)	119.9
Si(2)-C(55)-H(55A)	109.5
Si(2)-C(55)-H(55B)	109.5
H(55A)-C(55)-H(55B)	109.5
Si(2)-C(55)-H(55C)	109.5
H(55A)-C(55)-H(55C)	109.5
H(55B)-C(55)-H(55C)	109.5
C(61)-C(56)-C(57)	118.5(7)
C(61)-C(56)-Si(2)	118.4(5)
C(57)-C(56)-Si(2)	123.1(5)
C(58)-C(57)-C(56)	120.4(7)
C(58)-C(57)-H(57)	119.8

C(56)-C(57)-H(57)	119.8
C(59)-C(58)-C(57)	119.7(6)
C(59)-C(58)-H(58)	120.1
C(57)-C(58)-H(58)	120.1
C(58)-C(59)-C(60)	120.9(7)
C(58)-C(59)-H(59)	119.5
C(60)-C(59)-H(59)	119.5
C(61)-C(60)-C(59)	119.2(6)
C(61)-C(60)-H(60)	120.4
C(59)-C(60)-H(60)	120.4
C(60)-C(61)-C(56)	121.2(6)
C(60)-C(61)-H(61)	119.4
C(56)-C(61)-H(61)	119.4
C(70)-B-C(78)	113.5(5)
C(70)-B-C(86)	113.7(5)
C(78)-B-C(86)	103.3(4)
C(70)-B-C(62)	103.2(4)
C(78)-B-C(62)	112.5(5)
C(86)-B-C(62)	110.9(5)
C(67)-C(62)-C(63)	116.8(5)
C(67)-C(62)-B	123.1(5)
C(63)-C(62)-B	119.7(5)
C(64)-C(63)-C(62)	121.4(5)
C(64)-C(63)-H(63)	119.3
C(62)-C(63)-H(63)	119.3
C(65)-C(64)-C(63)	121.8(5)
C(65)-C(64)-C(68)	118.1(5)
C(63)-C(64)-C(68)	120.1(5)
C(64)-C(65)-C(66)	117.5(5)
C(64)-C(65)-H(65)	121.3
C(66)-C(65)-H(65)	121.3
C(65)-C(66)-C(67)	121.2(5)
C(65)-C(66)-C(69)	121.0(5)
C(67)-C(66)-C(69)	117.8(5)
C(62)-C(67)-C(66)	121.3(5)
C(62)-C(67)-H(67)	119.3

C(66)-C(67)-H(67)	119.3
F(2)-C(68)-F(1)	105.4(5)
F(2)-C(68)-F(3)	105.1(5)
F(1)-C(68)-F(3)	106.5(4)
F(2)-C(68)-C(64)	113.2(4)
F(1)-C(68)-C(64)	113.9(5)
F(3)-C(68)-C(64)	112.1(5)
F(5)-C(69)-F(4)	107.3(5)
F(5)-C(69)-F(6)	105.1(5)
F(4)-C(69)-F(6)	105.6(5)
F(5)-C(69)-C(66)	113.0(5)
F(4)-C(69)-C(66)	113.1(5)
F(6)-C(69)-C(66)	112.2(5)
C(71)-C(70)-C(75)	116.6(5)
C(71)-C(70)-B	122.9(5)
C(75)-C(70)-B	120.2(5)
C(70)-C(71)-C(72)	122.0(6)
C(70)-C(71)-H(71)	119.0
C(72)-C(71)-H(71)	119.0
C(73)-C(72)-C(71)	120.4(6)
C(73)-C(72)-C(76)	119.9(6)
C(71)-C(72)-C(76)	119.6(6)
C(74)-C(73)-C(72)	118.7(5)
C(74)-C(73)-H(73)	120.7
C(72)-C(73)-H(73)	120.7
C(73)-C(74)-C(75)	120.1(5)
C(73)-C(74)-C(77)	120.2(5)
C(75)-C(74)-C(77)	119.7(5)
C(70)-C(75)-C(74)	122.3(5)
C(70)-C(75)-H(75)	118.8
C(74)-C(75)-H(75)	118.8
F(7)-C(76)-F(8)	107.3(6)
F(7)-C(76)-F(9)	104.7(6)
F(8)-C(76)-F(9)	105.5(6)
F(7)-C(76)-C(72)	113.7(6)
F(8)-C(76)-C(72)	111.9(6)

F(9)-C(76)-C(72)	113.1(6)
F(10)-C(77)-F(11)	105.7(6)
F(10)-C(77)-F(12)	107.1(6)
F(11)-C(77)-F(12)	105.2(6)
F(10)-C(77)-C(74)	114.1(5)
F(11)-C(77)-C(74)	112.0(5)
F(12)-C(77)-C(74)	112.1(5)
C(79)-C(78)-C(83)	116.4(5)
C(79)-C(78)-B	120.5(5)
C(83)-C(78)-B	122.3(5)
C(78)-C(79)-C(80)	121.9(5)
C(78)-C(79)-H(79)	119.0
C(80)-C(79)-H(79)	119.0
C(81)-C(80)-C(79)	121.2(5)
C(81)-C(80)-C(84)	119.4(5)
C(79)-C(80)-C(84)	119.3(5)
C(80)-C(81)-C(82)	117.9(5)
C(80)-C(81)-H(81)	121.0
C(82)-C(81)-H(81)	121.0
C(81)-C(82)-C(83)	120.5(5)
C(81)-C(82)-C(85)	119.4(5)
C(83)-C(82)-C(85)	120.1(5)
C(82)-C(83)-C(78)	122.0(5)
C(82)-C(83)-H(83)	119.0
C(78)-C(83)-H(83)	119.0
F(13)-C(84)-F(15)	108.1(8)
F(13)-C(84)-F(14)	102.4(9)
F(15)-C(84)-F(14)	100.9(9)
F(13)-C(84)-C(80)	115.8(6)
F(15)-C(84)-C(80)	115.3(6)
F(14)-C(84)-C(80)	112.6(7)
F(17)-C(85)-F(16)	106.5(6)
F(17)-C(85)-F(18)	105.5(6)
F(16)-C(85)-F(18)	104.2(6)
F(17)-C(85)-C(82)	112.7(6)
F(16)-C(85)-C(82)	113.6(5)

F(18)-C(85)-C(82)	113.5(5)
C(87)-C(86)-C(91)	115.8(5)
C(87)-C(86)-B	125.2(5)
C(91)-C(86)-B	118.5(5)
C(88)-C(87)-C(86)	122.1(5)
C(88)-C(87)-H(87)	118.9
C(86)-C(87)-H(87)	118.9
C(89)-C(88)-C(87)	120.9(6)
C(89)-C(88)-C(92)	118.6(6)
C(87)-C(88)-C(92)	120.5(6)
C(88)-C(89)-C(90)	118.4(6)
C(88)-C(89)-H(89)	120.8
C(90)-C(89)-H(89)	120.8
C(89)-C(90)-C(91)	120.2(5)
C(89)-C(90)-C(93)	121.3(6)
C(91)-C(90)-C(93)	118.5(5)
F(21)-C(92)-F(19)	112.5(8)
F(21)-C(92)-F(20)	102.5(8)
F(19)-C(92)-F(20)	99.5(6)
F(21)-C(92)-C(88)	115.0(6)
F(19)-C(92)-C(88)	114.8(6)
F(20)-C(92)-C(88)	110.7(6)
F(22)-C(93)-F(24)	107.9(5)
F(22)-C(93)-F(23)	106.7(5)
F(24)-C(93)-F(23)	106.5(5)
F(22)-C(93)-C(90)	111.8(5)
F(24)-C(93)-C(90)	112.1(5)
F(23)-C(93)-C(90)	111.6(5)

Symmetry transformations used to generate equivalent atoms:

Table A5.8. Anisotropic displacement parameters ($Å^2 x\ 10^3$) for **6.6.2**. The anisotropic displacement factor exponent takes the form: $-2p^2[\ h^2\ a^{*2}U^{11} + ... + 2\ h\ k\ a^*\ b^*\ U^{12}\ ]$

	U^{11}	U^{22}	U^{33}	U^{23}	U^{13}	U^{12}
Pt	10(1)	11(1)	12(1)	-6(1)	-4(1)	1(1)
P(1)	10(1)	13(1)	11(1)	-5(1)	-2(1)	1(1)
P(2)	9(1)	12(1)	13(1)	-6(1)	-5(1)	1(1)
P(3)	12(1)	10(1)	13(1)	-5(1)	-4(1)	1(1)
Si(1)	11(1)	12(1)	11(1)	-5(1)	-4(1)	2(1)
Si(2)	34(1)	23(1)	18(1)	-10(1)	-6(1)	4(1)
C(1)	13(3)	11(3)	20(3)	-7(2)	-6(2)	0(2)
C(2)	17(3)	18(3)	11(3)	-6(2)	-4(2)	2(2)
C(3)	16(3)	34(4)	22(3)	-8(3)	-3(2)	-4(3)
C(4)	20(3)	39(4)	17(3)	-5(3)	-6(3)	-7(3)
C(5)	25(3)	27(4)	15(3)	-7(3)	-8(2)	-6(3)
C(6)	22(3)	21(3)	18(3)	-12(3)	-2(2)	-6(3)
C(7)	10(2)	12(3)	13(3)	-7(2)	0(2)	2(2)
C(8)	6(2)	12(3)	19(3)	-7(2)	-3(2)	1(2)
C(9)	14(3)	18(3)	23(3)	-8(3)	-6(2)	0(2)
C(10)	18(3)	11(3)	28(3)	-6(3)	-2(2)	-4(2)
C(11)	24(3)	18(3)	11(3)	0(2)	-1(2)	3(3)
C(12)	18(3)	15(3)	20(3)	-6(3)	-7(2)	4(2)
C(13)	8(2)	18(3)	17(3)	-10(2)	0(2)	-5(2)
C(14)	11(3)	16(3)	14(3)	-10(2)	-2(2)	-4(2)
C(15)	15(3)	12(3)	21(3)	-6(2)	-3(2)	-1(2)
C(16)	17(3)	16(3)	29(3)	-15(3)	-3(2)	5(2)
C(17)	17(3)	27(4)	24(3)	-16(3)	3(2)	-2(3)
C(18)	16(3)	18(3)	20(3)	-9(3)	-6(2)	-1(2)
C(19)	14(3)	16(3)	16(3)	-2(2)	-8(2)	0(2)
C(20)	18(3)	19(3)	19(3)	-8(3)	-1(2)	0(2)
C(21)	19(3)	20(3)	35(4)	-6(3)	-7(3)	1(3)
C(22)	16(3)	27(4)	21(3)	2(3)	-1(2)	-2(3)
C(23)	19(3)	28(4)	16(3)	-4(3)	-2(2)	9(3)
C(24)	17(3)	25(3)	14(3)	-7(3)	-6(2)	6(3)
C(25)	7(2)	14(3)	30(3)	-10(3)	-6(2)	1(2)

C(26)	18(3)	17(3)	29(4)	-4(3)	-2(3)	1(3)
C(27)	19(3)	29(4)	40(4)	0(3)	1(3)	3(3)
C(28)	19(3)	16(3)	60(5)	-15(3)	-5(3)	6(3)
C(29)	21(3)	33(4)	54(5)	-31(4)	-7(3)	1(3)
C(30)	12(3)	19(3)	33(4)	-13(3)	-8(2)	2(2)
C(31)	19(3)	9(3)	11(3)	-3(2)	-7(2)	5(2)
C(32)	17(3)	14(3)	26(3)	-6(3)	-11(2)	4(2)
C(33)	22(3)	19(3)	25(3)	-9(3)	-12(3)	-2(3)
C(34)	33(3)	15(3)	21(3)	-14(3)	-8(3)	4(3)
C(35)	21(3)	25(4)	25(3)	-14(3)	-2(3)	6(3)
C(36)	24(3)	15(3)	23(3)	-11(3)	-5(2)	-1(2)
C(37)	4(2)	10(3)	21(3)	-5(2)	-4(2)	-4(2)
C(38)	21(3)	11(3)	11(3)	1(2)	-6(2)	2(2)
C(39)	17(3)	17(3)	19(3)	-5(3)	3(2)	4(2)
C(40)	6(3)	24(3)	27(3)	-6(3)	-7(2)	2(2)
C(41)	27(3)	16(3)	23(3)	-9(3)	-12(3)	2(3)
C(42)	18(3)	20(3)	20(3)	-14(3)	-5(2)	-2(2)
C(43)	10(3)	15(3)	17(3)	-7(2)	-3(2)	3(2)
C(44)	21(3)	17(3)	18(3)	-3(3)	-10(2)	4(2)
C(45)	26(3)	21(3)	24(3)	0(3)	-15(3)	-3(3)
C(46)	23(3)	25(4)	26(4)	-5(3)	-12(3)	4(3)
C(91)	18(3)	13(3)	12(3)	-4(2)	-4(2)	-2(2)
C(47)	28(3)	13(3)	29(4)	-4(3)	-12(3)	8(3)
C(48)	16(3)	22(3)	17(3)	-9(3)	-4(2)	1(2)
C(49)	16(3)	16(3)	15(3)	-7(2)	0(2)	2(2)
C(50)	17(3)	26(3)	20(3)	-11(3)	-5(2)	2(3)
C(51)	26(3)	22(4)	28(4)	-7(3)	3(3)	-4(3)
C(52)	18(3)	27(4)	42(4)	-23(3)	4(3)	-11(3)
C(53)	20(3)	31(4)	33(4)	-24(3)	-1(3)	-2(3)
C(54)	11(3)	21(3)	25(3)	-14(3)	-1(2)	0(2)
C(55)	63(5)	51(5)	26(4)	-17(4)	-15(4)	-10(4)
C(56)	31(4)	30(4)	15(3)	-7(3)	-3(3)	4(3)
C(57)	28(3)	35(4)	18(3)	-5(3)	-2(3)	0(3)
C(58)	35(4)	28(4)	22(4)	-3(3)	-6(3)	12(3)
C(59)	43(4)	21(4)	15(3)	3(3)	-3(3)	-2(3)
C(60)	24(3)	37(4)	18(3)	-3(3)	-2(3)	-1(3)

C(61)	29(3)	23(4)	19(3)	-3(3)	-6(3)	8(3)
B	20(3)	9(3)	15(3)	-3(3)	-7(3)	-1(3)
C(62)	13(3)	14(3)	15(3)	-5(2)	-7(2)	1(2)
C(63)	16(3)	10(3)	12(3)	-1(2)	-4(2)	0(2)
C(64)	6(2)	13(3)	28(3)	-4(3)	-6(2)	1(2)
C(65)	14(3)	12(3)	17(3)	-9(2)	-7(2)	-1(2)
C(66)	14(3)	21(3)	13(3)	-5(2)	-4(2)	-1(2)
C(67)	10(3)	13(3)	18(3)	-4(2)	-3(2)	0(2)
C(68)	16(3)	17(3)	18(3)	-8(3)	-8(2)	4(2)
C(69)	34(3)	16(3)	15(3)	-8(3)	-6(3)	-5(3)
C(70)	21(3)	10(3)	15(3)	-6(2)	-3(2)	-1(2)
C(71)	19(3)	16(3)	19(3)	-10(3)	-1(2)	0(2)
C(72)	24(3)	16(3)	21(3)	-7(3)	-2(3)	-6(3)
C(73)	15(3)	19(3)	23(3)	-9(3)	-4(2)	1(2)
C(74)	22(3)	9(3)	18(3)	-8(2)	-5(2)	4(2)
C(75)	20(3)	15(3)	16(3)	-8(2)	-4(2)	0(2)
C(76)	30(4)	33(4)	16(3)	-8(3)	4(3)	-4(3)
C(77)	23(3)	27(4)	26(4)	-12(3)	-8(3)	2(3)
C(78)	17(3)	17(3)	13(3)	-4(2)	0(2)	-3(2)
C(79)	17(3)	14(3)	16(3)	-4(2)	-6(2)	1(2)
C(80)	28(3)	18(3)	17(3)	-7(3)	-7(3)	0(3)
C(81)	29(3)	26(4)	21(3)	-11(3)	-13(3)	-1(3)
C(82)	20(3)	18(3)	19(3)	-3(3)	-5(2)	-2(2)
C(83)	18(3)	18(3)	16(3)	-9(3)	-4(2)	0(2)
C(84)	46(4)	40(5)	33(4)	-28(4)	-17(3)	12(4)
C(85)	28(4)	41(4)	24(4)	-17(3)	-8(3)	3(3)
C(86)	18(3)	12(3)	13(3)	-4(2)	-6(2)	-2(2)
C(87)	13(3)	20(3)	17(3)	-6(3)	-5(2)	0(2)
C(88)	21(3)	13(3)	20(3)	-1(3)	-12(2)	1(2)
C(89)	18(3)	20(3)	20(3)	-4(3)	-8(2)	-5(2)
C(90)	13(3)	21(3)	14(3)	-7(3)	-6(2)	-4(2)
C(92)	25(3)	13(3)	45(4)	0(3)	-6(3)	3(3)
C(93)	20(3)	23(3)	22(3)	-5(3)	-5(2)	-5(3)
F(1)	39(2)	14(2)	19(2)	-7(2)	-12(2)	-1(2)
F(2)	32(2)	21(2)	23(2)	1(2)	-10(2)	-12(2)
F(3)	38(2)	20(2)	34(2)	-2(2)	-2(2)	13(2)

F(4)	80(3)	22(2)	21(2)	-13(2)	-11(2)	-3(2)
F(5)	30(2)	32(2)	16(2)	-5(2)	4(2)	-10(2)
F(6)	30(2)	49(3)	21(2)	-10(2)	-13(2)	-3(2)
F(7)	56(3)	98(4)	16(2)	6(3)	6(2)	17(3)
F(8)	157(6)	54(4)	37(3)	-32(3)	31(3)	-27(4)
F(9)	38(3)	107(5)	29(3)	-13(3)	14(2)	-33(3)
F(10)	29(3)	185(7)	48(3)	-45(4)	-21(2)	44(4)
F(11)	95(4)	27(2)	58(3)	6(2)	-59(3)	-11(3)
F(12)	81(3)	35(3)	51(3)	-30(2)	-46(3)	22(2)
F(13)	274(11)	121(6)	140(6)	-123(6)	-162(7)	154(7)
F(14)	315(14)	104(7)	122(7)	-101(6)	115(8)	-78(8)
F(15)	119(6)	188(9)	231(10)	-193(9)	-120(7)	87(6)
F(16)	67(3)	77(4)	47(3)	-36(3)	-42(3)	43(3)
F(17)	23(2)	70(4)	90(4)	17(3)	10(3)	13(2)
F(18)	46(3)	55(3)	82(4)	-47(3)	-36(3)	29(2)
F(19)	87(4)	23(3)	98(5)	0(3)	37(4)	20(3)
F(20)	154(7)	68(4)	73(4)	0(4)	-38(4)	67(5)
F(21)	58(4)	21(3)	417(16)	-80(6)	-82(6)	16(3)
F(22)	18(2)	58(3)	34(2)	-14(2)	-10(2)	3(2)
F(23)	30(2)	37(2)	50(3)	-29(2)	4(2)	-3(2)
F(24)	30(2)	33(2)	27(2)	2(2)	3(2)	-3(2)

Table A5.9. Hydrogen coordinates (x 10^4) and isotropic displacement parameters ($Å^2$x 10^{-3}) for **6.6.2**.

	x	y	z	U(eq)
H(1A)	8659	6617	8244	29
H(1B)	7745	6820	8802	29
H(3)	5332	7158	6295	30
H(4)	5155	7105	5170	32
H(5)	6618	7074	4310	27
H(6)	8246	7146	4556	23
H(9)	11355	9391	5656	22
H(10)	11586	10065	4382	24
H(11)	10648	9616	3707	23
H(12)	9515	8502	4287	20
H(15)	10805	4601	6431	19
H(16)	11557	4781	5221	23
H(17)	11336	5981	4263	26
H(18)	10325	7020	4500	21
H(20)	6471	5584	7275	22
H(21)	5188	4665	8084	31
H(22)	4028	5028	8957	29
H(23)	4163	6337	8993	27
H(24)	5385	7293	8141	22
H(26)	6615	8703	5796	28
H(27)	6164	10028	5697	41
H(28)	5915	10405	6717	38
H(29)	6159	9444	7852	38
H(30)	6643	8114	7954	24
H(32)	11446	9150	6880	22
H(33)	11153	10102	7457	25
H(34)	9514	10187	8117	25
H(35)	8145	9360	8168	27
H(36)	8442	8408	7578	23
H(38)	11779	7323	5889	18

H(39)	13297	6652	6112	23
H(40)	13884	6456	7197	23
H(41)	12924	6951	8057	25
H(42)	11386	7627	7840	21
H(44)	10743	6039	7844	23
H(45)	11932	5368	8590	29
H(46)	12103	3951	8949	30
H(91)	4853	8276	3065	17
H(47)	11133	3204	8522	29
H(48)	9973	3877	7748	21
H(50)	8215	4271	8351	24
H(51)	6895	3355	8494	32
H(52)	6216	3379	7489	33
H(53)	6856	4356	6330	30
H(54)	8214	5241	6164	22
H(55A)	9065	6722	9688	67
H(55B)	9461	7433	8912	67
H(55C)	9979	6555	9108	67
H(57)	9412	4935	9479	34
H(58)	8902	3550	9975	36
H(59)	7212	3175	10036	35
H(60)	6002	4171	9617	34
H(61)	6515	5553	9104	30
H(63)	6832	10061	1245	16
H(65)	6689	11165	2723	15
H(67)	6479	8680	3400	17
H(71)	7961	8791	716	21
H(73)	10784	8214	1283	22
H(75)	8186	7794	2852	20
H(79)	6705	7667	1075	19
H(81)	4221	8533	121	28
H(83)	4916	9336	1651	20
H(87)	7002	6705	2673	20
H(89)	4517	5857	4313	24